Karlsruhe Institute of Technology

Annual Report 2011

October 2012

Karlsruhe Nano Micro Facility (KNMF)

Dr. Jürgen Mohr, Dr. Susan Anson, Thomas Schaller

A colour version of this report is available for download
on the KNMF website (www.knmf.kit.edu)

KIT – University of the State of Baden-Wuerttemberg and
National Research Center of the Helmholtz Association

Karlsruhe Institute of Technology (KIT)
Karlsruhe Nano Micro Facility (KNMF)
Hermann-von-Helmholtz-Platz 1
76344 Eggenstein-Leopoldshafen
Germany

Phone: +49(721)608-23123
Fax: +49(721)608-26273
Email: knmf-useroffice@kit.edu

Table of Contents

KNMF – a Research Infrastructure Offering Open Access to Micro and Nano Technologies and Expertise for Academic and Industrial R&D Groups

Jürgen Mohr, Susan Anson, Thomas Schaller

Nano and micro technologies are recognised as being cross cutting and having relevance to a broad range of application areas [1]. As such they are key to innovative progress in the areas of health (e.g. integrated organic lasers for improved point – of care diagnostics), Information and Communication technologies (e.g. integrated Photonic elements), energy (e.g. self-organised structuring of electrodes for Lithium ion batteries), to name just a few examples from this report.

Indeed, to solve societal challenges in key application fields like micro and nano electronics, photonics, biotechnology, health and medical diagnostic or energy it is essential to bridge the so called valley of death that lies between scientific knowledge and market production. To cover the full R&D&I cycle and indeed link the full value chain, the bridge needs to be built on three pillars: technology, requiring adequate facilities, pilot deployment with the need of pilot lines and globally competitive manufacturing The first pillar which aims to transfer scientific knowledge to technology and functional principles is based on high risk developments and cost intensive and complex process equipment, process chains and infrastructure. It is globally recognized that taking the potential of scientific knowledge to innovation needs well equipped research infrastructures with competences in enabling and emerging micro and nano fabrication technologies, where users from academic and industrial organisations can enjoy open access to both not just equipment but also the essential know how [2, 3].

The Helmholtz Association (HGF) has recognised this potential and initiated the founding of the Karlsruhe Nano and Micro Facility (KNMF). KNMF has been established to facilitate access to high end technologies and expertise in the area of micro and nano structuring and characterisation. External users from academia and industry across the globe can access the nano- and micro technology laboratories, which pool key equipment with unique capabilities. KNMF complies with the Helmholtz guidelines on operating large scale user facilities and aims at being the leading micro and nano facility for a multitude of functional materials other than silicon not only in Germany but also in Europe.

Technologies offered

The selection of the technology portfolio of KNMF has been influenced by several factors of equal importance. Already existing technologies of the Helmholtz Program NANOMIKRO were chosen on account of their uniqueness and of the observed great demand by external organizations for access to this equipment, Secondly these technologies were complemented by additional high class equipment and expertise required to enhance existing external interest and collaborations . The third influential factor was a benchmarking study of international nano- and micro-oriented competence centres [4].

The technologies and equipment of KNMF is organized in three laboratories:

- KNMF laboratory for micro- and nanostructuring (opened in 2009)
- KNMF laboratory for microscopy and spectroscopy (opened in 2010)
- KNMF laboratory for synchrotron characterisation (opened in 2012)

At start the portfolio comprises eight technologies for structuring, and characterising functional materials and assemblies. There is an on-going investment programme in which new equipment is being commissioned and dedicated to be offered to KNMF users. The current status can be seen in Figure 1. In 2011 we added Dry etching technology (RIE/RIBE) to the portfolio. This opens up the possibility to combine silicon patterning with the already existing KNMF technologies. Patterning of thin metal layers down to nanometre structural size has already been demonstrated. Our lithography portfolio was complemented this year by highly advanced lithography methods comprising laser lithography and 2-photon 3-D laser writing. Laser lithography is a complementation to E-Beam lithography leading to more flexibility in testing new design approaches for micro structures with dimensions in the micron range. 2-photon 3-D laser writing opens up the possibility to fabricate truly 3D microstructures with nanometer features. Next year Nanoimprint Lithography will complete the technology offer. Also in 2013 we will establish a Helium Ion Microscope. With this machine, resolutions down to a few Angstöms only are possible with ion currents in the femtoamp range avoiding charging of non-conductive materials. In 2014 Atom Probe Tomography and Spectroscopy for chemical nano-synthesis will complete the offer in the laboratory for microscopy and spectroscopy. In the laboratory for synchrotron characterization additionally five methods will be made available in the next years, starting with Infrared Microscopy in 2013.

Currently, we offer a staggering total machine time of roughly 50.000 hours per year. In 2011 about 35 persons (scientists, technicians) were running the KNMF processes. The number will increase up to 50 persons in the next two years.

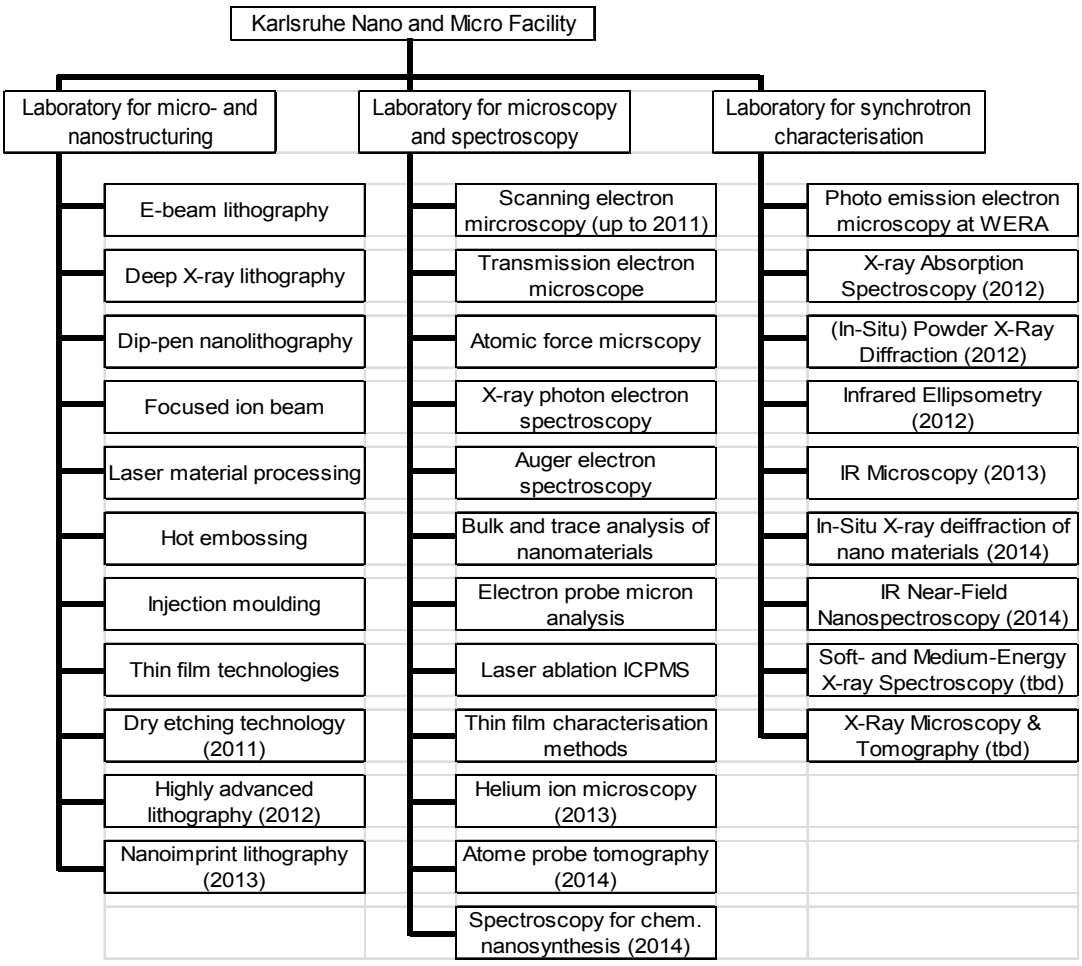

Fig. 1: Portfolio of KNMF as of today and future planning

Access and use of KNMF

A simple Peer Review process ensures transparent, open, and no fee access to KNMF for work intended for publication. Two calls per year are published and proposals are evaluated immediately after the close of the call. Full details of how to access KNMF can be found under http://www.knmf.kit.edu/ .

KNMF started operation in 2009 with 20 proposals submitted by external "users" in the first call which closed 15th January 2009. Since then the number of proposal has increased continuously reaching an average of 60 to 70 per call. Figure 2 shows the numbers of proposals submitted and accepted per call. The acceptance rate is in the range of 75% with slight differences for the different technologies. KNMF today is, as planned, still in the implementation phase which is characterized by an increase of the fraction of external use and which will result in an equal fraction of external and internal use in 2014. In 2011 the annual use by external users was about 25%, the forecast for 2012 is 40%.

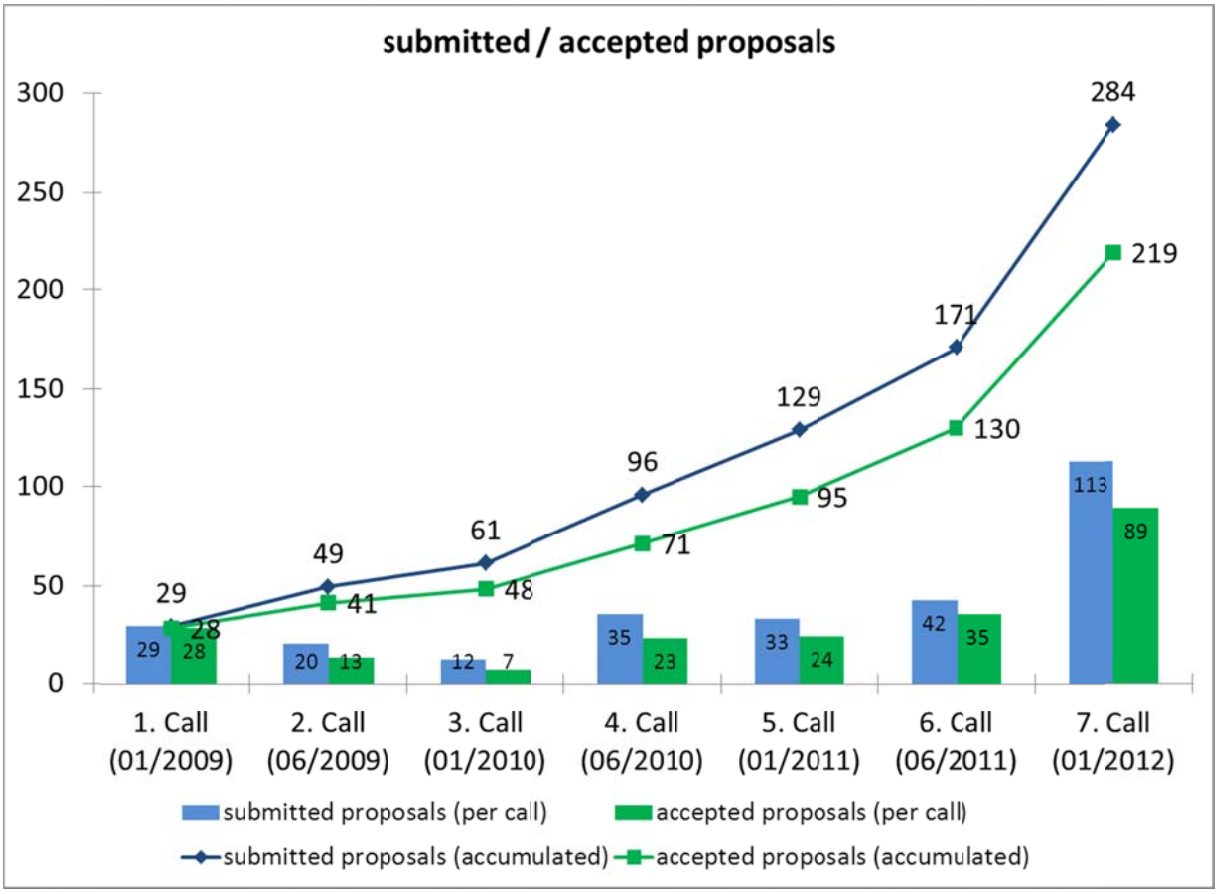

Fig. 2: Numbers of proposals submitted and accepted per call

Additionally proprietary users may access KNMF, this work is fully confidential and subject to full cost recovery. Usually these users are from industry. Figure 3 shows the type of organisation for users, including the proprietary work.

KNMF is not only intended for national users. Almost half of the users come from outside Germany, whereas 21% are from outside Europe. This demonstrates that KNMF's technology portfolio and competence is recognized as having worldwide relevance and also enables international groups to improve their scientific output (Figure 4).

Fig. 3: Type of organisation of users

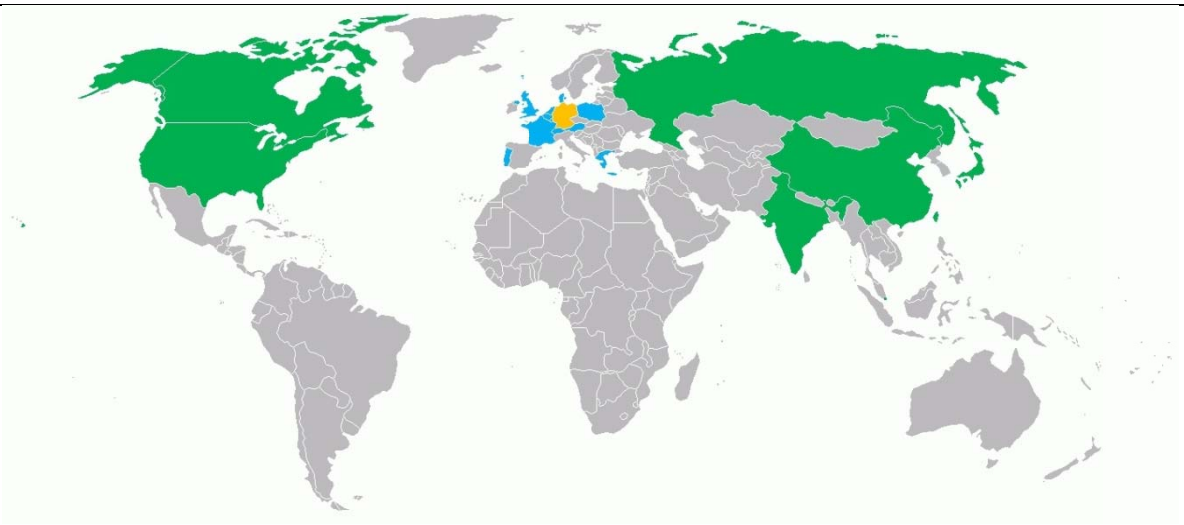

Fig. 4: Geographical origin of users
(accepted standard, long-term and fast-track proposals, call 1–7)

Call	1	2	3	4	5	6	7	Σ			
Germany	19	3	9	17	15	8	16	**87**	53%	**53%**	**Germany**
Austria				1			1	**2**	1%	**26%**	**Rest of Europe**
Belgium		1						**1**	1%		
Denmark					1	1		**2**	1%		
France			2	2		2	1	**7**	4%		
Greece	1							**1**	1%		
Luxemburg							1	**1**	1%		
Poland	2							**2**	1%		
Portugal					1	2	2	**5**	3%		
Switzerland		2		1	2	2	3	**10**	6%		
The Netherlands						1	1	**2**	1%		
United Kingdom	1			2		4	2	**9**	6%		
Canada	1	3			4	3		**11**	7%	**21%**	**Rest of the World**
China		1						**1**	1%		
India			1	1	1		2	**5**	3%		
Japan			1					**1**	1%		
Russia						2	1	**3**	2%		
Singapore							1	**1**	1%		
Taiwan				1		1		**2**	1%		
USA						7	3	**10**	6%		
Σ	*24*	*10*	*13*	*25*	*24*	*33*	*34*	***163***			

KNMF – a research facility

KNMF is not just an open access centre. Each of the technology clusters offered is engaged in in-house research, often in collaboration with other groups from within KIT or other Helmholtz centres. The driving force behind this research is furthering the technology state of the art, and pursuing innovation. Details of the latest advances can be read in the following section of this report.

KNMF has already demonstrated a huge impact on the scientific output in different nano and micro technology related fields. This is demonstrated by around 160 publications and presentations (more than 70 of them are in referenced journals) which are related to KNMF's activities. KNMF's users also received important prizes like the Leibniz Prize given to KNMF user Franz Pfeiffer from Technical University Munich in 2011.

User committee

In order to improve the level of our services and make them more relevant to the needs of our users we have established a User Committee. Nominations were requested by 11th October 2011. An election was held with electronic voting which closed 27th November 2011 and resulted on the formation of the committee. The elected members are:

- Prof. Dr. Sven Achenbach (Chair), University of Saskatchewan, Canada
- Prof. Dr. Florian Banhart, University of Strasbourg, France
- Dr. Erik Bründermann Ruhr-University of Bochum, Germany
- Dr. Jost Göttert, Louisiana State University, USA
- Prof. Dr. Lorenz Kienle, University of Kiel, Germany
- Dr. Karen Lienkamp (Co-Chair), University of Freiburg, Germany

International integration

KNMF recognizes that there is significant added value to be gained in forming contacts with peer organisations. As coordinating partner of the European research infrastructure for multimaterial micro and nanotechnologies EUMINAfab (http://www.euminafab.eu/) a FP7 I3 project running under the Capacities specific programme, we have taken the initiative to join forces with other access providing organisations. As a partner of the CSA action ACTMOST (http://www.actmost.eu/), a platform that pro-actively provides companies with access to cutting-edge micro-photonic technologies and knowledge we have a close link to application oriented activities in Photonics by supporting industry in the development of new and innovative photonic products. Particular benefit of such cooperation is not just the additional users attracted to KNMF by the broader circles of contact but also in being able to share knowledge about technological advances and also to learn of different approaches at the other access centres. We also welcome discussion with other similar organisations worldwide.

References

[1] High level group on Key Enabling Technologies, Final Report June 2011

[2] Green Paper on a Common Strategic Framework for EU Research and Innovation Funding

[3] Nanotechnology research directions for societal needs in 2020, Mihail C. Roco, Chad A. Mirkin, Mark C. Hersam, September 2010

[4] M. Kautt, K. Bittner S.M. Anson, EVA_1 Global Evaluation of Nano- and Micro-oriented Competence Centers, Forschungszentrum Karlsruhe 2006 (Wissenschaftliche Berichte FZKA 7253)

E-Beam Lithography

Peter-Jürgen Jakobs, Julian Hartbaum, Xin Liu, Tobias Wienhold

E-Beam-Lithography is operated in KNMF by the Institute of Microstructure Technology (IMT) for fabrication of high accurate structures in Nano- and Microscale. We use a state of the art Vector Beam – Tool from Vistec for 6" substrates with Ultra High Resolution and Extreme Wide Field (**VB6UHR-EWF**). We operate in two different ways: we realize patterns in extreme thick resist (3200 nm), only very few working groups are doing this worldwide and we also expose very small patterns, down to about 20 nm (depends on substrate stack). Below you will find some elected R&D activities which have been performed in 2011.

Magnetic nanoactuator system

This work focused on the fabrication of free-standing Ti beam cantilevers with critical dimensions of 50-400 nm covered by an integrated magnetic element at the front end. Main challenges were the patterning of nanostructures as well as the exact integration of a magnetic element on already structured substrates. Besides the advantages of E-Beam lithography at 100 kV the E-Beam unit Vistec VB6 UHR EWF gave the possibility to expose a substrate multiple times, each exposure aligned to the other. These repeated and aligned exposures, called direct-write (DW), allowed the development of metallic cantilevers with an integrated magnetic tip for magnetically induced deflection.

Three exposure steps were necessary for the final actuator structures. In a first step micrometer scale octagons were written, developed and electroplated with gold to serve as markers for the alignment of the following exposures. The cantilever pattern was realized in the second exposure step with critical dimensions below 100 nm. After pattern transfer from the resist in the Ti layer the third exposure was carried out only at small rectangles on the cantilevers front end allowing the deposition of magnetic layers or particles. A final isotropic etch leads to free-standing and movable structures.

On-chip Raman scattering with integrated organic lasers for improved point-of-care diagnostics

Raman scattering is an established optical method for the identification of specific molecules. The spectrum of the scattered light is directly related to the nuclear composition in the molecule, yielding a unique fingerprint obtained for each molecule. This effect may be applied to detect multiple molecules simultaneously in one single solution. Within this project we aim to make Raman scattering technology available to all-polymer chips. Therefore the excitation for Raman scattering is achieved by on-chip integrated organic lasers, which can be tuned over a wide range in the visible spectrum. Nanoparticles will be integrated onto the chip, offering signal amplification based on surface enhanced Raman scattering (SERS) in order to overcome the remaining polymer signal background. The integrated approach will be applied to point-of-care tumour diagnostic, based on the detection of tumour cells and on the identification and analysis of tumour-specific genetic alterations, such as mutations, gene amplifications and chromosomal aberrations. The device in development shall contribute to the urgent medical need for improvement of early tumour diagnostics, in particular the cost-effective realization of a next step towards individual tumour therapy.

The Raman chips are designed individually for external laser excitation and internal DFB (distributed feedback) organic laser excitation, as shown in Figure 1. To depress the background interference from polymer materials, a commonly used small molecule blend

Alq3:DCM for organic laser applications is adopted to construct the waveguide, which conveys the laser excitation to the Raman sites.

Within the project we developed a fabrication process including the creation of the replication tool and a process to perform multiscale replication of photonic and fluidic structures in TOPAS® 6013 COC (cyclo olefin copolymer) by thermal nanoimprint (Figure 2).

The one and two dimensional gratings have been exposed by the KNMF e-beam tool. Subsequently KIT developed a process to define and deposit the waveguide and laser gain material onto the chip.

The final chips were sealed by thermal bonding.

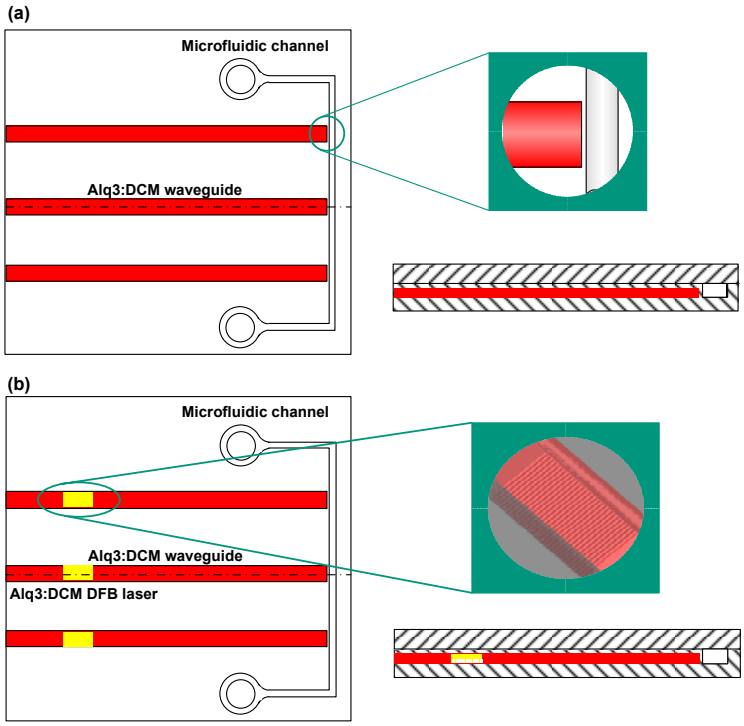

Fig. 1:
(a) 1st generation COC (Cyclo-Olefin-Copolymer) chip with external excitation.
(b) 2nd generation COC chip integrated with organic laser.

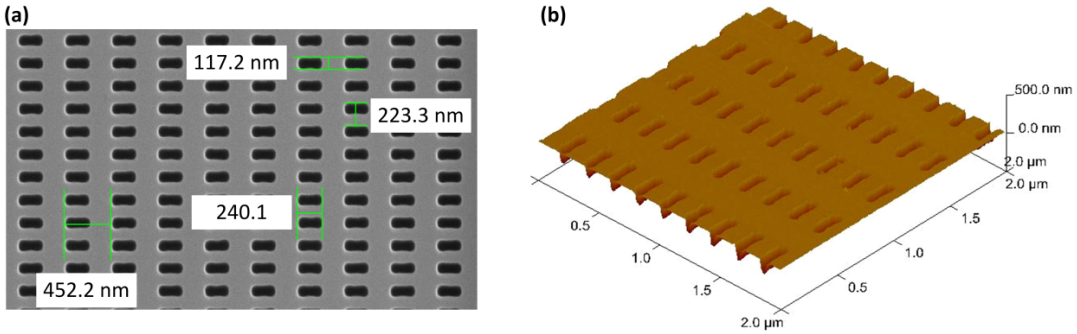

Fig. 2:
(a) SEM (scan electron microscope) photograph and
(b) AFM (atomic force microscope) photograph of two dimensional gratings on the silicon stamp for thermal nanoimprint.

Four batches of nanoparticles were fabricated out of Ag/Au/SiO_2 by USTAN and characterized by IPHT. A 1st generation of nanoparticles stabilised by tri-sodium citrate molecules was obtained by chemical reduction of silver ions with sodium borohydrate to form

spherical silver nanoparticles (Figure 3A). A photoreduction pathway was then used to tune the shape and consequently the plasmon resonance of the nanoparticles. Irradiated by a selected set of wavelengths, a slow growth of the nanoparticles was implemented to form decahedral and prism like nanoparticles (Figure 3B). The spectral range of plasmon resonance of the samples was tuned from 400 to 600 nm (Figure 3C).

Efforts then focused on purifying and concentrating the nanoparticles to allow their further electron microscopy and Raman characterisation as well as their future insertion in the devices.

IPHT characterized the nanoparticles. Transmission electron microscopy probed the shape of the nanoparticles. The most promising candidates for SERS spectroscopy with 633 nm excitation were nanoparticles with absorption maxima at 503 and 559 nm, respectively and triangular or rod-like shape. The zeta potential and the average radius was determined by Zetasizer Nano ZS instrument (Malvern). The dimension of both promising nanoparticles ranged from 40 to 65 nm. The zeta potential was -40 and -42 mV. Due to the negative zeta potential the cationic dye molecule rhodamine 6G was selected as samples to determine the Raman signal enhancement (Figure 3D).

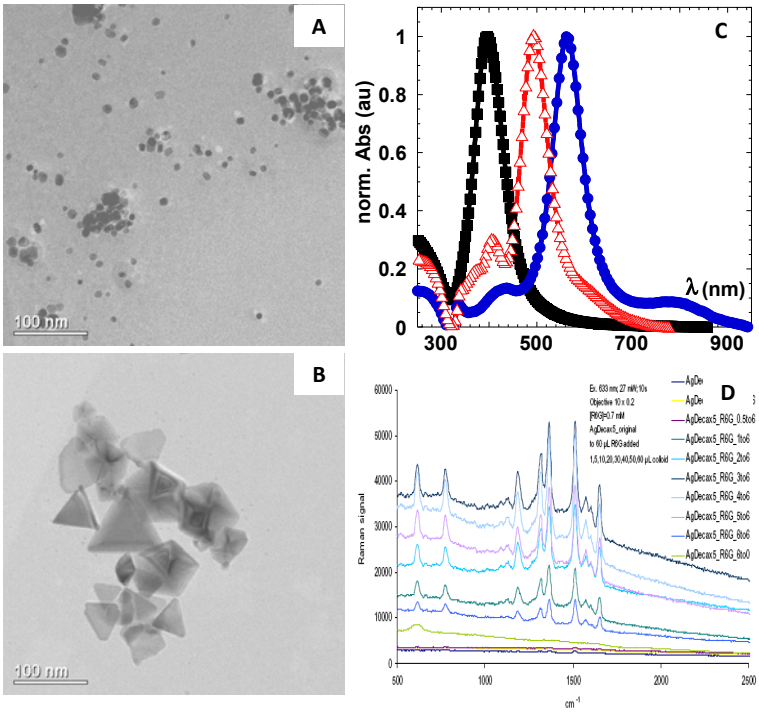

Fig. 3: Transmission electron microscopy images of the nanoparticles obtained by chemical reduction (A) and by photoreduction (B). Absorbance spectra showing the plasmon resonance shift with the synthetic conditions (C) and the enhancement Raman signal of Rhodamine 6G when in presence of silver nanoparticles (D).

Optofluidic dye-laser

Lab-on-a-chip systems made of polymers are promising for the integration of active optical elements, enabling e.g. on-chip excitation of fluorescent markers or spectroscopy. In particular, optofluidic distributed feedback (DFB) dye lasers, where the laser dye is dissolved in a liquid medium, have gained interest as they exhibit directed single-mode emission and wide spectral tunability.

Within this project first order DFB laser gratings were defined on a 4'' silicon wafer using electron beam lithography. To achieve wide spectral tunability of the lasers, resonator gratings with periods of 186 - 194 nm were structured with steps of 2 nm. To achieve low

laser thresholds, DFB gratings were structured on an area of 3000 x 300 µm. Reactive ion etching (RIE) was then used to transfer the photoresist patterns into the silicon wafer. Figure 2a) shows a cross-section of such a DFB grating etched into silicon.

Subsequently, aligned photolithography and a second RIE step were used to define liquid-core waveguides. To form the fluidic basins, a 20 µm thick layer of Ormocomp was spin-coated onto the pre-structured silicon wafer and patterns were defined by photolithography. These processes result in a hybrid stamp with nanometre-sized photonic resonator structures in silicon and micrometre-sized fluidic basin structures made of Ormocomp. Thermal nanoimprinting was used to replicate polymer chips made of Cyclic Olefin Copolymer (COC) from the hybrid master. This simultaneously defines photonic resonators, liquid-core waveguides, and fluidic reservoirs on the polymer chip. Subsequently, the fluidic structures were sealed with a second COC foil by thermal bonding. Figure 2b shows a finished optofluidic dye laser chip made of COC filled with the laser dye Pyrromethene 597 dissolved in benzyl alcohol.

Optical characterization of these laser chips showed ultra-high output pulse energies of more than 10 µJ and laser low thresholds of 2 µJ. Furthermore, tunability of the laser output wavelengths over a spectral range of 24 nm on a single chip was accomplished by varying the laser grating period in steps of 2 nm [1].

In conclusion, electron beam lithography, reactive ion etching and subsequent replication into polymer chips enable low-cost manufacturing of laser chips suitable for mass production. Wide laser tunability, ultra-high output pulse energies, and long operation times without external fluidic pumping make these on-chip lasers suitable for a wide range of lab-on-a-chip applications, e.g. on-chip spectroscopy, biosensing, excitation of fluorescent markers, or surface enhanced Raman spectroscopy (SERS).

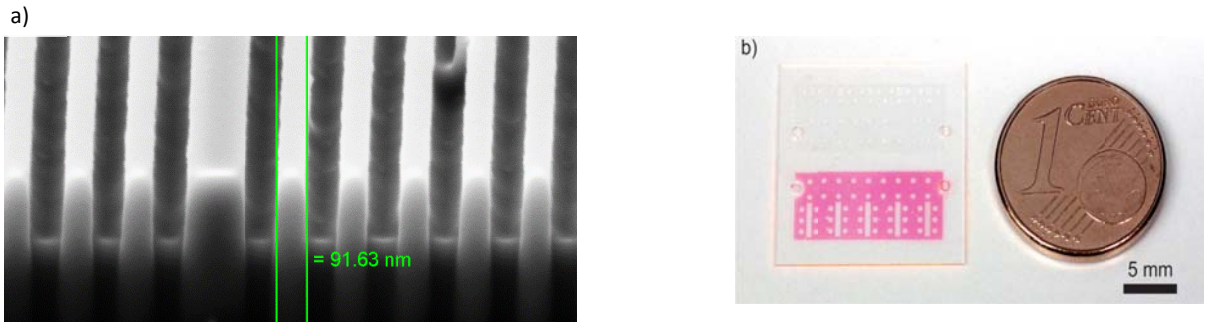

Fig. 3:
(a) Cross-section of a DFB laser grating with a grating period of 186 nm transferred into silicon.
(b) Photograph of an optofluidic chip made of COC. For comparison of the size we have added a one Eurocent coin. The fluidic basin is filled with the dye Pyrromethene 597 dissolved in benzyl alcohol. Within the fluid basin, five resonators with grating periods ranging from 186 to 194 nm are placed.

Reference

[1] T. Wienhold, F. Breithaupt, C. Vannahme, M.B. Christiansen, W. Dörfler, A. Kristensen, and T. Mappes, "Diffusion driven optofluidic dye lasers encapsulated into polymer chips", Lab on a Chip, DOI: 10.1039/C2LC40494J, 2012).

Deep X-ray Lithography

Martin Börner, Pascal Meyer, Jürgen Mohr, Vladimir Nazmov, Robert Palmer, Christian Rush

Three beamlines at the synchrotron source ANKA are operated in KNMF by the Institute of Microstructure Technology (IMT) for fabrication of high aspect ratio microstructures (HARMST). LITHO 1 and LITHO 2 are open to users, LITHO 3 is under commission and from 2014 will enable upscaled fabrication for multiscale dimensions. The in-house research focuses on process improvement and optimization as well as on the fabrication of new and innovative HARMST with HGF internal users. The following R&D activities were performed in 2011.

Quality control for deep x-ray lithography (DXRL) / preliminary metrology study

Three dimensional (3D) micro-scale parts require accurate and traceable metrology. In collaboration with the National Physical Laboratory, UK the first ever dimensional metrology study [1] on artefacts produced by deep x-ray lithography (holes and columns) has been performed. The test compared results from two co-ordinate measuring machines (CMMs) of different designs and specifications operated with similar measurement procedures in similar environments. Concerning diameter measurements (2D) taken 50 µm down from the surface, the measurement data taken at NPL and KIT/IMT are comparable within the combined uncertainties of the 2 CMMs. Maximum differences are: 0.3 µm for diameter and 0.4 µm for the LSC roundness (Figure 1)

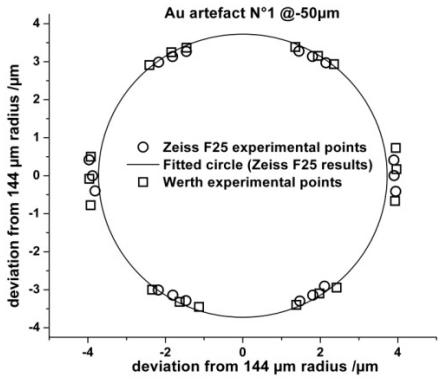

Fig. 1: Comparison of measurement data achieved with the F25 and the Werth CMM For better visualisation, each point has been translated by a vector of 144 µm pointing in the direction of the circle centre

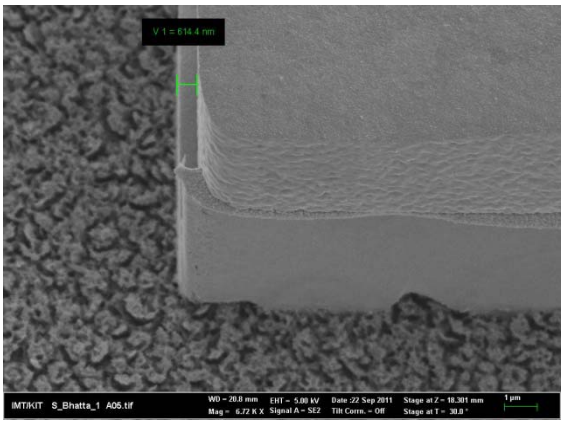

Fig. 2: SEM picture showing an alignment accuracy of 0.6 microns. Base layer of gold is around 7-8 micrometers and the upper layer is approximately 5 micrometers thick

Alignment studies for the fabrication of metamaterials

Meta-foils are all-metal free-standing electromagnetic metamaterials based on inter-connected S-string architecture. Lacking any substrate or embedding matrix, they feature arrays of parallel upright S-strings with each string longitudinally shifted by half an S compared to its neighbour to form capacitance-inductance loops. X-ray lithography is well suited to manufacture the foils which require small dimensions (in the order of 10 µm and

smaller and high accuracy); however precise alignment (< 1µm) of mask and substrate is mandatory.

Alignment studies, using the Jenoptik scanner with integrated alignment system at the beamline LITHO 1 show an alignment accuracy of 600 nm, which is very promising in view of the meta-foil fabrication (Figure 2).

Electromechanical tuning of dielectric resonator oscillators

In satellite, wireless, and automotive communication applications low priced, compact and robust fine-tuning methods are important for enabling low phase noise, frequency stable dielectric resonator oscillators (DROs) and DR-based filters. Due to miniaturization needs a novel electromechanical tuning (EMT) method based on RF-MEMS is developed. The EMT includes an electrostatically actuated MEMS beam-Mach-Zender Interferometer (MZI). Tuning is accomplished by varying the coupling coefficient between the MZI deformed ring and a DR. Deformation of the ring is done to increase the coupling between DR and MZI. The MZI-DR coupling coefficient variation results from applying an actuation voltage to a MEMS beam disposed besides a portion of the MZI. In this way, the DR is tuned and maintains high unloaded Q properties.

The properties of DR oscillators (DROs) utilizing the EMT scheme were determined with electromagnetic (EM) field simulations (Figure 3) and the manufactured samples will be used to verify the simulation results by measurements. First nickel samples (100µm in height) on 4”-silicon wafers have been fabricated (Figure 4). The gap between cantilever and structure is 1 µm.

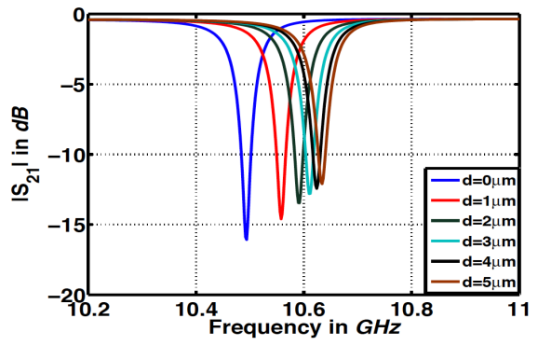

Fig. 3: Simulated transmission coefficient for different beam distances

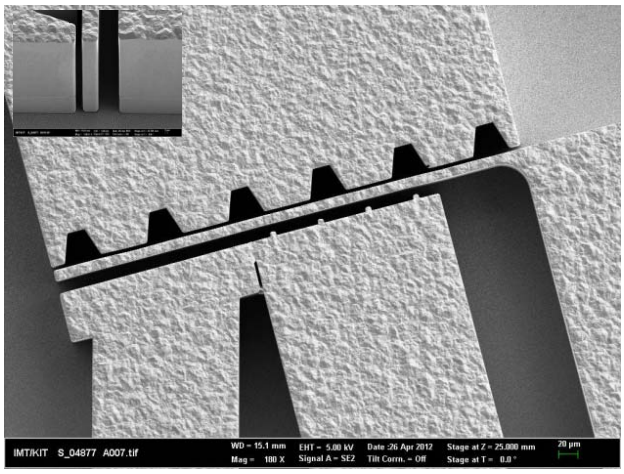

Fig. 4: Cantilever of a tunable capacitor (inlet: side view of the cantilever (height 100 µm))

Integrated photonic elements based on silicon for telecom applications

In MISTRAL, a BMBF funded joined project in the key technology of optical communication, high aspect ratio micro structures fabricated by the LIGA-technology are used to fabricate packaging structures which allow passive alignment with the highest possible accuracy of all components necessary to build up efficient optical receiving and transceiving units for future communication systems in fiber optical networks. In hybrid optical packaging tolerances of < 1 µm in a passive alignment process have to be achieved. The example in Figure 5 demonstrates pigtailing of a silicon photonic integrated circuit. The silicon chip is assembled vertically in a LIGA module. Light is coupled from the fibers to the chip by means of silicon

grating couplers. Measuring the coupling losses show additional losses due to the passive alignment concept of 2 dB maximum, which could be mostly attributed to a design error of the optical bench resulting in a 3µm offset between fiber and grating coupler [3]. Thus losses can be drastically reduced in case of an error free set-up.

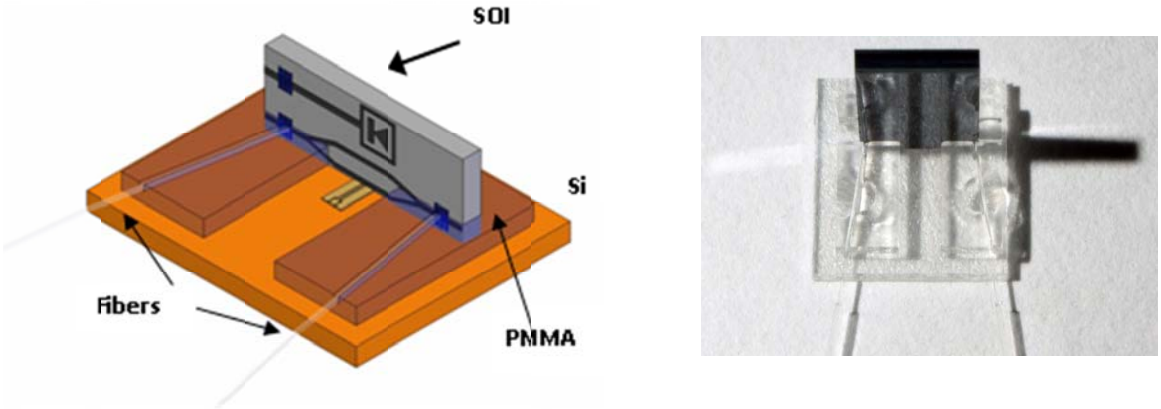

Fig. 5: Scheme of SOI (left) in replica assembled device (right)

High aperture x-ray lenses

Compound x-ray refracting lenses (CRL) show increasing interest in the last years as such lenses are rather simple in manufacturing and provide focusing of X-rays down to 100 nm in diameter. However, lenses with a continuous parabolic refractive surface have rather small effective apertures up to a few 100 microns only. Reducing the amount of absorbing material and thus, increasing the ratio of refracting surface to the absorbing material volume results in a so called mosaic lens with the minimal lateral dimension of the microstructures down to 10 microns with the necessary profiled surfaces [4]. Inclined X-ray exposures result in a 2D network of prism structures with a microstructure length up to 3 mm and sidewall roughness of about 10 nm (Figure 6). With such lenses an effective aperture of up to 1.2 mm could be achieved as it was demonstrated in X-ray imaging experiments with synchrotron radiation.

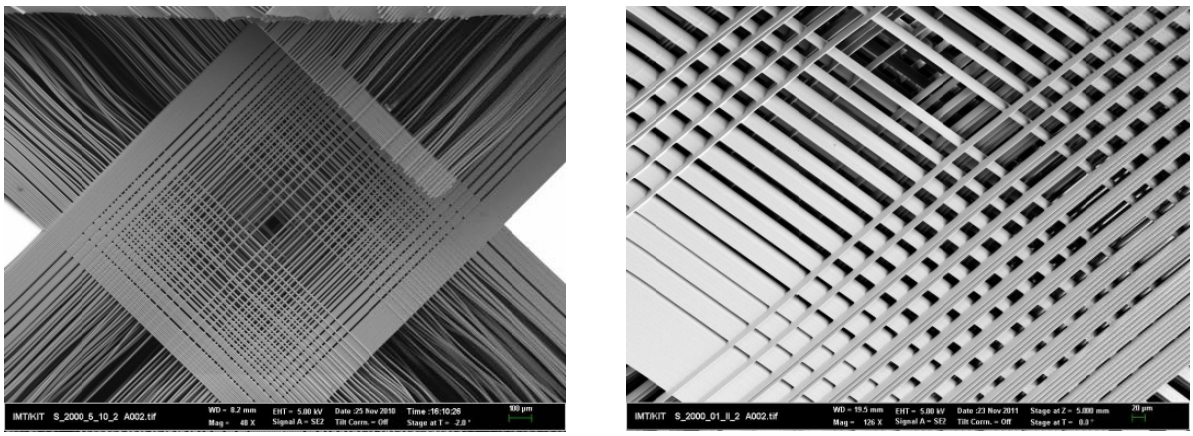

Fig.6: SEM image of 2D X-ray mosaic lens of 2 mm height (left) and a part of the lens (right), produced using inclined deep x-ray lithography.

Collaboration in in-house research

Helmholtz Center Geesthacht; Helmholtz Virtual Institute “New X-ray analytic methods in material science“, VI-NXMM (University of Kiel, Technical Universy Munich, Empa – Swiss Federal Laboratories for Materials Science and Technology); National Physical Laboratory (NPL).

References

[1] P Meyer, J D. Claverley and R K. Leach “Quality control for deep x-ray lithography (LIGA): a preliminary metrology study”, Microsystem Technologies: Volume 18, Issue 4 (2012) 415-421

[2] H.J. De Los Santos, Y. Chen and C. Rusch “Properties of metallic microwave-scale Mach-Zehnder interferometers for dielectric resonator tuning, ELECTRONICS LETTERS 14th Vol. 47 No. 8 (2011)

[3] L. Alloatti, D. Korn, R. Palmer, D. Hillerkuss, J. Li, A. Barklund, R. Dinu, J. Wieland, M. Fournier, J. Fedeli, H. Yu, W. Bogaerts, P. Dumon, R. Baets, C. Koos, W. Freude and J. Leuthold, 42.7 Gbit/s electro-optic modulator in silicon technology, Optics Express, Vol. 19, Issue 12 (2011) 11841-11851

[4] M. Simon, V. Altapova, T. Baumbach, M. Kluge, A. Last, F. Marschall, J. Mohr, V. Nazmov, H. Vogt, Refractive Optical Elements and Optical System for High Energy X-ray Microscopy AIP Conf. Proc. 1437, 116 (2012); doi: 10.1063/1.3703354

Laser Material Processing

Wilhelm Pfleging, Heino Besser, Nadine Kandora, Robert Kohler, Johannes Proell, Petra Severloh, Maika Torge

Within KNMF, the Institute of Applied Materials - Applied Materials Physics (IAM-AWP) supplies different kinds of laser micro-machining workstations: Ultrashort pulsed UV lasers operating at 193 nm and 248 nm are suitable for laser structuring and modification processes on micrometer and nanometer scale, especially for thin films and polymers. Other types of laser workstations are equipped with infrared laser sources which are used for thermally driven processes such as cutting and welding on micrometer scale. A new ultrafast and high repetition laser machining system ("femto/picosecond laser") was funded by KNMF in 2011 and will be installed in the "Laboratory for Micro- and Nanostructuring" at IAM-AWP in the mid of August 2012. By using this special configured workstation (e.g. three wavelengths, tunable pulse length), laser micro- and nanostructuring of multimaterial systems such as biomaterials, transparent materials as well as materials for energy devices (batteries) will be possible without inducing thermal impact whereby high repeatability and reproducibility will also be given.

The In-house research focuses on the development of new laser-assisted processes with special focus on thin films, polymers and battery materials. The following R&D activities have been performed from the entry into KNMF until the end of 2011.

Laser-assisted control of wettability of hydrogenated amorphous carbon films

A flexible and rapid surface functionalization of amorphous carbon films shows a great potential for various application fields such as biological surfaces and tribological systems. For this purpose, laser assisted modification and patterning of hydrogenated amorphous carbon thin films (a-C:H) with different hydrogen contents was investigated in cooperation with KNMF laboratory "Thin Film Technologies" for different laser process regimes [1]. At low laser fluences, especially significantly below the ablation threshold, a chemical modification of a-C:H films was initiated. In cooperation with M. Bruns (KNMF Laboratory for Microscopy and Spectroscopy, XPS) the formation of carboxyl groups at the surface was detected which can be correlated to the improved wetting of the films with water.

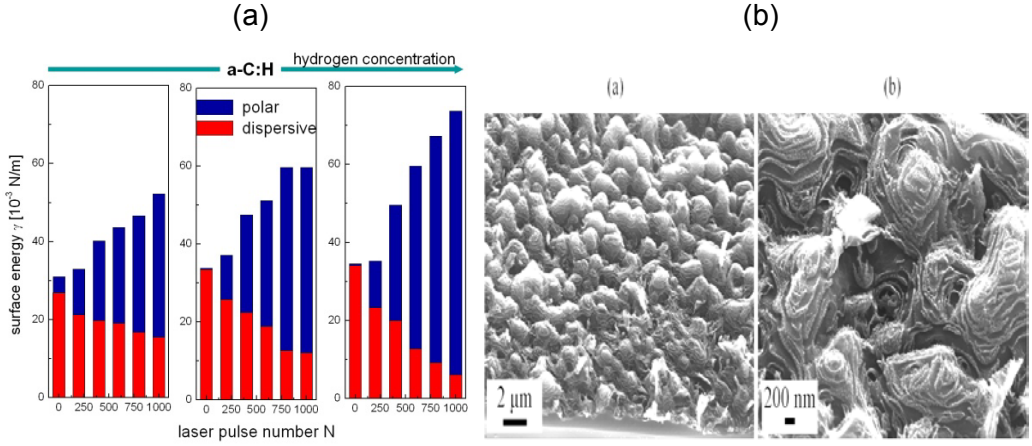

Fig. 1: Laser modification of hydrogenated amorphous carbon thin films; (a): surface energy and its polar and dispersive components as function of laser pulse number for different types of a-C:H films (laser fluence: 6 mJ/cm^2); (b): SEM image of a laser modified a-C:H film (laser fluence 80 mJ/cm^2) [1].

The surface energy shows a linear dependence on the laser pulse number. For laser fluences near the ablation threshold, a selective ablation of hydrogen enriched domains seems to be responsible for the formation of hierarchical structures including micro-hillocks with an overlaying structure on the nanometer scale. This artificial micro-/nano-topography shows a better wettability for polar and dispersive liquids [1].

Adjustment of nano-sized grain structures in lithium metal-oxides materials

Laser annealing was successfully developed and applied to unstructured and 3D-structured Li-Mn-O thin films [2, 3] in order to adjust the crystalline phase and grain size. The main advantages compared to conventional furnace annealing are significantly reduced processing times (seconds instead of hours) as well as a precise control of grain sizes as a function of annealing time and temperature [4, 5]. The latter fact is depicted in Figure 2. While the grains formed by laser-annealing show a prismatic topography with linking in between the grains and sizes up to 250 nm in lateral expansion, the grains obtained through furnace annealing for three hours at 700 °C are significantly larger (~500 nm) and form a craggy surface due to inhomogeneous grain orientation and size. It was shown that laser-annealing of Li-Mn-O thin films at 680 °C formed a spinel-like nano-crystalline phase [2]

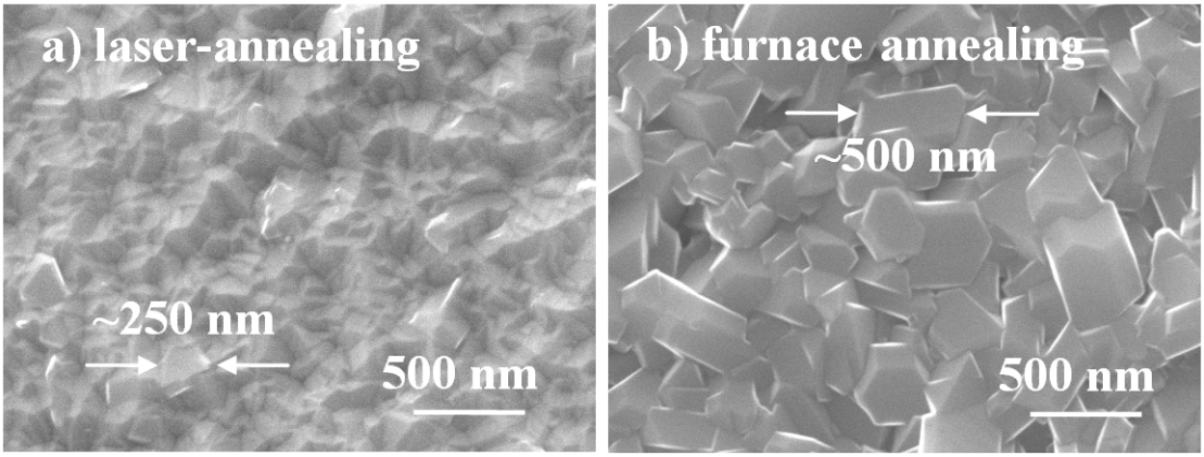

Fig. 2: SEM top view images of (a) laser-annealed and (b) furnace annealed Li-Mn-O thin films showing the grain sizes and grain structure. Laser-annealing was performed for t = 100 s at T = 680 °C under ambient air while furnace annealing was set-up for three hours at T = 700 °C under ambient air [2].

These studies were performed in cooperation with M. Bruns (KNMF Laboratory for Microscopy and Spectroscopy, XPS), the KNMF laboratory "Thin Film Technologies" and the Institute of Functional Interfaces IFG (KIT, AG Dr. Peter Weidler).

Formation of self-organized microstructures on composite materials

Within the last two decades lithium-ion batteries have emerged as the power source of choice for the high performance rechargeable battery market. Three dimensional battery architectures are under current scientific investigation since they can achieve large areal energy capacities, while maintaining high power densities. Electrode materials consisting of micro-/nano-scaled lithium-metal-oxide powders with approximately 5-15 wt-% of carbon black, graphite and polyvinylidene fluoride (PVDF) were coated as thick films (50-100 µm in thickness) on aluminum substrates. These composite materials were structured by excimer laser radiation. Under specific processing conditions, self-organized surface structures were formed. The appropriate laser fluences cover a broad range from 1 J/cm^2 up to 3 J/cm^2. The generated self-organized micro-cones show a height of about 20 µm. A material loss of

smaller than 10 wt-% could be achieved. Cross-section analysis and energy dispersive X-ray spectroscopy of the conical structures indicated that particles consisting of active material, the conductive additives as well as the binder material were preserved inside the conical structures [6]. It can be concluded that a selective ablation process induces the formation of the micro-sized cones on top of the porous surface while the composition of the microstructured active film particles themselves seems to be non-affected. This is an important result since a preferred removal of one component such as polymer or carbon black could result in a decrease in electrochemical performance.

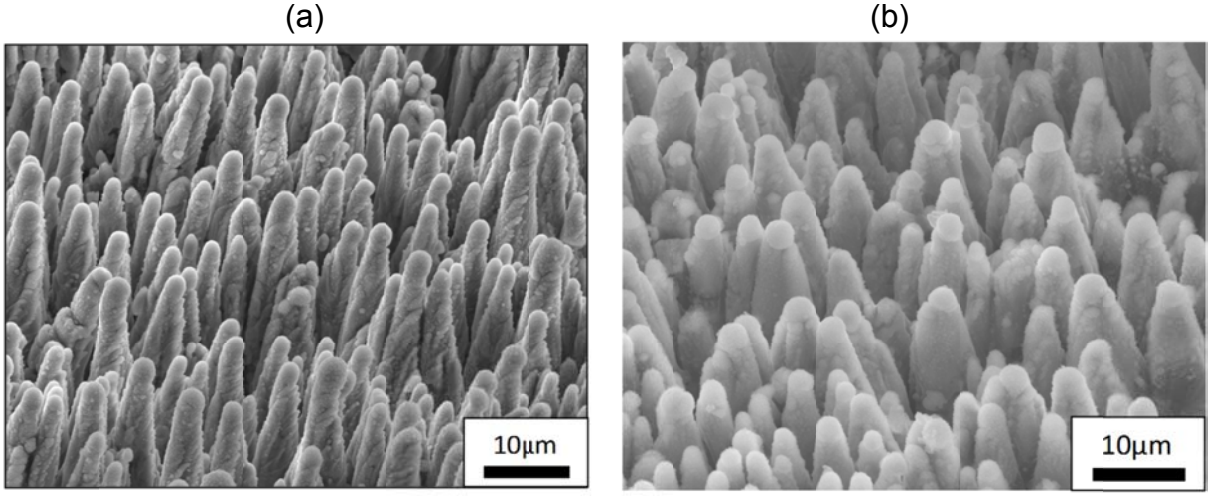

Fig. 3: SEM images of laser structured tape cast electrodes made of (a) LiCoO2 (b) Li(NiMnCo)O2

Generation of submicron periodical structures

A rapid and cost efficient fabrication of periodical micro- and nanostructures is of great interest for several application fields such as microoptics (e.g., interferometer, bragg gratings), biology (e.g., bio-active surfaces, control of wettability) or tribology (e.g., control of wettability, micro-reservoirs for lubricants). Therefore, for the use in KNMF, a rather new technical approach using phase shift masks for direct laser ablation was constructed (Figure 4a).

Periodic nanostructures such as grooves or holes with minimum structure sizes of 200 nm were fabricated using phase mask imaging with a laser source operating at a wavelength of 193 nm. Phase masks with linear gratings were used to fabricate parallel grooves while phase masks with crossed gratings could be used to realize periodic arranged holes with a diameter of about 200 nm. More complex structures were realized by arranging two subsequent phase masks. With four beam interference, the fabrication of sub-micron patterns with lines and holes was performed (Figure 4b). The contact angle of water was controlled within a broad range of 160° down to 13°. A combination of laser-assisted chemical modification at low laser fluence and laser surface patterning at high laser fluence is proposed for the flexible generation of hydrophilic and superhydrophobic surfaces [1].

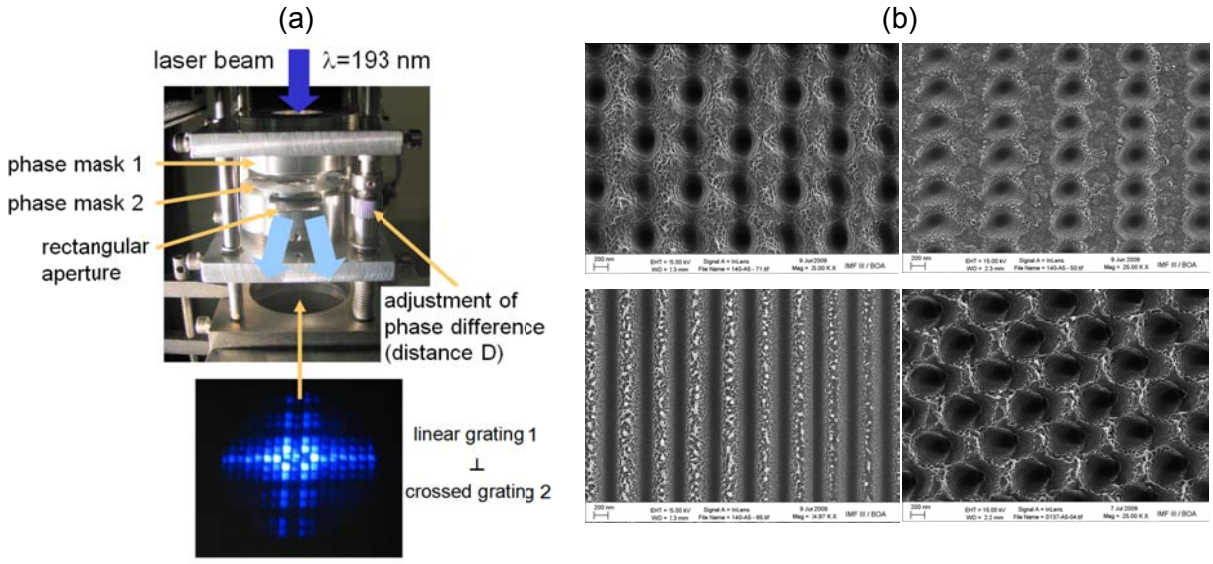

Fig. 4:
Generation of periodic submicron structures by laser ablation using phase masks;
(a): Experimental arrangement of mask holder and diffractive pattern of the laser beam;
(b) examples of laser-generated submicron-sized structures in amorphous carbon films with oxygen content (a-C:O).

Collaboration in in-house research

Paul Scherrer Institut (PSI), University of Birmingham, IREPA LASER, VITO - Lasercentrum Vlaanderen, KTH – Swedish Royal Institute of Technology, ATL Lasertechnik GmbH, Daimler AG, National Physical Laboratory (NPL)

References

[1] Pfleging, W., Kohler, R., Torge, M., Trouillet, V., Danneil, F. and Stuber, M., Control of wettability of hydrogenated amorphous carbon thin films by laser-assisted micro- and nanostructuring, Applied Surface Science 257(18), 2011, p. 7907-7912

[2] Proell, J., Kohler, R., Mangang, A., Ulrich, S., Ziebert, C. and Pfleging, W., 3D Structures in Battery Materials, Journal of Laser Micro Nanoengineering 7(1), 2012, p. 97-104

[3] Proell, J., Kohler, R., Torge, M., Ulrich, S., Ziebert, C., Bruns, M., Seifert, H.J. and Pfleging, W., Laser microstructuring and annealing processes for lithium manganese oxide cathodes, Applied Surface Science 257, 2011, p. 9968-9976

[4] Proell, J., Kohler, R., Adelhelm, C., Bruns, M., Torge, M., Heißler, S., Przybylski, M., Ziebert, C. and Pfleging, W., Laser modification and characterization of Li-Mn-O thin film cathodes for lithium-ion batteries, in Proc. of SPIE, Vol. 7921, 2011, San Francisco: p. 79210Q 1-14

[5] Proell, J., Kohler, R., Mangang, A., Ulrich, S., Bruns, M., Seifert, H.J. and Pfleging, W., Diode laser heat treatment of lithium manganese oxide films, Applied Surface Science 258(12), 2012, p. 5146-5152

[6] Kohler, R., Proell, J., Bruns, M., Ulrich, S., Seifert, H.J. and Pfleging, W., Conical surface structures on model thin film electrodes and tape cast electrode materials for lithium ion batteries, Applied Physics A, accepted for publication,

Micro Injection Moulding

**Volker Piotter, Klaus Plewa, Jochen Heneka,
Elvira Honza, Alexander Klein, Tobias Müller**

Using micro- or nanostructured tool inserts as masters for injection moulding allows the low cost fabrication of very small singular micro parts as well as the replication of large micro- or nanostructured areas. In both cases high geometric accuracies and small tolerances can be achieved especially if lithographically made mould inserts are applied. The process is predestined for medium and large scale production and offers a high economic efficiency. Besides the replication of polymer materials powder injection moulding (MicroPIM) allows micro fabrication of components made of a large variety of metals or ceramics. Currently under development are special variants like micro compression injection moulding or different kinds of multi-component replication, the latter reveal strong advantages with respect to reduced mounting expenditures and the capability to produce multi-functional devices.

The micro injection moulding (µIM)-lab at the IAM-WPT is currently equipped with 6 injection moulding machines which are all upgraded by special features like tool evacuation, variothermal temperization and special units for processing powder-filled feedstocks.

Micro compression injection moulding

Although µIM reaches a remarkable production performance there are still opportunities for improvements. One concerns the degree of replication accuracy of complex geometries. In conventional fabrication the so-called compression injection moulding method enjoys intensive application. To evaluate the potential for MicroPIM comparative trials have been performed at KIT. For this purpose a challenging master geometry was obviously meaningful. Therefore, a LIGA mould insert was chosen and a typical MicroCIM feedstock filled with 50Vol% zirconia powder was used. A direct comparison between the test geometries replicated by classical MicroPIM and the enhanced Micro-CPIM process had been performed. It turned out that the replication performance of Micro-CPIM is significantly better than the one reached with the pure MicroPIM procedure. However, differences are small and can only be detected using quite fine sized structures, see Figures 1 and 2. A more detailed description of the comparative trials can be found in [1].

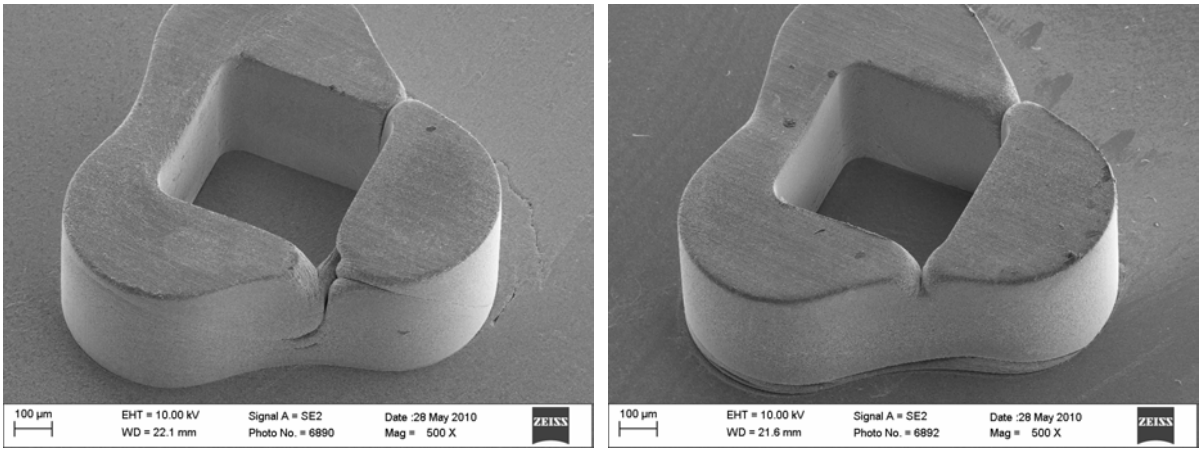

Fig. 1, 2: Sintered ceramic structure (housing for a rotary gear wheel pump). Shaping has been performed by pure MicroPIM process (left) and by Micro-CPIM variant (right).

Manufacturing of micro parts by electroplating on partially conductive templates

In order to reach the mass market of metal micro parts with very high surface qualities and finest structuring possibilities, a new process chain has been investigated. Using the two-component injection moulding process, partial conductive parts were produced which have been used as sacrificial templates for a following electroforming on these polymer moulds. The process is one promising replication method for economic mass production. Failure-free filling of the micro cavities, however, requires utilization of 2-component injection moulded templates. In a first shot a conductive plate is injected and in a second shot an insulating polymer is injected with micro structured openings to the conductive part which build the bottom of the cavities for electroplating [2].

Main challenges of this project were the transfer to an automated 2-C process and the investigation of the connecting area between insulating and conductive polymer [3]. Comparison with alternative processes for manufacturing of metal micro parts (here: MicroPIM) showed that the new procedure reaches better surface qualities and a bit higher replication accuracy.

As further improvement with the particular aim to replicate very thin isolated structures a combination of 2-C and foil insert injection moulding has been developed, see Figures 3 and 4.

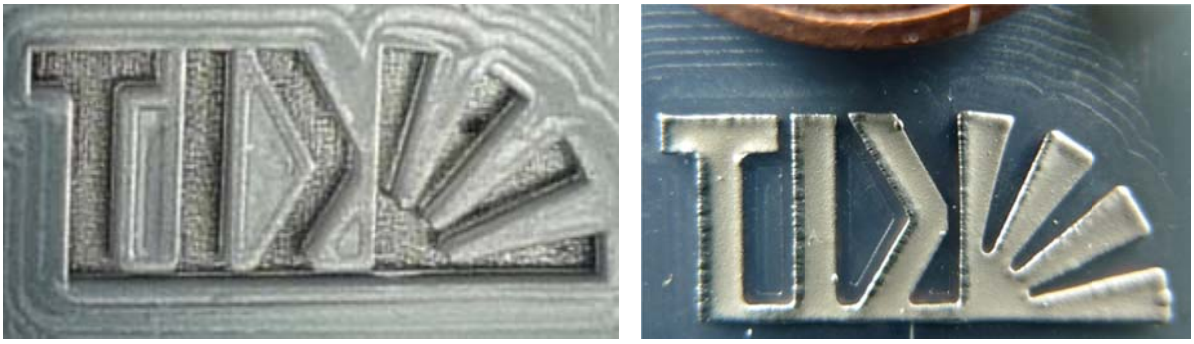

Fig. 3, 4: Template produced by combined two-component foil insert micro moulding, insulating PA 12 as side constraint on conductive Cu-foil (left), same template after electroforming with Ni (right, with rim of a 1-cent coin).

Two-component powder injection moulding (2C-PIM)

Typical MST products are not only characterized by their small dimensions, they also integrate a number of different functions in smallest space. The resulting assembly expenditure might be reduced by using integrative material structures. Accordingly, two-component injection moulding is considered to be a viable process for the economic series production of micro components from multi-functional materials. It offers the possibility for realization of hard/tough or conductive/non-conductive material combinations. An even extended challenge is the realization of two-component powder injection moulding which is characterized by the difficulty that the filling process does not only have to join two different materials, but this material connection also has to be ensured - or definitely unlocked - during debinding and sintering [4]. An interesting example for 2C-MicroPIM requiring considerable materials know-how is the creation of gear wheel and shaft components as shown by Figure 5. While the gear wheel was moulded using a zirconia feedstock the shaft is made of aluminum oxide ceramic. These materials are usually not compatible within a sintering process. Additionally, due to the variation of shaft diameter it is obvious that such a two-material combination could not be produced by a simple insertion of the shaft.

The 2C-MicroPIM procedure in general can be configured to obtain both mobile and immobile bonds. With respect to mobility, the composition of the feedstock mixtures and here especially the powder-binder ratio is of great importance: For immobile bonds the powder concentrations have to be nearly identical to achieve equal shrinkage rates [5].

For the mobile bonds, however, the shaft has to have a significantly higher shrinkage rate than the surrounding gear wheel. A further aspect concerns the sintering temperatures, which have to be adjusted in such a way that densification, i.e. shrinkage, of the inner part starts earlier, see Figure 6.

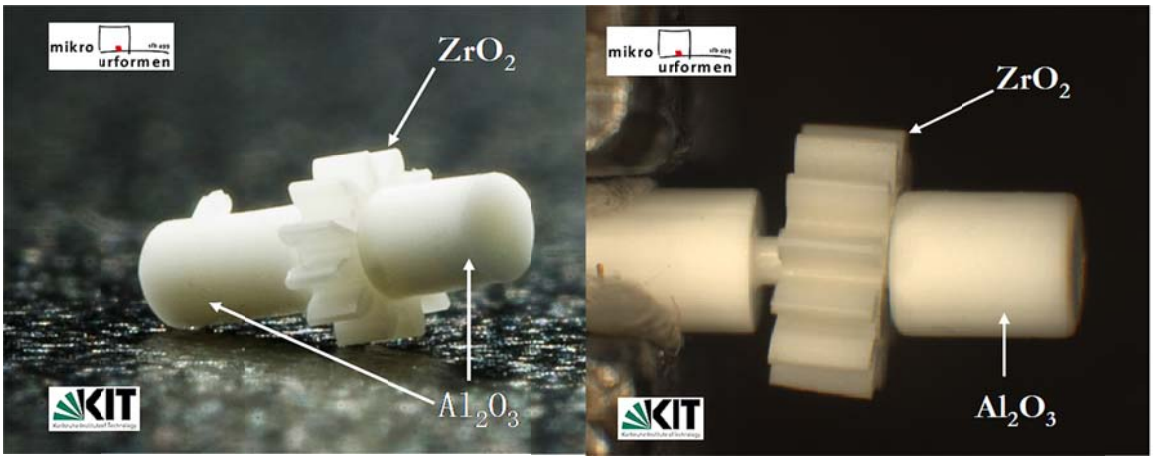

Fig. 5, 6: Fixed gear wheel made of zirconia on a shaft with reduced diameter (0.65 mm, top). Tilted, i.e. movable, microwheel on alumina shaft (bottom). Outer wheel diameter in both cases: approx. 2.93 mm.

Collaboration in in-house research

Freiburg University, IMTEK; RWTH Aachen, IKV; University of Erlangen-Nuremberg, LKT; Hannover University, IWK. Project “Structuring potential and limits of the LIGA-technique”, industrial partners: Arburg GmbH+Co KG, Männer GmbH, RKT GmbH, Scholz GmbH+Co KG.

References

[1] E. Honza, K. Plewa and V. Piotter: A comparative study of Micro Powder Injection Moulding (MicroPIM) and simultaneous Micro Powder Injection Compression Moulding (MicroPICM), Powder Injection Moulding, Vol. 6, No. 2, Inovar Communications Ltd. (2012) pp. 67-70.

[2] J. Prokop, C. Eberl, M. Funk, M. Prüfe, J. Lorenz, V. Piotter, M. Welz and H.-J. Ritzhaupt-Kleissl, Mechanical testing of micro samples produced by a novel LIGA related process chain, Microsystem Technologies, 17(2011) 281-288

[3] J. Heneka, J. Prokop, V. Piotter, M. Guttmann, H. Hanemann and K. Plewa: Variation of the use of LIGA Mold Inserts for the Fabrication of Single Polymeric- and Metallic-Microparts, Proc. of euspen 12th Int. Conference, published by euspen, ISBN 13: 978-0-9566790-0-0, Vol. 2, (2012) 92-95.

[4] V. Piotter: A review of the current status of MicroPIM, Part 1: Materials, processing, microspecific considerations and applications, Powder Injection Moulding, Vol. 5, No. 3, Inovar Communications Ltd. (2011) 27-36. Part 2: Screw injection units, simulation and process variants, Powder Injection Moulding, Vol. 5, No. 4, Inovar Communications Ltd. (2011) 25-30.

[5] A. Ruh, V. Piotter, K. Plewa, H.-J. Ritzhaupt-Kleissl and J. Hausselt: Development of Two-Component Micropowder Injection Molding (2C-MicroPIM) - Process Development, Int. J. Appl. Ceram. Technol. 8 (2011) 610–616.

Hot Embossing

Matthias Worgull, Marc Schneider, Markus Heilig, Michael Röhrig, Alexander Kolew, Heinz Dinglreiter, Hendrik Hoelscher

The in-house activities on hot embossing can be split into three groups: process development and technical improvements, material research and application-oriented process modifications focussed on optical, microfluidic, and biomimetic applications [7, 8].

Process development

The development activities in microthermoforming focussed on process reliability and fast cycle times [13]. Therefore, a system, including hardware and software, to control the pressure gradient during a microthermoforming cycle has been implemented [3, 6]. Temperature and pressure were identified as the main parameters to influence the profile of formed parts [15]. Microthermoforming on large scale has been demonstrated, using a mould insert with 117 microstructured areas of cell containers for tissue engineering [1, 9, 10].

A process to thermoform thin polymer films with typical thickness below 20 µm into a three dimensional shape has been developed based on a double layer system which reduces the risk of damaging the film during forming. The deformation of the foil has been studied using pre-structured films. Characterizing the local density of the structures experimental data were correlated with simulation results (Figure 1a).

By an extended microthermoforming process with a stack of two films hollow structures are achieved by simultaneous forming and bonding in one process step. The process results in a so-called “twin sheet” forming process or blow moulding process. By this process we achieve hollow structures with nanostructured surfaces inside or outside of the hollow body (Figure 1b).

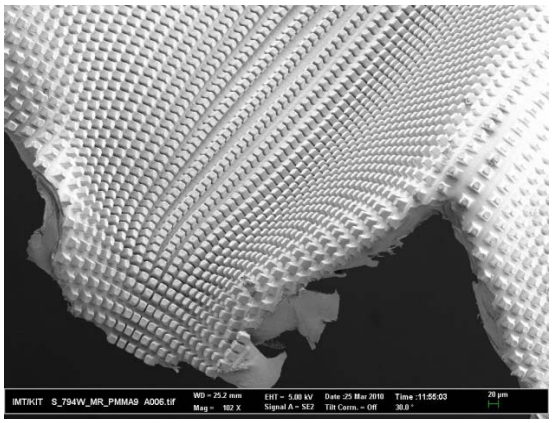

Fig. 1a: Mirothermoforming of a pre-structured polymer film (by hot embossing). Because of the different moulding windows the structures on the film remain after the thermoforming step.

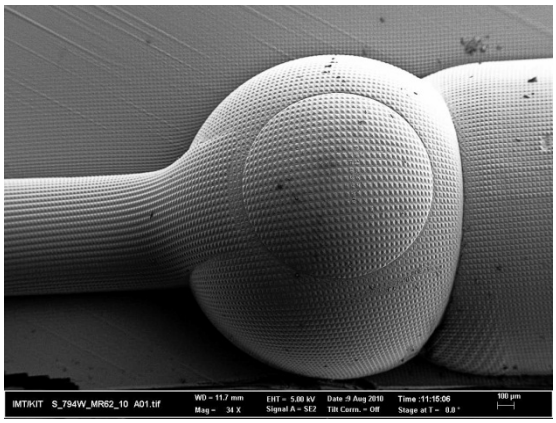

Fig. 1b: Blowmoulding of a pre-structured polymer film to achieve hollow bodies with structures inside or outside.

To achieve moulding temperatures in the range up to 500°C in hot embossing the existing heating systems has been improved. This allows extending the range of existing moulding materials [5].

The double sided hot embossing of two layer polymer stacks has been investigated (Figure 2a) and 2b) to achieve different surface properties of a moulded part (e.g. different wetting behaviour on top and bottom of the part) [2, 12, 14].

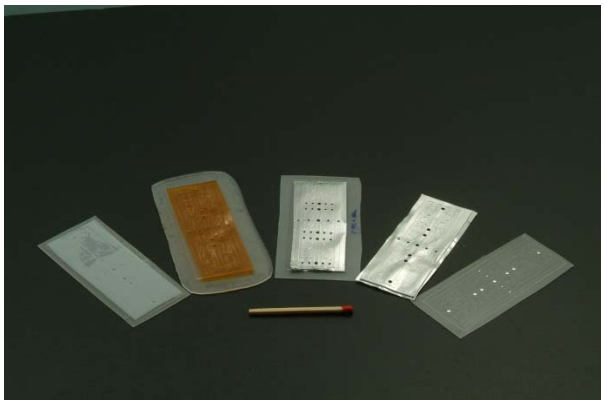

Fig. 2a) Diversity of double layer replication by hot embossing. Numbers of material combinations were identified, including amorphous and semicrystalline polymers and also metal foils.

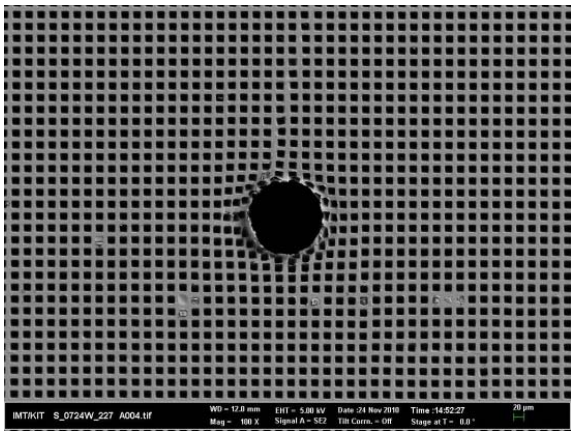

Fig. 2b) Detailed view of a so-called dispensing well plate with design-integrated holes through two layers of polymers. The different wetting behaviour will be underlined by an additional structuring to achieve a superhydrophobic state.

Also a two level, two step hot embossing process has been established to be able to fabricate hierarchical structures. In a first step, microstructures will be replicated. In a second step the top of these already moulded structures will be structured in a further embossing cycle using a different (e.g. with a nanostructures) mould insert. The results are micro-structures at level one and smaller structures on top at level two.

To achieve fine hairs down to the nano range is possible by pulling of polymer melts (hot-pulling process). The process development requires systematic investigation of the materials which are suitable for pulling, the temperature range and the structures of the mould insert using for the pulling step.

Material research

New applications can be implemented if new materials can be integrated into the process chains of replication or surface structuring [4, 16]. With the possibility to mould at temperatures up to 500 °C hot embossing in metallic glasses is possible (Figure 3). We use the replicated parts in a second step as mould insert for another hot embossing cycle and demonstrate a fast fabrication of mould inserts by replication a master in metallic glass [17].

In addition the surface structuring of 100% biodegradable materials was investigated and demonstrated. By this investigation we could show that micro and nanostructuring is not limited to polymers based on crude oil.

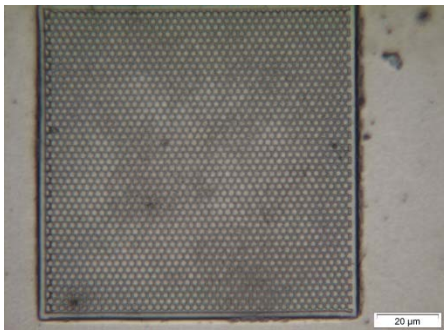

Fig. 3a: Metallic glass structured by hot embossing. The moulded parts were used as mould inserts for the replication of polymers

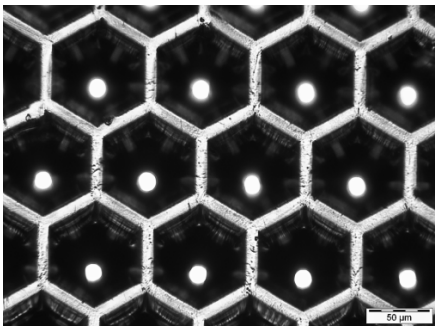

Fig. 3b: Metallic glass – detailed view of the honeycomb structures

Biomimetic inspired research

Using the process of hot embossing and hot pulling we investigate the controlled structuring of surfaces to achieve a controlled wetting behaviour on local areas. We demonstrate the change of the wetting behaviour by structuring up to the superhydrophobic state (Figure 5). Combining the structuring with thermoforming we achieve superhydrophobic behaviour also in three dimensional parts e.g. in fluidic channels.

Using the combination of two level hot embossing and hot pulling as third level we demonstrate the fabrication of Gecko-like structures by replication technologies (Figure 6). The adhesion characteristicsof these structures was identified by AFM. The influence of several design parameters like density, aspect ratio, and tip-shape on dry adhesion performance is systematically examined. In this way, it is revealed that hierarchy is favourable for artificial gecko-inspired dry adhesives made of stiff materials on the nanometer scale.

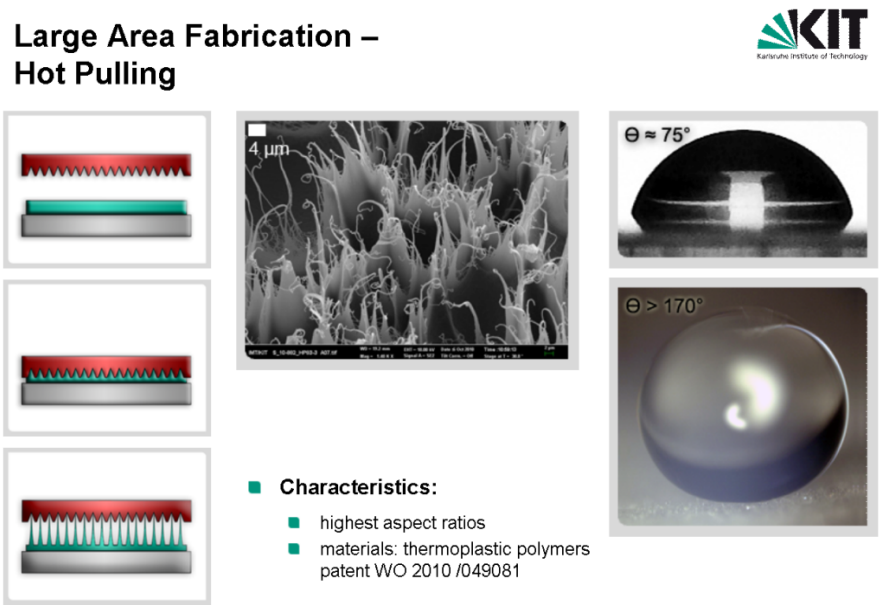

Fig. 5: Superhydrophobic surfaces fabricated by hot puling of fine hairs. By structuring the contact angle increase up to 170°

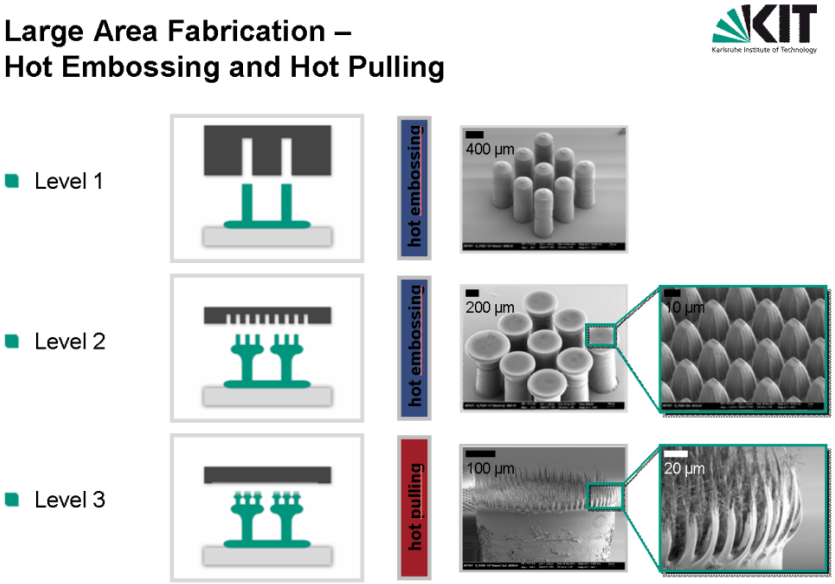

Fig.6: Hierarchical structuring by two level embossing and hot pulling. The first level is characterised by hot embossing of microstructures.

References

[1] U. Fernekorn, J. Hampl, F. Weise, C. Augspurger, Ch. Hildmann, M. Klett, A. Löffert, M.Gebinoga, K-F. Weibezahn, G. Schlingloff, M. Worgull, M. Schneider, and A. Schober. Microbioreactor design for 3-D cell cultivation to create a pharmacological screening system. Engineering in Life Sciences, 11(2):133–139, 2011.

[2] A. Kolew, D. Münch, K. Sikora, and M. Worgull. Hot embossing of micro and sub-micro structured inserts for polymer replication. Microsystem Technologies, 17(4):609–618, 2011.

[3] M.Heilig, S. Giselbrecht, A. Guber, and M. Worgull. Microthermoforming of nanostructured polymer films: a new bonding method for the integration of nanostructures in 3-dimensional cavities. Microsystem Technologies, 16(7):1221–1231, 2010. DOI: 10.1007/s00542-010-1072-2.

[4] K. Timm, C. Myant, H.A. Spikes, M. Schneider, T. Ladnorg, and M. Grunze. Cosmetic powder suspensions in compilant, fingerprintlike contacts. Biointerphases, 6(3):126–134, 2011.

[5] M. Worgull, A. Kolew, M. Heilig, M. Schneider, H. Dinglreiter, and B. Rapp. Hot embossing of high performance polymers. Microsystem Technologies, 17(4):585–592, 2011. DOI 10,.1007/s00542-010-1155-0.

[6] M. Heilig, M. Schneider, H. Dinglreiter, and M. Worgull. Technology of microthermoforming of complex three-dimensional parts with multi scale features. Microsystem Technologies, 17(4):593–600, 2011. DOI 10.1007/s00542-010-1203-9.

[7]M. Worgull, A. Kolew, M. Heilig, M. Schneider, M. Hartmann, and H. Dinglreiter. Heißprägen von polymeren Mikro- und Nanostrukturen.Galvanotechnik, pages 2558–2568, 2011.

[8] M. Worgull, A. Kolew, M. Heilig, M. Schneider, and H. Dinglreiter. Abformen von Mikro- und Nanostrukturen. Galvanotechnik, (4):928–936, 2011.

[9] A. Schober, U. Fernekorn, B. Lübbers, J. Hampl, F.Weise, G. Schlingloff, M. Gebinoga, M. Worgull, M. Schneider, C. Augspurger, Ch. Hildmann, M. Kittler, and M. Donahue. Applied nano bio systems with microfluidics and biosensors for three-dimensional cell culture. Mat.-wiss. u. Werkstofftech., 42(2), 2011.

[10] A. Schober, C. Augspurger, U. Fernekorn, K.-F. Weibezahn, G. Schlinglof, M. Gebinoga, M. Worgull, M. Schneider, C. Hildmann, F. Weise, J. Hampl, L. Silveira, I. Cimalla, and B. Lübbers. Microfluidics and biosensors as tools for NanoBioSystems research with applications in the ”Life Science”. Materials Science and Engineering B, 169:174 – 181, 2010.[

[11] M. Röhrig, M. Heilig, M. Schneider, A. Kolew, K. Kaiser, M. Guttmann,and M. Worgull. Universelle Fixierung von Shim-Formeinsätzen für die Mikro- und Nanoreplikation auf Basis von Polymerfolien. Galvanotechnik,101(7):1646 – 1653, 2010. ISSN 0016-4232 B 20696.

[12] B.E. Rapp, M. Schneider, and M. Worgull. Hot punching on an 8 inch substrate as an alternative technology to produce holes on a large scale. Microsystem Technologies, 16(7):1201 – 1206, 2010. DOI 10.1007/s00542-009-0943-x.

[13] M. Heilig, M. Schneider, H. Dinglreiter, and M. Worgull. Study on Influencing Factors in Micro Thermoforming and Micro Blow Molding. In 27th World Congress of the Polymer Processing Society (PPS-27), 2011. ISBN 978-9954-520-04-8.

[14] A. Kolew, M. Heilig, K. Sikora, D. Münch, and M. Worgull. Multi component hot embossing of micro- and nanosystems. In Conference proceedings Symp.on Design, Test, Integration and Packaging of MEMS/MOEMS (DTIP 2011), Aix-en-Provence, France, pages 284–287, May, 11 - 13th 2011. ISBN: 978-2-35500-013-3.

[15] M. Heilig, M. Schneider, T. Ide, and M. Worgull. Technology of microthermoforming of complex three-dimensional parts with multiscale features. In Conference proceedings Symposium on Design, Test, Integration and Packaging of MEMS/MOEMS(DTIP2010), Seville, Spain, pages 289–294, May 2010. ISBN: 978-2-35500-011-9.

[16] B. E. Rapp and M. Worgull. Combining indirect microfluidic systems with polymer components manufactured from photocurable perfluoropolyethers. In Conference proceedings Symp.on Design, Test, Integration and Packaging of MEMS/MOEMS (DTIP 2010), Seville, Spain, pages 299–300, May,05 - 07th 2010. ISBN: 978-2-35500-011-9.

[17] A. Kolew, K. Sikora, D. Münch, and M. Worgull. Replication of micro and sub-micro structures by means of hot embossed polymer inserts. In Conference proceedings Symp.on Design, Test, Integration and Packaging of MEMS/MOEMS (DTIP 2010), Seville, Spain, pages 339–343, May, 05-07th 2010. ISBN: 978-2-35500-011-9.

Focused Ion Beam

Torsten Scherer, Delphine Chassaing

The Focused Ion Beam (FIB) is operated in KNMF by the Institute of Nanotechnology (INT) mainly for the fabrication of TEM-lamellae, nano- and micro-patterning as well as cross-sectioning and 3D imaging of micro- and nanostructures. The system is equipped with various detectors for electron and ion imaging (SE, STEM, SI) and EDX spectroscopy as well as 4 different GIS (Gas Injection Systems), providing Pt-, C-, W-deposition and XeF_2 enhanced etching. The In-house research focuses on TEM-lamellae production for TEM investigation of multilayer structures, nanowires, SPD-materials as well as FIB imaging of cross sections of various types of samples including photonic crystals, plasmonic structures and gratings for x-ray applications respectively. Another focus is on micro contacting of nanowires and tensile testing of various types of samples as well as patterning of micro- and nanostructures. The following examples of R&D activities were performed up to end 2011.

Tensile testing and electrical contacting of metal nanowires

Metal nanowires produced via electrodepositing, which allows tuning of the wire size and structure, exhibit interesting material characteristics for applications in microelectronics and micro-electromechanical systems (MEMS), they are small in size and show high electrical conductivity combined with high mechanical strength. Noble metal nanowires are ideal building blocks for these applications due to their excellent electrical and mechanical properties [1, 2, 3]. FIB and the micromanipulation device were used to carry out the tensile test and to enable the electrical contacting for 4 point measurements of the wires (Figure1). In addition, TEM lamellae of the wires were produced to investigate the nanostructure in HRTEM (Figure 2).

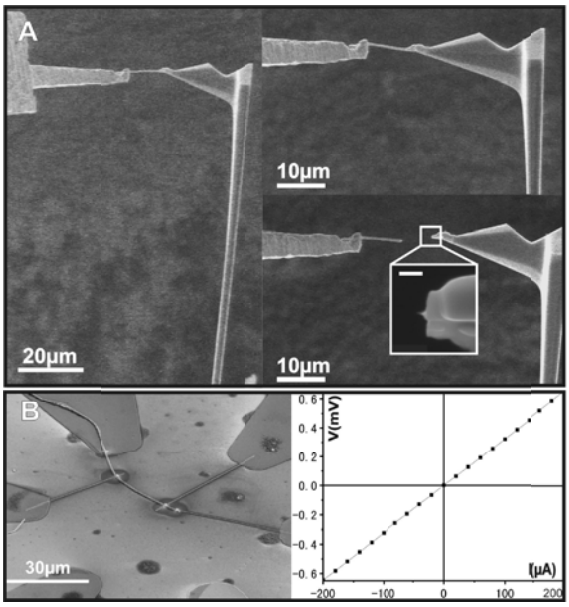

Fig. 1: Tensile testing (A) and measurement of electrical properties (B) of the nanowires. (A) SEM images taken during tensile testing. A Cu-wire was fixed by ion-beam-induced deposition of Pt between the micromanipulator probe and the AFM tip. SEM images are shown during loading (top right) and after wire failure (bottom right). The tensile strength of the wire is 650 MPa which is far higher than that of commercial bulk coarse-grained copper. (B) Measurement of electrical properties. SEM image of a single copper wire which is connected to four electrodes by ion-beam induced deposition of Pt (left). The linearity of the I(V) curve (on the right) indicates ohmic properties at room temperature. The resistance is 3.23 Ù, resulting in a resistivity of approx. 18.4 nÙ·m, which corresponds to the value of bulk copper.

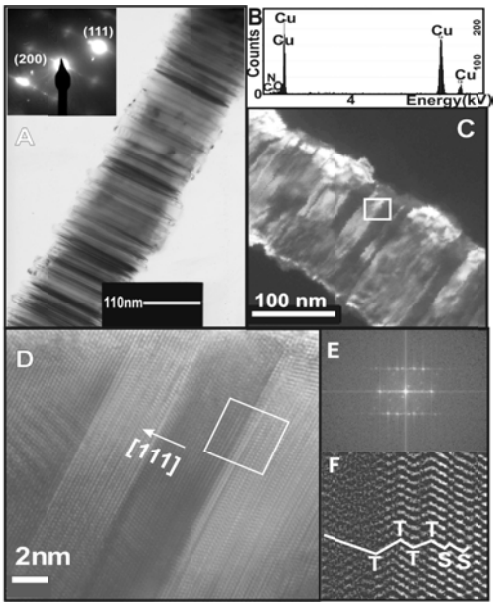

Fig. 2: TEM analysis of copper wires
(A) BF image of a typical copper wire and corresponding SAED pattern (inset). Lamellar structures dominate along the whole wire and are perpendicular to the wire axis. The SAED pattern recorded close to the [110] zone axis indicates that the copper wire is single-crystalline.
(B) Corresponding EDX indicates pure copper.
(C) DF TEM image of a copper wire.
(D) The HRTEM micrograph shows details of the region marked by the white square in Figure 2C. Lots of planar defects are visible in the bright regions in contrast to the much less defect-rich, dark regions.
(E) and (F) are the FFT pattern and the Fourier-filtered HRTEM image, respectively, taken from marked area in the HRTEM image (D). Band-like patterns in the FFT representation (E) indicate a significant contribution of twin defects. The letters T and S mark the twins and stacking faults, respectively, in the filtered HRTEM image (F).

Cross section imaging of gratings used for x-ray phase contrast imaging

For phase contrast imaging with conventional X-ray tubes as e.g. in computer tomography scanners (CT-scanners) special types of optical gratings are needed. In order to absorb high energy radiation, absorption gratings with periods of a few microns only and extreme aspect ratios (>80) are fabricated, by employing a modified LIGA process. However, above a critical structural height, structures collapse due to e.g. capillary effects. FIB was used to analyze the geometrical properties of the cross sections of gratings developed via a new variant of the LIGA process to overcome the aforementioned limitations. Figure 3 shows cross sections of one of the first test structures. FIB cuts using a high ion beam current of 21 nA were carried out overnight (> 12 hours) to obtain the requested high aspect ratios. The obtained cross sections allowed detailed investigations of possible structure collapse and defects introduced during the LIGA process [4].

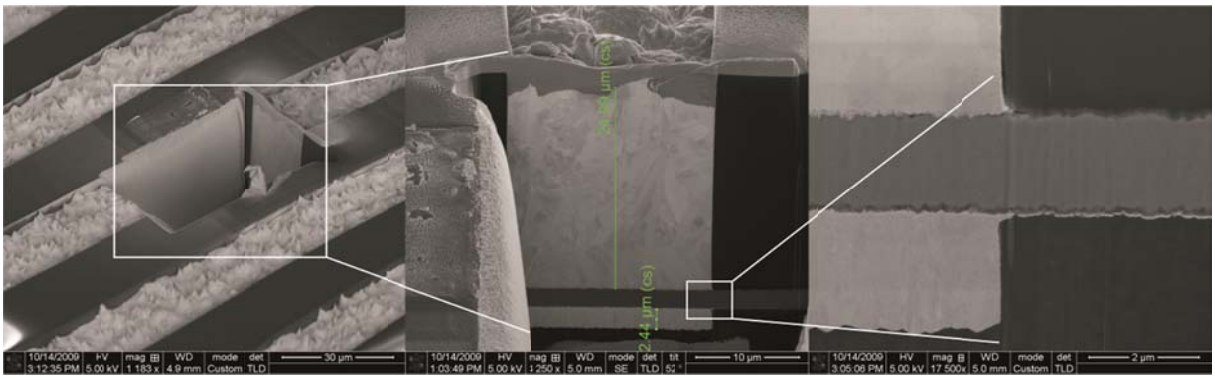

Fig. 3: First test structures for double sided gratings.

Microstructure analysis of tungsten refractory materials for future nuclear fusion power plants

Refractory materials, in particular tungsten base materials are considered as primary candidates for structural high heat load applications in future nuclear fusion power plants. Since physical and mechanical properties are influenced by the underlying microstructure, refractory alloys can behave quite different, even if their chemical composition is the same.

Due to their fabrication history (powder mixing, pressing, sintering, rolling, forging, or swaging) these materials have specific microstructures which lead to different fracture modes. The influence of the microstructure characteristics like grain size, anisotropy, texture, or chemical composition has been studied partly using FIB for 3D slice and view imaging and 3D reconstruction of the obtained slices (Figure 4 -5) [5]. Using 3D reconstructions of materials with different fabrication history we could analyze the shape, orientation and size of segregations (here La2O3) in the tungsten matrix.

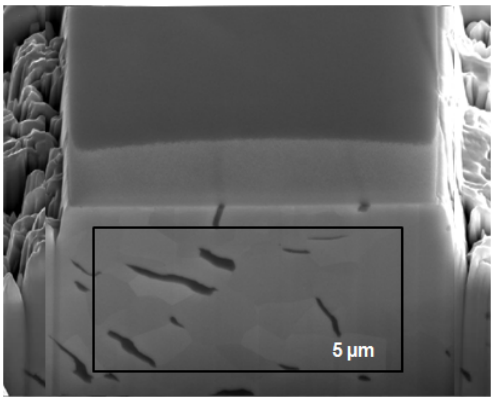

Fig. 4: SEM cross section image of tungsten with 1 % La2O3 particles. Sliced area of about 20x 10x 15 µm3. 2D imaging show needle like aggregates in the tungsten matrix.

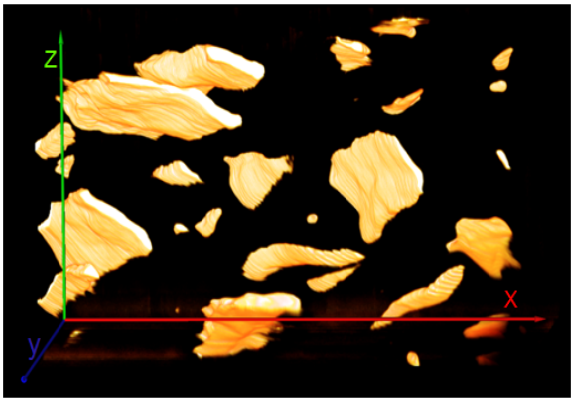

Fig. 5: 3D visualization of the sample in Figure 4 showing flake-like lanthanum oxide particles in tungsten matrix. 3D imaging allows a precise and quantitative interpretation of the real texture.

Fabrication of plasmonic lenses

Various plasmonic devices composed of nanoholes, nanoparticles, nanowires, etc. have been developed, they allow the reduction of the size of optical elements for applications such as focusing, waveguiding, sensing, and light trapping. Arrays of metallic nanoapertures have been extensively investigated and have become a fundamental plasmonic material showing potentials for sensing, lensing, color filtering, etc. Three finite-sized two-dimensional (2D) periodic arrays of metallic nanoapertures with the shape of nanowave, nanohole, and

nanodot have been developed [6]. SEM images of the three finite-sized 2D periodic arrays of metallic nanoapertures with the shape of nanowave, nanohole, and nanodot, respectively, are shown in Figure 6.

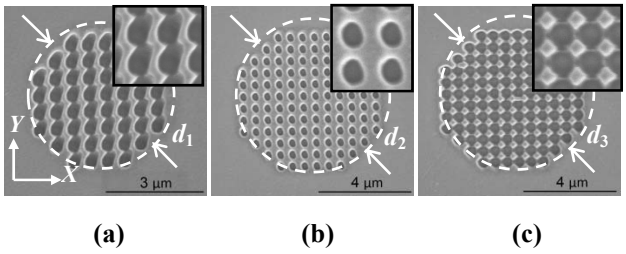

Fig. 6:
SEM images of the fabricated finite-sized 2D periodic arrays of metallic nanoapertures:
a) nanowaves,
b) nanoholes, and
c) nanodots.
The insets show details of the nanoapertures.

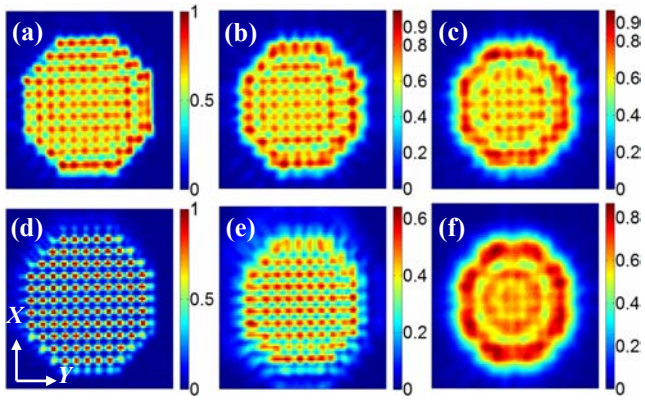

Fig. 7:
(a)-(f) The optical fields parallel to X-Y plane at three different Talbot distances (τ, 2τ and 3τ) from the output surface of the nanohole-shaped device. (a)- (c) for λ_623, (d)-(f) for λ_525.

All the devices were fabricated by FIB milling in a 200 nm gold film on a Pyrex wafer, and have the same array period of 500 nm in both X and Y directions. The nanoholes have a diameter of ~250 nm. The nanoapertures are in a square lattice to form an approximately circular pattern, with the diameter d1-d3, of 4.5, 6.2 and 6.2 μm for d1-d3, respectively. Using water as an output medium, although the operating wavelengths are larger than the array period, both the focusing and far-field plasmon Talbot effect are experimentally observed. Figure 7 shows the optical fields parallel to the X-Y plane at three different Talbot distances.

Investigation of cement based materials in aggressive aqueous environments

Cement based materials exposed to aggressive aqueous environments are subject to chemical changes affecting their durability. Due to concentration gradients between the pore solution of the material and the surrounding aqueous media reactive transport processes are initiated. By reactive transport processes chemical equilibria between pore solution and the solid phases will be disturbed and consequently dissolution and crystallisation reactions are triggered.

The FIB preparation technique enables detailed investigations of surface reactions by means of electron microscopic methods [7]. A scanning beam of gallium ions is applied in order to remove material from the sample surface with a spatial precision in nanometer scale. In this way, depth profile cuts were performed in order to investigate depth dependant chemical and structural properties of the surface near areas (Figures 8, 9).

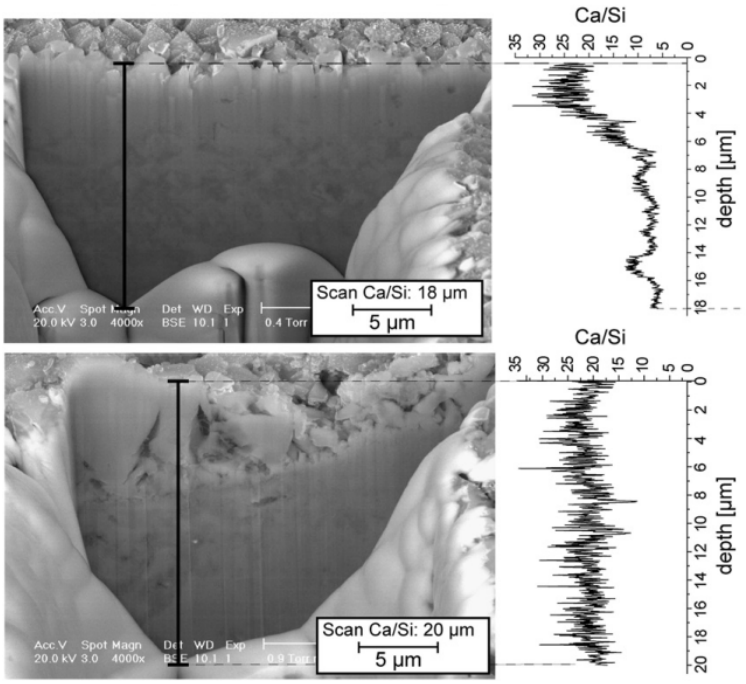

Fig. 8. microscopic investigation in the material/ water interface of mortar samples with features of local hydrolytic corrosion and spatial Ca/Si ratios by means of EDX line scans in intact and damaged area of the surface; (a) overview by means of optical microscopy, (b) ESEM images of the sample surface, (c) ESEM images and EDX measurements on FIB profile cuts.

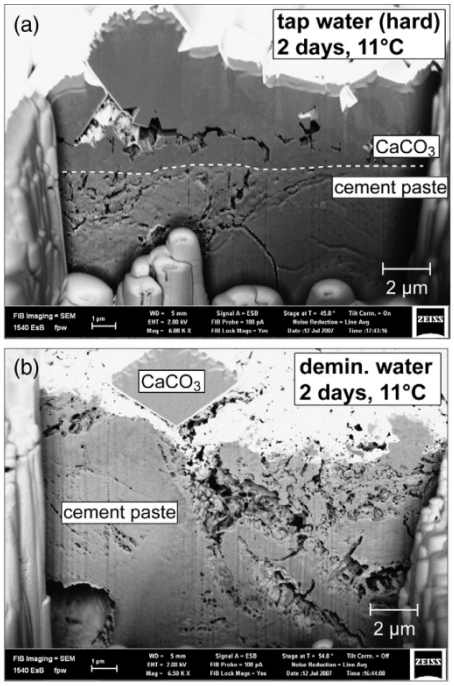

Fig. 9: SEM image of FIB cuts in the cement paste/water interface of a sample immersed for two days at 11 °C in (a) hard tapwater and (b) demineralized water.

For instance, the formation of calcium carbonate layers on the alkaline surfaces of the cement based materials not always acts as a protection against chemical attack. In the case that a dense covering layer of calcium carbonate crystals precipitates on the surfaces, a transport inhibiting effect was noticed. In certain cases, crystal growth on the surfaces even forces a further degradation of the materials, especially if the crystal growth is supplied by the pore solution of the underlying material. The FIB cut in the surface near area reveals structural properties of the covering layers. The permeability of the surface layer was sufficient to sustain continuous crystallization processes by a steady supply of OH--ions from the pore solution of the cementitious substrate material.

The results presented here illustrate that, the chemical and structural properties of the material/water interface have a consequential influence on reactive transport processes. In particular the compactness of crystalline covering layers on the surfaces of the materials, related to crystallization mechanisms, is of relevance. In this context, the focused ion beam preparation technique- combined with common chemical and mineralogical investigations - is a versatile tool for the elucidation of the interrelationship between changes in chemical composition and structural properties.

Collaboration in in-house research

Institute for Applied Materials (IAM), Institute of Functional Interfaces (ITG); Institute of Microstructure Technology (IMT)

References

[1] Zhong, S., Koch, T., Wang, M., Scherer, T., Walheim, S., Hahn, H. and Schimmel, T. (2009), Electrodeposition: Small 20/2009. Small, 5: n/a. doi: 10.1002/smll.200990098

[2] T. Scherer, S. Zhong and T. Schimmel, Tensile Testing of Microstructures - An Easy Method to Study the Mechanical Properties of Microsamples, Imaging & Microscopy, Issue 1, Vol. 13, 44-47 (2011).

[3] T. Scherer, S. Zhong and T. Schimmel, Tensile Testing of Microstructures - An Easy Method to Study the Mechanical Properties of Microsamples, online at Imaging and Microscopy: http://www.imaging-git.com/science/scanning-probe-microscopy/tensile-testing-microstructures. (5/13/11).

[4] J. Kenntner, T. Grund, B. Matthis, M. Boerner, J. Mohr, T. Scherer, M. Walter, M. Willner, A. Tapfer, M. Bech, F. Pfeiffer, I. Zanette, and T. Weitkamp, “Front and Backside Structuring of Gratings for Phase Contrast Imaging With X-ray Tubes,” in Developments in X-RayTomography VII, SPIE Conference Proceedings 7804, (2010), pp. 780408–01–10.

[5] M. Rieth, D. Armstrong, B. Dafferner, S. Heger, A. Hoffmann, M. Hoffmann, U. Jäntsch, C. Kübel, E. Materna-Morris, J. Reiser, M. Rohde, T. Scherer, V. Widak, H. Zimmermann, Advances in Science and Technology Vol. 73 (2010) pp 11-21, doi:10.4028/www.scientific.net/AST.73.11

[6] The Focusing and Talbot Effect of Finite-Sized Two-Dimensional Periodic Arrays of Metallic Nanoapertures in High-Index Medium, Yiting Yu, Delphine Chassaing, Torsten Scherer, Benjamin Landenberger, and Hans Zappe, (in preparation)

[7] M. Schwotzer, T. Scherer, A. Gerdes, Protective or damage promoting effect of calcium carbonate layers on the surface of cement based materials in aqueous environments, Cement and Concrete Research 40 (2010) 1410–1418.

Dip-pen Nanolithography

Michael Hirtz, Harald Fuchs

Our group, stationed at the Institute for Nanotechnology (INT) offers access to two high-end DPN platforms (DPN 5000 and NLP 2000) in the framework of KNMF. Dip pen nanolithography (DPN) is a technique first developed by Piner et al. in the Mirkin group [1]. In DPN, a fine tip as also used in atomic force microscopy is coated with a chemical ink and then brought into contact with a substrate to transfer the ink onto the surface, similar to the way a quill writes, though here with the size and precision in the nanoscale. The more advanced setups developed in the last decade feature now the use of arrays of tips (instead of a single tip) which allows a bigger thru-put and large area covering by parallelization of the lithographic process. By the use of so called “inkwells” (microfluidic chips that math the feature sizes of the cantilever arrays), it is possible to deliver different inks to each particular cantilever in such an array, allowing for multiplexed writing (i.e. the integration of different inks in one process step and within the same pattern with high registry). The main strengths of DPN are the possibility of arbitrary pattern generation (maskless, direct write) in combination with high resolution (sub-micron- to nano-scale, depending on the specific ink/substrate system), mild process conditions and multiplexing.

Lipid-DPN for Biological Applications

Lipid-DPN (L-DPN) is a writing technique for DPN that was developed in-house by our group at the INT. It creates artificial membranes and membrane stacks by using a carrier phospholipid (DOPC) as ink that can be admixed with almost arbitrary functionalized lipids [2, 3]. The obtained structures can be used in biological experiments as bio-compatible interface for the presentation of proteins and bioactive compounds [4] or as sensor elements (see photonic applications). We are working closely together with biologists (in-group and with Prof. Cato from KIT-ITG) in a project that aims at elucidating the rapid response of mast cells to steroids like cortisone (e.g. in anti allergic drugs). The first results from this work is data on the dose dependant response of mast cells to a model allergen (Dinitrophenol, DNP) patterned by this technique (Figure 1) [5]. Ongoing studies now focus on the interaction of steroids with this recognition and activation events on patterned surfaces. In addition to this we dedicate parts of our in-house research time to further our knowledge of the writing process in L-DPN by studying e.g. the transport from tip to surface [6] and the organization of the lipid membrane stacks in the written structures. [7]

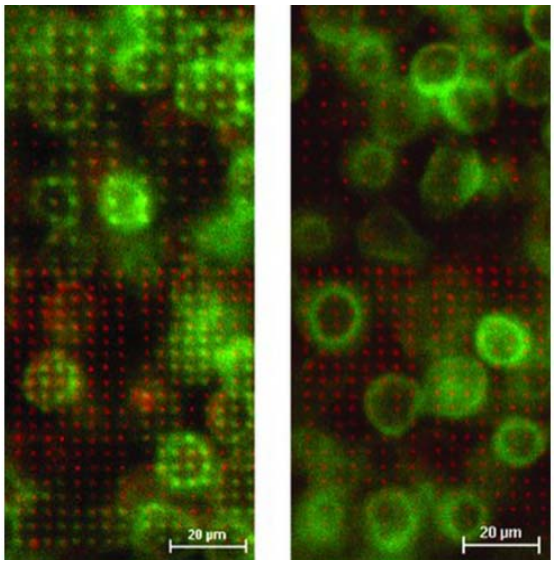

Fig. 1: Mast cells with fluorescently labeled anti-DNP receptor (green) on a DOPC pattern (red) containing DNP (left) and without DNP admixing (right). Interaction and co-localisation of the receptor with the mast cells is only observed in the presence of DNP in the pattern. Scale bars correspond to 20 µm.

Click-chemistry DPN

If covalent attachment of chemicals is desired, DPN is usually performed with a thiol ink on gold surfaces. To expand the limits of such a narrow band of ink/substrate systems for covalent attachment we are establishing click-chemistry based approaches to the immobilization of molecules onto surfaces by DPN. In collaboration with the Lahann group (IFG) we demonstrated the feasibility of click-chemistry DPN (CC-DPN) on versatile chemical vapor deposition (CVD) coatings that enable click-chemistry functionality on almost arbitrary substrates (glass, silicon, PDMS, PMMA, PTFE and more). [8] For siliconoxide and glass surfaces we have developed a facile two step functionalization procedure that allows for CC-DPN on these surfaces without need for elaborated CVD processes. Ongoing research in close cooperation with the group of Prof. Bastmeyer (ZI I) aims at the application of CC-DPN for the immobilization of bio-active compounds for cell culture experiments.

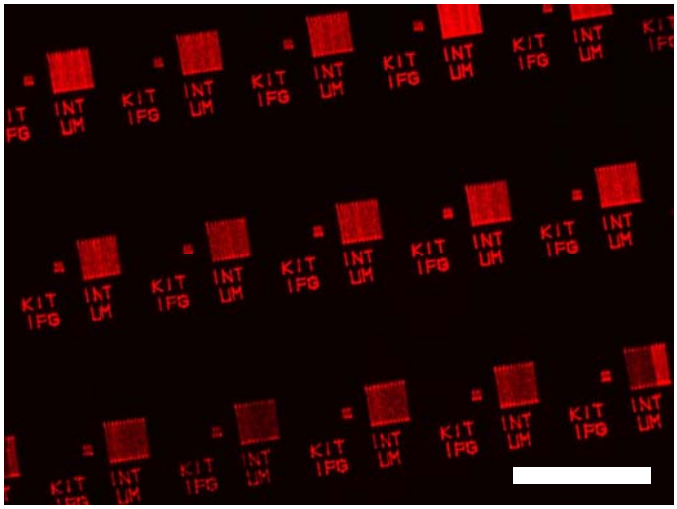

Fig. 2: Example of CC-DPN with an Alexa-Fluor 555 azide ink on a CVD coated silicon surface. The single line width was measured by AFM to be about 100 nm. Scale bar corresponds to 35 µm.

Photonic applications and functionalization of prestructured devices

Due to the relative inexpensiveness of the involved substances and processing steps, L-DPN can potentially be used in the field of label free sensing. We demonstrated the feasibility of lipid diffraction gratings (Figure 3) for this purpose. By admixing of biotinilated lipids to the carrier ink used to write the grating structures binding sites are introduced that allow for specific binding of streptavidin to the gratings. Upon binding a drop in diffraction signal can be detected that is depending on the concentration of analyte. The detection is very specific (can be done in full serum) and also sensitive (down to the nanomolar regime). [9]

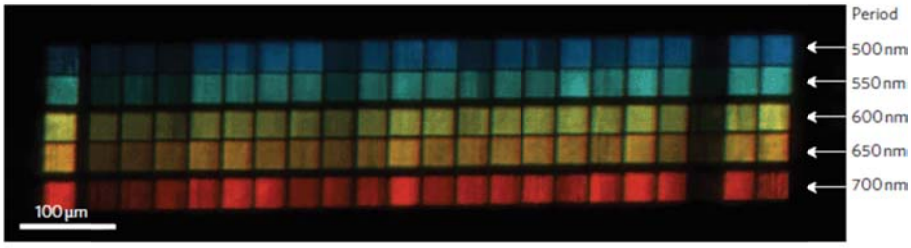

Fig .3. White light diffraction by lipid gratings of different periodicity. Scale bar corresponds to 100 µm.

Due to its mild process conditions, high registry and precision and as a direct writing approach, DPN offers a wide variety of post-functionalization possibilities on pre-manufactured structures that would be very hard to functionalize by other means. We demonstrated e.g. the integration of lipid structures into a chip featuring a network of

microfluidic channels and waveguides to selectively address active regions [10] or the application of lipids and azide inks to a resonator cantilever device (Figure 4, unpublished).

Fig. 4: Microresonator beam with fluorescent lipid functionalization (red). Micro Device fabricated by Ionescu group, EPFL Lausanne. Scale bar corresponds to 10 µm.

Collaboration in in-house research

We are closely cooperating with the KIT based groups of Prof. Bastmeyer (ZI I), Prof. Cato (KIT-ITG), Prof. Krupke (KIT-INT), Prof. Lahann (KIT-IFG), PD Mappes (KIT-IMT) and Prof. Schimmel (KIT-INT). In addition, we have a strong partnership with the company NanoInk (Chicago, USA) developing and testing new approaches in DPN.

References

[1] Piner, R. D.; Zhu, J.; Xu, F.; Hong, S.; Mirkin, C. A. “Dip-Pen" Nanolithography”, Science 1999, 283, 661-663.

[2] Lenhert, S.; Sun, P.; Wang, Y.; Fuchs, H.; Mirkin, C. A. “Massively parallel dip-pen nanolithography of heterogeneous supported phospholipid multilayer patterns”, Small 2007, 3, 71-5.

[3] Lenhert, S.; Mirkin, C. A.; Fuchs, H. In situ lipid dip-pen nanolithography under water ,Scanning 2010, 32, 15-23.

[4] Sekula, S.; Fuchs, J.; Weg-Remers, S.; Nagel, P.; Schuppler, S.; Fragala, J.; Theilacker, N.; Franzreb, M.;Wingren, C.; Ellmark, P.; Borrebaeck, C. A. K.; Mirkin, C. A.; Fuchs, H.; Lenhert, S. Multiplexed lipid dip-pen nanolithography on subcellular scales for the templating of functional proteins and cell culture. Small 2008, 4, 1785-93.

[5] Sekula-Neuner, S.; Maier, J.; Oppong, E.; Cato, A. C. B.; Hirtz, M.; Fuchs, H. Allergen Arrays for Antibody Screening and Immune Cell Activation Profiling Generated by Parallel Lipid Dip-Pen Nanolithography, Small 2012, 8, 585-591.

[6] Biswas, S.; Hirtz, M.; Fuchs, H. Measurement of Mass Transfer during Dip-Pen Nanolithography with Phospholipids. Small 2011, 7, 2081-6.

[7] Hirtz, M.; Corso, R.; Sekula-Neuner, S.; Fuchs, H. Comparative Height Measurements of Dip-Pen Nanolithography-Produced Lipid Membrane Stacks with Atomic Force, Fluorescence, and Surface Enhanced Ellipsometric Contrast Microscopy, Langmuir 2011, 27, 11605-11608.

[8] Chen, H.-Y.; Hirtz, M.; Deng, X.; Laue, T.; Fuchs, H.; Lahann, J. Substrate-independent dip-pen nanolithography based on reactive coatings, Journal of the American Chemical Society 2010, 132, 18023-18025.

[9] Lenhert, S.; Brinkmann, F.; Laue, T.; Walheim, S.; Vannahme, C.; Klinkhammer, S.; Xu, M.; Sekula, S.; Mappes, T.; Schimmel, T.; Fuchs, H. Lipid multilayer gratings. Nature Nanotechnology 2010, 5, 275-9.

[10] Schelb, M.; Vannahme, C.; Welle, A.; Lenhert, S.; Ross, B.; Mappes, T. Fluorescence excitation on monolithically integrated all-polymer chips. Journal of Biomedical Optics 2010, 15, 041517.

Thin Film Technology

Harald Leiste

Facilities for thin film development on two dimensional and three dimensional substrates are operated in KNMF by the Institute for Applied Materials (IAM-AWP). The employed PVD-processes are magnetron sputtering, arc ion plating and PDV/CVD-hybride processes. In the scope of these facilities thin films of different compositions and properties can be developed in terms of mechanical, magnetic, electrical or optical applications. The r.f. and DC-magnetron processes in the nonreactive and reactive mode are open to users, beside other methods, and allow complete new system properties. The in-house research focuses on process improvement and optimization as well as on the fabrication of new materials and concepts. The following R&D activities were performed in 2011.

Conditions for epitaxial growth of TiN thin films on MgO substrates

In order to deposit thin epitaxial films on single crystal substrate materials, it is necessary to choose deposition conditions so that surface diffusion and growth rates are suitable. The most important parameter are the substrate temperature during deposition, the dwell time for surface recovery and a low growth rate. Therefore a radiation heater was used which is based on two halogen lamps below the substrate holder (Figure 1). By the radiation of the heater the substrate temperature can be stabilized up to 550°C during coating.

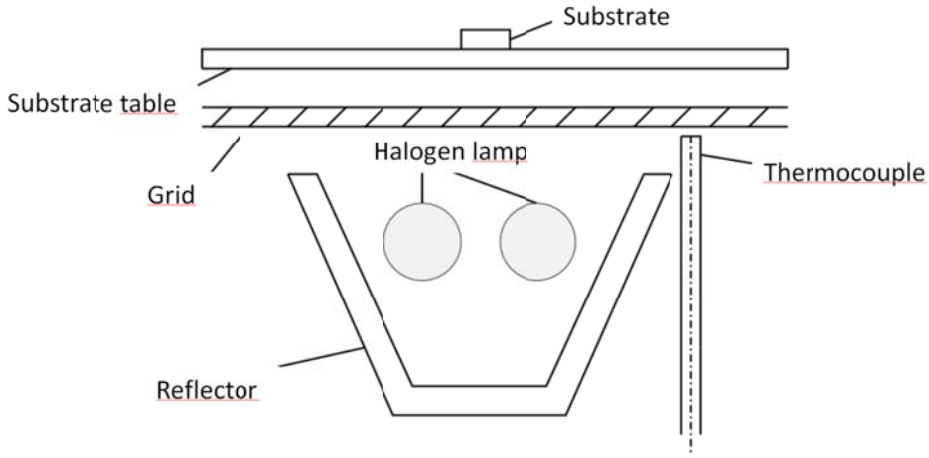

Fig. 1: Substrate heater with halogen lamps built in the coating facility

The thin film deposition was carried out by DC-magnetron sputtering in a nonreactive atmosphere by using a 6 inch diameter target of stoichiometric TiN. As a substrate material (100)-oriented MgO single crystals were used. Prior to the assembly in the coating chamber, the substrates were cleaned by ultrasonic Aceton treatment. The deposition process starts with setting the temperature, followed by a plasma etching process to clean up the surface. A dwell time for surface recovery is added with the subsequent coating time. The film thickness of 250 nm was realized by a DC-power of 30 W resulting in a growth rate of 5nm/min. This is the lowest value of the DC-power to realize stable condition of the plasma configuration during the deposition.

Microstructure of the films

The substrate temperature has a dominant influence on the growth behaviour of the TiN-film. The intensity in the X-ray diffraction (Bragg-Brentano-Mode) shows a decrease of the (111)-

line of TiN with the increasing temperature, demonstrated on a silicone substrate, while the intensity of the (002)-line on the MgO-substrate rises. Figure 2 shows the schematic behaviour of the microstructure of the TiN-Film.

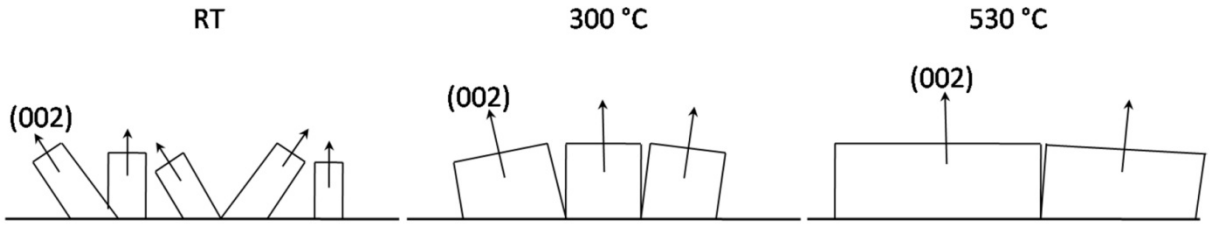

Fig. 2: Schematic behaviour of the growth temperature dependant microstructure and growth orientation

The dwell time for surface recovery was chosen to 0, 2, 5 and 10 min. Without any recovery time the TiN film grew in a relaxed state with a lattice parameter similar parallel and perpendicular to the substrate surface. For values of 2 min and 5 min of

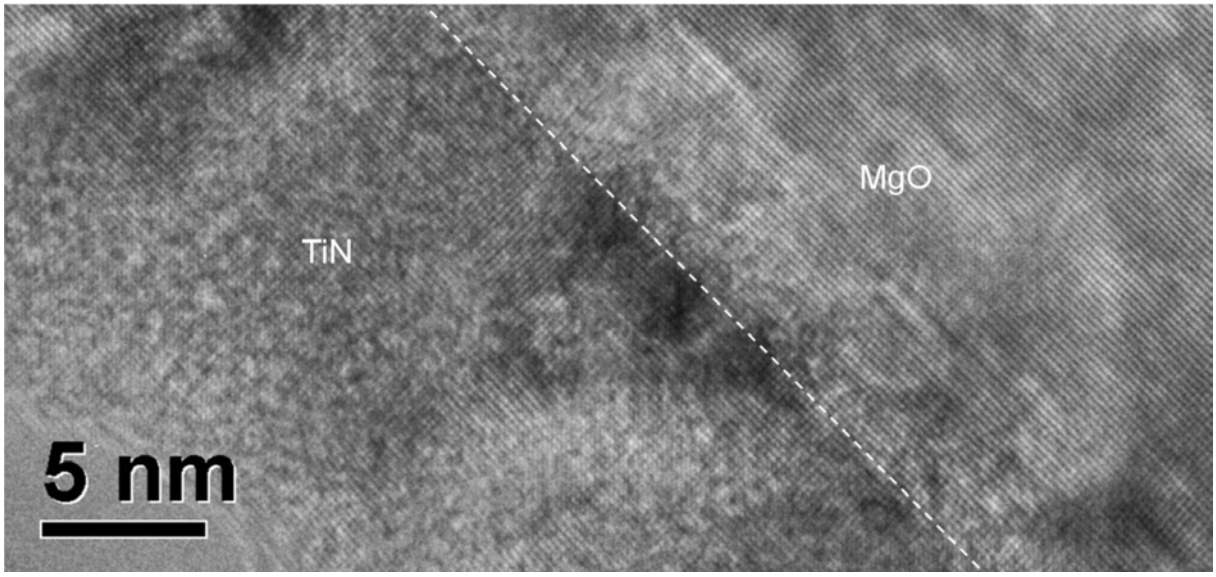

Fig. 3: High resolution TEM-image of the growth interface between substrate (MgO) and film (TiN), (Deposition temperature 530°C)

dwell time the film grew epitaxic and for a dwell time of 10 min the (002)-line vanishes because of poisoning of the surface by contamination. Best results concerning the epitaxic growth have been obtained at a dwell time of 5min. For TEM investigations of the microstructure of the films, the coated substrates have been prepared as a cross section, so that the growth direction is within the image plane. In the HRTEM images (Figure 3) the lattice planes of the substrate and the film are visible. The TiN-film shows a direct growth on the MgO substrate in a epitaxic way without any interface regions.

Collaboration in in-house research

Universities of: Kassel, Kaiserslautern, Aachen, Leoben (Austria), Uppsala (Sweden), Linköping (Sweden), Coimbra (Portugal), Leeds (UK)

Firms: Daimler, TKS, TZO, Walter, Gühring, Balzers, Rockwell Collins

Research Centres: FHG-IWM Freiburg, KIST (Korea), Asociation de la Industria Navarra Cordovilla – Pamplona, Spain

Dry Etching Using RIE(ICP)/RIBE

Daniel Häringer, Julian Hartbaum, Alban Muslija, Christian Lay, Mario Schmitt, Manfred Kohl

A dry etching cluster from Oxford Instruments, having a RIE / ICP (System 100 with a ICP 380 source) and a RIBE process chamber, is operated in KNMF by the Institute of Microstructure Technology (IMT) for fabrication of Si, SiO_2 and Si_3N_4 microstructures as well as various metal (Ti, Cr) structures. A special feature of the dry etching cluster is the Ionfab 300 Plus RIBE tool (RIBE: Reactive Ion Beam Etching) used for structuring of special metal alloys, in particular magnetic alloys consisting of Ni, Co, Fe, shape memory alloys (NiTi) and ferromagnetic shape memory alloys (NiMnGa). The in-House research focuses on process development and optimization as well as on the fabrication of complete nano devices.

Magnetic nanoactuator system

The magnetic nanoactuator development focused on the fabrication of free-standing Ti beam cantilevers with critical dimensions of 50-400 nm covered by an integrated magnetic element at the front end. Main challenges were the patterning of nanostructures as well as their release from the substrate to get movable cantilevers. Resist nanostructures are written by E-beam lithography at 100 kV. A reactive ion etching tool (Oxford Instruments Plasmalab 100 ICP 380) was used to transfer the nanopattern in a metallic layer system consisting of gold and titanium.

Three etching steps were performed to get freestanding and movable nanocantilevers like is seen in Figure 1. In a first etching step the resist pattern was transferred into a 20 nm gold layer which serves as hard mask for the following and second etching step of a 50 nm titanium layer (Figure 1 upper left). For the last etching step isotropic etching of silicon leads to partially released beam structures allowing deflection in out-of-plane direction.

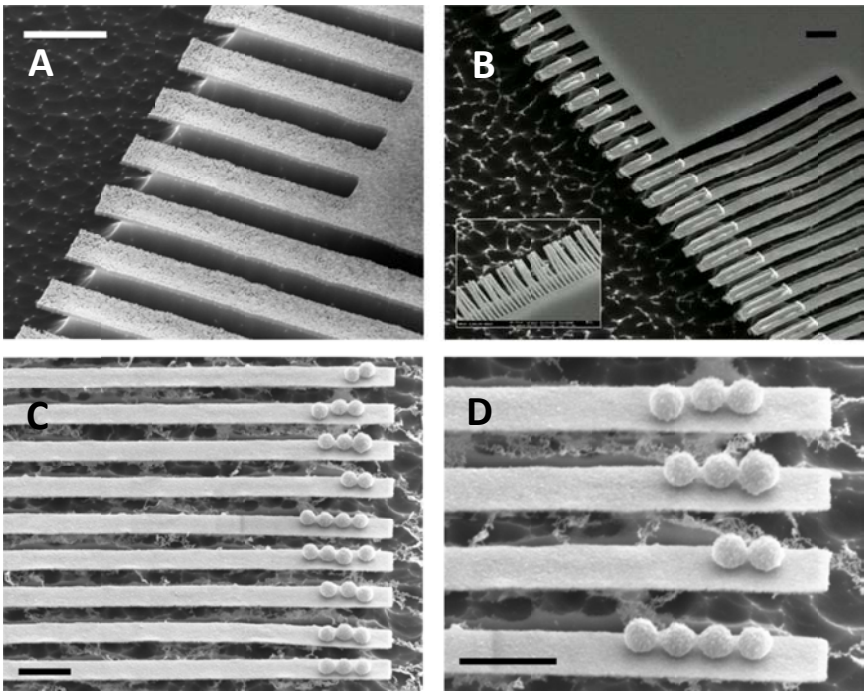

Fig. 1: SEM images of actuator nanostructures etched by a reactive ion etching tool Plasmalab 100 ICP 380 from Oxford Instruments. Etching chemistry consists of Ar and SF6/O2 for Au and Ti/Si, respectively. The scale bar is 1 µm.

SOI based silicon cantilever structures fabricated via cryo process

Silicon structures in the submicron range can be fabricated on the Oxford RIE/ICP etching tool at the IMT using the so called deep cryo etching process. In this process, at very low temperatures (~ -120°C) a temporary passivating layer is generated on the structure sidewalls. Thus, highly smooth and vertical sidewalls can be etched in a reproducible way with aspect ratios up to 3. The layer dimensions of the used SOI are: Device (Si): ~ 500 nm, BOX (SiO_2): ~ 5 µm, and Handle (Si): ~ 650 µm.

The layout consists of the already well-known bar and bridge structures with lateral dimensions from 100 nm up to 4 µm, formerly used for etch tests with single silicon.

During the cryo process, the BOX acts as an etch stop layer. After the 500 nm of silicon have been etched, the substrate is exposed to a wet etching process using 5% HF, for 2.5 hours. Thereby the oxide layer under the silicon device is removed isotropically. The etch rate is approx. 1.8 µm/h, the total etching depth of the BOX was measured to be ~ 4.5 µm (no etching through). The following pictures show the different fabricated cantilever structures (notice the remaining SiO_2 on the ground).

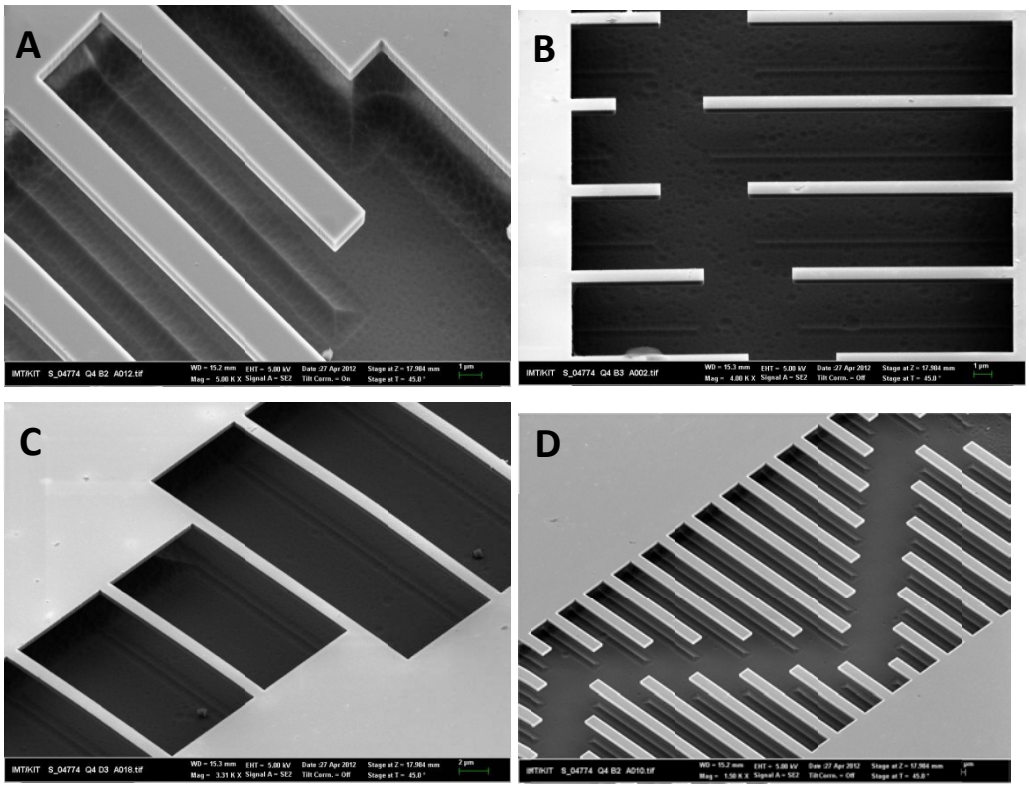

Fig. 2: SEM images of the isotropic etch front of the SiO2 (A), 500 nm wide cantilever structures (B), 1 µm wide free-standing bridges (C) Critical length concerning deflection (D).

High precision positioning of plasmonic nanoparticles

The high precision positioning development focused on the fabrication of plasmonic nanostructures by filling dry etched pores of silicon with metallic nanoparticles. First, resist nanostructures are written by E-beam lithography at 100 kV, followed by a reactive ion etching (RIE) process using SF_6 and O_2 as process gases performed on an Oxford Instruments dry etching cluster to transfer the resist pattern into the silicon substrate. SF_6 plasma reacts chemically at -80 °C with the Si to SiF_4 in addition to an always present physical etching mechanism. A flow of 100 sccm of SF_6 combined with a fraction of 10 % of O_2 is used at a RF power of 50 W and an absolute pressure of 50 mTorr. The SEM images

(Figure 3 A - C) show different pre-patterned silicon substrates, in parts with a variable gap size from 40 nm (right) down to 15 nm (left). Due to the etch conditions the etch process is distinct isotropic with the result of pores having a truncated cone shape. Therefore the pores have to be described by two diameters (see Figure 3 D).

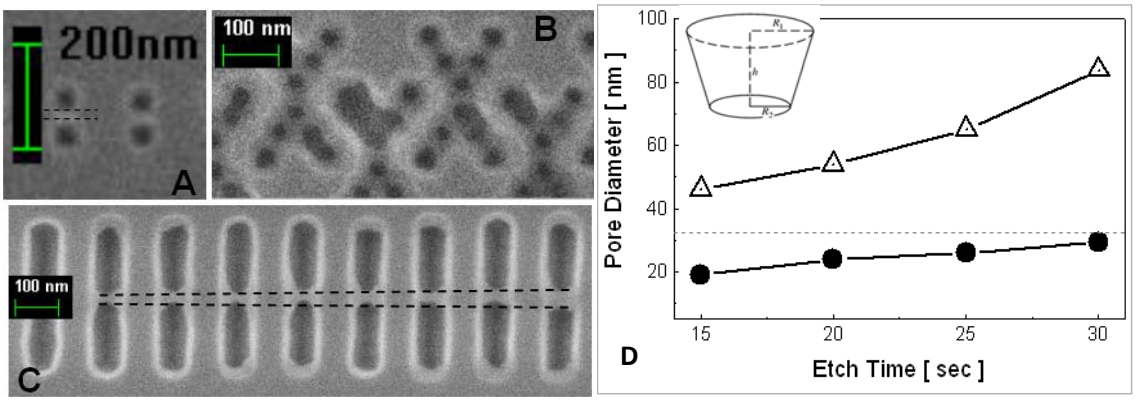

Fig. 3: Pre-patterned silicon substrate for plasmonic nanostructures. SEM images of a double pore arrangement with a tailored gap of 20 nm, indicated by the dotted lines (A), multi-pore design forming a V – shaped nanostructure (B), dipole-like nanostructures (C). Resulting diameters for truncated cone shaped pores as a function of the etch time. Circles (•) give the diameter of the bottom of the pores, whereas triangles (Δ) give the diameter of the top. The layout nominal value of 32.5 nm is indicated by the dotted line (D).

Filling the cavities of the pre-patterned templates with metallic nanoparticles results in a base device for photonic circuits, offering plasmonic applications like nano-antennas, meta materials and metal optics.

Ion beam etching of Ni-Mn-Ga thin films with the RIBE cluster tool

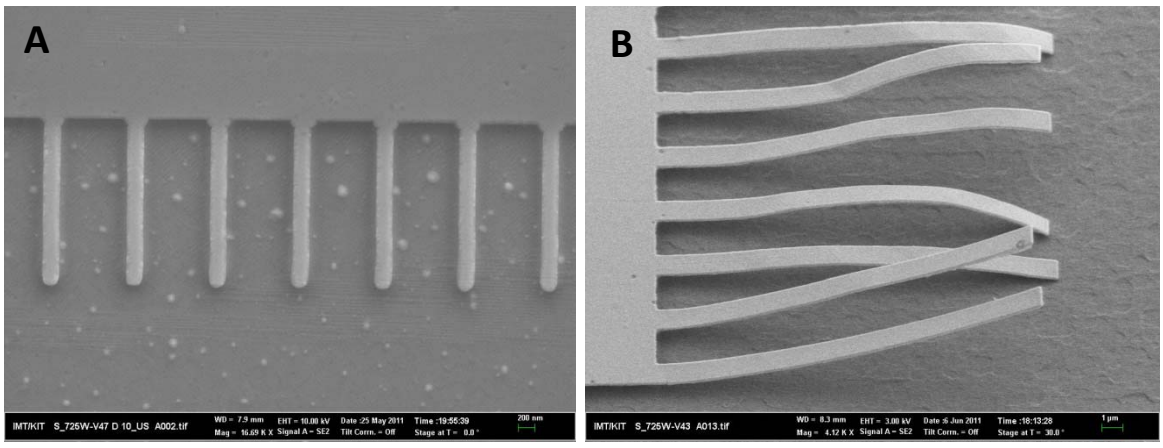

Fig. 4: SEM micrograph of single beams after resist stripping. The thickness and width are 125 nm and 180 nm respectively (A). SEM micrograph of free standing Ni-Mn-Ga beams after sacrificial layer etch. The thickness, width and length are 125 nm, 1 µm and 20 µm respectively (B).

Ni-Mn-Ga is a ferromagnetic shape memory alloy. It combines the shape memory effect and ferromagnetic properties, enabling micro- and nanometer sized actuators. The Ni-Mn-Ga layer is produced by epitaxial sputter deposition on a single crystalline MgO substrate and a Cr buffer layer. The Cr layer will be used to release free-standing Ni-Mn-Ga nanostructures from the substrate in a sacrificial layer process. As Ni does not form any volatile etch products, only physical etching is possible. Therefore structuring is done using ion beam etching (IBE) with Ar ions. The angle of incidence is varied to reduce sidewall roughness.

Figure 4 A shows Ni-Mn-Ga beams with line widths of 180 nm. Under-etching of the Cr layer results in redeposition which can be removed by wet chemical etching or with a Cl_2 and O_2 based reactive ion etch (RIE) process. The resulting free-standing Ni-Mn-Ga nanostructures are shown in Figure 4 B [4].

Free standing double beams

Nano-mechanical systems promise increased speed, resonance frequencies and integration density with respect to their counterparts on the microscale. With the capability of mass sensing in the order of zeptogram as well as force sensing in the order of attonewton, they also offer new applications such as mass detection of small molecules.

The nano double beam shown in Figure 5 was fabricated using dry etching technologies only. A photo resist is structured and its pattern is transferred to a gold layer with a purely physical attack of a reactive ion beam etching (RIBE) step. Gold can now be used as a hard mask for an anisotropical etch of the titanium layer. This is a chemical dry etching process, therefore called reactive ion etching (RIE). Another RIE process is used to isotropically etch the silicon, thus undercutting the double beam to make it free standing.

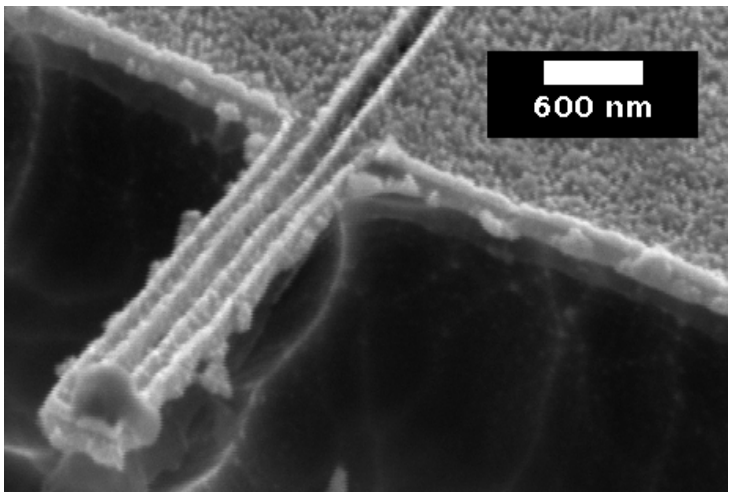

Fig. 5: A double beam with 100 nm wide arms made from 100 nm thick titanium and a 10 nm gold layer.

References

[1] Mario Schmitt, Anja Backen, Sebastian Fähler and Manfred Kohl; Ferromagnetic Shape Memory Nanoactuators “IEEE NANO - 12th International Conference on Nanotechnology”.

[2] Daniel Häringer, Peter Jakobs, Gang Chen, Maksym Yarema, Wolfgang Heiss, and Manfred Kohl; High Precision Positioning of Plasmonic Nanoparticle Based on Damascene Process. “IEEE NANO - 12th International Conference on Nanotechnology”.

[3] Maksym Yarema, Stefan Pichler, Dominik Kriegner, Julian Stangl, Olesya Yarema, Raimund Kirchschlager, Sajjad Tollabimazraehno, Markus Humer, Daniel Häringer, Manfred Kohl, and Gang Chen, Wolfgang Heiss, “ From a high precision synthesis of monodisperse Indium, Tin, and Indium-Tin colloidal nanocrystals to transparent Indium-Tin-Oxide nanoelectrodes“, ACS Nano, 2012, 6 (5), pp 4113–4121.

[4] M. Schmitt, A. Backen, S. Fähler, M. Kohl, Freely Movable Ferromagnetic Shape Memory Nanostructures for Actuation, Microelectronic Engineering (2012), doi: http://dx.doi.org/10.1016/j.mee.2012.07.045.

Transmission Electron Microscopy

Christian Kübel, Di Wang, Kiran Chakravadhanula, Eglantine Courtois, Aaron Kobler, Torsten Scherer, Robby Prang, Delphine Chaissing, Emma Tröster

An image corrected FEI Titan 80-300 Transmission Electron Microscope (TEM) is operated in the KNMF by the Institute of Nanotechnology (INT) for high-end structural characterization in materials sciences using a combination of atomic resolution imaging, nanoscale compositional analysis and nanoscale 3D imaging. The TEM work is supported by Focused Ion Beam (FIB) and classical polishing techniques for preparation of high-quality samples. In-house research focuses on optimizing the performance of the existing microscopy techniques, developing new techniques for nanoscale crystallographic analysis (ACOM-TEM) and the development of in-situ mechanical and electrical characterization of materials inside the TEM. In addition, in-house research is used for high-end characterization of a range of nanomaterials for HGF and KIT internal partners. A selection of the R&D activities performed in 2011 is shown below:

Strain mapping of triple and quadruple junctions in deformed nanocrystalline palladium

The thermal stability of nanocrystalline (nc) materials is an important issue for applications and thus of high technological interest. Grain growth occurs in polycrystalline materials to reduce the contribution to the total energy of the system introduced by the amount of grain boundary (GB) area A^{GB}. Therefore, the high density of interfaces in nc materials is likely to provide a significant driving force for grain growth, which can be expressed by the product of A^{GB} and the specific GB energy γ^{GB}. Systematic studies of grain growth at room temperature and at elevated temperatures show that the thermal stability of nc materials can be improved either by addition of solutes or lattice defects. However, most of these studies neglect the contribution of triple and quadruple junctions, which have a significant influence on grain growth in nc materials. This work is motivated by recent results showing that the initially nc material produced by inert gas condensation could be stabilized against room temperature grain growth by severe plastic deformation. Such a material was inspected by aberration-corrected high resolution TEM using the image corrected FEI Titan 80-300 under NCSI conditions. Figure 1a shows a triple junction ($\Sigma3{:}\Sigma3{:}\Sigma9$) consisting of two intersecting $\Sigma3$ twin boundaries and a $\Sigma9$ grain boundary which is connected to a quadruple junction ($\Sigma3{:}\Sigma3{:}\Sigma3{:}\Sigma9$) via the $\Sigma9$ grain boundary. It seems most likely that this configuration had formed during deformation in which multiple twins merged. A comprehensive strain analysis of the triple junction using the geometric phase analysis (GPA) is presented and compared with a molecular dynamics (MD) simulation (Figure 2). The strain field of the core of the triple junction unequivocally shows dislocation character (Figure 2); that is, a tensile and a compressive part occurred in a dipole arrangement opposite to each other. The intersecting boundaries result in a net translation of a Burgers vector corresponding to a lattice dislocation in an fcc metal (result from the MD simulation). The strain tail emerging close to the triple junction in the experimental strain maps of Figure 2 (shear and rotation) is not thought to be characteristic for an isolated configuration ($\Sigma3{:}\Sigma3{:}\Sigma9$) as modeled. However, it might reflect a local feature necessary to sustain a mechanical equilibrium for the specific configuration here. An analysis of the rigid-body rotation along the $\Sigma9$ grain boundary (Figure 1b) yields two rotational defects (disclinations) of opposite sign forming a dipole (Figure 1c). This accounts for a short range strain field since back stresses of the opposite disclination

are balancing it. The presence of such a disclination dipole embodied in a grain boundary is thought to act as a stabilizing element for nanostructured materials hindering grain growth. Further it appears to be an important by-product of materials exhibiting multiple twinning. Based on the observation that the core of the triple junction showed the characteristics of a dislocation strain field, its energy was estimated to be $1.7 \cdot 10^{-9}$ Jm^{-1} using $\frac{1}{2}Gb^2$. [1]

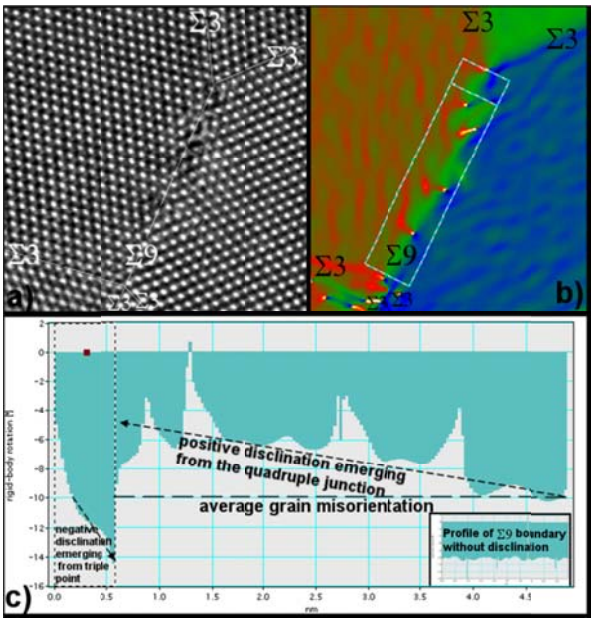

Fig. 1: (a) Aberration corrected HRTEM image in <110> orientation showing the region around the triple junction and the quadruple junction of a deformed ncPd grain. (b) Corresponding rotation map (rigid-body rotation). (c) A rotational strain profile was measured along the Σ9 boundary indicated by the frame in (b). Two gradients of opposite sign occur along the Σ9 boundary forming a disclination dipole. The inset shows the profile of a simulated Σ9 boundary without disclination for comparison.

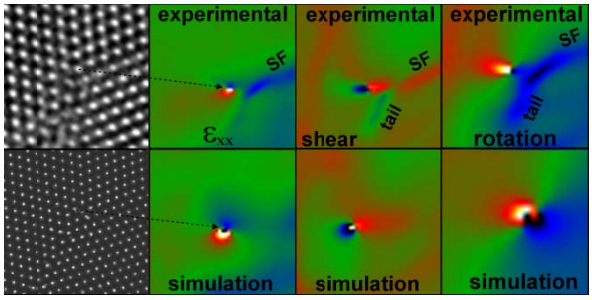

Fig. 2. Comparison of the experimental strain maps (top) with a MD simulation (bottom) for the core of the triple junction. The black dotted lines indicate the position of the terminating extra plane in the triple junction.

3D imaging of defects in crystalline superlattices of CdS clusters by electron tomography

It is well established that well-defined, monodisperse semiconductor clusters can be crystallized to form macroscopic superlattice structures. These semiconductor clusters offer great potential for application in optics, electronics and for biological labeling due to their defined electronic and photophysical properties. Surprisingly, even in case of bimodal size distributions, it is possible to form crystalline superlattices of clusters. These crystals offer the possibility to study crystal defects and packing effects at the nanometer scale in materials. As these crystals are nanometer to micron sized, electron tomography is ideally suited to characterize the packing of the clusters in the crystalline superlattice. As a real space technique, electron tomography offers the unique possibility to directly image the 3D crystal lattice of these cluster crystals in real space, which enables direct imaging of characteristic defects such as vacancies and dislocations in 3D.

In this project, thiopenyl capped CdS clusters with an average core diameter of 2.3 nm corresponding to an idealized composition of $Cd_{130}S_{103}(SPh)_{54}$ were analyzed. The crystalline packing of these clusters can be directly seen in HRTEM and HAADF-STEM images

(Figure 3). Using HAADF-STEM tomography, the 3D structure of these crystals was reconstructed revealing a simple cubic packing of the CdS clusters (Figure 4). A more careful analysis of the crystalline packing shows a high defect density within the crystals with dislocations as well as individual and extended vacancies directly visible in 3D (Figure 5a). Surprisingly, it is even possible to incorporate disordered clusters with significantly larger diameter in extended areas of the crystal without disturbing the overall crystal orientation significantly (Figure 5b). Despite these defects, the individual CdS clusters are highly correlated and exhibit a fixed orientation relationship of the CdS crystal structure and the cluster superlattice with two CdS nanocrystal in the superlattice unit cell. [2]

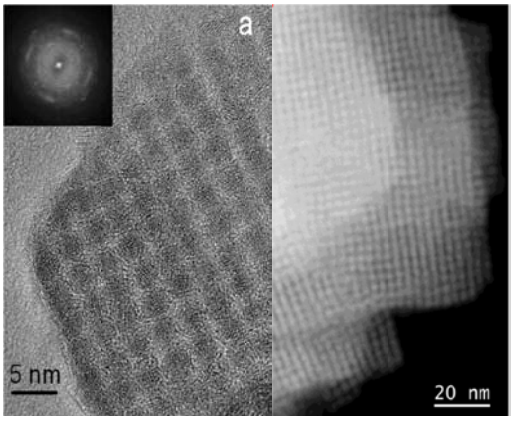

Fig. 3: HRTEM and HAADF-STEM images of the crystalline superlattice packing of the CdS clusters.

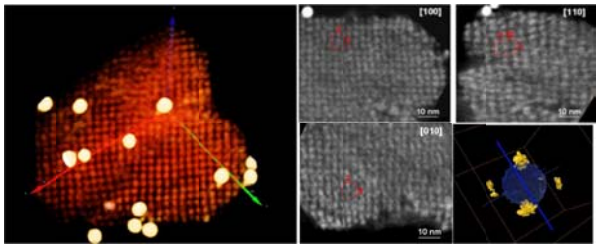

Fig. 4. Volume rendering of the CdS cluster packing and digital slices along the main crystallographic direction of the super-lattice with 3D power spectrum.

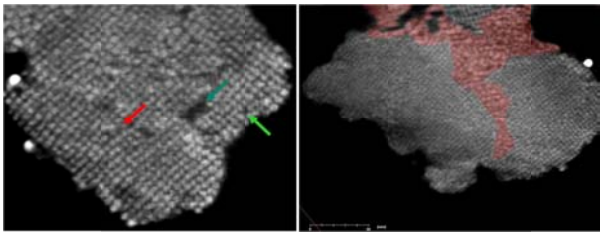

Fig. 5. Digital slices ([100] orientation, 0.4 nm thick) through the 3D reconstruction of the CdS cluster superlattice: a) revealing a dislocation (red) as well as extended and single vacancies (green) and b) showing the incorporation of larger clusters (red) within the cluster superlattice.

Size selected silicon nanocrystals

Monodisperse silicon nanocrystals (ncSi) have been prepared from polydisperse alkyl capped ncSi by density gradient ultra-centrifugation (DGU) and by fractionated crystallization. The monodisperse fractions were characterized by HAADF-STEM (Figure 6) to determine the absolute average silicon core size (in the range of 1.0 - 2.2 nm) with a polydispersity of about 1.05. This enabled the measurement of the optical properties (Figure 7), the absolute quantum yield (Figure 8) and the lifetime of photoluminescence of alkyl-capped silicon nanocrystals as a function of size. The absolute quantum yield and lifetime are found to monotonically decrease with decreasing nanocrystal size, which implies that non-radiative vibrational and surface defect effects overwhelm spatial confinement effects that favor radiative relaxation. Visible emission absolute quantum yields as high as 43% speak well for the development of “green” silicon nanocrystal color-tunable light emitting diodes that can potentially match the performance of their toxic heavy metal chalcogenide counterparts. [3, 4]

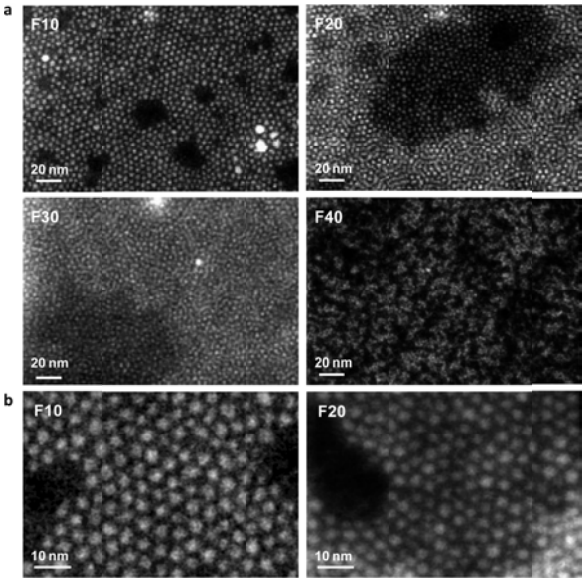

Fig. 6: Size analysis of monodisperse ncSi fractions. (a) HAADF-STEM images of fractions 10, 20, 30, and 40 with an average diameter of 2.2, 1.5, 1.3 and <1.0 nm. (b) Magnified HAADF-STEM images of fractions 10 and 20.

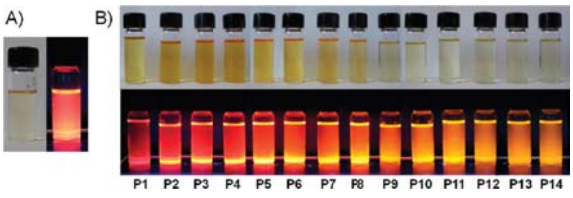

Fig. 7: Allylbenzene-capped silicon nano-crystals (AB-ncSi). (A) Ensemble solution of polydisperse AB-ncSi under ambient light (left) and under photoexcitation at 365 nm (right). (B) Visible emitting AB-ncSi fractions obtained using size-selective precipitation under ambient light (top) and under photoexcitation at 365 nm (bottom).

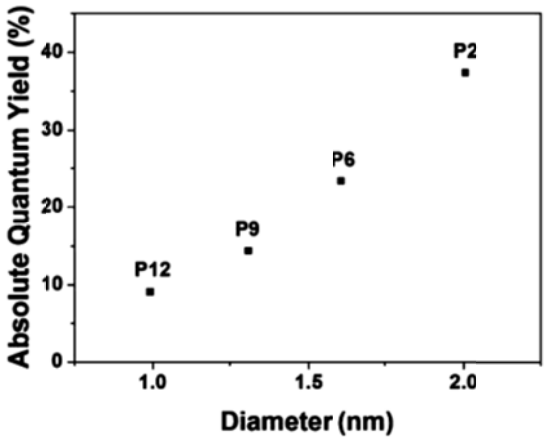

Fig. 8: AQY plotted against mean particle diameter, as determined from HAADF-STEM for fractions P2, P6, P9, and P12

Silicon nanocrystals embedded in mesoporous silica

In the scientifically and technologically important field of periodic mesoporous silicas (PMS), periodic mesoporous hydridosilica (meso-HSiO1.5) has been an “impossible” material for a long time. It is the archetype of a completely interrupted silica open framework material: its pore walls are comprised of a three-connected three-dimensional network that should be so thermodynamically unstable that any mesopores present would immediately collapse upon removal of the mesopore template. In this study it was shown that meso-HSiO1.5 can be synthesized by template-directed self-assembly of HSi(OEt)3 under aqueous acid-catalyzed conditions and after template extraction remains stable to 300 C. Above this temperature, bond redistribution reactions initiate a metamorphic transformation which eventually yields periodic mesoporous nanocrystalline silicon-silica, meso-ncSi/SiO2, a nanocomposite material in which brightly photoluminescent silicon nanocrystallites are embedded within a silica matrix throughout the mesostructure (Figure 9). Another approach to prepare silicon nanocrystals embedded in a mesoporous organosilica (ncSi-PMO) is self-assembly of oligo(triethoxysilylethylene) capped silicon nanocrystals (Figure 10). In both cases, the integration of the properties of silicon nanocrystallinity with silica mesoporosity provides a wealth of new opportunities for emerging nanotechnologies. [5, 6]

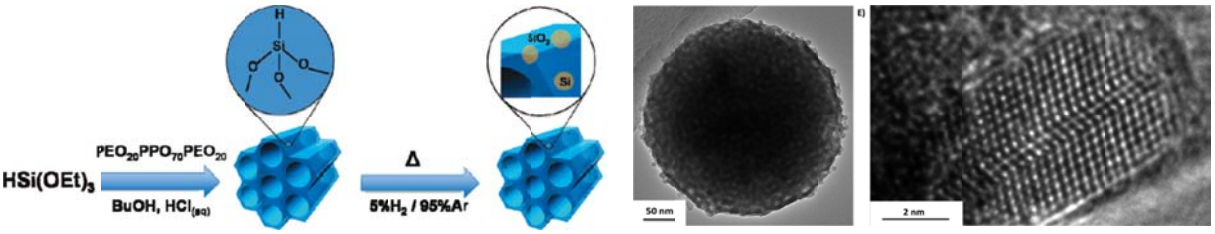

Fig.9: Schematic of the material preparation and BF-TEM image of the mesoporous silica together with a HRTEM image of a silicon nanocrystal at the edge of the mesoporous silica.

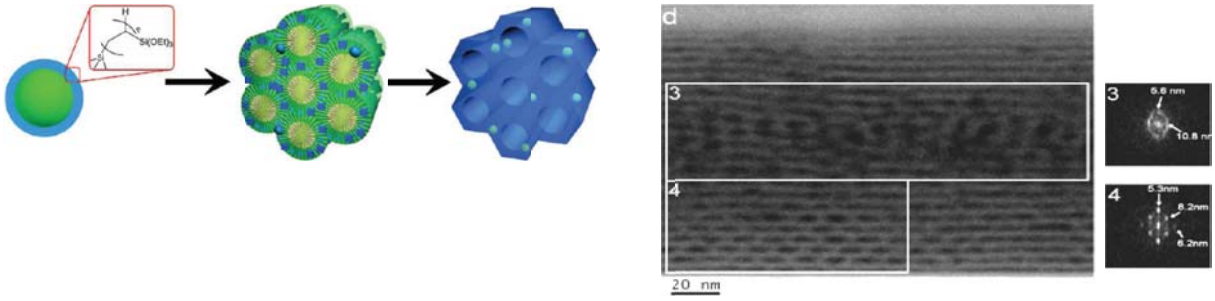

Fig.10: Schematic of the material preparation and HAADF-STEM analysis of FIB-prepared cross sections of a spin-coated ncSi-PMO thin film after template removal; FFT images of the selected regions are shown to the right. A close-packed ordered mesoporous structure is observed close to the substrate−film and the film−air interfaces. Between the ordered layers is a region with a disordered mesoporous structure.

Site-specific chirality in magnetic transitions

Site-specific energy loss magnetic dichroism measurements (Figure 11) of the technologically interesting Heusler alloy Ni_2MnSn have been performed. We confirm the theoretical prediction that under certain conditions, two different atoms on non-equivalent lattice sites give dichroic signals with opposite signs. With this, it is possible to distinguish the magnetic moments of atomic columns that are merely 1.5 Å apart. [7]

Automated crystal orientation mapping for quantitative crystallographic analysis

We have established automated crystal orientation mapping (ACOM) inside the TEM for quantitative crystallographic analysis of nanocrystalline materials with 1 nm spatial resolution. The ACOM-TEM data acquisition is based on the commercial ASTAR package offered by Nanomegas, which we have combined with up-STEM in order to enable fast acquisition of STEM reference images in addition to the orientation maps for in-situ analysis. In addition, we have developed extensive data analysis tools based on Mtex for a reliable quantitative analysis of grain size distribution and grain size anisotropy, twin density and texture. We have used this approach e.g. to analyze the microstructural changes in nanocrystalline palladium (ncPd) strained to different levels (Figure 12/13). One observation is that the twin density evolution depends strongly on the initial twin density, which in turn is sensitive to the sputter conditions of the ncPd films used.

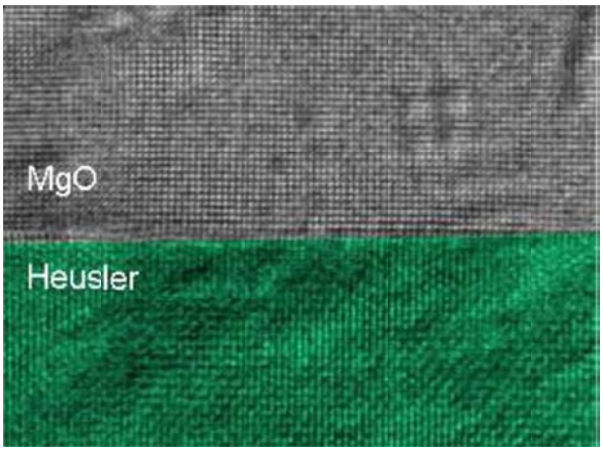

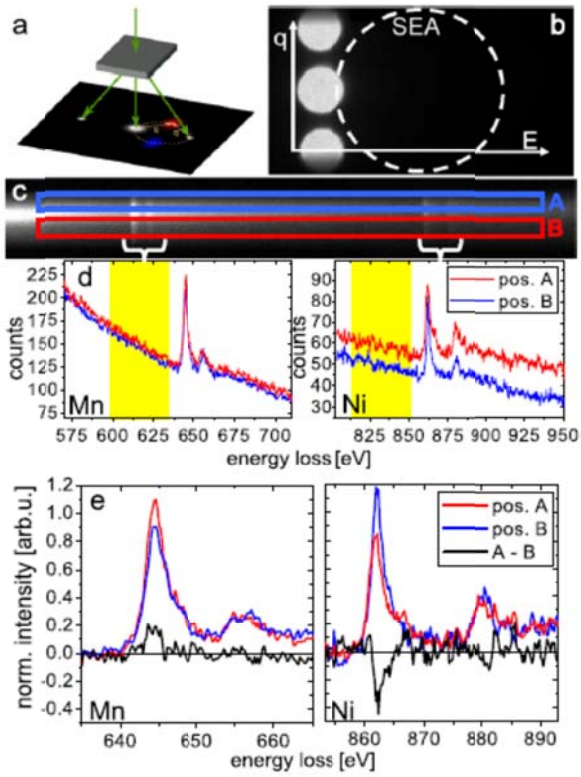

Fig. 11: (top left) Aberration corrected TEM image of the MgO/Ni2MnSn interface (a) sketch of the measurement geometry. (b) Diffraction image of the sample tilted in three beam condition with the axis of the diffraction spots (q) aligned perpendicular to the energy dispersive axis (E) of the spectrometer. The dashed circle indicates the position of the spectrometer entrance aperture during measurement. (c) EEL spectrum measured at a sample thickness of 25 nm. Intensity profiles (d) have been taken from the rectangles A (red) and B (blue) which indicate the regions of different dichroic signs. The yellow bars mark the energy windows used for background subtraction. (e) Resulting EMCD spectra for Mn (left) and Ni (right).

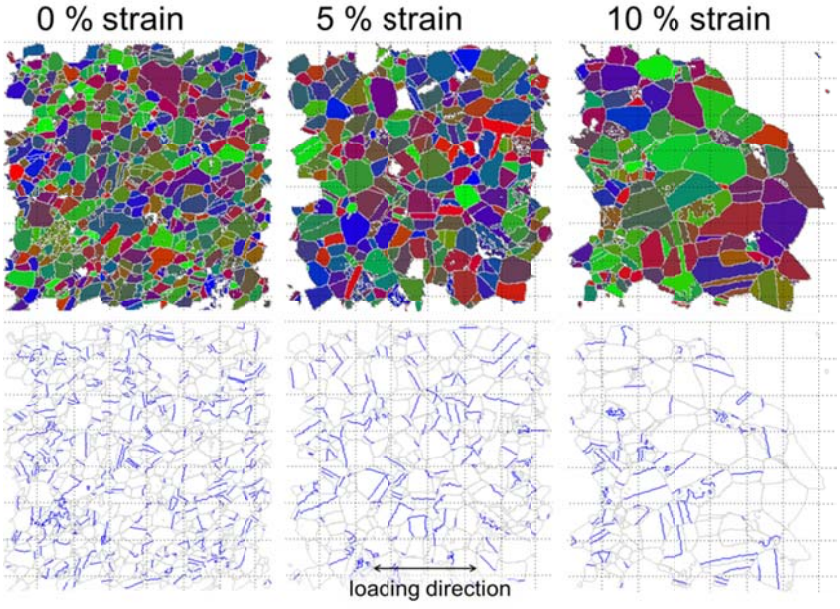

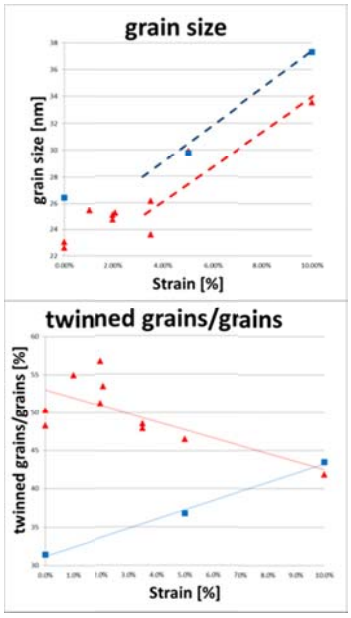

Fig. 12 (left): ACOM-TEM orientation maps and twin boundaries observed in strained.

Fig. 13 (right): Grain size and twin density evolution during straining for two nanocrystalline palladium films grown with different internal stresses (tension-red, compression-blue).

Collaboration in in-house research

Technical University Darmstadt, Helmholtz Institute Ulm, European Institute for Transuranium Elements, University of the Saarland, University Kaiserslautern, Grenoble Institute of Technology, University Leiden, University of Antwerp.

References

[1] H. Rösner, C. Kübel, J. Ivanisenko, L. Kurmanaeva, S. Divinski, M. Peterlechner, G. Wilde, Strain mapping of a triple junction in nanocrystalline Pd Acta Mat., 2011, 59, 7380-7387, DOI: 10.1016/j.actamat.2011.08.020.

[2] T. Levchenko, C. Kübel, Y. Huang, J.F. Corrigan, From molecule to materials: crystalline superlattices of nanoscopic CdS Chem. Eur. J., 2011, 17(51), 14394-14398, DOI: 10.1002/chem.201102487.

[3] M. Mastronardi, F. Hennrich, E. Henderson, F. Maier-Flaig, C. Blum, J. Reichenbach, U. Lemmer, C. Kübel, D. Wang, M. Kappes, G. Ozin, Preparation of Monodisperse Silicon Nanocrystals Using Density Gradient Ultracentrifugation J. Am. Chem. Soc., 2011, 133(31), 11928-11931, DOI: 10.1021/ja204865t.

[4] M. Mastronardi, F. Maier-Flaig, D. Faulkner, E. Henderson, C. Kübel, U. Lemmer, G.A. Ozin, Size-Dependent Absolute Quantum Yields for Size-Separated Colloidally-Stable Silicon Nanocrystals Nano Lett., 2012, 12, 337-342; DOI: 10.1021/nl2036194.

[5] Z. Xie, E.J. Henderson, Ö. Dag, W. Wang, J.E. Lofgreen, C. Kübel, T. Scherer, P.M. Brodersen, Z.-Z. Gu, G.A. Ozin, Periodic Mesoporous Hydridosilica – Synthesis of an “Impossible” Material and its Thermal Transformation into Brightly Photoluminescent Periodic Mesoporous Nanocrystal Silicon-Silica J. Am. Chem. Soc., 2011, 133, 5094-5102, DOI: 10.1021/ja111495x.

[6] M. Guan, W. Wang, E.J. Henderson, Ö. Dag, C. Kübel, I.L. Moudrakovski, J. Thomson, J. McDowell, H. Zhang, G.A. Ozin, Photoluminescent Nanocrystal-Silicon-Embedded Periodic Mesoporous Organosilica J. Am. Chem. Soc., 2012, 134(20), 8439–8446, DOI: 10.1021/ja209532e.

[7] I. Ennen, S. Löer, C. Kübel, D. Wang, A. Auge, A. Hütten, P. Schattschneider, Site-specific chirality in magnetic transitions J. Magn. Mag. Mat., 2012, 324, 2723-2726: DOI: 10.1016/j.jmmm.2012.03.050.

Atomic Force Microscopy

Richard Thelen, Michael Röhrig, Tobias Meier, Hendrik Hölscher

Atomic force microscopy (AFM) was invented more than 25 years ago. Different to several other techniques it allows the analysis of non-conducting sample surfaces without sophisticated sample preparation. Therefore, it is nowadays widely used for the inspection of sample surface down to the atomic-scale [1].

The experimental set-up of an AFM is based on a simple idea. It detects forces acting between a sample surface and a sharp tip that is mounted on a soft leaf spring (the so-called cantilever). A feedback system, which controls the vertical z-position of the tip on the sample surface, keeps the deflection of the cantilever (and thus the force between tip and sample) constant. Moving the tip relative to the sample of the surface by means of piezoelectric drives, the actual z -position of the tip is recorded as a function of the lateral position with very high precision. The obtained data represent a map of equal forces which can be interpreted as the surface topography.

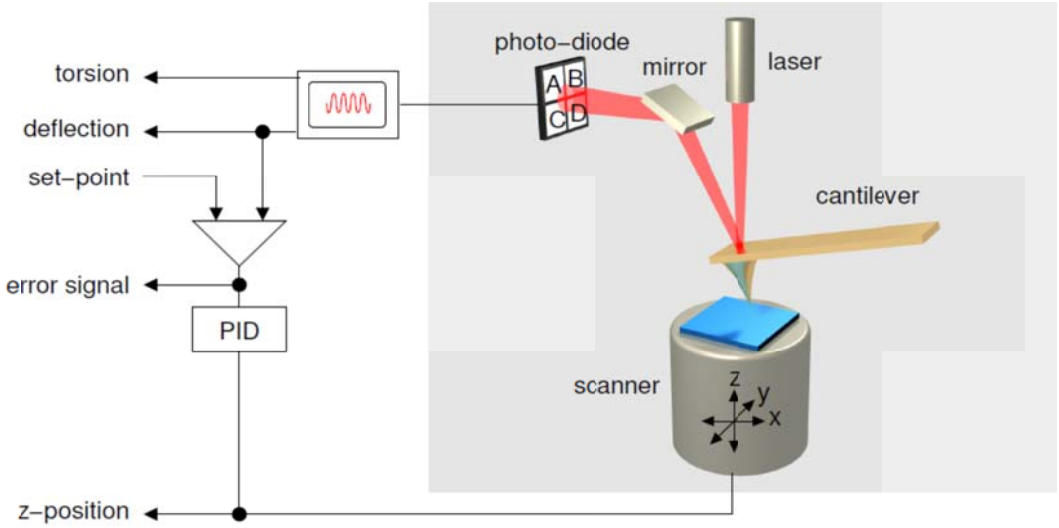

Fig. 1: Principle of an atomic force microscope working with the laser beam deflection method. Deflection (normal force) and torsion (friction) of the cantilever are measured simultaneously by measuring the lateral and vertical deflection of a laser beam while the sample is scanned in the x-y-plane. A schematic of the feedback system is shown by solid lines. The actual deflection signal of the photo diode is compared with the set-point chosen by the experimentalist.

The AFM cluster of the KNMF provides three types of AFMs with different imaging options. Samples can be analysed in ambient conditions as well as in liquids. Typical scan sizes can be as large as 800 µm x 800 µm and as small as 100 nm x 100 nm. The lateral resolution depends on the radius of the tip which is between 10-20 nm. The vertical resolution is typically better than 1 nm.

Figure 2a) displays an example of the resolution obtained in liquids. The topography image shows the DNA adsorbed on a mica substrate in buffer solution. Such a resolution can be routinely obtained. Using cantilevers with magnetic tips it is also possible to image the magnetic properties of a sample surface. Figure 2b) shows the magnetic contrast of a floppy disk using so-called magnetic force microscopy (MFM).

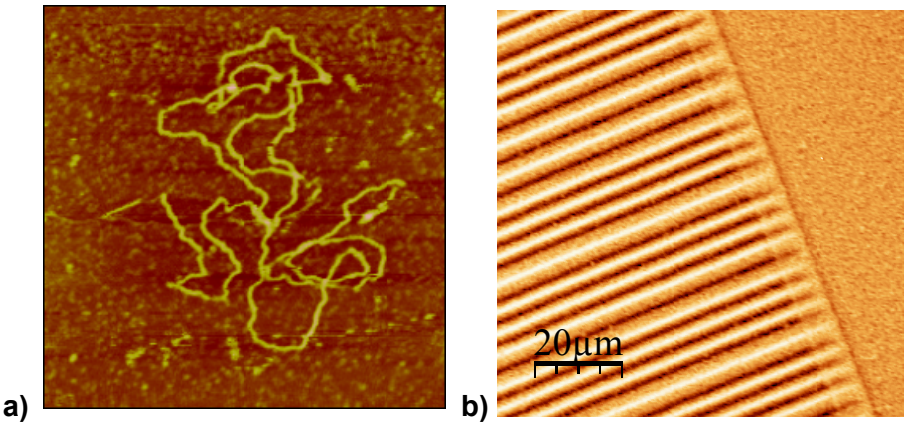

Fig 2: a) Topography of DNA adsorbed on mica imaged in buffer solution by tapping mode AFM. (Scan size 600 nm x 600 nm) b) Magnetic contrast obtained on a conventional 1.44 MB floppy disk.

In addition to the topography it is also possible to measure the contact potential difference (CPD) between the sample and the cantilever using Kelvin probe force microscopy (KPFM). In this way it is possible to simultaneously investigate the topography and CPD of CIGS solar cells with high resolution. As shown in Figure 3, it is easily possible to analyse the CIGS absorber surface with a high resolution by KPFM [2, 3].

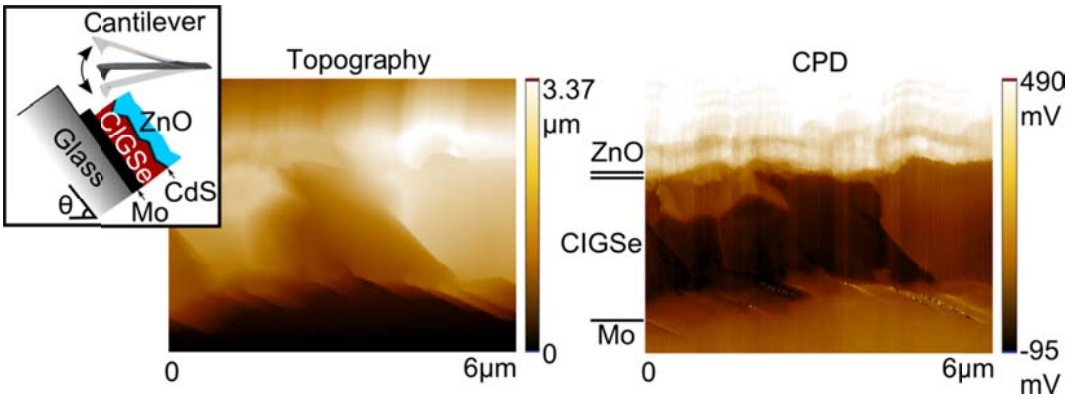

Fig 3: KPFM measurements from an untreated cross section of a CIGSe solar cell. The topography and CPD images are shown on the left and the right respectively. The ZnO, CIGSe, Mo layers of the solar cell can be easily distinguished from top to bottom.

Another field of application for AFM is the analysis of adhesion on nanostructured surfaces. Geckoes for example are well-known for their ability to climb on walls and ceilings due to the unique adhesion properties of their toes covered with nanohairs. Applying 3D direct laser writing, artificial hierarchical gecko-type structures can be designed and fabricated down to nanometer dimensions. In this way, the elastic modulus and the length scale of the gecko's setae can be closely matched. Since the parameters of the structures can be easily changed with 3D laser writing, this technique is perfect for design studies of dry adhesives. Measuring the adhesion forces by atomic force microscopy, the influence of several design parameters like density, aspect ratio, and tip-shape on dry adhesion performance were therefore systematically examined [4]. In this way, it was revealed that hierarchy is favourable for artificial gecko-inspired dry adhesives made of stiff materials on the nanometer scale.

Collaboration in in-house research

Christian-Albrechts-Universität Kiel, University of Tübingen.

References

[1] H. Hölscher, “Atomic Force Microscopy and Spectroscopy”. In: Dynamical Force Spectroscopy and Recognition (ed. by A. R. Bizzari and S. Cannistraro), Taylor & Francis, pp. 51-91 (2012)

[2] Z. Zhang, X. Tang, W. Witte, O. Kiowski, M. Hetterich, U. Lemmer, M. Powalla, and H. Hölscher. “Reevaluation of the beneficial effect of Cu(In,Ga)Se2 grain boundaries using Kelvin probe force microscopy”, Appl. Phys. Lett. 100, 203903 (2012)

[3] Z. Zhang, X. Tang, W. Witte, O. Kiowski, U. Lemmer, M. Powalla, and H. Hölscher. “Kelvin probe force microscopy on untreated cross sections of Cu(In,Ga)Se2 thin film solar cells” Appl. Phys. Lett. 99, 042111 (2011)

[4] M. Röhrig, M. Thiel, M. Worgull, and H. Hölscher. „3D Direct Laser Writing of Nano- and Microstructured Hierarchical Gecko-Mimicking Surfaces”. Small (2012); doi 10.1002/smll.201200308

X-ray Photoelectron Spectroscopy

Michael Bruns, Surface Analysis & PVD Coatings Group

X-ray photoelectron spectroscopy (XPS) is the most widely used surface analysis technique to provide both quantitative atomic concentration and chemical state information of the detected elements. X-ray irradiation of surfaces results in the emission of photoelectrons whose energies are characteristic of its constituting elements. The information depth is approximately 5–7 nm. Angle-resolved XPS offers non-destructive resolution of structures within the XPS sampling depth, e.g. layer ordering, composition and thickness can be determined. Moreover, XPS can be utilized for sputter depth profiling to characterize thin films and multilayer systems by quantifying matrix-level elements as a function of depth.

The in-house research focuses on surface analytical characterization of (polymer) modified surfaces based on a number of cutting-edge projects within the Barner-Kowollik group, of sputtered barium strontium titanate thin films for tunable passive microwave applications in collaboration with the Binder group, and energy storage materials in collaboration with the Pfleging team (cf. Laser Material Processing). In all cases XPS was used as one of the few characterization methods which give precise information of the molecular composition of the modified surfaces.

Photoclickable surfaces for profluorescent covalent polymer coatings

The nitrile imine-mediated tetrazole-ene cycloaddition reaction (NITEC) is a powerful and versatile conjugation tool to covalently ligate macromolecules onto variable (bio)surfaces. When using intrinsically heterogeneous cellulose it is challenging to substantiate the surface modification by grafting of a small molecule as depicted in Scheme 1. The favourable approach is the observation of the evolution of the different C 1s and N 1s XPS species. While no signal was detected in the N 1s spectrum of cellulose (Figure 1a), a low-intensity peak could be observed for **Cel-Tet** at 400.4 eV (Figure 1b), which is indicative of the nitrogen-containing tetrazole being present. The main C 1s contributions of the non-modified cellulose **Cel-OH** are 288.2eV and 286.7 eV for O-C-O and C-O-C/C-OH components, respectively. Although the theoretical structure of cellulose does not comprise carbonyl moieties, an O=C-O component at 289.6 eV can be detected and certainly originate from oxidation that can readily occur on natural fibers such as cellulose. The weak contribution at 285.0 eV (C-C, C-H) is caused by hydrocarbon contamination. However, the cellulose signals are very strong in this region and prevent any accurate detection of a contribution – which would be very low – from the tetrazole handle. However, the clear increase of the C-C/C-H component at 285.0 eV and of the O=C-O peak at 289.2 eV prove the formation of a grafted (meth)acrylic polymer (**Cel-2b-d**, Figure 1c). [1]

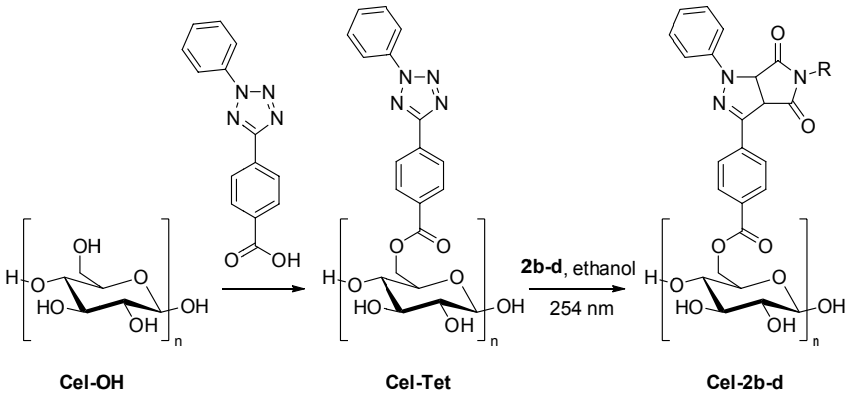

Scheme 1: Strategy for surface modification of cellulose by NITEC through esterification of cellulose with carboxyl-functionalized tetrazole and subsequent photo-grafting of a (meth)acrylic polymer 2b-d.

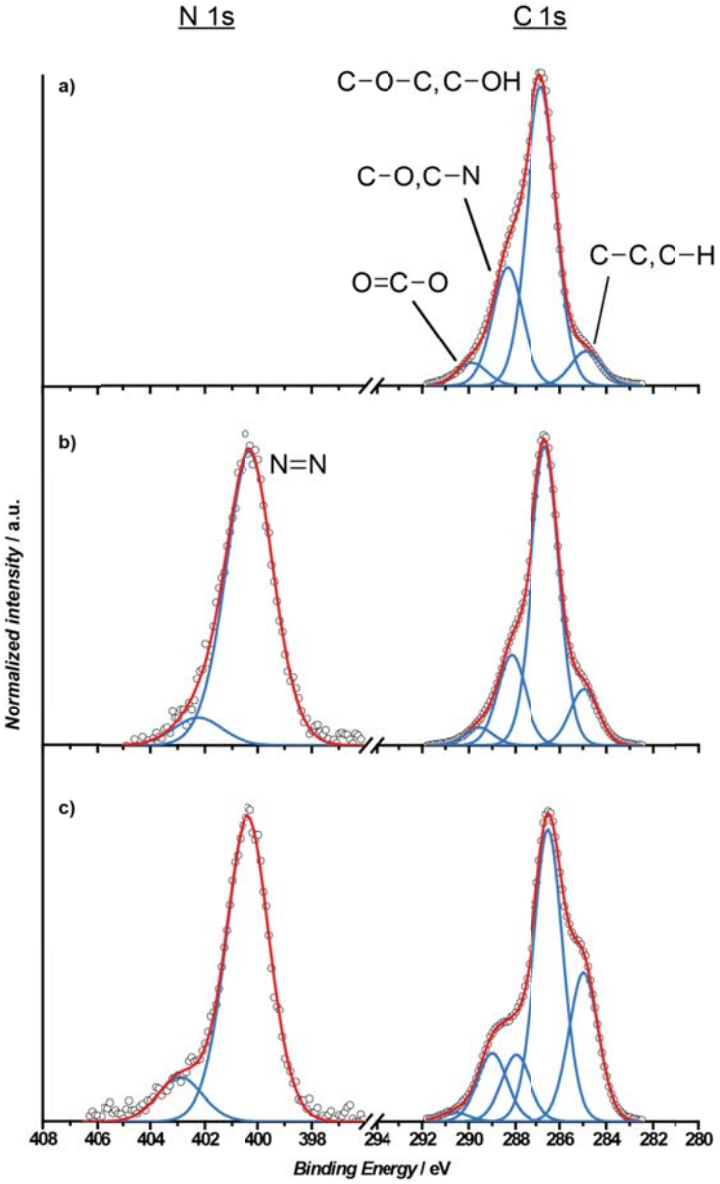

Fig.1: Comparison of the N 1s and C 1s XPS spectra of Cel-OH (a), Cel-Tet(b), and Cel-2b (c). All Spectra are normalized to maximum intensity.

Photo-induced macromolecular functionalization of cellulose via nitroxide spin trapping

This contribution presents a new radical-trapping method for the modification of cellulose by mild UV-induced functionalization of photoinitiator-modified cellulosic substrates with pre-formed nitroxide-functionalized macromolecules. XPS was used as a key method to prove the grafting of hydrophobic TEMPO-functionalized polystyrene onto cellulose without the need for any additive. Again the C 1s multiplett of cellulose evolves with the proportion of the different carbon-based bonds present on its surface following each modification step, cf. Figure 2. The esterification of **Cel-OH** with **5** can be readily detected since the C-C/C-H contribution increases by a factor of close to 6 taking the main cellulose peak (286.7 eV) as a reference. Thus, the cellulose substrate has been efficiently decorated with photoinitiating sites at its surface (**Cel-PI**). The bottom graph in Figure 2 corresponds to the C 1s spectrum of the **Cel-PS** sample after thorough rinsing with fresh DCM and acetone. The observed spectrum is substantially different from the spectra of **Cel-OH.** The main peak is now clearly associated with hydrocarbons (285.0 eV), revealing an efficient coverage of the surface with a carbon-rich material, *i.e.*, polystyrene. Furthermore, a new low-intensity signal appeared close to 291.8 eV and can unambiguously be assigned to a π-π*-transition arising from the presence of an aromatic system. Although **PI** also possesses an aromatic cycle and thus the latter is also present in **Cel-PI**, its concentration is too low to be detected. [2]

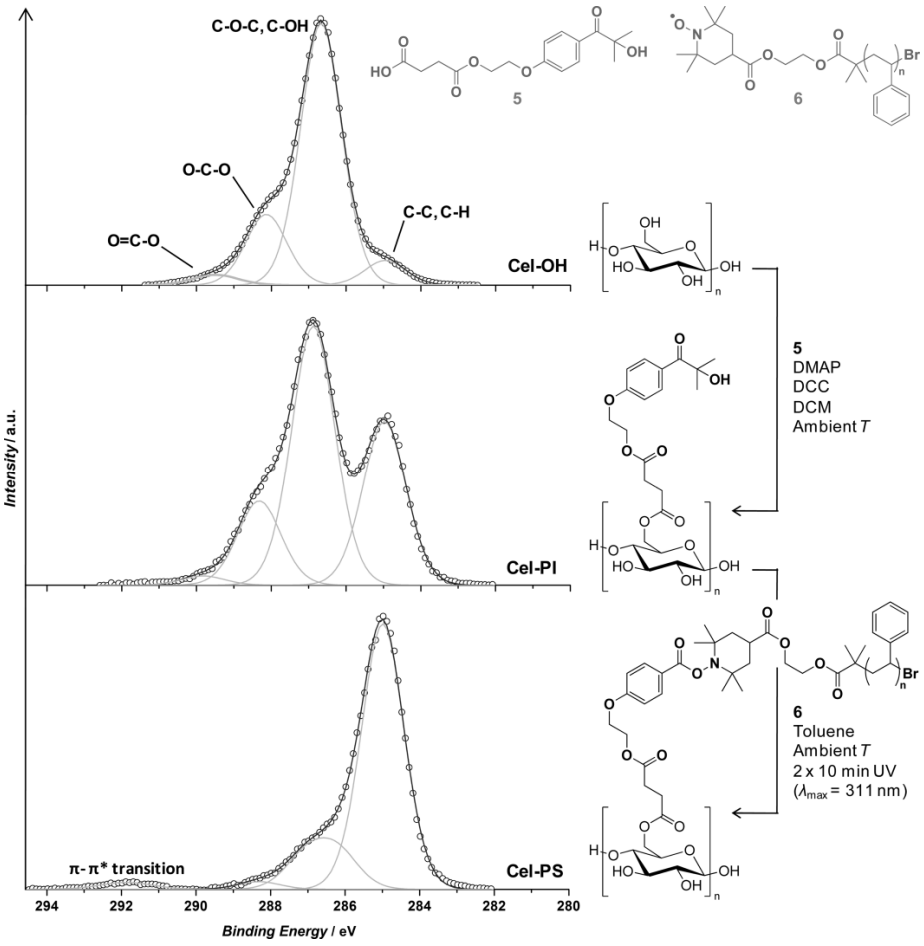

Fig. 2: C 1s XPS spectra of cellulose before modification (top, Cel-OH), after esterification with modified Irgacure 2959 photoinitiator5 (middle, Cel-PI), and after UV-induced nitroxide radical trapping/grafting with TEMPO-functionalized poly-styrene 6 (bottom, Cel-PS). All spectra are normalized to maximum intensity.

Sputtered barium strontium titanatethin films for tunable passive microwave applications

Barium strontium titanate ($Ba_{1-x}Sr_xTiO_3$, BST) is a promising material for tunable passive microwave applications due to the wide range of the dielectric constant dependency on the electric field strength. This characteristic dielectric behaviour allows its use for phase shifters, filters, and matching networks. This contribution focuses on XPS characterization of novel iron-doped $Ba_{0.6}Sr_{0.4}(Ti_{1-x}Fe_x)_{1+x}O_{3-\delta}$ thin films prepared by means of r. f. magnetron co-sputtering.

In particular, XPS proves the achieved elemental composition in a non-destructive manner and, via sputter depth profiles, the homogeneous iron dopant distribution throughout the films. The main components for Ba^{2+} (Ba $4d_{5/2}$ = 87.9 eV), Sr^{2+} (Sr $3d_{5/2}$ = 132.7 eV), Ti^{4+} (Ti $2p_{3/2}$ = 458 eV), and O^{2-} (O 1s = 529.2 eV) are attributed to Me-O bonds in barium strontium titanate and are in a good agreement with literature.

Two Fe $2p_{3/2}$ components at 710.2 eV and 712.3 eV binding energy can be attributed to Fe^{2+} and Fe^{3+}, respectively. Together with electron paramagnetic resonance spectroscopy results these findings prove the desired incorporation of iron in the ABO3 perovskite. [3, 4]

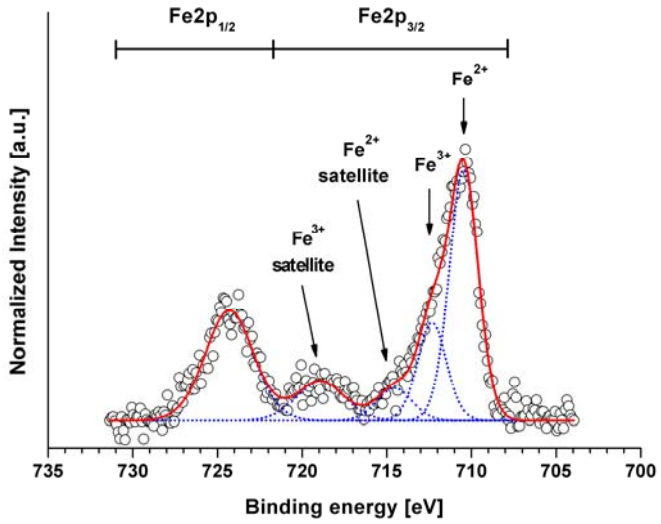

Fig.3: Fe 2p XPS spectrum of a Fe-doped BST thin film.

Collaboration in in-house research

B. Holländer, Peter Grünberg Institute (PGI-9), Forschungszentrum Jülich: Rutherford Backscattering Spectrometry (RBS).

References

[1] M. Dietrich, G. Delaittre, J. P. Blinco, A. J. Inglis, M. Bruns, and C. Barner-Kowollik, Photoclickable Surfaces for Profluorescent Covalent Polymer Coatings, Adv. Funct. Mater. 22 (2012) 304–312.

[2] G. Delaittre, M. Dietrich, J. P. Blinco, A. Hirschbiel, M. Bruns, L. Barner and C. Barner-Kowollik, Photo-Induced Macromolecular Functionalization of Cellulose via Nitroxide Spin Trapping, Biomacromolecules 13 (2012) 1700–1705.

[3] F. Stemme, M. Bruns, H. Geßwein, M. Schroeder, M. Sazegar, M. D. Drahus, R.-A. Eichel, F. Paul, J. Haußelt, and J. R. Binder, Effects of thermal processing and iron doping in co-sputtered barium strontium titanate thin films, Journal of Materials Science, 2012, DOI 10.1007/s10853-012-6640-7.

[4] F. Stemme, H. Geßwein, M. D. Drahus, B. Holländer, C. Azucena, J. R. Binder, R.-A. Eichel, J. Haußelt, and M. Bruns, Characterization of non-stoichiometric co-sputtered Ba0.6Sr0.4(Ti (1-x)Fe(x))(1+x)O(3-δ) thin films for tunable passive microwave applications, Analytical and Bioanalytical Chemistry, 403 (2012) 643-650.

Auger Electron Spectroscopy

Tobias Weingärtner, Christel Adelhelm, Thomas Bergfeldt

An Auger electron spectrometer (Physical Electronics 680 Auger Nanoprobe) is operated in KNMF by the analytical group of the Institute of Applied Materials - Applied Material Physics (IAM-AWP).

Design parameters of our equipment

Auger electron spectroscopy (AES) provides information about the composition and to some extent the chemical state within nanometer sized, solid and vacuum stable, non-insulating materials, of rough, multilayer and fracture surfaces. In combination with Ar ion sputtering and Zalar rotation depth profiles to 1000 nm are available.

Semi-quantitative analysis of Li to U is possible by including sensitivity factors and quantitative analysis standards in the calculation. The practical detection limit ranges from 0.5 to 5 at%. The element distribution is shown by point and area analysis, linescans, depth profiles and element mappings. The practical lateral resolution begins at 24 nm and the depth resolution varies between 0.5 to 5 nm depending on the energy of the Auger electrons. The spot of the low energy ion gun has a size of about 0.5 mm. In situ fracture of samples with liquid N2 cooling can be used for grain boundary analysis.

History of AES at KIT

Long before KNMF was founded, AES was involved in co-operations with internal (KIT) and external scientific as well as with industrial partners. From 2009 to mid 2011 external commercial customers order AES investigations in direct contact to IAM-AWP and since the 7th call (2011) via KNMF. “User access to the KNMF installation Auger electron spectroscopy“ means that we give advice about the best strategy of analytical investigation, and that we perform, summarize and evaluate the AES analysis and the results. Since the 4th call in 2010 the number of accepted standard proposals rises gradually but has not yet reached the number of commercial proposals.

Measurement possibilities overview

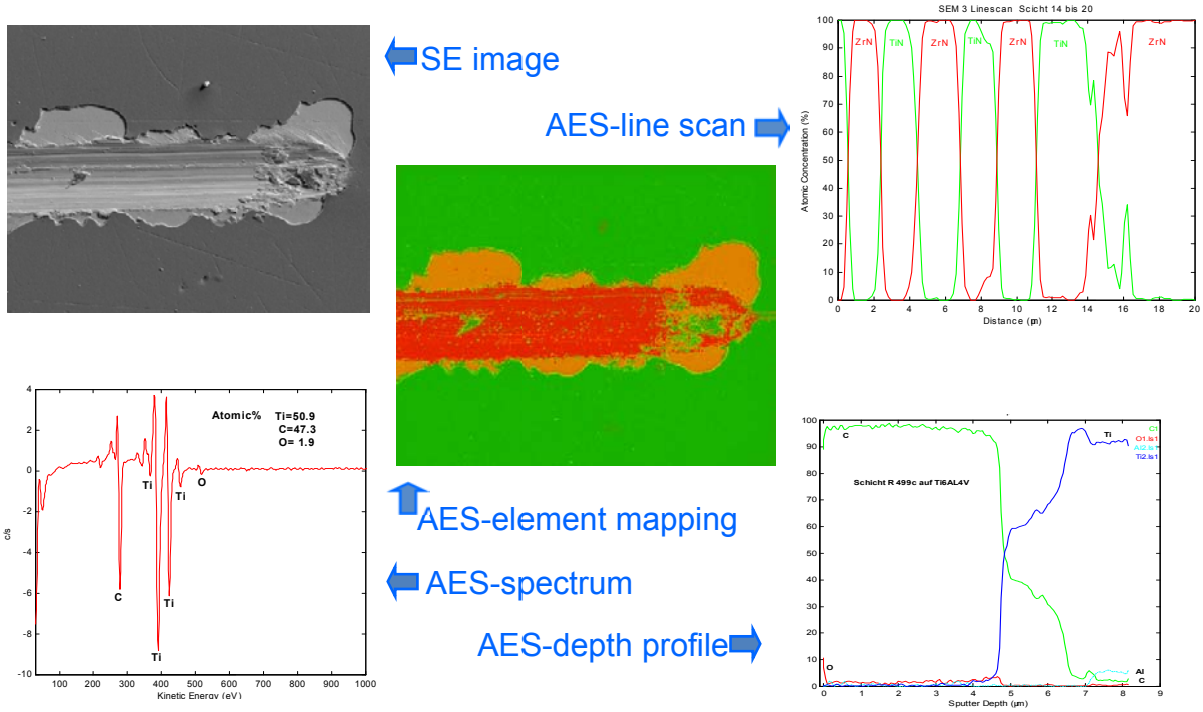

The following examples point out the capability of the AES investigations.

Depth profile

At the department of “thin film technology” of IAM-AWP FeCoHf/TiN/NiO (20/2/20 nm) multilayers for high frequency sensor applications are developed. Auger electron spectroscopy is the most suitable analytical tool to determine the elemental composition of the nano layers and the interfaces. Figure 1 shows the depth profile of the first triple-layer and Figure 2 gives an overview of the whole multilayer.

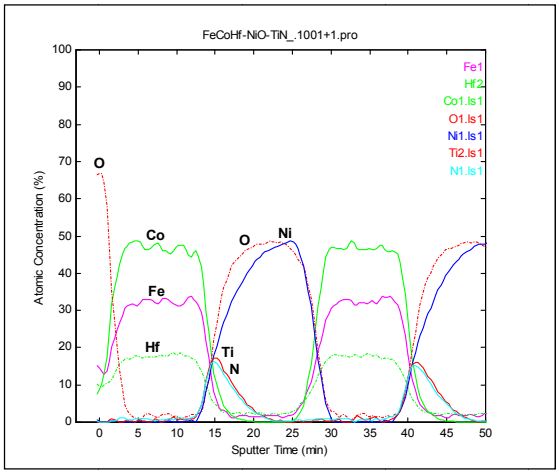

Fig. 1: FeCoHf/TiN/NiO element profile, first triple layer

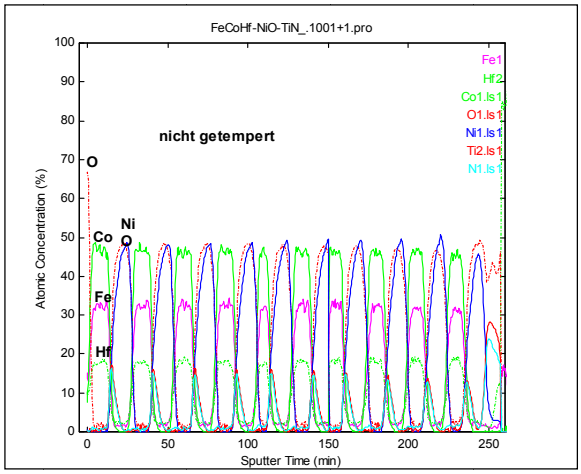

Fig. 2: sequence of 30 layers

The 20 nm thick FeCoHf- and NiO-layers are detectable as separate layers, while the 2 nm thick TiN-layer is in the range of the depth resolution of the instrument.

One of the first KNMF tasks for us was the investigation of phase boundary from nanoparticles on alloy surfaces (a nano medicine and nano energy application). Ti nanoparticles, deposited by laser application, could be identified by AES. On the surface of the nanoparticle at least titanium oxide could not only be detected by the accompanying Oxygen but also by the chemical shift of the Titanium Auger peak.

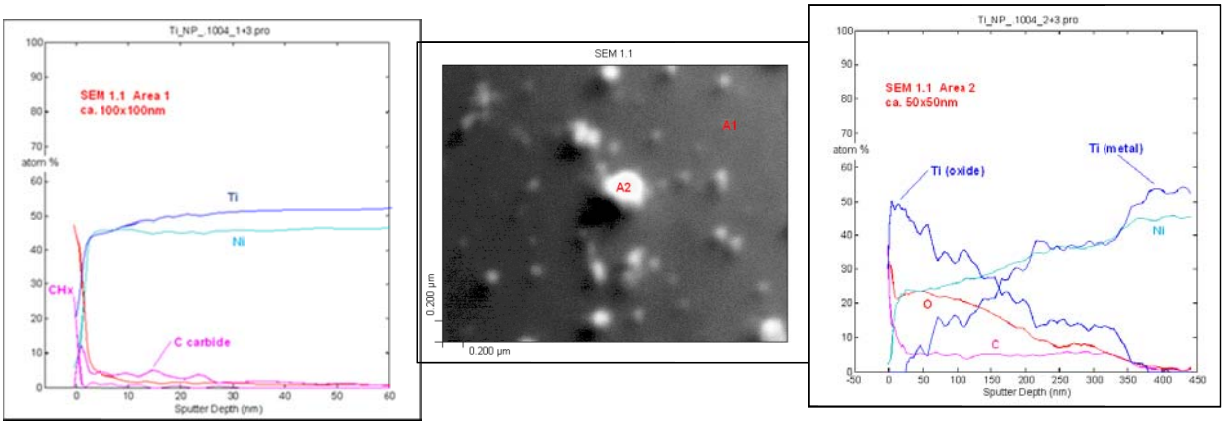

Fig. 3: Ti nanoparticle on NiTi stent material

Element mapping

At the “mechanical characterization” laboratory the mechanical behaviour of various materials is tested. The following sample is a heat and mechanically treated steel material. During the treatment some corrosion effects are observed. In Figure 4 you can see a FIB crater through a corroded area on the steel, which was analyzed by AES element mapping (Figure 5).

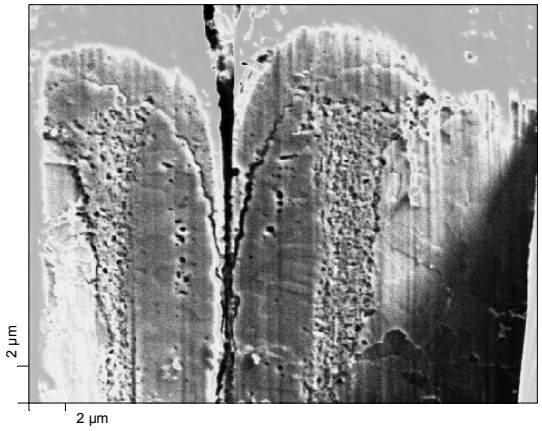

Fig. 4: SEM of a corroded area on steel

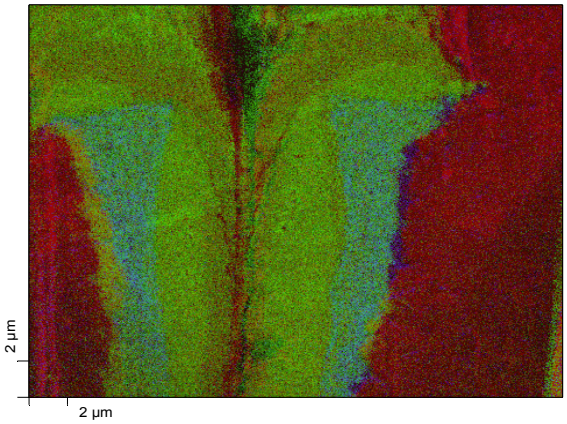

Fig. 5: RGB element mapping overlay red = Fe, green = O, blue = Cr

Element mapping on a in-situ-fractured MoSiB pattern

From the Materials Sciences Division of the Lawrence Berkeley National Laboratory in USA we received some MoSiB patterns. The fracturing of these samples was performed in our AES chamber under ultra-high vacuum. After the cut one sees the fresh grain boundaries or the trans-crystalline fracture area which had not previously been exposed to the atmosphere.

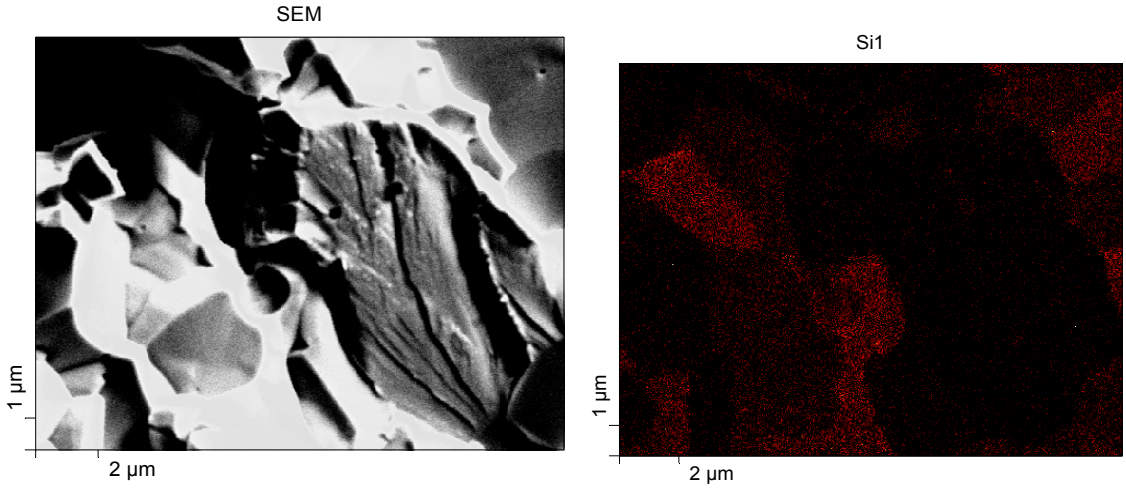

Fig. 6: SEM (left) and Si-elemental map (right) of a fresh fractured area of a MoSiB pattern.

References

[1] Klever, C.; Stüber, M.; Leiste, H.; Nold, E.; Seemann, K.; Ulrich, S.; Brunken, H.; Ludwig, A.; Thede, C.; Quandt, E. Multifunctional FeCo/TiN multilayer thin films with combined magnetic and protective properties, Advanced Engineering Materials, 11(2009) S.969-75

[2] Zdravkov, V.I., Kehrle, J., Obermeier, G.; Gsell, S.; Schreck, M.; Müller, C., Krug von Nidda, H.A., Lindner, J., Moosburger-Will, J.; Nold, E.; Morari, R., Ryazanov, V.V.; Sidorenko, A.S.; Horn, S.; Tidecks, R.; Tagirov, L.R., Reentrant superconductivity in superconductor/ferromagnetic-alloy bilayers, Physical Review B, 82(2010) S.054517/1-13

[3] Lemberg, J.A.; Middlemas, M.R.; Weingärtner, T.; Gludovatz, B.; Cochran, J.K.; Ritchie, R.O., On the fracture toughness of fine-grained Mo-3Si-1B (wt.%) alloys at ambient to elevated (13000C) temperatures, Intermetallics, 20(2012) S.141-154

Bulk and Trace Analysis

Christel Adelhelm, Thomas Bergfeldt

Bulk and Trace Analysis (BTA) of nano materials is a technology cluster at the analytical group of the Institute of Applied Materials - Applied Material Physics (IAM-AWP) and consists of different analytical methods:

X-Ray Fluorescence Spectrometry, XRF (S4 Pioneer, Bruker AXS) is a non-destructive method for quick qualitative and semi-quantitative analysis. In combination with reference materials it is also a precise quantitative element determination. In samples like powders, solids, paste, films, liquids with sizes of 10 to 50000 µm elements like (B) F to U can be analyzed in the concentration range from ppm to 100 % depending on the atomic mass.

Atomic or Optical Emission Spectrometry by Inductively Coupled Plasma, ICP-AES or ICP-OES (OPTIMA 4300 DV, PerkinElmer) is widely used in inorganic analysis of aqueous solutions and metals, oxides, nitrides, carbides etc. dissolved by acids. The echelle grating optical system combined with prisms and two detectors enables simultaneous measurement of all elements except noble gas, halogens, hydrogen, oxygen and nitrogen. The element concentrations range from below 1 µg/g (depending on sensitivity) to 50 % in solids and < 0.001 to 100 mg/L in liquids. Reference or matrix matched standard solutions enable precise element determinations.

Mass Spectrometry by Inductively Coupled Plasma, ICP-MS (7500ce, Agilent) is the preferred analytical method for isotope and Ultra trace analysis. The quadrupole mass spectrometer equipped with off-axis Omega lenses and an octopole Reaction System (ORS) to eliminate polyatomic interferences covers the mass range from 6 to 260, i.e. Li to U. Depending on sensitivity the element concentrations vary from 1 ng/g to 1000 µg/g in dissolved solids or < 0.001 to 1000 µg/L in aqueous solutions.

Carrier Gas Heat Extraction, CGHE (TC 600, LECO) is one of the only reference methods to determine Oxygen and Nitrogen. Solid samples are heated in a graphite crucible in a metal bath at 2600°C with He as carrier gas. Released CO and CO2 are detected by IR and N2 by thermal conductivity. The concentrations range from < 0.1 µg/g to 50 %.

In a Carbon-Sulfur-Analyzer (CS 600, LECO) solid samples are combusted in a high frequency furnace under oxygen flow and the formed CO2 and SO2 are detected by IR-cells. Typical samples are inorganic and organic samples and the C and S concentrations range from 5 µg/g to 100%.

Bulk and Trace Analysis, BTA, is not only part of KNMF but is also part of the HGF programs NUKLEAR, FUSION, NANOMIKRO, EE, and REUN. Before 2009 IAM-AWP was contacted directly for external scientific as well as industrial co-operations and by external commercial customers. Since the 7th call (2011) orders for BTA came via KNMF. “User accesses to the KNMF installation BTA“ means, that the specialists at the IAM-WPT laboratory give advice about the best strategy of analytical investigations and (not the user) perform the BTA analysis, summarize and evaluate the results.

From 2009 to 2011 different analyses on a multitude of various samples have been performed for external customers including: noble metals in catalysts by ICP-OES, analysis of catalysts by XRF and ICP-OES, trace analysis in tungsten wire with ICP-OES, main compounds and impurities in Li4SiO4 and the main compounds and impurities in VEK glass. Names of most commercial partners cannot be communicated, as confidentiality about partner and analytical results was agreed on.

As Bulk and Trace Analysis of research material is no routine analysis the analytical group of IAM-AWP participates in or organizes round robin tests.

Collaboration in in-house research

The following table gives an overview of the main Bulk and Trace Analysis of the reporting period (2009-2011) related to the HGF programmes and institutes of the KIT.

NANOMIKRO	**Institutes**
Precise determination of Li, metals (Co, Fe, Ni, Al, Ti, Si, Ti, V) and oxygen in and trace analysis of powder or thin layers of cathode materials for Li-ion batteries by ICP-OES, CGHE,CS, XRF [2].	IAM-AWP, IAM-WPT, INT
Chemical analysis of new anode materials (oxides of Ti-Sn, Al-Sn, Cr-Ti, Ni-Ti) for Li-ion batteries by ICP-OES, CGHE, XRF [1].	INT
Determination of oxygen in Pt Nano powder and Pt determination in cells after treatment with Pt Nano powder by CGHE resp. ICP-OES	IFG
Chemical analysis of Au lenses or Au microstructures by XRF or ICP-OES produced by LIGA technique	IMT
Nonmetal analysis of Ni, NiW and NiAl as LIGA material by CGHE and CS	IAM-WBM, IMT
Ultra trace analysis of SiO_2 Nano Powder by ICP-OES and ICP-MS	ITC-TAB, QNano (EU-funded infrastructure for nanomaterial safety testing)
FUSION	
Determination of main compounds, metal and nonmetal impurities in ceramic breeding blanket Li_4SiO_4 [3] or Li_4SiO_4 – Li_2TiO_3	IAM-WPT,
Round robin of the determination Al, As, Co, Cu, Mo, Nb, Ni, Sb, Sn, Ti, Zr in EUROFER 97-3 (reference steel in fusion reactor) by ICP-OES	IAM-AWP, BAM, H.C. Starck, Saarstahl, Thyssen-Krupp, Voestalpine
Chemical analysis by ICP-OES, CS, CGHE supports the development of Y_2O_3 doped ODS alloys.	IAM-AWP
Impurities in Pb17Li are determined periodically in the liquid metal corrosion loop PICOLLO by ICP-OES	IAM-WPT
6Li and 7Li isotopes are precisely determined in Pb17Li (metal breeding blanket) by ICP-MS for neutron calculations and Tritium release.	INR, TU Dresden
NUKLEAR	
Impurities are controlled in the liquid metal PbBi corrosion loop CORRIDA and Al solubility of Al_2O_3 in liquid Pb is determined by ICP-OES	IAM-WPT
Element analysis of reaction products from the core melt MOCKA by XRF	IKET
REUN and EE	
With optimized method parameters CGHE was enabled to determine oxygen and nitrogen in dried biomasses for the investigation of hydrothermal gasification of wet biomass	IKFT
Slags and fly ash was characterized by ICP-OES, XRF, and CS-Analyzer for the investigations on ecologically efficient thermal processes in waste-to-energy plants.	ITC-TAB
A sensitive determination of Ba in brine with ICP-OES was developed to investigate the kinetic of barium sulfate precipitation. [4] These analysis support the investigation of efficient use of geothermal energy	IKET

Table 1: BTA for in-house research of the KIT

References

[1] Issac, I.; Scheuermann, M.; Becker, S.M.; Bardaji, E.G.; Adelhelm, C.; Wang, D.; Kübel, C.; Indris, S.: Nanocrystalline Ti2/3Sn1/3O2 as anode material for Li-ion batteries. Journal of Power Sources, 196(2011) S.9689-9695

[2] Ketterer, B.; Vasilchina, H.; Seemann, K.; Ulrich, S.; Besser, H.; Pfleging, W.; Kaiser, T.; Adelhelm, C.: Development of high power density cathode materials for Li-ion batteries. International Journal of Materials Research, 99(2008) S.1171-76

[3] Knitter, R.; Fischer, U.; Herber, S.; Adelhelm, C.: Reduction of impurities and activation of lithium orthosilicate breeder materials. Journal of Nuclear Materials, 386-388(2009) S.1071-73

[4] Canic, T.; Bauer, S.; Kuhn, D.; Adelhelm, C.; Seibt, A.; Möllmann, G.U.: Untersuchung der Kinetik von Barytausfällungen aus Geothermalwasser unter dem Einfluss von Scherung und verschiedenen typischen Wärmetauscher-Geometrien. Forschungsjahrbuch Erneuerbare Energien 2010

Thin Film Characterisation Methods

Harald Leiste

For thin film characterisation different instruments are operated within KNMF by the Institute for Applied Materials (IAM-AWP). The composition, structure, properties and behaviour of thin films can be measured. The priority of characterisations is on the microstructure (by XRD and Raman spectroscopy), the mechanical and the magnetic property.

The in-house research focuses on the process improvement and optimization of the XRD characterisation, i.e. to establish the reciprocal space mapping which is a method for the characterisation of epitaxial thin films. The following R&D activities have been performed in 2011.

Reciprocal space map – a method for epitaxial thin films

A new method for thin film characterisation by the use of a 4 circle diffractometer (Figure1) was established. The set-up (Seifert 3003 HR) is equipped with a Cu X-ray tube, followed by a (220) Ge-bicrystal monochromator. The sample is mounted on a goniometer stage in order to adjust it in Omega, Chi, Phi, x, y and z axis. Prior to the measurement, the instrument has to be adjusted according the sample geometry and orientation by a complex adjustment of the circles.

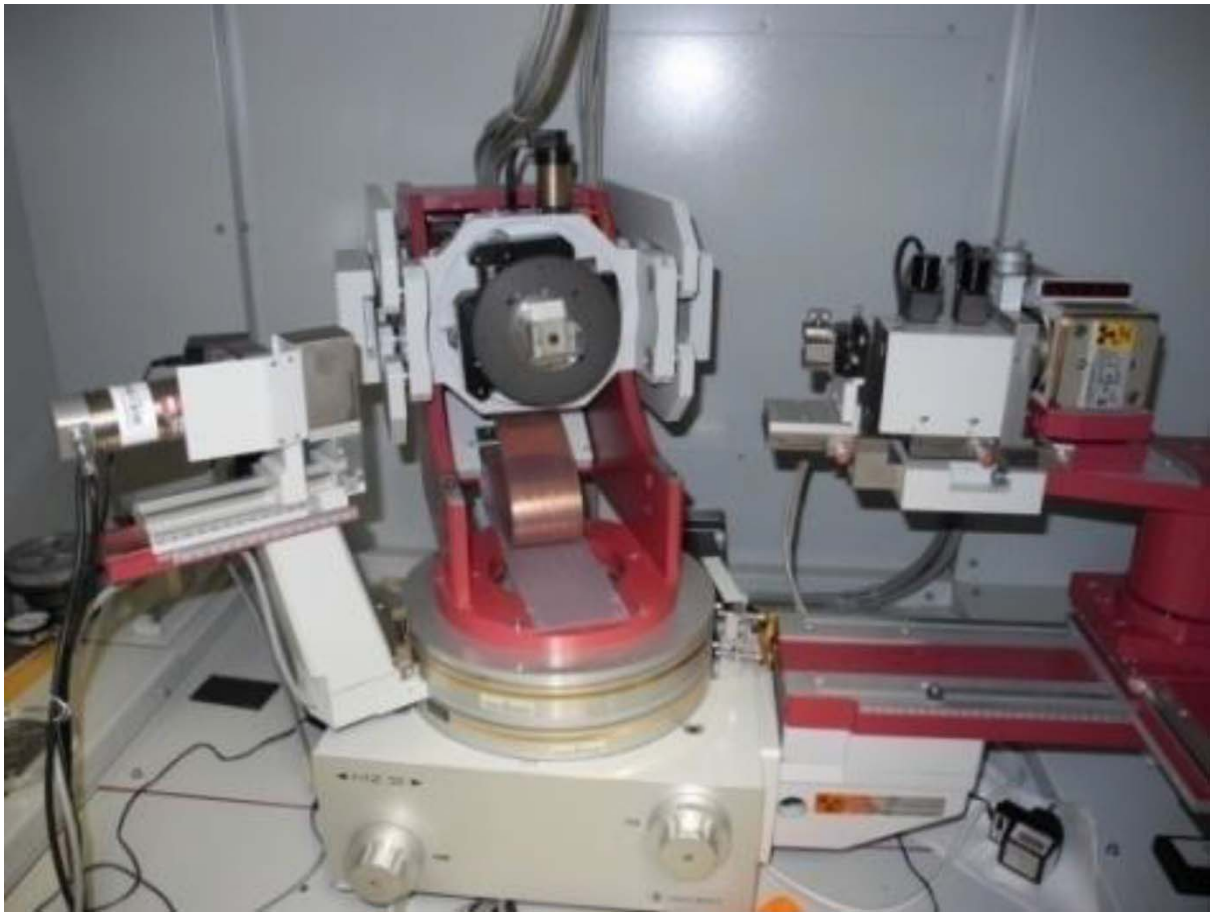

Fig. 1: 4-circle diffractometer right: Cu-x-Ray-tube and monochromator; center: sample holder; left: scintillation counter

Microstructure of the films

By the reciprocal space mapping (RSM) the intensity of a diffraction line of the substrate and film can be analysed by scanning the reciprocal q-space. This method allows to determine the reciprocal lattice constant of a film in the direction parallel (q||) and perpendicular (q⊥) to the surface as well as to deduce the lattice constant in both directions. It can be decided if the lattice of a film is pseudomorph strained or the film has grown fully relaxed.

The method was used to characterise a TiN film deposited at 530°C on (001) oriented MgO-substrates with the cubic lattice constant of 0.4240 nm (TiN) and 0.4213nm (MgO), respectively. Figure 2 shows a reciprocal space map of the symmetric (002) lines with the upper more intense line of the MgO substrate and the lower and broader line of the TiN thin film.

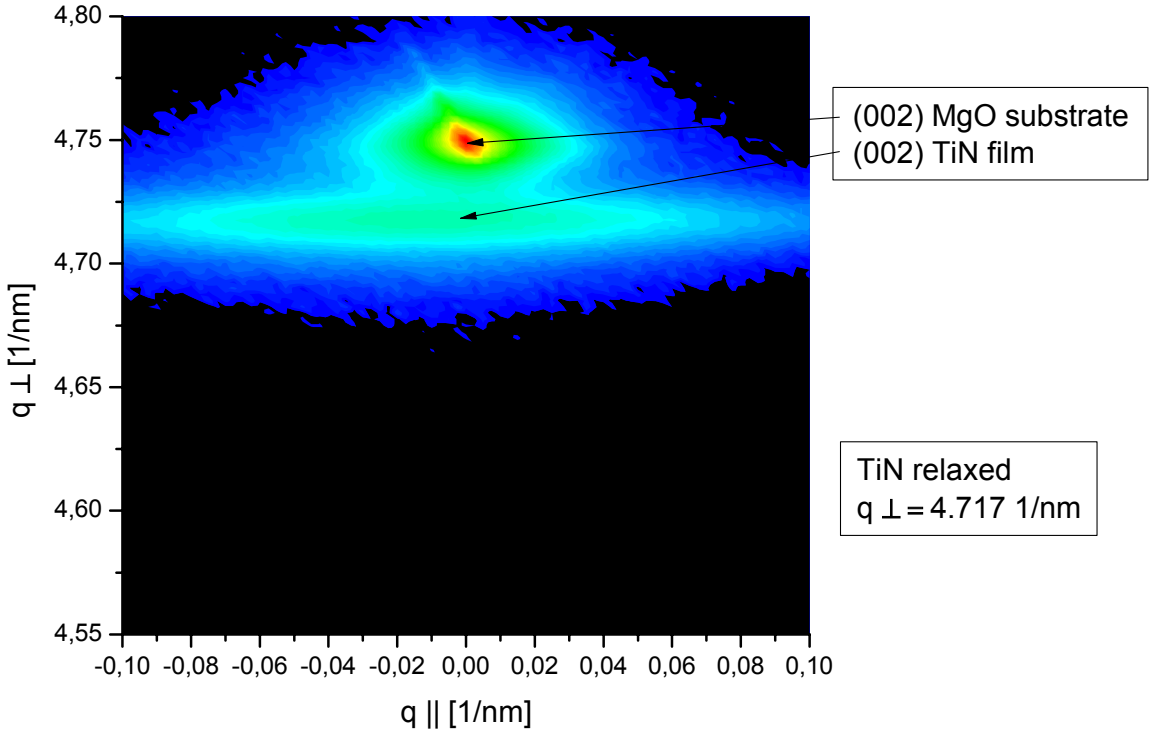

Fig. 2: RSM of the (002) positions of a TiN-film deposited at 530°C on MgO-single crystal substrate

In Figure 3 the asymmetric (113)-line of a TiN film and a MgO substrate are presented. The q-values of TiN film are measured to 7.0625 1/nm for q⊥ and 3.356 1/nm for q|| which gives a lattice constant of a⊥=0.4248 nm and 0.4213 nm for a|| away from the relaxed position. The TiN lattice is tetragonal distorted by the epitaxial growth, and it can be concluded that the film has grown pseudomorph.

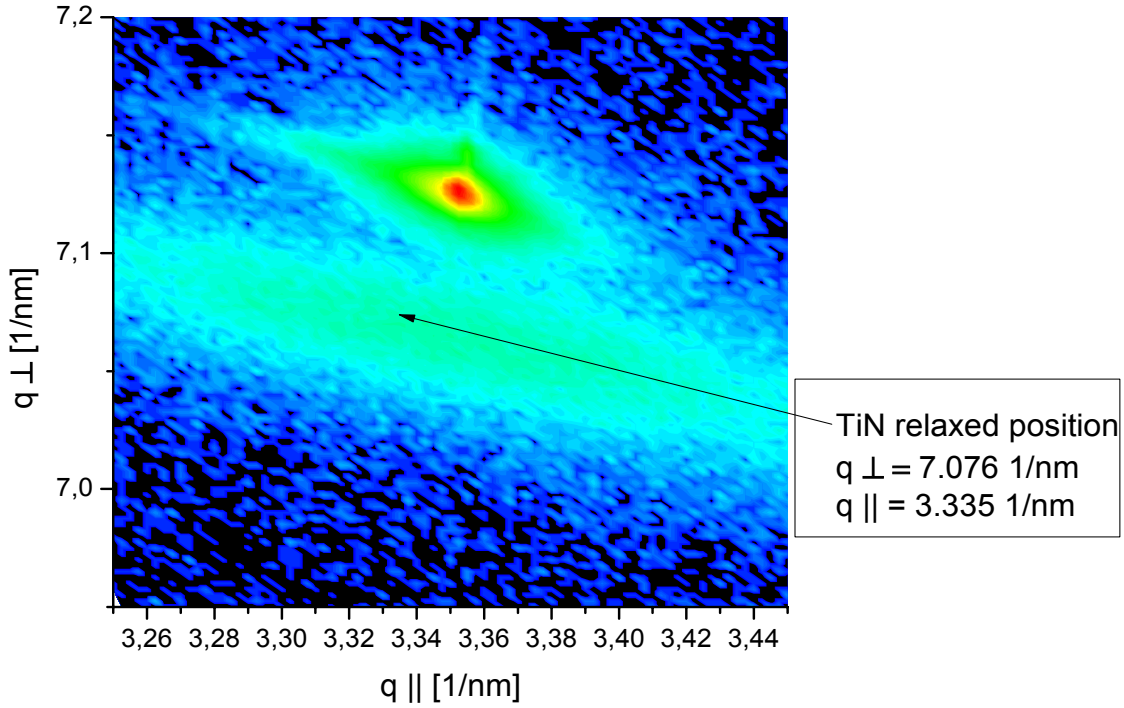

Fig. 3: RSM of the (113) position of a TiN-film deposited at 530°C on a (001)-oriented MgO single crystal substrate

The reciprocal space mapping method was established and verified on the TiN/MgO-system and can be offered to user of the KNMF.

For TiN thin films deposited on MgO substrates at a temperature of 530°C, it can be concluded that epitaxial growth is possible by magnetron sputtering. The characterisation of epitaxial films concerning their orientation dependent lattice constant is possible. It has been shown, that the film grows in a pseudomorph microstructure.

Collaboration in in-house research

Universities of: Kassel, Kaiserslautern, Aachen, Leoben (Austria), Uppsala (Sweden), Linköping (Sweden), Coimbra (Portugal), Leeds (UK)

Firms: Daimler, TKS, TZO, Walter, Gühring, Balzers, Rockwell Collins
Research Centres: FHG-IWM Freiburg, KIST (Korea), Asociacion de la Industria Navarra Cordovilla – Pamplona, Spain

Publication List

The following list gives details of publications in highly rated journals which have resulted from KNMF user projects. These should each acknowledge the use of KNMF facilities.

(published before the end of 2011, reported to KNMF by 30th September 2012)

Authors	Title	Published in	Year
Hsien-Yeh Chen, Michael Hirtz, Xiaopei Deng, Thomas Laue, Harald Fuchs, and Joerg Lahann	Substrate-Independent Dip-Pen Nanolithography Based on Reactive Coatings	J. Am. Chem. Soc.	2010
S. Engin, V. Trouillet, C. M. Franz, A. Welle, M. Bruns, and D. Wedlich	Benzylguanine Thiol Self-Assembled Monolayers for Immobilization of SNAP-tag Proteins on Microcontact printed Surface Structures	Langmuir	2010
D.M. Klymyshyn, M. Börner, D.T. Haluzan, E.G. Santosa, M. Schaffer, S. Achenbach, J. Mohr	Vertical High-Q RF-MEMS Devices for Reactive Lumped Element Circuits	IEEE Transactions on Microwave Theory and Techniques	2010
A. Rashidian, D. M. Klymyshyn, M. Tayfeh Aligodarz, M. Boerner, and J. Mohr	SU-8 Resonator Antenna	Antennas and Propagation Society International Symposium (APSURSI), 2010 IEEE	2010
A. Rashidian, D. M. Klymyshyn, M. Tayfeh Aligodarz, M. Boerner, J. Mohr	Development of Polymer-Based Dielectric Resonator Antennas for Millimeter-wave Applications	Progress In Electromagnetics Research C	2010
M. Mastronardi, F. Hennrich, E. Henderson, F. Maier-Flaig, C. Blum, J. Reichenbach, U. Lemmer, C. Kübel, D. Wang, M. Kappes, G. Ozin	Preparation of Monodisperse Silicon Nanocrystals Using Density Gradient Ultracentrifugation	J. Am. Chem. Soc.	2011
Z. Xie, E.J. Henderson, Ö. Dag, W. Wang, J.E. Lofgreen, C. Kübel, T. Scherer, P.M. Brodersen, Z.-Z. Gu, G.A. Ozin	Periodic Mesoporous Hydridosilica − Synthesis of an “Impossible” Material and Its Thermal Transformation into Brightly Photoluminescent Periodic Mesoporous Nanocrystal Silicon-Silica Composite	J. Am. Chem. Soc.	2011
T. Levchenko, C. Kübel, Y. Huang, J.F. Corrigan	From molecule to materials: crystalline superlattices of nanoscopic CdS	Chem. Eur. J.	2011
A. S. Goldmann, T. Tischer, L. Barner, M. Bruns, C. Barner-Kowollik	Mild and Modular Surface Modification of Cellulose via HeteroDiels-Alder (HDA) Cycloaddition in the Solid State	Biomacromolecules	2011
N. Zydziak, C. Hübner, M. Bruns, C. Barner-Kowollik	One-step Functionalization of Single-Walled Carbon Nanotubes (SWCNTs) with Cyclopentadienyl Capped Macromolecules via Diels-Alder Chemistry	Macromolecules	2011

Authors	Title	Published in	Year
B. Liu, J. Yang, M. Yang, Y. Wang, N. Xia, Z. Zhang, P. Zheng, W. Wang, I. Lieberwirth, C. Kübel	Polyoxometalate Cluster-contained Hybrid Gelator: A New Concept of Constitution of Hybrid Organogels with Highly Ordered Supramolecular Ribbons	Soft Matter	2011
Hendrik Wagner, Yong Li, Michael Hirtz, Lifeng Chi, Harald Fuchs and Armido Studer	Site specific protein immobilization into structured polymer brushes prepared by AFM lithography	Soft Matter	2011
D.G. Macdonald, C. Kübel, J.F. Corrigan	Ferrocenyl Functionalized Silver-Chalcogenide Nanoclusters	Inorg. Chem.	2011
Michael Hirtz, Rémi Corso, Sylwia Sekula-Neuner, Harald Fuchs	Comparative Height Measurements of Dip-Pen Nanolithography-Produced Lipid Membrane Stacks with Atomic Force, Fluorescence, and Surface Enhanced Ellipsometric Contrast Microscopy	Langmuir	2011
Simon Rutishauser, Irene Zanette, Timm Weitkamp, Tilman Donath, and Christian David	At-wavelength characterization of refractive x-ray lenses using a two-dimensional grating interferometer	Appl. Phys. Lett.	2011
T. Thuering, P. Modregger, T. Grund, J. Kenntner, C. David et al.	High resolution, large field of view x-ray differential phase contrast imaging on a compact setup	Appl. Phys. Lett.	2011
H. Rösner, C. Kübel, J. Ivanisenko, L. Kurmanaeva, S. Divinski, M. Peterlechner, G. Wilde	Strain mapping of a triple junction in nanocrystalline Pd	Acta Mat.	2011
Stephan Frank, Patric A. Gruber, Ulrich A. Handge, Ralph Spolenak	In situ studies on the cohesive properties of a- and b-Ta layers on polyimide substrates	Acta Materialia	2011
W. Gruber, S. Chakravarty, C. Baehtz, W. Leitenberger, M. Bruns, A. Kobler, C. Kübel, and H. Schmidt	Strain Relaxation and Vacancy Creation in Thin Platinum Films	Physical Review Letters	2011
A. Rashidian, D. M. Klymyshyn, M. T. Aligodarz, M. Börner, J. Mohr	Photoresist-Based Polymer Resonator Antennas: Lithography Fabrication, Strip-Fed Excitation, and Multimode Operation	IEEE Antennas and Propagation Magazine	2011
G. Devaraju, A.P. Pathak, N.S. Rao, V. Saikiran, D. Wang, T. Scherer, A.K. Mishra, C. Kübel	Ion beam treated strained AlGaN/GaN multi quantum wells: HAADF- STEM, HRTEM, Raman and HRXRD characterizations	Radiation Effects and Defects in Solids	2011
D. M. Klymyshyn, M. Tayfeh Aligodarz, A. Rashidian, M. Börner, J. Mohr	Photoresist-based resonator antenna array	Proceedings of the 6th German Microwave Conference	2011

User Reports

Users awarded no fee access to KNMF facilities by the KNMF Peer Review Board are required to publish the work as soon as possible after completion. Additionally, in order that we can monitor the progress of individual user projects they are requested to submit reports on the work. The reports also form the basis of the User contributions to this, the first annual KNMF report.

List of contributors

(Reports received by 30th September 2012)

Proposal ID	Proposal Title	Name	Organisation	Country
2008-001-000006	Microoptical retroreflector	Jürgen Jahns	FernUniversität Hagen	Germany
2008-001-000020	Laser generated rib structures for optical waveguides	Ulrich Teubner	Hochschule Emden/Leer - University of Applied Sciences	Germany
2009-001-000022	Micro-fabrication of grating structures for a first dedicated lab-based small-animal phase-contrast microCT prototype setup	Franz Pfeiffer	Technische Universität München	Germany
2009-001-000034	Bio-patterned surfaces for studying glucocorticoid-mediated regulation of mast cell activation	Andrew Cato	Karlsruhe Institute of Technology (KIT)	Germany
2009-001-000047	Patterning of biomolecules on a Surface Acoustic Wave biosensor using Dip Pen Nanolithography for multi-analyte detection of cardiac biomarkers	Electra Gizeli	Institute of Molecular Biology and Biotechnology (IMBB)	Greece
2009-002-000119	Biomedical Phase-Contrast Imaging at Elevated X-Ray Energies	Franz Pfeiffer	Technische Universität München	Germany
2009-002-000126	Fabrication of RF MEMS Circuits	Melissa Schaffer	TRLabs	Canada
2009-002-000137	Fabrication of Thick Polymer-based Antenna Structures	David Klymyshyn	University of Saskatchewan	Canada
2009-002-000138	Fabrication of x-ray interferometer gratings for phase contrast imaging with divergent sources	Christian David	Paul Scherrer Institut	Switzerland
2009-003-000157	Large acceptance lens for focusing an undulator beam	Alfred Baron	RIKEN SPring-8 Center	Japan

Proposal ID	Proposal Title	Name	Organisation	Country
2010-003-000186	Micro-fabrication of an absorption grating for 2D X-ray grating interferometry	Irene Zanette	European Synchrotron Radiation Facility (ESRF)	France
2010-003-000230	Electron Tomography of nanoparticles in III-V semiconductors	Wolfgang Jäger	Christian-Albrechts-Universität zu Kiel (CAU)	Germany
2010-003-000238	Study of Deformation Behaviour in Molecular Crystals	Chilla Malla Reddy	Indian Institute of Science Education and Research (IISER), Kolkata	India
2010-004-000270	Screening of the Surface Structure and Modification of Carbon Nanotubes and Cellulose	Christopher Barner-Kowollik	Karlsruhe Institute of Technology (KIT)	Germany
2010-004-000342	TEM Characterization of Semiconductor Nanocrystals	Anand Pathak	University of Hyderabad	India
2010-004-000365	Metallic Micro Nailheads MAde by LiG process - MiNiMAL	Felix Greiner	Technische Universität Darmstadt	Germany
2010-004-000368	Injection-molded photonic crystal slabs for surface contrast microscopy	Yousef Nazirizadeh	Christian-Albrechts-Universität zu Kiel (CAU)	Germany
2010-004-000369	Fabrication of optimized diffraction gratings for differential phase contrast imaging on a compact setup	Thomas Thüring	Paul Scherrer Institut	Switzerland
2010-004-000370	Interface effects on magnetic moments in multilayers	Inga Ennen	Technische Universität Wien	Austria
2010-004-000374	Multi-period nanostructured OLEDs for enhanced outcoupling efficiency	Michael Rädler	Christian-Albrechts-Universität zu Kiel (CAU)	Germany
2010-005-000387	Point defect concentrations in nanocrystalline metallic films	Harald Schmidt	Technische Universität Clausthal	Germany
2010-005-000399	Solvothermal conversion of T1 cadmium thiophenolates into a crystalline superlattice of the largest characterized CdS nanoclusters	John Corrigan	The University of Western Ontario	Canada
2010-005-000416	Phase seperation in amorphous and partially crystallized SiCx	Harald Schmidt	Technische Universität Clausthal	Germany

Proposal ID	Proposal Title	Name	Organisation	Country
2011-005-000477	Laser Assisted Micro-texturing of Surface Nitrided Ti-6Al-4V	Jyotsna Dutta Majumdar	Indian Institute of Technology (IIT)	India
2011-005-000483	Structural study of Metal-Oxide-Semiconductor devices based on SiGe and CdSe nanocrystals grown for flash memory applications	Sergey Levichev	Universidade do Minho	Portugal
2011-005-000493	Preparation of reactice surface areas by DPN for site selective self assembly of virus-like particles	Christina Wege	Universität Stuttgart	Germany
2011-006-000517	STEM tomography of whole cells	Niels de Jonge	Vanderbilt University School of Medicine	USA
2011-006-000532	Investigation on the elemental distribution in amorphous IndiumZinc Oxide Phases	Jörg Schneider	Technische Universität Darmstadt	Germany
2011-006-000538	Nanoscale growth twins for the development of grain boundary engineered structures	Andrea Hodge	University of Southern California	USA
2011-006-000545	Laser-assisted localized contact angle modifications for thermoplastics in Lab-on-a-Chip applications	Frank Schwemmer	Albert-Ludwigs-Universität Freiburg	Germany
2011-006-000556	Fundamentals of design and investigations of the characteristics of optoelectronic devices on the basis of controlled self-organization processes, self-assembly and super-structuring in the epitaxial alloys of III-V semiconductors	Pavel Seredin	Voronezh State University	Russia
2011-006-000569	Controllable preparation of Cu and Cu/Cu2O core/shell nanoparticles	Andrew Wheatley	Cambridge University	United Kingdom
2011-006-000608	Crystalline superlattices of nanoscopic binary ME and ternary MM'E materials	John Corrigan	The University of Western Ontario	Canada
2011-007-000774	Optimization of interferometric phase contrast imaging for dental imaging with higher energies up to 100 keV	Ciamak Abkai	Sirona Dental Systems GmbH	Germany
2012-007-000843	Design of 3D-micro batteries by combining laser-assisted printing and surface structuring	Alberto Pique	US Naval Research Laboratory	USA

Final Reports as submitted by the Users

Proposal 2008-001-000006

Microoptical retroreflector

Jürgen Jahns

FernUniversität Hagen
Hagen
Germany

Final Report

1. Project goals:

We report on the fabrication of a one-dimensional micro-retroreflector array with a pitch of 100 micrometers. The array was fabricated by x-ray lithography and the LIGA process in a 1 mm thick PMMA layer and subsequently covered with Au. The area of the array is 1 mm x 10 mm. The high precision of the LIGA-based fabrication process allows one to use the element in spectrometers. The motivation of this work is to use the high precision of 2D lithographic masks (with a spatial resolution of typically 0.1 micrometers) to generate optical element which are suitable for applications in spectroscopy and for ultrashort pulses. Here, specifically, the purpose is the implementation of the micro-retroreflector as a transversal filter for optical femtosecond pulses. Both goals, highly precise fabrication and excellent optical performance, were successfully demonstrated.

2. Project results:

Direct LIGA was used for the fabrication of the micro-retroreflectors. For that a thick resist layer was structured by synchrotron x-ray radiation. Due to the excellent collimation of the X-rays, the pattern of the 2D mask is transferred into the resist layer with almost no changes in the slope of the structural sidewall; sidewall inclination is less than 1 mrad. The micro-retroreflector array was fabricated in a 1 mm thick PMMA layer and subsequently covered with Au. The area of the array is 1 mm x 10 mm. The figure shows an SEM picture of the resulting micro-retroreflector.

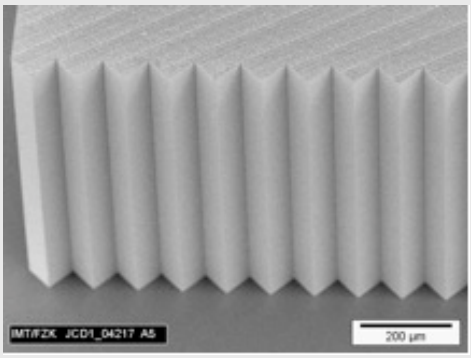

For characterization of the element, the surface profile and roughness were measured. The high structural precision along the sidewall can be seen from the figure as well as low sidewall roughness; edge rounding for this sample can be estimated to be in the range of 2.5 µm. A profile scan taken with a confocal microscope (see figure) confirming the precision of the generated profile. Surface roughness measurements were performed with an atomic force microscope. The measured values are R_a = 16.1 nm with a standard deviation of 0.9 nm.

Karlsruhe Nano Micro Facility (KNMF)
Karlsruhe Institute of Technology (KIT)
Hermann-von-Helmholtz-Platz 1
76344 Eggenstein-Leopoldshafen
Germany

User Office
Phone: +49 (721) 608-3123
Fax: +49 (721) 608-6273
Email: knmf-useroffice@kit.edu
Web: www.knmf.kit.edu

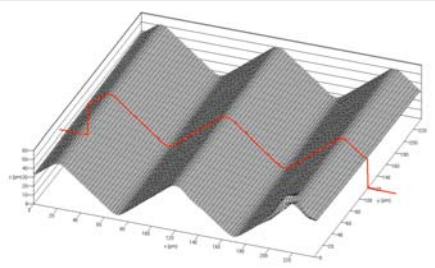

To test the fabricated structures optically, a diffraction experiment was performed. For this purpose, a collimated beam obtained from a point source (PS) with a broad spectrum illuminated the RA. Here, in different experiments, a white-light source and a femtosecond laser, were used for that purpose. The reflected light then passed through a diffraction grating. A modulated spectrum is observed in the far-field for a tilt angle ⍰>0. In that case, the beamlets reflected off two neighbouring facets of the retroreflector experience a discrete time-delay $\tau_r = 2w\sin\gamma/c$ where *w* is the pitch of the array (in our case, *w*=100 micrometers). The amplitude in the optical far-field is generated by the superposition of ten or more beamlets (depending on how many facets are illuminated).

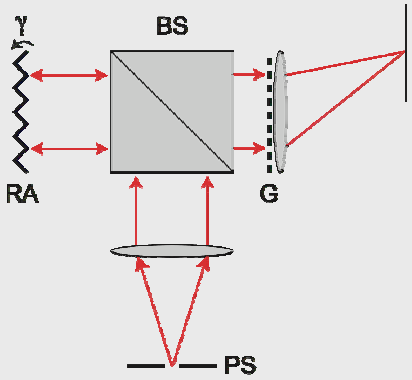

A typical spectrum obtained with light from a fs-laser (Spectra Physics Mai Tai SP) and measured with a monochromator is shown in the next figure. Noticeable are, in particular, the sharp peaks and the high contrast. Both are an indication of the high quality of the fabricated device. Using simple geometric considerations one can estimate that the tolerances on the 90° angles of the retroreflector facets are less than 0.1°.

Karlsruhe Nano Micro Facility (KNMF)
Karlsruhe Institute of Technology (KIT)
Hermann-von-Helmholtz-Platz 1
76344 Eggenstein-Leopoldshafen
Germany

User Office
Phone: +49 (721) 608-3123
Fax: +49 (721) 608-6273
Email: knmf-useroffice@kit.edu
Web: www.knmf.kit.edu

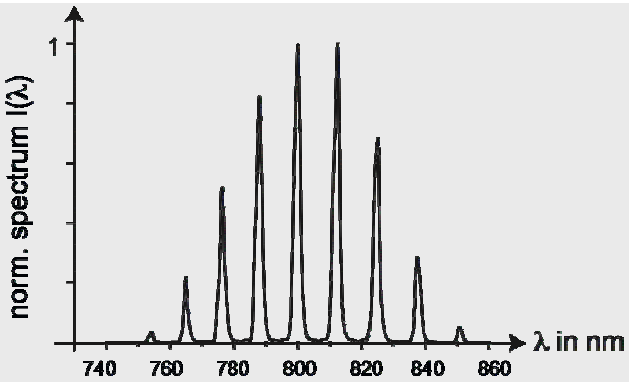

In conclusion, one can say that in order to obtain the high precision that is need for the temporal filtering of femtosecond pulses and for spectroscopic applications, the exact definition of the LIGA-fabricated structure is essential.

3. Publications:

J. Jahns, Th. Seiler, J. Mohr, M. Börner, Micro-retroreflector array fabricated by the LIGA process, Proc. SPIE vol. 7716 (2010).

M. Bohling, Th. Seiler, B. Wdowiak, J. Jahns, J. Mohr, M. Börner, Highly precise micro-retroreflector array fabricated by the LIGA process and its application as tapped delay line filter, Appl. Opt., vol. 51, pp 5989-5995 (2012).

J. Jahns, M. Bohling, Th. Seiler, B. Wdowiak, J. Mohr, M. Börner, Micro-retroreflector array fabricated by LIGA, OSA Ann. Meeting 2012, paper no. FTu3A.29

4. Comments:

Proposal 2008-001-000020

Laser generated rib structures for optical waveguides

Ulrich Teubner

Hochschule Emden/Leer - University of Applied Sciences
Emden
Germany

Note: *Please fill in this report form and save/print it as a PDF file, then upload it to the KNMF proposal submission system. A cover page containing proposal title, proposer name(s), and technologies selected will be added by the system. A link for the download of the complete report as a PDF file will be displayed in the system.*

Final Report

1. Project goals (max. 1.800 characters)**:**

Laser generated rib structures for optical waveguides

H.J. Brückner[1)], U. Teubner[1)], W. Pfleging[2)]

With the rapid growth of optical and microstructure technologies during the last decades also the development of integrated optical components has gained high importance. A critical point in that case are the high costs of semiconductor technologies conventionally deployed in the production of optoelectronic chips for communication applications. Glass or plastic materials are here considered as a low cost alternative [1]. A focus can be seen in designing optical waveguides for temperature, pressure or biochemical sensors [2, 3].

The objective of our work is the fabrication of optical single mode waveguides with a high numerical aperture for sensor applications in the visible spectral range. The strong guiding, prerequisite for compact chips is achieved especially in rib waveguides due to the high index difference between the core material and the surrounding air. As a substrate we use PMMA bulk material on which ridges are micromachined by ablation using pulsed laser radiation (excimer laser, ultra short pulse laser). The confinement of the optical mode in vertical direction is a consequence of the locally increased refractive index in PMMA after subsequent exposure to UV-radiation. The resulting index profile depends on the exposure conditions as e. g. power density, exposure time, pulsed or continuous irradiation. Within the frame of the present work we used two methods to modify the refractive index. The simplest one is the large area irradiation of the sample by uniform UV lamp radiation. A more complex alternative leading to a stronger index modification is the writing exposure using KrF-excimer laser radiation below the ablation threshold. The quality of the optical guiding will be presented and discussed for the different preparation methods.

2. Project results (max. 7.000 characters + figures)**:**

We used 3 mm thick sheets (PLEXIGLAS FORMMASSE 7N, Evonik Röhm GmbH) as substrates for the waveguides. The structure design is schematically drawn in fig. 1.

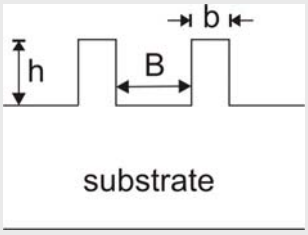

Fig. 1: Cross-section of the micromachined rib in PMMA

The rib height h and the inter-rib distance B were chosen to be larger than 10 µm and 30 µm, resp., in order to avoid a cross-talk between neighbouring waveguides. The rib width was varied between 2 µm and 14 µm.

The material ablation between the rib waveguides has been achieved using two different laser systems: An ArF excimer laser Lambda LPX 210i with a pulse time of about 20 ns at 193 nm, and a ultra short pulse (USP) laser Clark-MXR CPA-2110 with a pulse time of about 150 fs at a center wavelength of 775 nm, a maximum energy of 1 mJ and a repetition rate of 1 kHz.

After profiling the rib structures, the index modification was done using two alternative UV-sources: a high power mercury vapour lamp yielding a uniform power density of 10 mW/cm² in the spectral range of 240-260 nm. The total exposure dose was controlled by the exposure time which varied from a few minutes up to one hour. For the laser beam exposure we used a KrF excimer laser with 5 ns pulse time and 300 Hz repetition rate at 248 nm. The beam diameter was of approx. 15 µm on the sample surface, the sample was displaced by a microstage.

Microscope pictures taken from structures ablated by excimer laser radiation are shown in fig. 2. It can be seen that the fabricated ribs show a trapezoid cross section with an edge steepness reduced to approx. 15° relative to the rectangular profile. As a consequence the top width of the ribs is reduced by 1-2 µm in comparison to the design width. Moreover, this results in triangular profiles with a reduced rib height h for design widths of less than 4 µm. The triangular structures did not show guiding properties and will not be considered further on. As compared to this excimer laser material ablation, the treatment using USP-laser leads to ribs with steeper edges (fig. 3).

The guiding properties were investigated analyzing the mode field at the waveguide output. To that purpose light of 676 nm was directly coupled to the waveguide using a single mode fibre. The intensity distribution at the output is shown in fig. 4 for different waveguides.

As seen from fig. 4b), the ArF laser structured ribs show weak single mode wave guiding already after ablation, without any further UV post-exposure. The light confinement becomes stronger with a subsequent large area exposure using a UV-lamp (fig. 4c).

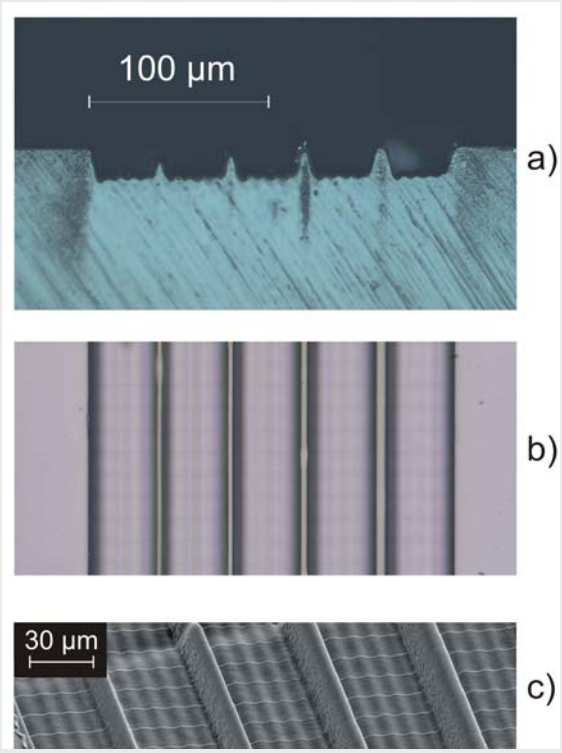

Fig. 2:
Rib waveguides in PMMA, structured by excimer laser ablation (193 nm)

a) cross section
b) top view
c) surface structure (SEM)

design width b of the ribs:
2µm, 4µm, 6µm, 8µm (from left)

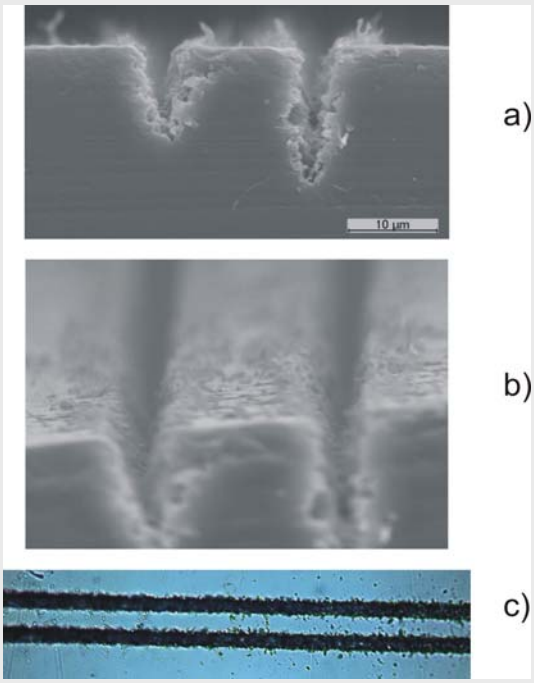

Fig. 3:
Rib waveguides in PMMA, structured by ultra short pulse laser ablation (775 nm)

a) and b)
Cross section of a 14 µm wide rib (SEM)

c) Top view of a 9 µm wide rib

Karlsruhe Nano Micro Facility (KNMF)
Karlsruhe Institute of Technology (KIT)
Hermann-von-Helmholtz-Platz 1
76344 Eggenstein-Leopoldshafen
Germany

User Office
Phone: +49 (721) 608-3123
Fax: +49 (721) 608-6273
Email: knmf-useroffice@kit.edu
Web: www.knmf.kit.edu

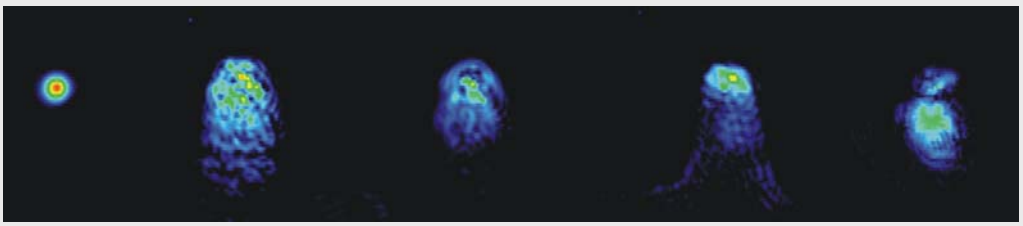

Fig. 4: Intensity distribution at the output of different waveguides at 676 nm
a) singlemode fiber, mode field diameter of 4,2µm (reference)
b) 8µm rib waveguide (ArF excimer laser ablation), without UV post-exposure
c) 8µm rib waveguide (ArF excimer laser ablation), UV-lamp post-exposure
d) 8µm rib waveguide (ArF excimer laser ablation), KrF laser post-exposure
e) 9µm rib waveguide (USP-laser ablation), UV-lamp post-exposure

Analyzing the intensity distribution at the output of 8 µm ribs yields the 1/e mode field diameters in vertical and horizontal directions, resp. These are given in fig. 5 as a function of the exposure dose.

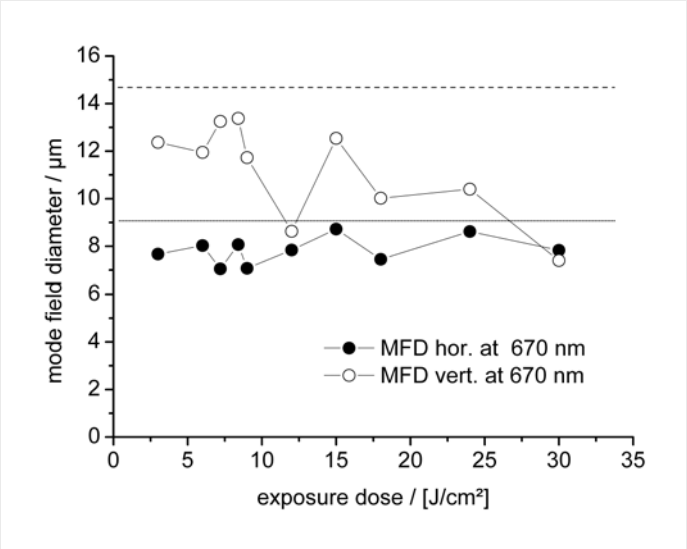

Fig. 5:
Mode field diameters of 8 µm rib structures (ArF excimer laser ablation) as a function of dose of UV-lamp post-exposure. The horizontal lines indicate the mean values of structures without post-exposure

The horizontal mode field diameter remains unchanged by the UV exposure and is nearly the same as the top width of the waveguide rib. In vertical direction, no guiding should occur in a non exposed waveguide. The result however suggests that a weak index modification took place during the ablation process outside of the rib. The significant decrease of the vertical mode field diameter is due to the increasing index with the exposure dose leading to a nearly round spot of about 7.5 µm at 30 J/cm². A stronger confinement is achieved after pulsed exposure using a KrF

excimer laser (fig. 4d). The vertical diameter becomes smaller than the horizontal one (approx. 6 µm). Unlike the excimer laser ablated ribs, the USP-laser ablated samples show no light guiding directly after structuring. Irradiation by the UV lamp with a dose of 31 mJ/cm² leads to wave guiding in a 9µm wide rib structure with a slightly larger spot diameter (fig. 4e) as compared to excimer laser written ribs at the same dose.

The absorption of UV radiation in PMMA leads to a partial side chain scission and an increase of the refractive index [4, 5, 6]. In a simple approximation we assume an exponential decay characterizing the index profile of the exposed waveguides in the vertical y-direction:

$$n(y) = n_0 + \Delta n \cdot \exp(-y/h_y)$$

with Δn being the maximum index change at the surface and n_0 the index of the unmodified bulk material. h_y is the depth in the structure where the index change has decreased to 1/e of its maximum value. In horizontal direction the guided mode is mainly confined by the width of the rib. In order to estimate the index change Δn as well as h_y, mode field calculations based on the method of finite elements have been performed. The results of the numerical mode calculations, varying Δn and h_y independently, for a waveguide with the fabricated cross section dimensions are shown in fig. 6. The comparison with our measurements yields the parameters $\Delta n \approx 0.004$ und $h_y \approx 2$ µm for excimer laser ablated ribs in combination with UV-lamp post-exposure. The stronger confinement of the mode in vertical direction for samples where the post-exposure is done by pulsed excimer radiation shows that a stronger index increase is achieved by that method as compared to UV-lamp exposure.

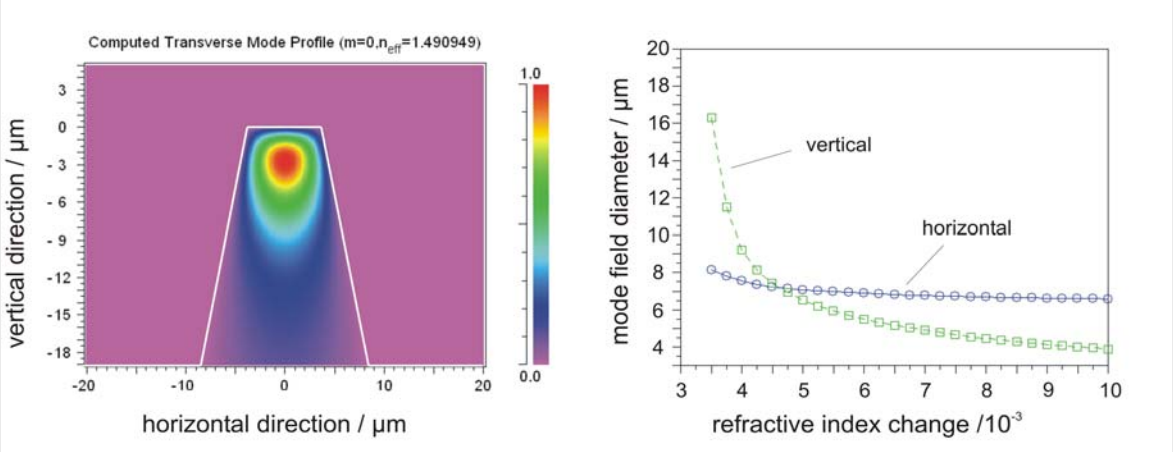

a) b)

Fig. 6: Mode field simulation for a rib waveguide (wavelength 676 nm, top rib width 7,5 µm, h_y=2 µm)
a) electrical field distribution of the fundamental mode for Δn=0,004
b) mode field diameter (at 1/e of the max. electrical field) as a function Δn

Karlsruhe Nano Micro Facility (KNMF)
Karlsruhe Institute of Technology (KIT)
Hermann-von-Helmholtz-Platz 1
76344 Eggenstein-Leopoldshafen
Germany

User Office
Phone: +49 (721) 608-3123
Fax: +49 (721) 608-6273
Email: knmf-useroffice@kit.edu
Web: www.knmf.kit.edu

Absorption losses in the waveguides have been evaluated directly as the ratio between in- and output powers. They were corrected with respect to the theoretical coupling loss from the launching single mode fiber to the elliptical guided mode and the Fresnel losses between the fiber-air and air-chip interfaces. For the excimer laser ablated ribs the lowest absorption losses are of 8-10 dB/cm for the best guiding structures. The losses are lower for the USP-laser ablated structures. Here the evaluation yields best values in the range of around 4-8 dB/cm.

The waveguide losses in the rib structures are higher than values obtained with excimer laser written buried waveguides [7]. In the latter case the substrate surface was not damaged, the wave guiding was achieved by the index increase only and the losses are of the order of 1 dB/cm in the spectral range at 670nm. As for the mode confinement and the guiding properties they are comparable in all cases. We come to the conclusion that the high absorption losses in the rib structures depend primarily on the surface quality. It seems that the surface quality of the USP-laser ablated rib structures is higher than the excimer laser machined one. Further detailed investigations to that problem are in progress.

References

[1] Keil, H. H. Yao, C. Zawadzki: Integrated Optical Switching Devices for Telecommunications Made on Plastics, Plastics in Telecommunications VIII, London (1998), Conf. Dig. pp 11-17; U. Teubner: Miniaturized Optical Components in Polymers for Optical Networks and Sensors, SPIE **5454** (2004) 31-40

[2] J. Mueller J, D. Zurhelle, K. Fischer, A. Loeffler-Peters, R. Hoffmann: Integrated Optical Pressure Sensor With Coupling Structures, Proc. SPIE 1794: 167 – 178 (1993)

[3] D. A. Chang-Yen, B. C. Gale: An Integrated Optical Biochemical Sensor Fabricated Using Rapid Prototyping Techniques, Proc. SPIE 4982 San Jose (USA) (2003)

[4] W.F.X. Frank, A. Schoesser, A. Stelmaszyk, J. Schulz: Ionizing radiation for fabrication of optical waveguides in polymers, SPIE **CR63**, pp. 65-83, 1996.

[5] C. Wochnowski, S. Metev, G. Sepold: UV-Laser-Assisted Modification of the optical properties of Polymethylmethacrylate, Appl. Surf. Sci. 154/155 pp. 706-711, 2000

[6] A. Fernandez, H.J. Brückner, S. Tiedeken, W. Neu: Guided Mode Analysis of Optical PMMA-Waveguides Structured by Direct Excimer Laser Irradiation, Journal of Optical Communications 2, pp. 45-48, 2004

[7] W. Pfleging,, R. Adamietz, H. J. Brückner, M. Bruns, A. Welle: Laser-assisted Modification of Polymers for Microfuidic, Microoptics and Cell Culture Applications, Proc. of SPIE Vol. 6459, 645907-1 –, 645907-12 (2007)

Proposal 2009-001-000022

Micro-fabrication of grating structures for a first dedicated lab-based small-animal phase-contrast microCT prototype setup

Franz Pfeiffer

Technische Universität München
Garching
Germany

Final Report

1. Project goals (max. 1.800 characters)**:**

The overall goal of the proposed project was to micro-fabricate x-ray optical grating structures to further develop and apply the potential of **x-ray phase-contrast imaging for pre-clinical, small-animal imaging applications**.

The **first part of the proposal** to the KNMF (2/3 of the requested structures) concerned the fabrication of grating structures for a first small-animal phase-contrast microCT bench-top prototype setup. The main motivation for this was to first explore a compact gantry system that can be implemented into an in-vivo small-animal phase-contrast computed tomography (PC-CT) scanner. The purpose of the present study was to assess the accuracy and quantitativeness of the described gantry in both absorption and phase-contrast.

The **second part of the proposal** included also grating structures (about 1/3 of the requested material) for complementary measurements at synchrotron sources. The aim of this study was to assess the biomedical potential of x-ray phase-contrast imaging for preclinical research. Specifically, the potential of phase-contrast imaging for tumor detection should have been evaluated on the basis of an ex-vivo murine model of pancreatic cancer.

2. Project results (max. 7.000 characters + figures)**:**

(1) First part of the proposal: Development and testing of a prototype gantry system for preclinical x-ray phase-contrast computed tomography

One of the main shortcomings of existing biomedical x-ray imaging systems is their limited contrast in soft-tissue. This limitation can principally be addressed by phase-sensitive imaging methods, which provide considerably improved soft-tissue contrast. Over the past years, several phase-sensitive x-ray imaging techniques have been developed. They can be categorized into three methods: free-space propagation, analyzer-based, and interferometric phase-contrast imaging. For grating interferometers, increased soft-tissue contrast was first demonstrated at synchrotron-sources. Recent studies on biological specimen using grating interferometers at laboratory x-ray sources also show excellent imaging results with improved contrast and great potential for medical imaging is envisioned. These findings have triggered the start of development efforts toward dedicated medical imaging systems for preclinical and clinical use.
In this work, we present the first experimental results from such a dedicated compact x-ray phase-contrast gantry system, which we have developed for future implementation into an in-vivo small-animal phase-contrast computed tomography (PC-CT) scanner. We present PC-CT cone-beam imaging results of a fluid phantom, highlighting the complementary information contained in the conventional and PC-CT signal channels. The aim of this study was to investigate the quantitative accuracy of compact cone-beam

phase-contrast and absorption-based CT protocols. We particularly show in this work that the system yields the three-dimensional distribution of attenuation coefficient and refractive index decrement of the different liquids contained in the phantom.

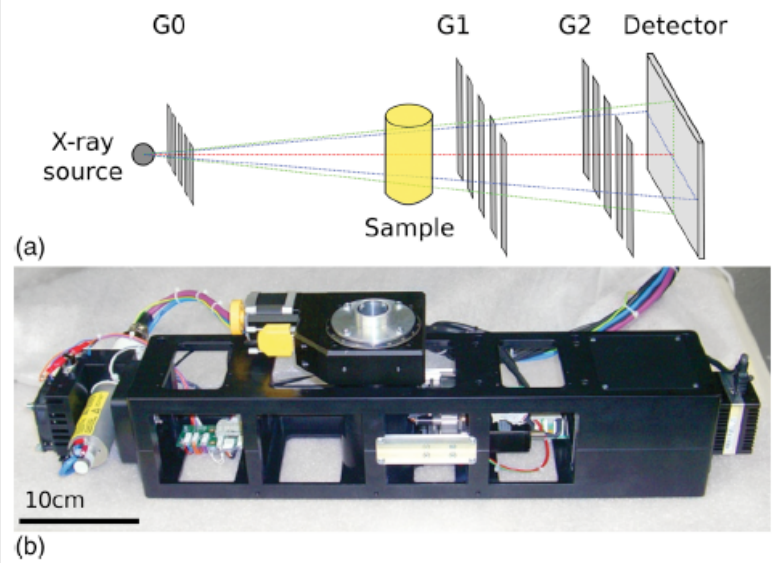

Fig. 1: *X-ray phase-contrast gantry. (a) Schematic drawing of the three grating interferometer in compact cone-beam geometry with source grating G0, phase grating G1 and analyzer grating G2. (b) Photograph of the setup with a total length of 73 cm [Tapfer et al, Medical Physics, 2011].*

The gantry setup (Fig. 1) consists of a tungsten x-ray source (RTW, MCBM 65B-50 W, focal spot size approximately 50 microns in diameter), a rotation stage connected with a PMMA sample holder and a camera assembly. The camera assembly comprises a scintillator and a 1.3 mega-pixel cooled 14-bit CCD camera with an effective pixel size of 30 microns and a fixed focus lens in front. The source-to-sample and the sample-to-detector distances are approximately 280 and 210 mm respectively, such that the field of view (FOV) at the position of the sample is 40 mm, sufficient to visualize a mouse.
With the given geometrical constraints that the gantry has to fit into a preclinical scanner, a design energy of 23 keV was chosen and the interferometer is operated in the first fractional Talbot distance as a compromise between a compact, but yet sensitive setup with sufficient transmission through a mouse. The phase grating has nickel structures, inducing a pi/2 phase shift and the source and analyzer gratings contain highly absorbing gold structures. The total setup length of 49 cm (x-ray source to detector), or 73 cm with housing, is the most compact existing three grating setup and sufficiently small to fit into a rotating gantry of a small-animal scanner.
To experimentally assess the quantitative accuracy of the compact phase-contrast gantry system, a phantom study in absorption and phase-contrast was performed. The phantom comprised six polypropylene tubes (7 mm diameter, 0.5 ml) mounted on a holder that was embedded in a water filled PMMA container of approximately 3 cm in diameter. The tubes were filled with accurately defined substances of well-known chemical liquids and salts to cover a range of attenuation coefficients and refractive index decrements.

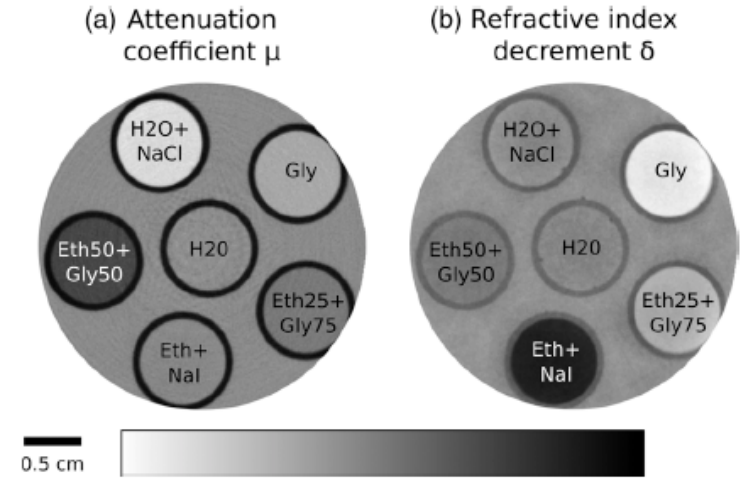

Fig. 2: *Absorption- and phase-contrast CT scans of the fluid phantom. (a) Absorption contrast displays the spatial distribution of the absorption coefficient. (b) Phase-contrast depicts the spatial distribution of the decrement of the refractive index [Tapfer et al, Medical Physics, 2011].*

Figure 2 shows the central absorption and phase-contrast tomograms of the fluid phantom. For an increased signal-to-noise ratio, 50 adjacent transverse slices were averaged. Quantitative data of attenuation coefficient and the phase-shift for each liquid substance were extracted from these tomographic reconstructions by a region-of-interest (ROI) analysis, with each region covering approximately 80% of the center of the individual tubes. As a conclusion, we found that calculated and measured data agree well-the maximum relative deviation for any liquid is approximately 4%.

(2) Second part of the proposal: Evaluation of phase-contrast CT in an ex-vivo pancreatic ductal adenocarcinoma mouse model using brilliant synchrotron radiation

This study now aims at assessing the biomedical potential of x-ray phase-contrast imaging for preclinical research. Specifically, the potential of phase-contrast imaging for tumor detection and characterization is evaluated in a genetically engineered mouse model of pancreatic ductal adenocarcinoma (PDAC). This study covers a broad range of tomographic imaging setups with measurements of one ex-vivo mouse specimen. In order to estimate what is achievable with a grating-based phase-contrast setup in principle, synchrotron benchmarking imaging with high x-ray dose and high spatial resolution was performed. This mouse specimen was also measured at the same experimental synchrotron setup with greatly reduced acquisition parameters at preclinically dose-compatible conditions.
Conventional x-ray attenuation contrast images and phase-contrast images were obtained using a Talbot-(Lau) interferometer. The synchrotron source measurements were carried out at beamline ID 19 of the European Synchrotron Radiation Facility (ESRF) in Grenoble, France. Images were recorded with a two-grating Talbot interferometer and scintillator/lens-coupled CCD detector. CT reconstruction was performed using a standard filtered backprojection algorithm. For attenuation contrast, a Ram-Lak filter and for phase contrast, a Hilbert filter was used. Strongly phase shifting materials, like for example bone, produce streaking artifacts, similar to metal implants in conventional CT. To reduce the magnitude of the streaks, a

straightforward method was applied during reconstruction of the phase-contrast data, i.e. the differential phase sinogram was weighted with the squared value of the visibility. This approach suppresses the bone signal as bone scatters strongly and hence causes a low weighting of the corresponding area in the differential phase sinogram. All attenuation and phase contrast reconstructed CT slices were post-processed with a sharpening filter.

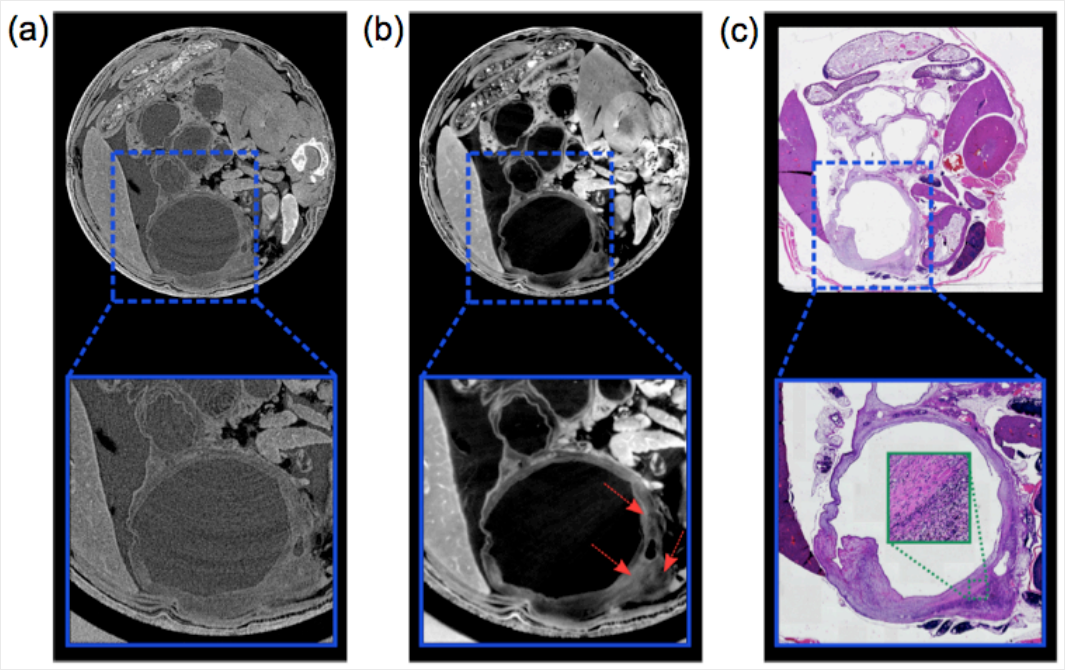

Fig. 3: *Transverse slices of synchrotron data and histology. (a) Absorption CT image (top), Zoom (bottom).(b) Phase-Contrast CT image (top), Zoom (bottom). The arrows highlight differences in tissue composition. (c)Histology (top), Zoom (bottom).*

Figure 3 shows transverse slices of the attenuation (a), phase-contrast image (b) and the corresponding histology slice (c). Please note that the shown x-ray and histology slices are slightly tilted with respect to one another, with best agreement at the lower right part of the pancreatic intraepithelial neoplasias (PanIN), which is investigated. Moreover, please note in the histologic slice that the upper right part of the wall of the PanINs is deformed due to the cutting procedure. The areas in the phase image that are highlighted with arrows, exhibit a difference in gray value, which reflects the difference in tissue composition that is evident in histology. The conventional attenuation contrast image does not reveal this information and image contrast in general is inferior. Tissue heterogeneity is recognized as an important aspect of tumor biology resulting in regional differences in therapy response. Therefore non-invasive detection of tumor heterogeneity is of great interest in tumor characterization and response monitoring. Based on these results, we conclude that grating-based phase contrast implies great potential for preclinical imaging. Besides an overall improved visibility of general anatomy, in particular tumor heterogeneity was clearly visible in great detail and overall significantly better visible with phase contrast compared to attenuation contrast. We believe that this study facilitates the use and further development of grating-based phase-contrast for biomedical imaging applications.

3. Publications (please stick to the user guidelines for publications and acknowledgements on www.knmf.kit.edu):

Publications (based on KNMF proposals, **with** KIT co-author):

1. Zanette, I. *et al.* Trimodal low-dose X-ray tomography. *Proceedings of the National Academy of Sciences* **109**, 10199–10204 (2012).
2. Potdevin, G. *et al.* X-ray vector radiography for bone micro-architecture diagnostics. *Phys. Med. Biol.* **57**, 3451–3461 (2012).
3. Jensen, T. H. *et al.* X-ray phase-contrast tomography of porcine fat and rind. *Meat Science* **88**, 379–383 (2011).
4. Tapfer, A. *et al.* Development of a prototype gantry system for preclinical x-ray phase-contrast computed tomography. *Med. Phys.* **38**, 5910 (2011).
5. Herzen, J. *et al.* X-ray grating interferometer for materials-science imaging at a low-coherent wiggler source. *Rev. Sci. Instrum.* **82**, 113711 (2011).
6. Jensen, T. *et al.* Directional x-ray dark-field imaging of strongly ordered systems. *Phys. Rev. B* **82**, 1–8 (2010).
7. Herzen, J. *et al.* X-ray grating interferometer for imaging at a second-generation synchrotron radiation source. *Proc. SPIE* **7804**, 780407 (2010).
8. Kenntner, J. *et al.* Front- and backside structuring of gratings for phase contrast imaging with x-ray tubes. *Proc. SPIE* **7804**, 780408 (2010).
9. Weitkamp, T. *et al.* Recent developments in x-ray Talbot interferometry at ESRF-ID19. *Proc. SPIE* **7804**, 780406 (2010).

Publications (based on KNMF proposals, **without** KIT co-author):

1. Hahn, D. *et al.* Numerical comparison of X-ray differential phase contrast and attenuation contrast. *Biomed Opt Express* **3**, 1141–1148 (2012).

4. Comments (max. 1.800 characters):

none

Proposal 2009-001-000034

Bio-patterned surfaces for studying glucocorticoid-mediated regulation of mast cell activation

Andrew Cato

Karlsruhe Institute of Technology (KIT)
Eggenstein-Leopoldshafen
Germany

Final Report

Bio-patterned surfaces for studying glucocorticoid-mediated regulation of mast cell activation

1. Project goals (max. 1.800 characters)**:**

Mast cells play an important role in mediating allergic reactions. They express high affinity receptors (FcεRI) on their surfaces which when bound to IgE and cross-linked lead to degranulation, release of preformed lipid mediators and increased expression of pro-inflammatory cytokine genes. These allergic and inflammatory actions of mast cells are inhibited by glucocorticoids that are well-known as mainstream therapy in many immunological disorders. The anti-allergic and anti-inflammatory actions of glucocorticoids studied so far are long term effects requiring approximately 16 h or more to be effective. Glucocorticoids and other steroids are however known to act in a rapid and non-genomic manner to rescue many inflammatory symptoms. However the mechanisms underlying such rapid actions of glucocorticoids have not been fully investigated.

As a first step in understanding this phenomenon, we aimed to analyse IgE-FcεRI mediated signalling using nanofabricated ligand arrays and to quantitatively evaluate localized receptor clustering and subsequent signalling upon pre-exposing mast cells to glucocorticoids. Dip-pen nanolithography (DPN) was the method of choice for the surface patterning because of its unique properties in integrating functional biomolecules on subcellular length scales with high resolution and high throughput. We also plan to immobilize glucocorticoids onto the patterned surfaces and to find out whether they could act to inhibit FcεRI activation through a membrane bound receptor without the need to enter the cell.

For the surface patterning 2, 4-dinitrophenyl (DNP)-capped phospholipids were used. Mast cells, either established lines or primary cells derive from wild-type or knock-out mice, were sensitized with anti-DNP IgE antibody which enable them to be clustered to the DNP headgroups on the phospholipids. We also plan to link to the phospholipids to steroidal ligands (cyclopentano-phenanthrene compounds) or nonsteroid ligands with tetracyclic quinoline cores or dihydrobenzofurane derivatives that would hopefully trigger activation of membrane bound glucocorticoid receptors. After clustering, activation of the mast calls will be analysed biochemically by phospho-antibody labelling, degranulation or by calcium release.

2. Project results (max. 7.000 characters + figures)**:**

In our work we could show that the bioactive lipid with the allergenic head group 1,2-dipalmitoyl-*sn*-glycero-3-phosphoethanolamine-N-[6-[(2,4-dinitrophenyl)amino]hexanoyl] (DNP-cap-PE) when mixed with DOPC phospholipid can be co-patterned onto glass surfaces via DPN lithography (Fig. 1). In order to generate arrays of allergen microfluidic inkwells capable of simultaneously delivering different lipid mixtures to tips were used. Tip arrays were coated with ink mixtures containing increasing amounts of DNP headgroups (2.5 to 10 mol%) admixed to the carrier lipid DOPC with 1 mol% content of rhodamine-labeled lipid. Using an M-type 12-tip array (DPN 5000 system, NanoInk Inc.) for the lithography process presented in Figure 1, one tip from the array can generate dot structures within a 66 µm × 80 µm area in one lithography step. This area allows for 6 dots × 8 dots with 10 µm spacing. If the lithography is repeated ten times, one tip in the array can cover an area of 66 µm × 800 µm making 480 dots. Tips with 66 µm spacing in one array can cover an area of 780 µm × 800 µm, giving 5760 dots in total, in less than 5 min of the lithography process. This number of features in the array is sufficient to gain statistical information on antibody-recognition of the allergen on the surface or cell response to the allergen pattern.

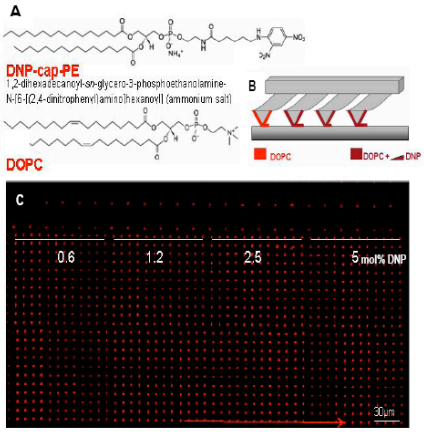

Figure 1. Multiplexed lithography of phospholipids with allergenic headgroups. (A) Chemical structures of DOPC carrier lipid and allergenic phospholipid DNP-cap-PE. (B) Schematic illustration of the multiplexed patterning of different lipid mixtures (C) Fluorescence image of nanoarrays composed of DOPC and increasing amounts of DNP phospholipid with the rhodamine labelled lipid admixture

The biological activity of the allergen arrays was assessed by applying and analyzing the response of sensitized, fluorescently labelled mast cells used as sensors on the DNP arrays. Clustering of the anti-DNP IgE antibody on RBL-2H3 mast cells exposed to the nanopatterned surface was visualized by using Alexa Fluor® 488-labelled IgE. The labelled antibody was used to sensitise the mast cells to make them visible in live cell imaging. The cells were placed over the pattern and binding the surface containing the 30% DNP (evident by the yellow dot) and not the area containing only the DOPC is clearly visible (Fig. 2). With no haptenated lipid present, the cells remained rounded and mostly detached from the patterned surface. When the bilayers contain DOPC and DNP, the cells flatten and spread out. Clustering of IgE receptor on mast cells initiates signal transduction that leads to degranulation and release of chemical mediators. This process is accompanied by polymerisation of cytoskeletal actin leading to spread of the rounded cell and ruffling caused by extension of lamellipodia. The clear morphological changes allow us to establish that the receptors clustered by the haptenated lipid stimulate a cellular response.

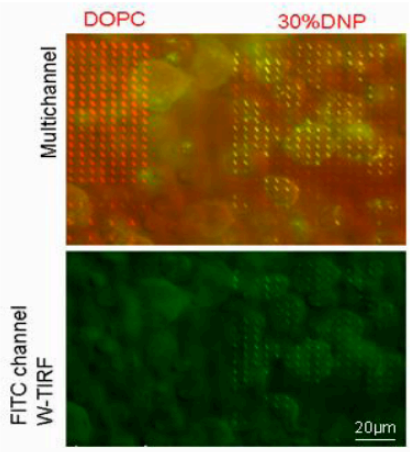

Figure 2. RBL-2H3 mast cells FcεRI receptor (labelled green with Alexa 488-IgE antibody) clustering on DNP patterns labelled red with rhodamine. Antibody-receptor clusters (green) are co-localized (in yellow) over the 30% patterned DNP ligand but not over the DOPC control.

In cases where this process is not yet clearly visible, the cell activation could be detected via staining with phosphotyrosine anti-body. One of the very early events following cross-linking of the IgE receptor is tyrosine phosphorylation brought about by the recruitment of various kinases to the cross-linked receptor. This can be monitored by immunofluorescence with an anti-phosphotyrosine antibody staining. To confirm that receptor-clustering, observed via live-cell imaging on DNP arrays, indeed triggers activation of intracellular signaling, we analyzed the total tyrosine phosphorylation at the DPN–Fc□RI clusters. RBL-2H3 mast cells were sensitized for 2 h with anti-DNP IgE, loaded onto the array, allowed to settle on the dots for different periods of time, and then fixed and stained with anti-phosphotyrosine antibody. Quantification of the phosphorylation events showed that approx. 2

min after cross-linking nearly 18% of the cells were activated in terms of positive phosphotyrosine signal rising to 45% at 5 min time point (Fig. 3).

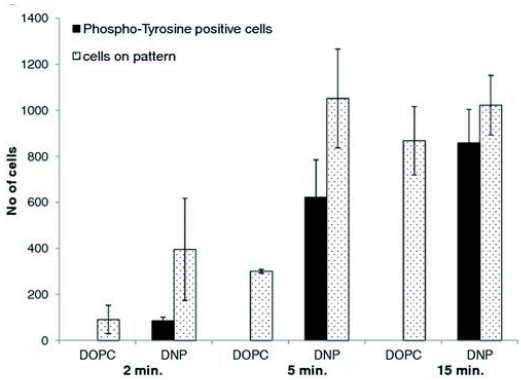

Figure 3. Activation of mast cells on DNP arrays. RBL-2H3 mast cells, sensitized for 2 h with anti-DNP IgE antibody, were loaded onto the samples, allowed to adhere, then fixed and stained with anti-phosphotyrosine antibody. Quantification of the number of activated cells on 10 mol% DNP and DOPC arrays followed over 15 min. Empty bars show the number of cells scored on the DOPC and DNP samples at the indicated time point. Filled bars show the number of activated cells where co-localization of the phosphorylated tyrosine signal over the DNP dot was detected.

In summary, DPN technique was shown to be feasible for patterning of the allergenic phospholipids on surfaces suitable for cell analysis. Patterning of the allergen arrays was performed on DPN 5000 platform. Mast cells activation on DPN patterned surfaces was analyzed by visualization of the receptor clustering and via biochemical staining with anti-phosphotyrosine antibody. Both performed at the facility using Nikon inverted fluorescence microscope.

3. Publications (please stick to the user guidelines for publications and acknowledgements on www.knmf.kit.edu)**:**

1. S. Sekula-Neuner , J. Maier, E. Oppong, A. C.B. Cato, M. Hirtz, H. Fuchs, Allergen Arrays for Antibody Screening and Immune Cell Activation Profiling Generated by Parallel Lipid Dip-Pen Nanolithography, **Small**, 2012 Feb 20;8(4):585-91.

2. A.C.B. Cato, E. Oppong and S. Sekula-Neuner, **2011**, Micropatterned surfaces as tools for the study of the rapid non-genomic actions of steroid receptors. Book chapter in Advances in Rapid Sex-Steroid Action, **Springer** Science+Business Media, ISBN: 978-1-4614-1763-7

4. Comments (max. 1.800 characters)**:**

Proposal 2009-001-000047

Patterning of biomolecules on a Surface Acoustic Wave biosensor using Dip Pen Nanolithography for multi-analyte detection of cardiac biomarkers

Electra Gizeli

Institute of Molecular Biology and Biotechnology (IMBB)
Heraklion, Crete
Greece

Note: *Please fill in this report form and save/print it as a PDF file, then upload it to the KNMF proposal submission system. A cover page containing proposal title, proposer name(s), and technologies selected will be added by the system. A link for the download of the complete report as a PDF file will be displayed in the system.*

Final Report

1. Project goals (max. 1.800 characters)**:**

The purpose of the visit is to implement the Dip Pen Nanolithography (DPN) facilities available in KIT to pattern protein molecules on a Surface Acoustic Wave (SAW) device in order to develop a multi-analyte biosensing chip for clinical applications. In particular the proposed system will be used for patterning stripes of different lipids with differently functionalized head groups for the subsequent acoustic detection of their specific interaction with proteins. The immobilization will take place on a novel SAW device platform based on microfluidics integration ("microfluidics-on-SAW", "µF-on-SAW").

The objectives targeted through this collaboration are the following:
• Adjustment of the multi-probe DPN setup of KIT, so as to be compatible with the biochips provided by IMBB-FORTH.
• Optimization of the conditions for efficient patterning of 4 different lipids on the sensor surface, in rectangular-shaped stripe arrays. The functionality of lipid head groups upon immobilization will be investigated via specific binding with their corresponding proteins. The parameters to be investigated are, in brief, the speed of direct DPN "writing" on the surface, the quantity of sample needed.
• Development of a method for efficient and accurate alignment of the plastic microfluidic module (provided by the IMBB-FORTH) on the sensor chip.
• Exploration of the detection limits and sensitivity of the µF-on-SAW after DPN patterning. It will be possible to define the minimum width of printed antibody rectangle that will give detectable signal upon the antibody interaction with its corresponding biomarker.

2. Project results (max. 7.000 characters + figures)**:**

- **Establishment of the DPN patterning methodology on µF-on-SAW; process characteristics:**

Each sensor domain (defined by the microfluidic channels) covers a surface area (1.76 mm^2) much larger than the tip array can pattern in a single step (0.073 mm^2). Therefore, it is impossible to achieve the desired pattern within each rectangular domain with a single pass of the probe array, but only through sequential steps. As the desired domain width is covered by the total writing width (910 µm) of the array, the latter does not need to be shifted laterally. On the other hand, as the array patterns 80 µm in the forward direction it has to be moved 20 times in order to complete the 1600 µm required (Fig. 1(b)). The result of these DPN steps reveals a patterned domain with indeed sharp edges at the borders (Fig. 1(c)). Sharp edges

are desirable for SAW sensors in order to minimize scattering of acoustic waves at the edges, and would be difficult to achieve with other microarray methods such as inkjet printing or micropin spotters. This procedure, though, is quite time-consuming because of the many small rectangles that should be added to complete the sub-area domain. Indicatively, approximately 10 min were required for an 80x910 μm^2 pattern area (at 5 μm^2/s average writing speed), while approximately three hours for one domain (without accounting for the time needed to frequently re-dip the tips in the ink wells due to the ink consumption and gradual decrease of pattern quality).

An alternative approach is based on the experimentally verified observation that, under particular humidity conditions, patterned lipids exhibit a rather fluidic behaviour and spread laterally on the surface to form supported lipid bilayers when hydrated on hydrophilic surfaces. This spreading effect is further enhanced by the non-covalent but physisorptive interaction between the lipids and the surface. Thus, a large lipid spot or "blob" for example can spread into a circular-shape, single- or multi-stack bilayer structure if the proper humidity conditions exist (there is usually a distribution of single- and multi-layer lipids, depending on the humidity and writing speed conditions). Following this approach, one entire sensor domain (Fig. 1(a)) was patterned within only 10 min as the detach-redip-reapproach procedure was repeated far less times than the previous option (two to six times, depending on the lipid case, see the following section for details). In addition, closely patterned blobs (as close as neighbouring tips allow) can spread enough as to merge and eventually form a uniform structure with linear, sharp edges parallel to the wavefront (Fig. 1(d)). In the present approach the lipid blob array was patterned in the same direction as the microchannel axis.

- **Patterning design and conditions:**

In order to pattern multiple species, the optimum patterning conditions (e.g., dipping and inking time, number of lipid blobs, etc.) were investigated for four different lipids: (i) a mixture of DOPC with DNP-lipids (10 mol%, doped with rhodamine); (ii) a mixture of DOPC with DOGS-NTA-Ni lipids (30 mol%, doped with fluorescein); (iii) a mixture of DOPC with biotin-lipids (4 mol%, doped with fluorescein) and (iv) fluorescein-labeled DOPC for control acoustic experiments. At 70% relative humidity lipids behave like liquid crystals and can coat tips once in contact with the ink well. For the first dipping, the tips were left for 25-30 min in contact with the ink, whereas the subsequent re-dippings lasted 5-7 min for DNP lipids, biotin-lipids and DOPC, and 10 min for NTA-Ni lipids, all taking place at 70% humidity. Right after inking the probes could write a uniform array of spots (or "blobs"). The writing duration was: 5 s for the DNP lipids and DOPC, 10 s for biotin lipids, and 15-20 s for NTA-Ni lipids, which is tremendously faster than the time required during the initial, direct-write patterning approach. This resulted in an overall printing time of 10 min (including the re-dip steps) for each domain. All different lipids are patterned on the same device, which is then stored at specific humidity conditions (overnight in desiccator at 25% humidity) so in principle they will not spread the same. Therefore, an investigation of the extent of spreading under the given storage humidity conditions was carried out and consequently a definition of the proper pattern design for each lipid type (i.e., how many arrays and how big spacing between them). After overnight storage in the desiccator the spreading was symmetrical on both sides of the initial array; the following values represent the spread pattern width (Fig. 2): (i) 950±50 µm for the DNP-lipids, (ii) 330±30 µm for the NTA-Ni lipids, (iii) 580±50 µm for the biotin lipids and (iv) 1050±50 µm for the DOPC lipids. Conclusively, the pattern of the entire SAW device included fourteen arrays all together (the following seven in duplicates symmetrically above and below the device horizontal axis) so that the entire 1600 µm acoustic aperture is covered with spread lipids: one DNP-lipid

array in µF4; three NTA-Ni-lipid arrays 300 µm apart in µF3; two biotin-lipid arrays 300-350 µm apart in µF2; one DOPC array in µF1 (Fig. 2).

- **Acoustic experiments:**

Once the patterned acoustic biochip was removed from the desiccator, the microfluidic module was assembled on it under microscope inspection. The biosensing experiments included the following injections (Fig. 3(a)): (i) PBS for rinsing excessive lipid multilayers until stabilization of the acoustic signal, (ii) BSA (1 mg/mL) as a blocking agent to prevent non-specific interactions of analytes and fill possible gaps (non-patterned regions) on the biosensor domain, followed by PBS wash step and (iii) analyte binding (100 µg/mL), followed by a PBS wash step. This procedure was repeated in all microchannels in a sequential way for the following analytes: anti-DNP IgE in µF4, interacting with DOPC/DNP lipids via an antibody–antigen-like interaction; his-tagged GFP in µF3, interacting with patterned DOPC/DOGS–NTA–Ni lipids via the histidine residues that bind a bivalent cation (e.g., Ni^{2+}) complexed with an N-nitrilotriacetate (NTA); streptavidin in µF2, interacting with patterned DOPC/biotin lipids via biotin–avidin bond; all three mentioned proteins sequentially in µF1, interacting with pure DOPC as control experiments. The acoustic response appears in the sensogram of Fig. 3(b), where only the specific interaction (and control) steps appear for simplicity reasons (the BSA blocking steps have been omitted). In previous experimental procedures with the µF-on-SAW where the receptor adsorption was accomplished in situ in a flow-through manner, the experimental time was longer by at least 30 min per microchannel, i.e., at least 2 h for the entire biochip. This duration was even longer when two-step immobilization was needed, namely, protein G and antibody, for the subsequent specific binding of cardiac markers. The interactions of anti-DNP IgE with DNP-lipids and streptavidin with biotin-lipids were clearly detected (DPh_{IgE}=2.5±0.3 deg, DPh_{strept}= 1.2±0.2 deg), whereas the his-GFP interaction with NTA-Ni lipids was slightly above the detection limit of the sensor ($DPh_{his\text{-}GFP}$=0.3±0.2 deg). Indicatively for the streptavidin interaction, Fig. 4(a-c) shows the fluorescent images of the patterned biotin-lipids (green), the bound streptavidin (red) and their overlap as a verification of the interaction. Control experiments were carried out in µF1 where DOPC with no functional groups was patterned. No phase change was detected after injection of anti-DNP IgE antibody, streptavidin, or his-GFP, implying negligible non-specific binding between the analytes and the lipids without functional head groups.

Karlsruhe Nano Micro Facility (KNMF)
Karlsruhe Institute of Technology (KIT)
Hermann-von-Helmholtz-Platz 1
76344 Eggenstein-Leopoldshafen
Germany

User Office
Phone: +49 (721) 608-3123
Fax: +49 (721) 608-6273
Email: knmf-useroffice@kit.edu
Web: www.knmf.kit.edu

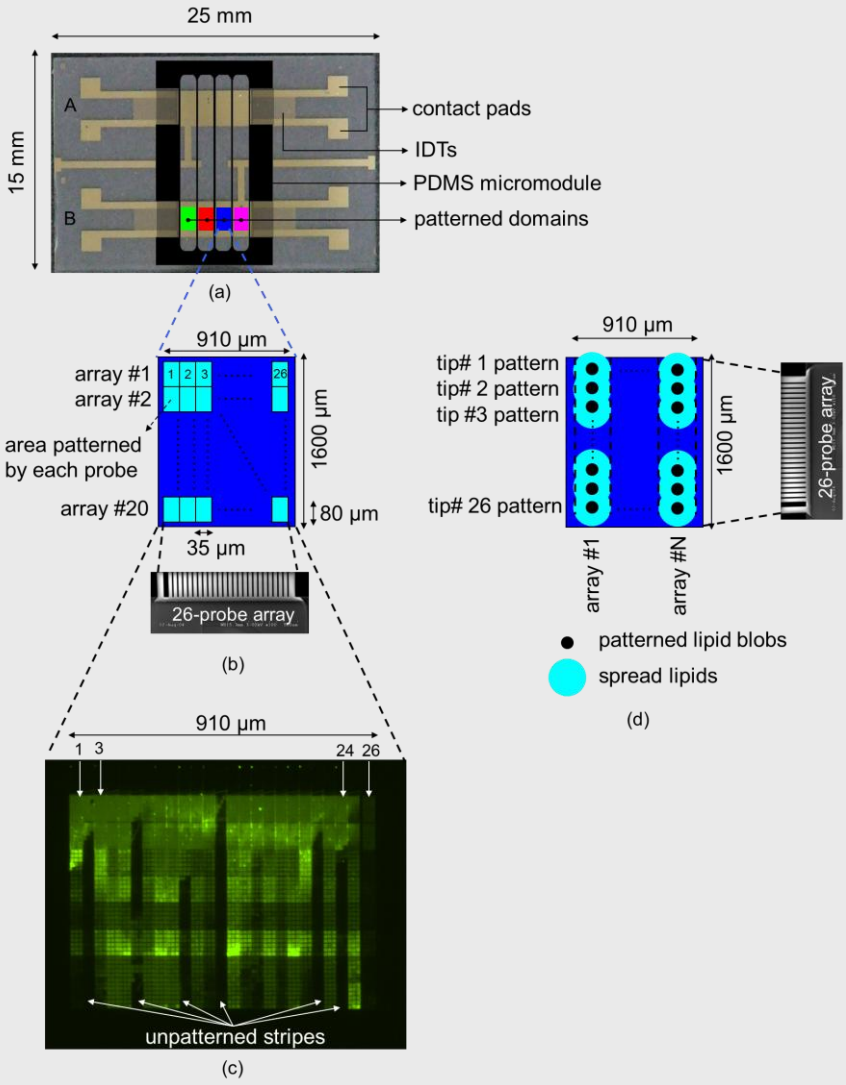

Fig. 1 (a) Real image of a dual-SAW-device biochip with the ”footprint” of the four microfluidic channels. (b) Zoomed domain with a schematic of the direct-write concept for filling the area with small lipid rectangles using the 26-probe array; each probe patterns one small rectangle. (c) Fluorescence microscopy image (4x) of biotin lipids patterned via the direct-write concept. (d) The patterning approach based on spreading of lipid blobs.

Karlsruhe Nano Micro Facility (KNMF)
Karlsruhe Institute of Technology (KIT)
Hermann-von-Helmholtz-Platz 1
76344 Eggenstein-Leopoldshafen
Germany

User Office
Phone: +49 (721) 608-3123
Fax: +49 (721) 608-6273
Email: knmf-useroffice@kit.edu
Web: www.knmf.kit.edu

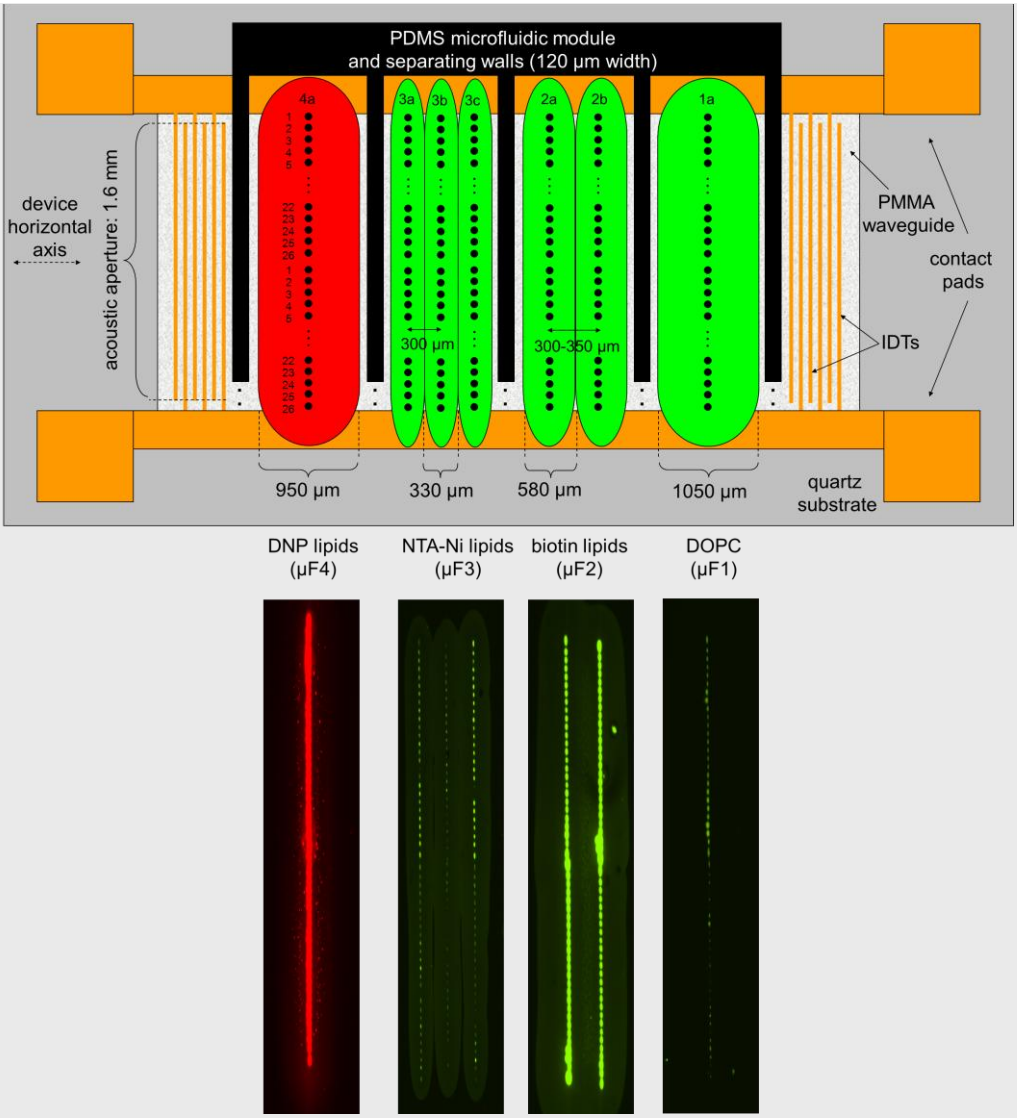

Fig. 2 Top: schematic of the design and arrangement of the four different lipid arrays on the sensor. Bottom: fluorescent microscope images (4x magnification) of the four patterned lipid types at the domains corresponding to the schematic of the top figure.

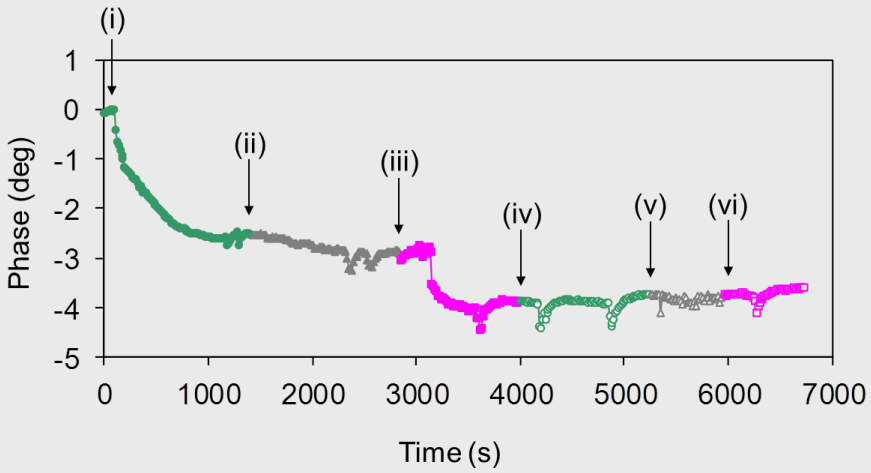

Fig. 3 Acoustic sensogram of the probed interactions between the patterned functionalized lipids with their corresponding biomolecule analytes: (i) anti-DNP IgE on DNP lipids, (ii) his-GFP on NTA-Ni lipids, (iii) streptavidin on biotin lipids, (iv) anti-DNP IgE on DOPC, (v) his-GFP on DOPC and (vi) streptavidin on DOPC. The concentrations in all cases were 100 µg/mL. BSA blocking and PBS rinsing steps are not marked for simplicity reasons. Some signal spikes are due to the syringe pump.

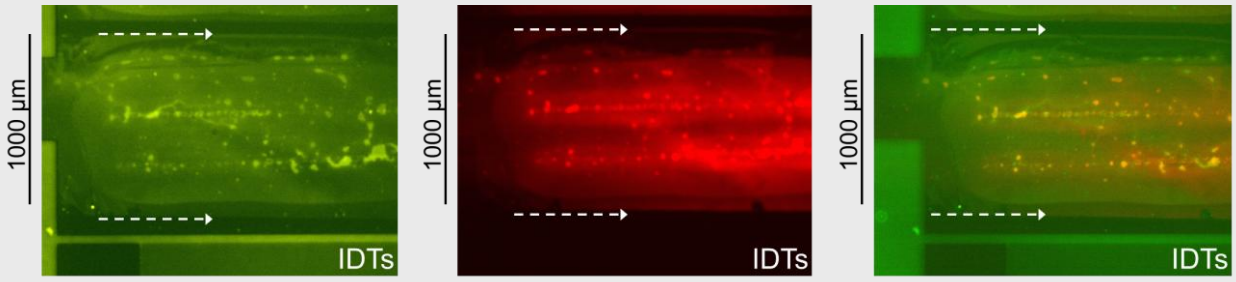

(a) (b) (c)

Fig. 4 Fluorescent microscope images of streptavidin (100 µg/mL) binding to patterned biotin lipids on the acoustic sensor: (a) biotin-lipids, (b) streptavidin and (c) overlay of (a) and (b). In all cases the images were taken at 4x magnification and the dashed lines indicate the borders of the area domain on the sensor, as defined by the microchannel walls.

3. Publications (please stick to the user guidelines for publications and acknowledgements on www.knmf.kit.edu):

K. Mitsakakis, S. Sekula-Neuner, S. Lenhert, H. Fuchs, E. Gizeli, "Convergence of Dip-Pen Nanolithography and acoustic biosensors towards a rapid-analysis multi-sample microsystem", Analyst 137 (2012) 3076

4. Comments (max. 1.800 characters)**:**

- The user had full access to the required facilities. The planning with the experts of the machine use was efficient and there were no delays. This was very important given the fact that the user stayed there for only 2 months.
- The project has led to a joint publication between IMBB-FORTH and KIT.
- Further prospects for joint projects have been opened, also in the field of cell detection (as DPN patterning can regulate cell adhesion and on the other hand SAW devices are suitable for cell detection).

Karlsruhe Nano Micro Facility (KNMF)
Karlsruhe Institute of Technology (KIT)
Hermann-von-Helmholtz-Platz 1
76344 Eggenstein-Leopoldshafen
Germany

User Office
Phone: +49 (721) 608-3123
Fax: +49 (721) 608-6273
Email: knmf-useroffice@kit.edu
Web: www.knmf.kit.edu

Proposal 2009-002-000119

Biomedical Phase-Contrast Imaging at Elevated X-Ray Energies

Franz Pfeiffer

Technische Universität München
Garching
Germany

Final Report

1. Project goals (max. 1.800 characters):

This proposal is a **continuation and long-term extension** of a previously submitted KNMF proposal (no. 5068), within which we received grating structures that were successfully used for first phase-contrast X-ray imaging experiments concerning the feasibility of small-animal imaging applications in April 2009 at ESRF [publication in preparation]. While the previous proposal specifically targeted micro-structures for low-energy phase-contrast microCT applications (15-35 keV), the present Long-Term Proposal (LTP) will focus on **structures for higher energy** x-ray phase-contrast radiography and tomography applications. The structures will be tested and used at synchrotron radiation sources (ESRF/ Grenoble) and dedicated lab-based x-ray infrastructures (TU Munich), which are currently in construction.

Goals. The overall intention of this long-term proposal was the development, characterization and implementation of grating structures which open the future translation of x-ray phase-contrast imaging to clinical CT applications. Mainly two goals were adressed with this proposal:
- **Goal 1.** Characterization and experimental implementation of grating structures for clinically relevant x-ray energies (for future human CT applications) of in the **high energy range of 80-120 keV** using synchrotron x-ray sources.
- **Goal 2.** Implementation of a compact grating geometry into a **first pre-clinical small-animalphase-contrast CT scanner** with rotating gantry and testing of highly divergent fan- and cone-beam CT setups.

2. Project results (max. 7.000 characters + figures):

Goal 1. Quantitative grating-based X-ray phase contrast tomography at 82 keV

Purpose. In the past few years grating-based X-ray phase contrast imaging has increasingly aroused interest as the method has been successfully adapted to work with laboratory X-ray sources. The high potential to enormously improve the soft-tissue contrast compared to standard absorption-based tomography has been multiply demonstrated at synchrotrons and at laboratory-based setups. Due to certain requirements on the gratings, the examinations have so far mostly been limited to X-ray energies below 35 keV. However, advances in the grating manufacturing process give access to higher energies and open up new possibilities to apply the technique in industrial testing or medical imaging.
Method. A grating interferometer measures a small local refraction signal of X-rays that is correlated to the gradient of the phase shift caused by an object [7]. A phase grating creates an interference pattern with periodic intensity modulations at certain distances downstream. An object in the beam causes variations of these intensity modulations that can be resolved with a conventional X-ray detector by using an analyzer grating.
The conventional absorption signal is recorded at the same time and using a reconstruction algorithm based on filtered backprojection, quantitative information on the attenuation coefficient μ and the

refractive index decrement δ distribution within the object can be obtained. The performance of the grating interferometer regarding the phase information and the resulting image quality strongly depends on the efficiency of the analyzer in absorbing the incident X-rays. The grating structures are made of gold, but grating periods of only a few micrometers still demand very high aspect ratios when moving to higher X-ray energies. Recently, the manufacturing of gratings with heights of more than 100 µm at an aspect ratio of up to 40 keV became feasible and guarantee a high absorption above the absorption edge of gold (80.72 keV).

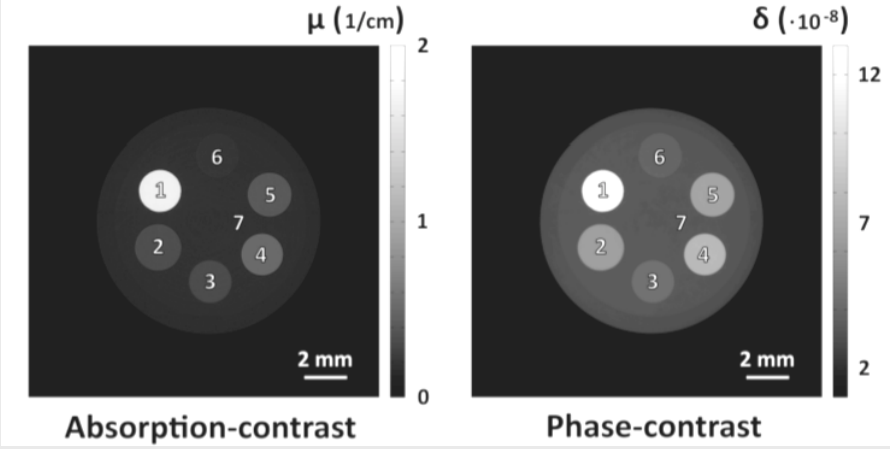

Fig. 1: *Reconstructed slices of the phantom in phase (right) and absorption contrast (left) from measurements at the ESRF at 82 keV. [1: Titanium, 2: Teflon, 3: PV-C, 4: Aluminum, 5: Glass, 6: PMMA, 7: Cupper, 8: Bronze, 9: Water].*

To explore the image formation process and to demonstrate the quantitativeness of the method at high energies, a phantom consisting of well-defined solid materials (PMMA, teflon, glass, PV-C, Ti, Al, Cu) covering a wide range of densities as well as electron densitites has been scanned with high resolution (pixel size: 8 µm) at an X-ray energy of 82 keV at the beamline ID19 of the European Synchrotron Radiation Facility (ESRF, Grenoble, France).

Material	μ (1/cm)	Δμ (1/cm)	μ_{theo} (1/cm)	δ (·10⁻⁸)	Δδ (·10⁻⁸)	δ_{theo} (·10⁻⁸)	SNR_δ	SNR_μ	SNR_δ/SNR_μ
Titanium	1,676	0,009	1,738	12,75	0,03	12,79	442,7	192	2,31
Teflon	0,343	0,007	0,356	6,52	0,02	6,52	146,4	20,6	7,11
PV-C	0,321	0,008	0,314	4,43	0,02	4,43	46,7	17,8	2,62
Aluminum	0,517	0,008	0,527	7,94	0,02	7,95	214	42,9	4,99
Glass	0,411	0,007	0,419	6,8	0,02	6,79	159,6	29,3	5,45
PMMA	0,207	0,007	0,207	3,97	0,02	3,96	25,2	3,1	8,13
Water	0,182	0,008	0,182	3,44	0,02	3,43	-	-	-

Table 1: *Analysis results of the attenuation coefficients, refractive index decrements and signal-to-noise-ratios with respect to water for all materials used in the phantom. Theoretical values have been calculated based on NIST databases.*

Results. The attenuation coefficients μ and the refractive index decrements δ have been calculated from the reconstructed image data. In both cases 100 slices have then been averaged to one final image (Figure 1) to finally specify the coefficients of the materials in 50x50 pixel sized regions-of-interest. In addition, the signal-to-noise-ratios with respect to water have been determined for all materials.
Conclusions. By now grating-based X-ray phase contrast imaging at 82 keV is practicable and offers the known advantages over the conventional absorption-based X-ray imaging as better image quality and the quantitative determination of the refractive index decrements δ in addition to the attenuation coefficients μ. These results consolidate the high expectations on the method for various applications in the future.

Goal 2. Implementation of gratings into first a preclinical small-animal x-ray phase-contrast CT scanner

The prototype scanner consists of a standard rotating micro-CT gantry (with x-ray source, specimen opening, and a flat-panel detector) and comprises additionally a three-grating Talbot-Lau interferometer to extract multimodal x-ray projection images. This allows the system to deliver conventional transmission images (TI), differential phase-contrast images (PCI), and dark-field scattering images (DFI). In the first step of the development, the compact gantry was built and operated stand-alone in rotating sample mode. A previous and preparatory performance study was conducted, which showed that the gantry performs well and quantitatively accurately.

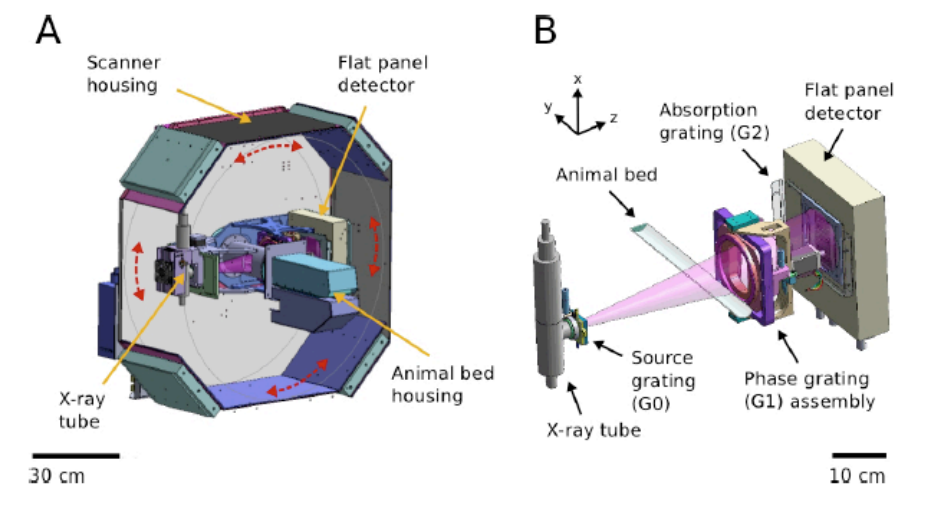

Fig. 2: *Technical drawing of the first preclinical phase-contrast CT scanner. (A) Scanner housing with rotating gantry (gantry movement indicated by red arrows). The gantry contains the x-ray tube on one end and the at panel detector on the other end and is oriented horizontally in the displayed view. The overall scanner housing dimensions are approximately 95 cm in width, 100 cm in height, and 85 cm in depth. (B) Three-grating interferometer, which is contained within the gantry [Tapfer et al, PNAS, 2012].*

In the final configuration presented here, the gantry is now implemented into a typical preclinical micro-CT scanner housing, featuring an animal bed, animal monitoring and gas anesthesia with enlarged field of view (FOV) and a flat-panel imaging detector. In order to manipulate the grating positions with high precision for alignment, several motors are installed to rotate, tilt and shift the gratings. Fig. 2 shows a schematic 3D view of the scanner and schematic drawing of the grating interferometer.

To asses how the preclinical scanner and adaptive differential phase recovery method perform in CT measurements, two samples were measured. The tomographic reconstructions in absorption and phase contrast were then evaluated in terms of image quality and reconstruction accuracy. The first sample is a well defined fluid phantom, which was used for the quantitative reconstruction analysis. The second sample was formalin fixated porcine rind, which consists of several layers of soft-tissue. This sample was used for the benchmarking of the soft-tissue enhancement capabilities of the presented scanner.

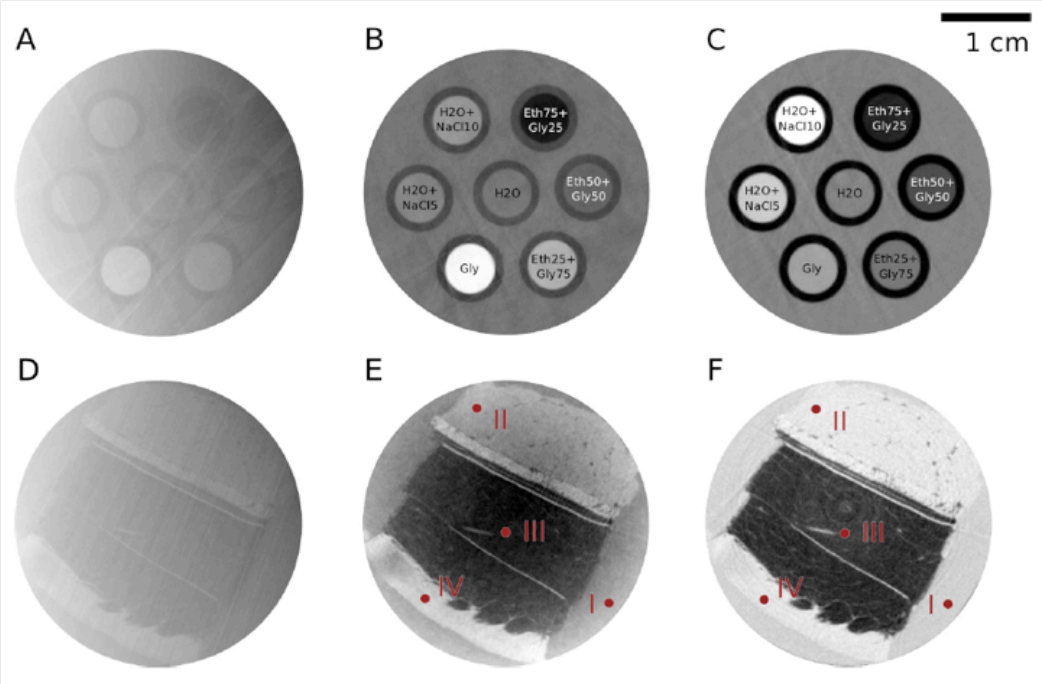

Fig. 2: *Quantitative reconstructions of the fluid phantom (top) and the porcine rind sample (bottom). To reduce image noise, the reconstructions were averaged over 30 adjacent slices for the fluid phantom and over 5 slices for the porcine rind. (A) and (D) Phase contrast without adaptive differential phase recovery. (B) and (E) Phase contrast with adaptive differential phase recovery. (C) and (F) Attenuation contrast. Labels: Fluid phantom (top): H2O+NaCl10 - Water and 10% NaCl solution, Eth25Gly75 - 25% Ethanol and 75% Glycerol solution; other substances are named accordingly. Porcine rind (bottom): (I) formalin background, (II) muscle, (III) two layers of subcutis (divided by connective tissue), (IV) dermis/epidermis [Tapfer et al, PANS, 2012].*

Fig. 3 shows the tomographic reconstruction of the two samples: (A) and (D) phase contrast without applying the adaptive phase recovery method (ADPR) method, (B) and (E) phase contrast using the aforementioned ADPR method, (C) and (F) attenuation contrast. From this figure the importance of accurate phase recovery is directly noticeable and one can conclude that the method performs well in the sense that no artifacts remain in the corrected reconstructions [(B) and (E)].
In order to assess whether the tomographic reconstruction also yields quantitatively accurate results regarding the linear attenuation coefficient and decrement of the refractive index, the mentioned phantom study was evaluated quantitatively. A quantity derived from conventional CT scans, which is commonly used in clinical CT scanners, is the Hounsfield unit. A corresponding quantity can be defined for phase images. To discriminate between these two Hounsfield units, the conventional attenuation Hounsfield units are referred to as HU-A and the phase Hounsfield units as HU-P. The mentioned phantom comprised seven polyethylene tubes that were embedded in a water-filled plastic container of approximately 3 cm in diameter. The individual tubes were filled with chemically pure liquids and mixtures with salts to span a range of Hounsfield units in absorption and phase contrast. To evaluate the accuracy of the experimentally measured HU-A and HU-P, theoretical Hounsfield units were calculated for comparison.

Region of interest	HU-A(m)	HU-A(c)	HU-P(m)	HU-P(c)
Fluid Phantom				
Ethanol (75%)+ Glycerol (25%)	-251 ± 9	-260	-112 ± 6	-114
Ethanol (50%)+ Glycerol (50%)	-157 ± 9	-161	-17 ± 6	-18
Ethanol (25%)+ Glycerol (75%)	-41 ± 10	-39	99 ± 7	100
Glycerol	94 ± 12	105	236 ± 8	235
H2O + NaCl (5%)	230 ± 14	230	32 ± 7	29
H2O + NaCl (10%)	466 ± 15	463	61 ± 6	57
H2O	0 ± 14	0	0 ± 7	0
Porcine rind				
Formalin background (I)	-9 ± 7	-	-37 ± 7	-
Muscle (II)	31 ± 7	-	12 ± 6	-
Subcutis (III)	-251 ± 11	-	-198 ± 7	-
Dermis/Epidermis (IV)	25 ± 9	-	57 ± 8	-

Table 2: *Quantitative analysis of the performed CT scans of the fluid phantom (top) and porcine rind sample (bottom). Measured (m) and calculated (c) attenuation (HU-A) and phase (HU-P) Hounsfield units are quoted for different region of interests (ROI). Fluid phantom (top): The HU data was extracted from a ROI analysis covering the central 80 % of the individual substance containers of 30 averaged adjacent transverse CT slices. The standard deviation is quoted as error. Porcine rind sample (bottom): The measured Hounsfield units of a ROI analysis (region marked with red circle in Fig. 3) of the different tissue composites and formalin background are quoted. The standard deviation is quoted as error.*

Table 2 contains the measured and calculated HU-A and HU-P for all substances in the phantom. From this table it is obvious that calculated and measured HU data agree well, the maximum deviation is 4 HU for phase and 11 HU for absorption. This means that the proposed ADPR method does allow for quantitatively accurate CT reconstruction of Hounsfield phase and attenuation units.

The potential of the phase-contrast scanner for biomedical imaging was examined by scanning a porcine rind sample as it contains different layers of soft-tissue. For a quantitative comparison of both contrast modes, Hounsfield units for the different types of tissues were determined at the indicated positions in Fig. 3 (red colored circles, 20 pixel in diameter) and are also quoted in Table 2. Whereas the subcutis (III) can be identified well in both the phase contrast image (F) and absorption contrast image (E), especially the muscle (II) and dermis / epidermis (IV) can be more clearly distinguished from the embedding medium formalin (I) and in particular from one another in phase contrast. This visual observation is also reflected in the quantitative HU data in Table 2. As very clearly visible for the fluid phantom study, also for biological tissues, absorption and phase contrast are complimentary. When comparing attenuation and phase contrast, it should be noted that for conventional attenuation contrast no gratings and in particular no analyzer grating G2, which absorbs approximately half of the x-ray photons and hence decreases counting statistics, are needed. However, grating-based phase contrast on the other hand makes two perfectly registered and complimentary images available in one CT scan.

In order to take the next step towards a translation of x-ray phase contrast to clinical CT applications, we developed a first preclinical CT scanner. The main challenge in the transition from bench-top systems with rotating sample to a rotating gantry scanner were phase artifacts that are caused by minute changes in the grating alignment during gantry rotation. Using the proposed adaptive differential phase recovery method, these artifacts could be addressed. This correction procedure was applied to all differential phase projection images in the CT scan of the fluid phantom and a quantitatively accurate reconstruction of attenuation and phase Hounsfield units was demonstrated. This implies that phase artifacts, which were caused by gantry rotation in the differential phase projection images were accurately corrected and one can conclude that the presented procedure performs robust. Moreover, we have demonstrated clearly the general feasibility of phase-contrast in a preclinical scanner. The now available complimentary information in absorption and phase contrast images does imply great potential for improved diagnosis and therapy response monitoring in preclinical imaging.

We believe that this work represents a crucial milestone in translating x-ray phase-contrast imaging from proof-of-principle experiments to preclinical imaging applications on small-animal models (in the mid-term future) and finally to human phase-contrast CT applications (in the long-term future).

3. Publications (please stick to the user guidelines for publications and acknowledgements on www.knmf.kit.edu):

Publications (based on KNMF proposals, **with** KIT co-author):

1. Tapfer, I. *et al.* First results from a preclinical small-animal phase-contrast CT scanner with a rotating gantry. *Proceedings of the National Academy of Sciences*, accepted (2012).
2. Zanette, I. *et al.* Trimodal low-dose X-ray tomography. *Proceedings of the National Academy of Sciences* **109**, 10199–10204 (2012).
3. Potdevin, G. *et al.* X-ray vector radiography for bone micro-architecture diagnostics. *Phys. Med. Biol.* **57**, 3451–3461 (2012).
4. Jensen, T. H. *et al.* X-ray phase-contrast tomography of porcine fat and rind. *Meat Science* **88**, 379–383 (2011).
5. Tapfer, A. *et al.* Development of a prototype gantry system for preclinical x-ray phase-contrast computed

tomography. *Med. Phys.* **38**, 5910 (2011).
6. Herzen, J. *et al.* X-ray grating interferometer for materials-science imaging at a low-coherent wiggler source. *Rev. Sci. Instrum.* **82**, 113711 (2011).
7. Jensen, T. *et al.* Directional x-ray dark-field imaging of strongly ordered systems. *Phys. Rev. B* **82**, 1–8 (2010).
8. Herzen, J. *et al.* X-ray grating interferometer for imaging at a second-generation synchrotron radiation source. *Proc. SPIE* **7804**, 780407 (2010).
9. Kenntner, J. *et al.* Front- and backside structuring of gratings for phase contrast imaging with x-ray tubes. *Proc. SPIE* **7804**, 780408 (2010).
10. Weitkamp, T. *et al.* Recent developments in x-ray Talbot interferometry at ESRF-ID19. *Proc. SPIE* **7804**, 780406 (2010).

Publications (based on KNMF proposals, **without** KIT co-author):

1. Hahn, D. *et al.* Numerical comparison of X-ray differential phase contrast and attenuation contrast. *Biomed Opt Express* **3**, 1141–1148 (2012).

4. Comments (max. 1.800 characters):

none

Proposal 2009-002-000126

Fabrication of RF MEMS Circuits

Melissa Schaffer

TRLabs
Saskatoon, Saskatchewan
Canada

Note: *Please fill in this report form and save/print it as a PDF file, then upload it to the KNMF proposal submission system. A cover page containing proposal title, proposer name(s), and technologies selected will be added by the system. A link for the download of the complete report as a PDF file will be displayed in the system.*

Final Report

1. Project goals (max. 1.800 characters):

Ever smaller radio frequency (RF) wireless transceivers and sensors are challenging traditional technologies for realizing high performance passive RF devices such as inductors and capacitors, and especially the integration of these into compact front-end circuits such as filters, couplers, and feed structures. Passives can account for a large percentage of components used in mobile devices. RF microstructures can provide performance improvements, reduced size and weight, and even radically different transceiver architectures. RF reactive device microstructures can realize highly integrated reactive lumped element circuits to replace bulky transmission line versions or provide additional capabilities. Popular fabrication approaches are often based on surface micromachining, which tends to constrain devices to thin layer planar geometries. A less common approach is to exploit the vertical dimension, which can provide greater levels of integration and improved performance. Deep X-ray lithography (XRL) produces vertical structures, which enables reduction of the lateral footprint of RF reactive devices, providing better performance at higher frequencies. A compelling application for these devices is for implementing highly integrated "all-MEMS" reactive lumped-element-based circuits to replace bulky transmission-line versions. With switched or variable reactance elements, lumped-element circuits could be made tunable. Effective integration of both capacitive and inductive reactive elements together to form complex circuits without sacrificing performance is increasingly advantageous for realization of compact wireless and sensor components.

The main goal of the project was to further demonstrate the potential of the "all-MEMS" reactive lumped element-based circuit concept, through improvements to lumped element performance and processes and the application of these to new circuits such as filters and couplers. A secondary goal was to improve feature variation in example circuit elements to reduce the RF performance variation.

2. Project results (max. 7.000 characters + figures):

Inductive [1] and capacitive [2] reactive lumped elements were further developed, and these structural features incorporated together to propose new RF reactive lumped element-based filter [3] and coupler [4] circuits operating in the 5 GHz and 11 GHz regions.

The couplers are 4-port circuits, and are structurally and functionally the most complicated circuits developed to date which have been 2-port circuits. Processing for RF applications involved applying a thick X-ray sensitive polymer layer on top of a substrate for exposure. To fabricate metal devices/circuits, a microwave substrate was coated with a thin metal seed layer under the thick polymer layer, then the exposed and developed polymer layer was used as a sacrificial electroforming template for growing tall metal structures (in nickel, and also for the first time in gold) from the seed layer into the voids. The polymer template was removed, then finally the metal seed layer was etched away to electrically isolate the metal conductors. Fig. 1 shows some of the latest capacitive and inductive features with improved performance [5]. Devices feature impressive vertical structure, including a 54:1 aspect ratio, 1.3µm-wide cantilever gap (W_c) in 70 µm-thick metal (Fig. 1a.). A 0.6 pF capacitor has Q-factors of 95 at 5.6 GHz and 214 at 3.5 GHz, and a structurally compatible 1.2 nH loop inductor has Q-factor of 47 at 6.8 GHz and self-resonant frequency of 18.8 GHz. In addition, a procedure was developed (VM-TEST) [6] for extracting metal material properties for vertically oriented structures for compact RF circuits using electrostatically actuated cantilever structures.

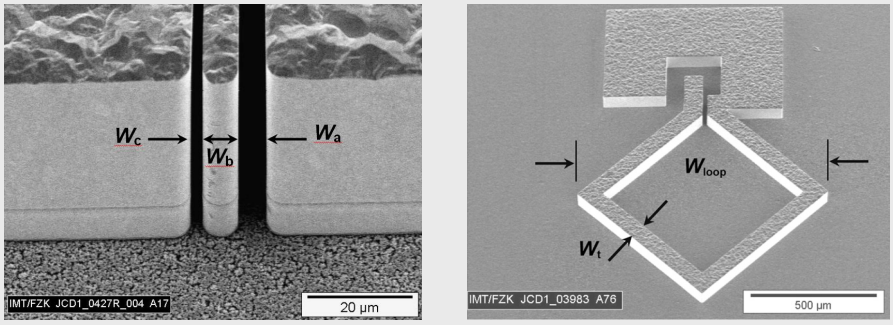

(a.) (b.)

Fig. 1: Thick-metal RF MEMS capacitive and inductive features built with deep XRL, with improved processing and performance (70 µm thick, nickel structure) [5]: (a.) Inclined view (tip) of cantilever beam and air gaps (W_c = 1.3 µm, capacitance gap aspect ratio 54:1 in nickel, 77:1 in PMMA prior to electroplating); (b.) inclined view of structurally compatible 1-loop inductor.

These tall-metal reactive device features have been extended successfully to demonstrate complicated lumped-element functional circuits such as filters and couplers [5]. These are entirely new circuit structural architectures with high performance and compact size. For instance, we have integrated vertically oriented capacitive and inductive structural features in a single thick (> 0.25 mm) metal layer process to realize compact lumped element low-pass filter and 4-port quadrature coupler microstructures (Fig. 2) [5] operating at frequencies up to 12 GHz, that are a fraction of the size of their traditional distributed counterparts. Using similar metal processing, we have also demonstrated thick metal microstrip diplexers [7] based on compact folded half wavelength resonators, and have implemented tall conductor (250 µm) coplanar waveguide circuits such as a wideband bandpass filter with compact unit cells based on the electromagnetic bandgap concept [8].

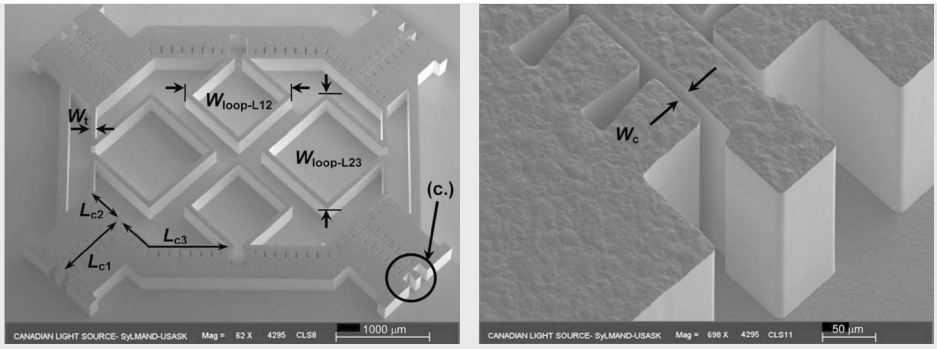

(a.) (b.)

Fig. 2: Fabricated 5.6 GHz, lumped element 3-dB quadrature coupler (265 µm thick, nickel structure): (a.) structure overview; (b.) magnified view of port and capacitance gap (W_c = 11.5 µm, gap aspect ratio 23:1 in 265 µm nickel, 30:1 in 340 µm PMMA).

A persistent problem with these tall RF devices and circuits which can limit their practical usefulness is metal height homogeneity in the electroplated structures. Metal heights can easily vary by ±20%, and are difficult to control due to different electroplating growth rates with a wide variety of feature sizes. Metal height variation makes devices difficult to interface and can result in large performance variations in the circuit.

Mechanical lapping and polishing, with chemical electropolishing was investigated as an effective method of planarizing the surface of tall electroplated nickel microstructures for RF applications [9]. Plastic deformation of the metal during mechanical lapping and polishing results in metal smearing over the supporting PMMA electroplating template, resulting in burrs. In the case of RF structures, small capacitive gap features completely smear over, resulting in electrical short circuits. Fig. 3 demonstrates the effects of the process on a capacitive gap circuit feature (nom. 11.5 µm width, Ni on Alumina) [10]. The entire sequence is performed with the PMMA template in place (removed here for imaging).

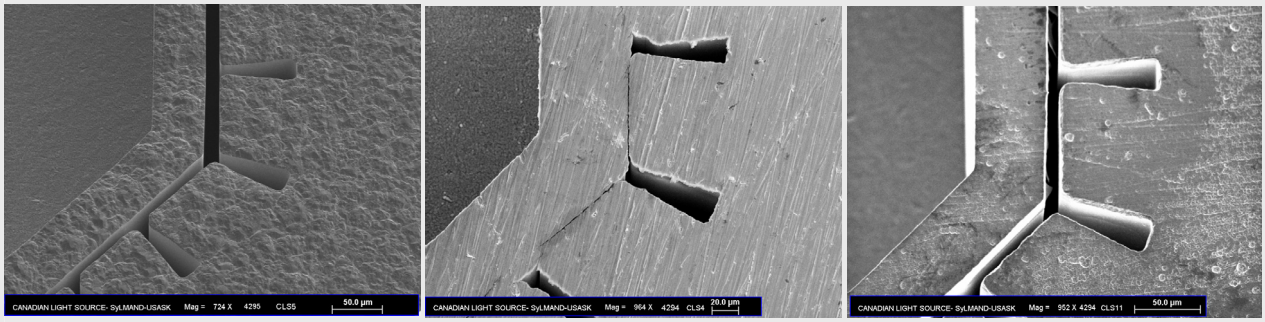

(a.) (b.) (c.)

Fig. 3: Lapping, polishing and electropolishing process [10]: (a.) Unpolished gap feature (ave. 265 µm Ni height); (b.) Gap feature after mechanical lapping/polishing with complete metal smearing shorting the gap (ave. 220 µm Ni height); (c.) Gap feature after electropolishing with reopened gaps (ave. 220 µm Ni height).

Karlsruhe Nano Micro Facility (KNMF)
Karlsruhe Institute of Technology (KIT)
Hermann-von-Helmholtz-Platz 1
76344 Eggenstein-Leopoldshafen
Germany

User Office
Phone: +49 (721) 608-3123
Fax: +49 (721) 608-6273
Email: knmf-useroffice@kit.edu
Web: www.knmf.kit.edu

The effects of planarization on a fabricated 12 GHz 3rd order Chebyshev lowpass filter were demonstrated [10] on a 220 µm (Ni on Alumina) structure, with capacitance gap widths of 8 µm (28:1 aspect ratio). Increased average electroplated metal height to 280 µm resulted in an additional 0.4 dB of pass-band ripple, which was mostly removed from the response after the planarization procedure.

3. Publications (please stick to the user guidelines for publications and acknowledgements on www.knmf.kit.edu)**:**

[1] E. Gono-Santosa, D. M. Klymyshyn, D. Haluzan, M. Börner, S. Achenbach, J. Mohr, "RF MEMS Inductors Fabricated Using Deep X-ray Lithography", *Proc. High Aspect Ratio Micro-Structure Technology (HARMST 2009)*, Saskatoon, Canada, June 2009, pp. 197-198.

[2] D. M. Klymyshyn, D. T. Haluzan, M. Börner, S. Achenbach, J. Mohr, T. Mappes, "High aspect ratio vertical cantilever RF-MEMS variable capacitor," *IEEE Microwave & Wireless Component Letters*, vol. 17, no. 2, pp. 127-129, Feb. 2007.

[3] E. Gono-Santosa, D. M. Klymyshyn, M. Börner, D. Haluzan, S. Achenbach, J. Mohr, "High-Aspect-Ratio RF Low-pass Filter Fabricated Using Deep X-ray Lithography", *Proc. High Aspect Ratio Micro-Structure Technology (HARMST 2009)*, Saskatoon, Canada, June 2009, pp. 199-200.

[4] M. Schaffer, D. M. Klymyshyn, "High Aspect Ratio Microstructure Coupler Concept," *Proc. IASTED Int. Conf. Antennas, Radar, Wave Propagation (ARP2009)*, Banff, July 2009, pp. 113-117.

[5] D. M. Klymyshyn, M. Börner, D. Haluzan, E. Gono Santosa, M. Schaffer, S. Achenbach, J. Mohr, "Vertical High-Q RF-MEMS Devices for Reactive Lumped Element Circuits", *IEEE Trans. on Microwave Theory and Techniques*, Vol. 58, No. 11, Nov. 2010, pp. 2976-2986.

[6] D. T. Haluzan, D. M. Klymyshyn, S. Achenbach, M. Börner, J. Mohr, "VM-TEST: Mechanical property measurement using electrostatically actuated vertical MEMS test structures fabricated in thick metal layers," *Microsystem Technologies*, Vol. 18, No. 4, 2012, pp. 443-452.

[7] H. C. Jayatilaka, D. M. Klymyshyn, M. Börner, J. Mohr, "Compact Thick Metal Diplexer with Multi-Coupled Folded Half Wavelength Resonators," *Progress In Electromagnetics Research C (PIERC)*, Vol. 18, 2011, pp. 1-8.

[8] D. M. Klymyshyn, H. C. Jayatilaka, M. Börner, J. Mohr, "High-Aspect-Ratio Coplanar Waveguide Wideband Bandpass Filter With Compact Unit Cells," *IEEE Trans. on Microwave Theory and Techniques*, Vol. 57, No. 11, Nov. 2009, pp. 2753-2760.

[9] S. Kissling, K. Bade, M. Börner, D. M. Klymyshyn, "Electropolishing as a method for deburring high aspect ratio nickel RF MEMS," *Microsystem Technologies*, Vol. 16, No. 8-9, August 2010, pp. 1361–1367.

[10] D. M. Klymyshyn, M. Börner, S. Kissling, D. Haluzan, G. Wells, M. Schaffer, E. Gono-Santosa, S. Achenbach, P. Meyer, J. Mohr, "Mechanical Planarization with Electropolishing to Improve the Performance of High-Aspect-Ratio RF MEMS Circuits", *Proc. High Aspect Ratio Micro-Structure Technology (HARMST 2011)*, Hsinchu, Taiwan and Himeji, Japan, June 2011, (2 pp.)

4. Comments (max. 1.800 characters)**:**

We have demonstrated the feasibility of implementing reactive lumped-element-based circuits using a thick single-metal-layer deep XRL process to fabricate complicated circuits. The key to this was the integration of vertically oriented capacitive and inductive loop structural features in a single thick (> 0.25 mm) metal layer process. The circuits typically are a fraction of the size of their traditional distributed counterparts.

Though demonstrating impressive performance and structure, improvements can be made. Some fabrication issues remain, for instance electroplated metal height homogeneity which limits performance and practical implementation. Good progress has been made with planarization techniques, however an additional problem with these circuit microstructures has been short circuits in the tall capacitive gap structures following planarization. Reduction in the lateral circuit size is also feasible, and could dramatically increase the useful operating frequency, possibly by a factor of 2 to the 15-20 GHz range. These new circuits could potentially have best-in-class performance.

D. M. Klymyshyn

Proposal 2009-002-000137

Fabrication of Thick Polymer-based Antenna Structures

David Klymyshyn

University of Saskatchewan
Saskatoon SK
Canada

Note: *Please fill in this report form and save/print it as a PDF file, then upload it to the KNMF proposal submission system. A cover page containing proposal title, proposer name(s), and technologies selected will be added by the system. A link for the download of the complete report as a PDF file will be displayed in the system.*

Final Report

1. Project goals (max. 1.800 characters)**:**

One of the biggest obstacles to further miniaturization of RF wireless devices is the antenna, often based on thin metallic microstrip "patch" structures, which can occupy large lateral areas. Dielectric resonator antennas (DRAs), on the other hand, are three dimensional structures with lateral dimensions that can be several times smaller than traditional planar patches and offer superior performance including very high radiation efficiency and large bandwidth for miniaturized wireless and sensor applications. Ceramic-based DRAs have been mostly limited to simple structures (such as rectangular and circular shapes) since the hardness of ceramic requires diamond cutting tools which restricts their widespread use for high volume commercial applications.

A new approach to facilitate the adoption of DRAs for commercial applications is to use polymer-based materials. The natural softness of polymers will dramatically simplify fabrication and their low relative permittivity will further enhance the impedance bandwidth of the DRAs. Various polymer types with special characteristics could be used to fulfill the requirements of particular applications or achieve certain benefits. Another advantage derived from this approach is the capability of mixing polymers with a wide variety of fillers to produce composite materials. If properly combined and designed, these engineered composite materials can be developed to meet unique and custom performance requirements not achievable by traditional materials.

The main goal of the project was to demonstrate the potential of deep X-ray lithography (XRL) for lithographic-based fabrication of DRA structures in thick polymer and ceramic-polymer materials, and to develop novel proof-of-principle compact antenna structures with high RF performance at microwave frequencies.

2. Project results (max. 7.000 characters + figures)**:**

Instead of machining hard ceramics, fabrication of DRA structures was demonstrated for the first time with direct deep XRL, for polymer-based antenna structures with different portions of ceramic content. To produce successful and viable antenna structures, three different methods were pursued, using both positive and negative tone resists.

In the first method the structures were lithographically fabricated avoiding an intermediate molding step using SU-8 as a photosensitive resist filled with fine ceramic powder with particles in the submicron range. In the second and third methods a polymethylmethacrylate (PMMA) mold was first fabricated by XRL, and then SU-8/MMA mixed with the high ceramic powder content was injected into the mold. In these methods a final step of crosslinking for SU-8 and polymerization for MMA was also required.

Optimized fabrication parameters allowed the production of high quality antenna structures as thick as 2.3 mm. Pure thick photoresists and photoresist-ceramic microcomposites were exposed and developed, released from a sacrificial substrate, and the patterned structures attached to a microwave substrate and used directly as dielectric devices. These "soft" X-ray sensitive photoresist-ceramic composite materials have dielectric properties which make them suitable for direct use as DRAs [1, 2], and without sintering [3], which would limit achievable fine-feature geometries. DRAs of 2 mm thickness fabricated by direct deep X-ray exposure have been demonstrated (see Fig. 1a). An alternate approach fabricates pure photoresist frames by deep XRL, then injects polymer-ceramic composite into the frames to form antenna elements (Fig. 1b). An element with 32% impedance bandwidth and 4.9 dBi gain at 26.1 GHz, and stable radiation patterns with low cross-polarization has been demonstrated [4]. Deep XRL also enables fabrication of structures with fine features (Fig. 1c, 1.8 mm tall fractal structure) [5] and complex geometries such as array structures [6] that would be very difficult using other fabrication techniques.

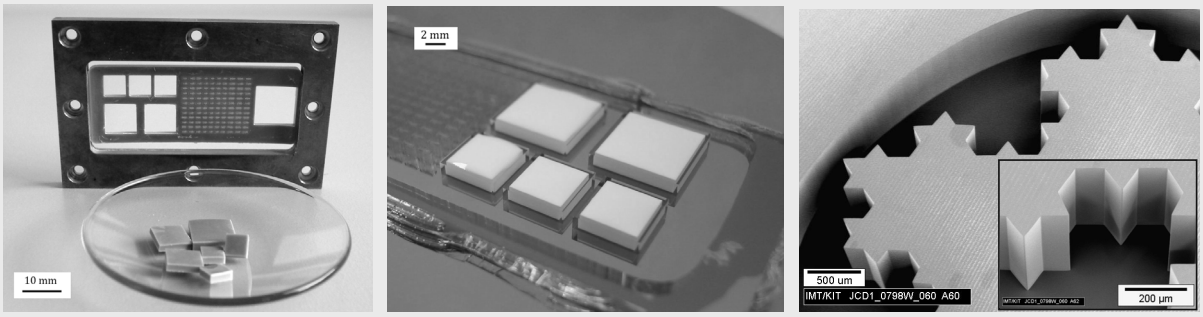

(a) (b) (c)

Fig. 1: (a) 2 mm-thick direct X-ray exposed photoresist-ceramic composite DRAs (SU-8, 48 wt% alumina powder)[3]; (b) photo-resist frames filled with polymer-ceramic composite (SU-8, 60 wt% alumina powder) [3]; (c) lithographically fabricated 1.8 mm-thick polymer-based fractal antenna element [5].

This new approach to use polymer-based dielectric materials (as in [3]), is particularly interesting as the natural softness of polymers could dramatically simplify fabrication of dielectric elements by enabling lithographic batch fabrication. We have also made progress in techniques for composite dielectric material properties measurement [7]. Another particularly interesting approach from a simplified fabrication perspective is with frame-based fabrication (as in Fig. 1b.), but keeping a "permanent frame", rather than removing it in the process sequence, which

was demonstrated to have only a slight effect on performance [8]. In addition, particular performance improvements can be obtained with feeding mechanisms taking advantage of vertical metal structure, for instance reducing the size of conventional DRAs by up to 50%, and enabling modes offering additional control over frequency response [9].

3. Publications (please stick to the user guidelines for publications and acknowledgements on www.knmf.kit.edu)**:**

[1] A. Rashidian, M. T. Aligodarz, D. M. Klymyshyn, M. Boerner, J. Mohr, "Photodefinable Microcomposites for Antenna Applications," *Proc. IEEE Int. Symp. on Antennas and Propagation (APS 2010)*, Toronto, Canada, 4 pages, 2010.

[2] A. Rashidian, D. M. Klymyshyn, M. T. Aligodarz, M. Boerner, J. Mohr, "SU-8 Resonator Antenna," *Proc. IEEE Int. Symp. Antennas & Prop*, Toronto, Canada, 4 pages, 2010.

[3] A. Rashidian, D. M. Klymyshyn, M. Boerner, J. Mohr, "Deep X-ray Lithography Processing for Batch Fabrication of Thick Polymer-based Antenna Structures," *Journal of Micromechanics and Microengineering*, vol. 20, p. 025026 (11 pp.), 2010.

[4] A. Rashidian, D. M. Klymyshyn, M. T. Aligodarz, M. Boerner, J. Mohr, "Development of Polymer-based Dielectric Resonator Antennas for Millimeter-wave Applications," *Progress In Electromag. Research C*, vol. 13, pp. 203-216, 2010.

[5] A. Rashidian, D. M. Klymyshyn, M. T. Aligodarz, M. Börner, J. Mohr, "Microwave Performance of Photoresist-Alumina Microcomposites for Batch Fabrication of Thick Polymer-Based Dielectric Structures," *Journal of Micromechanics and Microengineering*, vol. 22, p. 105002 (9 pp.), 2012.

[6] D. M. Klymyshyn, M. T. Aligodarz, A. Rashidian, M. Boerner, J. Mohr, "Photoresist-based Resonator Antenna Array," *6th German Microwave Conf.*, Darmstadt, Germany, 4 pages, 2011.

[7] A. Rashidian, M. T. Aligodarz, D. M. Klymyshyn, "Dielectric Characterization of Materials using a Modified Microstrip Ring Resonator Technique," *IEEE Trans. on Dielectrics and Electrical Insulation*, Vol. 19, pp. 1392-1399, 2012.

[8] A. Rashidian, D. M. Klymyshyn, M. T. Aligodarz, M. Börner, J. Mohr, "Photoresist-based polymer resonator antennas with permanent frame," *IET Electronics Letters*, Vol. 48, pp. 475–477, 2012.

[9] A. Rashidian, D. M. Klymyshyn, M. T. Aligodarz, M. Boerner, J. Mohr, "Photoresist-based polymer resonator antennas: lithography fabrication, strip-fed excitation, and multimode operation," *IEEE Antennas and Propagation Magazine,* Vol. 53, pp. 16-27, 2011.

4. Comments (max. 1.800 characters)**:**

Our new "Polymer Resonator Antennas" (PRAs) could be especially strategic for emerging wireless device applications, providing new capabilities not currently available for batch fabrication of complex structures with exceptional functional properties.

This work is establishing our group as early "pioneers" in the area of polymer microstructured RF antennas, as evidenced by our recent recognition in top journals. For instance, [3] was included in *J. Micromechanics & Microengineering* "Year's Best Papers from 2010" for "novelty, significance and potential impact on future research" (JMM claimed to be the "#1 MEMS journal" by Impact Factor (2010)). Our IEEE APS Magazine paper [9], was recently awarded the prestigious "2012 IEEE Antennas and Propagation Society Edward E. Altshuler Prize Paper Award" for the "*best paper published in the IEEE APS Magazine in 2011"* on the basis of "its technical quality and value, clarity of presentation, innovation, and impact". *IEEE APS Magazine* is one of the top IEEE antenna journals.

A follow-on KNMF project (2011-005-000500), is currently underway to further improve the polymer dielectric materials and fabrication processes for antenna applications. Specifically, these include: 1) better photoresist and photoresist-ceramic composite materials; 2) optimized exposure and pre/post exposure processes; 3) better excitation and integrated feed structures.

D. M. Klymyshyn

Proposal 2009-002-000138

Fabrication of x-ray interferometer gratings for phase contrast imaging with divergent sources

Christian David

Paul Scherrer Institut
Villigen PSI
Switzerland

Final Report

1. Project goals (max. 1.800 characters):

The goal of this proposal was to develop bendable gratings for X-ray differential phase contrast imaging. This development addressed a severe problem encountered in many cases when grating interferometry is used on conventional x-ray tubes. In order to keep the set-up compact and to obtain sufficient flux (especially in combination with microfocus x-ray tubes) and at the same time allow for an acceptable field of view, the divergence angle is typically many degrees. For a set-up with planar gratings, the contrast breaks down as soon as the x-rays penetrate the grating structures at angles close to or larger than 1/(aspect ratio). This can only be avoided by tilting the grating structures such that they point towards the source point. The most practical way to achieve this is to bend the grating structures in a cylindrical shape.

We therefore proposed to modify the X-ray lithography and electroplating process, such that it can be applied to bendable substrates instead of the presently used brittle silicon wafers.

The following imaging setup configurations have been proposed:

Grating set 1 (40 keV, 3rd TD, s=810 mm)				
Grating type	Period	Material / height	Area	Radius of curvature
Phase shifting	3.57 µm	Nickel / 14 µm	60 mm x 20 mm	602 mm
Absorption	2.40 µm	Gold / >50 µm	60 mm x 20 mm	810 mm
Grating set 2 (40 keV, 1st TD, s=270 mm)				
Grating type	Period	Material / height	Area	Radius of curvature
Phase shifting	3.57 µm	Nickel / 14 µm	60 mm x 20 mm	200 mm
Absorption	2.40 µm	Gold / >50 µm	60 mm x 20 mm	270 mm
Grating set 3 (40 keV, 3rd TD, s=270 mm)				
Grating type	Period	Material / height	Area	Radius of curvature
Phase shifting	2.40 µm	Nickel / 14 µm	60 mm x 20 mm	133 mm
Absorption	2.40 µm	Gold / >50 µm	60 mm x 20 mm	270 mm

2. Project results (max. 7.000 characters + figures):

Grating fabrication

The choice of the substrate material was one of the key questions to be addressed within this proposal. The constraints for the material were given firstly by its compatibility with the fabrication process (yet the

parameters could be changed), secondly by its bending properties and thirdly by a high transmission for X-rays at the design energy. Mainly three materials were under consideration; silicon, titanium and quartz glass. The silicon wafers of 150µm thickness turned out to be difficult to process, causing a high rate of defective gratings. Furthermore, despite of the small thickness it might be too brittle for the required bending radii. Titanium proved to be compatible with the process after adapting some parameters (for instance a longer soft bake time compared to silicon) and offers strong bending properties. The main disadvantage of this material is the comparably high attenuation, requiring the substrates to be extremely thin (50-140µm could be achieved). Quartz glass turned out to be a difficult material for the processing and also for the later handling by the user.

As a result of the material study, all gratings were fabricated on 140 µm thick titanium substrates.

Experiments
All of the three configurations have been set up and their performance has been evaluated. Grating set 1 and 2 were tested in the Talbot mode (2 gratings), while for grating set 3, a Talbot-Lau configuration could additionally be set up by using an absorption grating (p=2.4µm) as a source grating.
Firstly, the fringe visibility was determined by using the standard approach of stepping the absorption grating in equidistant steps over one period. Secondly, the increase of the horizontal size of the FOV could be determined by comparing the visibility map of the measurements with bent and planar gratings, respectively.

	Visibility		**horizontal field of view**	
	Talbot config	**Talbot-Lau config**	**planar**	**bent**
Grating set 1	2 %	-	40 mm	60 mm (max)
Grating set 2	2 %	-	13 mm	60 mm (max)
Grating set 3	1 %	7 %	13 mm	60 mm (max)

While the size of the horizontal field of view could be significantly increased (especially for the more compact configurations 2 and 3, the measured visibility was rather poor. The reason for this lies in the ciritical requirement of spatial coherence by the grating sets, in particular for a Talbot configuration. Increasing spatial beam coherence by using a Talbot-Lau configuration in grating set 3 allowed to significantly increase the visibility.
The next steps will focus on the optimization of the grating parameters (e.g. by relaxing the coherence requirement) and on the further investigation of the design of compact grating interferometry using Talbot-Lau configurations.
In summary, the results of the proposal were a success. This can also be seen from the fact that the developed technique is now also requested by other user groups of the KNMF. We thank the involved persons for their excellent work, and we are looking forward to continue the collaboration in future.

3. Publications (please stick to the user guidelines for publications and acknowledgements on www.knmf.kit.edu):

T. Thüring, P. Modregger, T. Grund, J. Kenntner, C. David, and M. Stampanoni, *Applied Physics Letters* ***99***, 041111 (2011)

Proposal 2009-003-000157

Large acceptance lens for focusing an undulator beam

Alfred Baron

RIKEN SPring-8 Center
Sayo-gun, Hyogo
Japan

Note: *Please fill in this report form and save/print it as a PDF file, then upload it to the KNMF proposal submission system. A cover page containing proposal title, proposer name(s), and technologies selected will be added by the system. A link for the download of the complete report as a PDF file will be displayed in the system.*

Final Report

1. Project goals (max. 1.800 characters):

The goal of this project is the fabrication, performance verification, and optimization of a lens having very large acceptance (2 to 3 mm) and modest (~0.5 m) focal length x-ray energies between about 15 and 25 keV (with only specific energies in this range targeted). It was hoped that this would allow highly efficient focusing of an x-ray undulator beam, in the horizontal, to a spot size of about 5 to 10 microns (FWHM). This is very much a common problem across many synchrotron radiation facilities, were the very asymmetric source parameters, with a large (~0.5 mm) source size in the horizontal leads makes it difficult to efficiently focus a beam. For a ~50 micron horizontal focal size, essentially 100% of an undulator beam can be focused in this energy range using a bent cylindrical or toroidal mirror. However, for smaller focal spot sizes, the mirrors become prohibitively large (ie: ~2m long). Meanwhile the aperture of conventional CRLs is too small to allow high efficiency. Multilayer mirrors are possible, but tend to be lossy, complicated to set up and greatly perturb the beam propagation direction. It was hoped that the prism lens might provide a better option. One should emphasize, that efficiency for a given spot size is the major issue here – if one only wants a small spot size, and is willing to sacrifice efficiency, then other options (mirrors, CRLs) are possible.

2. Project results (max. 7.000 characters + figures):

Fabrication

Lenses verified were fabricated by deep X-ray lithography. (Using instruments at KNMF…). Finally three prism lenses were prepared. (The specifications are…).

Verification

Lenses optimized for performance at 21.7 keV were fabricated at and sent to SPring-8 for measurement. The performance of three lenses was measured using the setup in the figure.

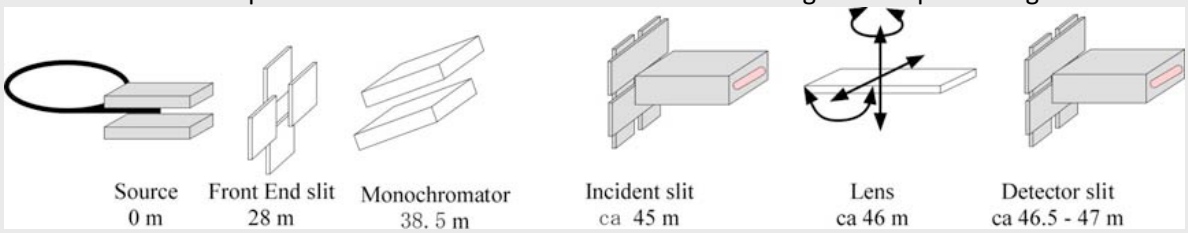

The vertical acceptance of the lenses was found to be 40 to 60 microns depending on fabrication details and the focal spot sizes were 12 or 13 microns, including an estimated 10 micron source size contribution as

Karlsruhe Nano Micro Facility (KNMF)
Karlsruhe Institute of Technology (KIT)
Hermann-von-Helmholtz-Platz 1
76344 Eggenstein-Leopoldshafen
Germany

User Office
Phone: +49 (721) 608-3123
Fax: +49 (721) 608-6273
Email: knmf-useroffice@kit.edu
Web: www.knmf.kit.edu

shown in figure. Both of these parameters were within accepted values.

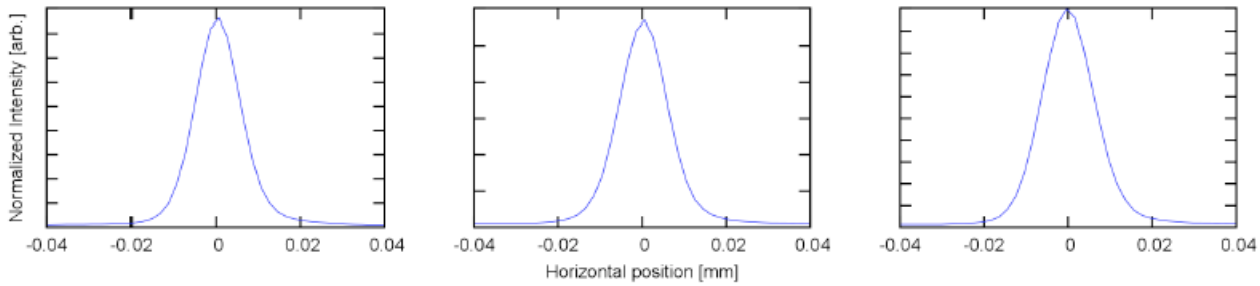

The horizontal acceptance was then measured as shown red blue lines in figure. A full aperture of 2.4 to 2.5 mm was found and a FWHM of about 0.6 to 0.7 mm. This is significantly larger than that (~0.3 mm FWHM) obtained with a silicon CRL, however still not at the level of 2mm in the FWHM as desired. If the intensity profile was a Gaussian function with FWHM of 0.5 mm, the best efficiency was 69 % as shown red lines in figure.

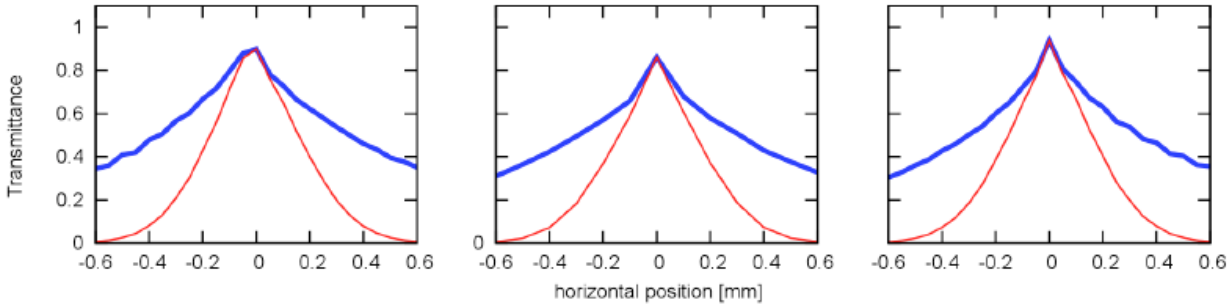

Thus, in the final desired configuration (right panel in the figure above), we estimate losses of about a factor of 4 in throughput. However, this could be effective optic only if using ingenuity to set the optics configuration making beam width at the lens narrower than 1 mm FWHM, for example, by using some compound focusing setup (mirror + lens).

3. Publications (please stick to the user guidelines for publications and acknowledgements on www.knmf.kit.edu):

Hiroshi Fukui, Markus Simon, Vladimir Nazmov, Jürgen Mohr, Kenneth Evans-Lutterodt, Aaron Stein, Alfred Q.R. Baron Large aperture refractive lenses for momentum resolved spectroscopy with hard X rays (In Preparation)

4. Comments (max. 1.800 characters):

We have obtained the lens properties for plane wave radiation and are now considering how to proceed. As mentioned in section 2, compound focusing is required to efficiently use the prism lens for our purpose. We should consider elaborately designed prism lenses to focus X rays propagating along non-simple paths.

Karlsruhe Nano Micro Facility (KNMF)
Karlsruhe Institute of Technology (KIT)
Hermann-von-Helmholtz-Platz 1
76344 Eggenstein-Leopoldshafen
Germany

User Office
Phone: +49 (721) 608-3123
Fax: +49 (721) 608-6273
Email: knmf-useroffice@kit.edu
Web: www.knmf.kit.edu

Proposal 2010-003-000186

Micro-fabrication of an absorption grating for 2D X-ray grating interferometry

Irene Zanette

European Synchrotron Radiation Facility (ESRF)
Grenoble Cedex 9
France

Final Report

1. Project goals (max. 1.800 characters)**:**

The goal of this project was to fabricate and characterize two-dimensional (2D) absorption gratings for 2D grating interferometry, and use these gratings for multimodal imaging and metrology. The 2D absorption grating has a mesh-type structure where 75% of the surface area is covered by gold. We proposed to obtain the desired structure by fabricating orthogonal absorbing lines on both sides of the silicon wafer.

2. Project results (max. 7.000 characters + figures)**:**

Two 2D absorption gratings, i.e. 2 gratings with nominally the same specifications, numbered 004 and 005, were obtained through this proposal as described above. They were characterized in a 2D grating interferometer at the beamline ID19 of the European Synchrotron Radiation Facility (ESRF) at an X-ray energy of 23 keV. The 2D absorption gratings have been tested in two configurations:

(i) with two crossed line phase gratings, and
(ii) with a genuine 2D phase grating.

Note that 1D and 2D phase gratings were not obtained as part of this proposal; they have been instead provided by a different institute.

The implementation of set-up (i) allowed to measure the angle between the absorbing lines on the two sides of the wafer; this angle should have been ideally of 90 degrees. The 1D phase gratings were mounted on two rotation stages for independent alignment with the respective absorbing lines. This alignment is a standard and easy procedure in grating interferometry and it is based on the moiré effect arising from the superposition of the two periodic patterns (i.e. the self image of G1 and the absorption pattern of G2) when the gratings are slightly tilted with respect to each other. By rotating the phase gratings around the optical axis until no moiré fringes are visible on the radiographic image, we were able to measure sub-degree deviations of orthogonality of the absorption grating lines. In particular, we measure a deviation of 0.25 degrees for grating 005, and of 0.33 degrees for grating 004. These deviations from orthogonality satisfy the specifications requested in the proposal.

Moreover, it should be noted that the visibilities obtained with these gratings were very high, around 37% - 39%. The high visibilities indicate that the thickness of the absorbing lines was sufficiently high to absorb most of the incoming radiation.

During the characterization measurements, however, we revealed some defects in both the 2D absorption gratings. These defects are present only on one of the two sides of the wafer (as shown in figure 1), and are probably caused by the (new) double-side fabrication process.

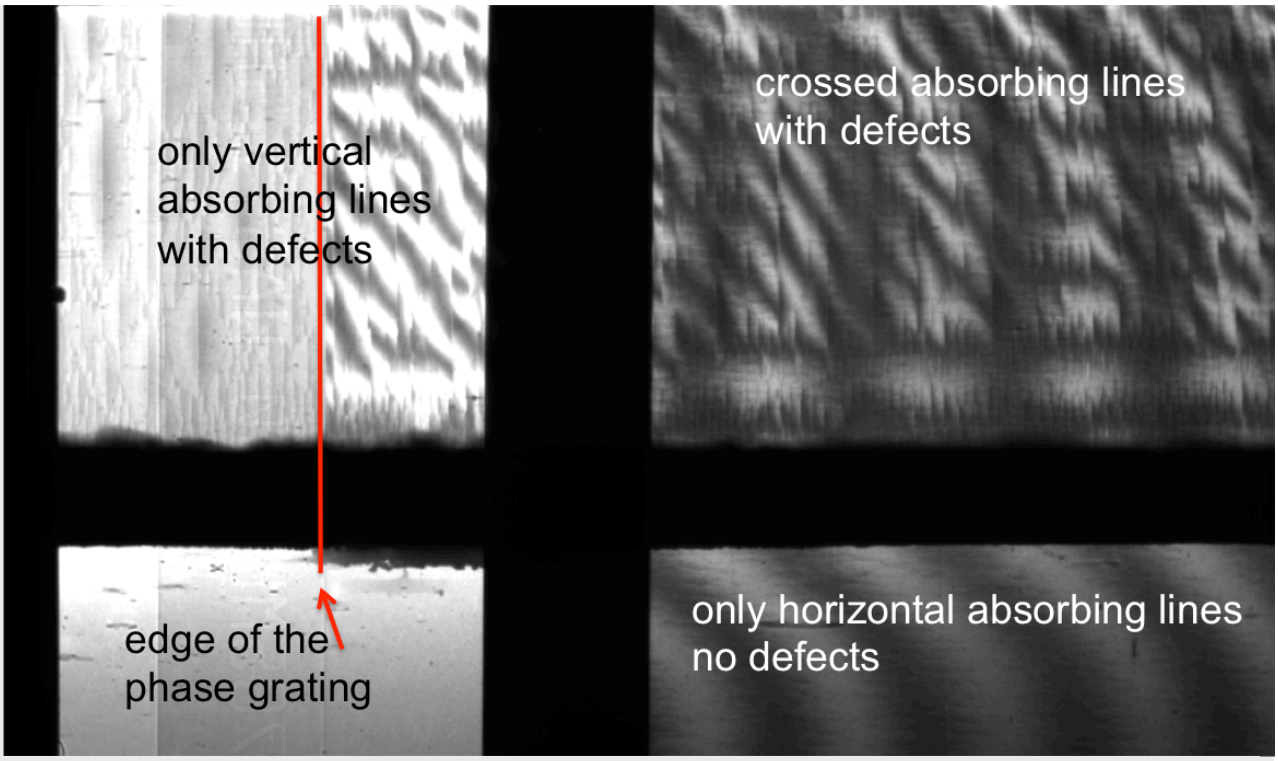

Figure 1: Defects in the 2D absorption grating. More details can be found in the main text.

After the characterization process, we used the best performing grating, grating 004, and we implemented a 2D grating interferometer of the type (ii) for imaging. Using only two gratings (instead of three gratings as in set-up (i)) has the advantage of reducing the number of grating substrates in the beam path (i.e. reducing absorption), but also of simplifying the interferometer mechanics. With this instrument, we measured demonstrator samples (see, as an example, the false-color dark-field image of an ant in figure 2) in phase-stepping mode.

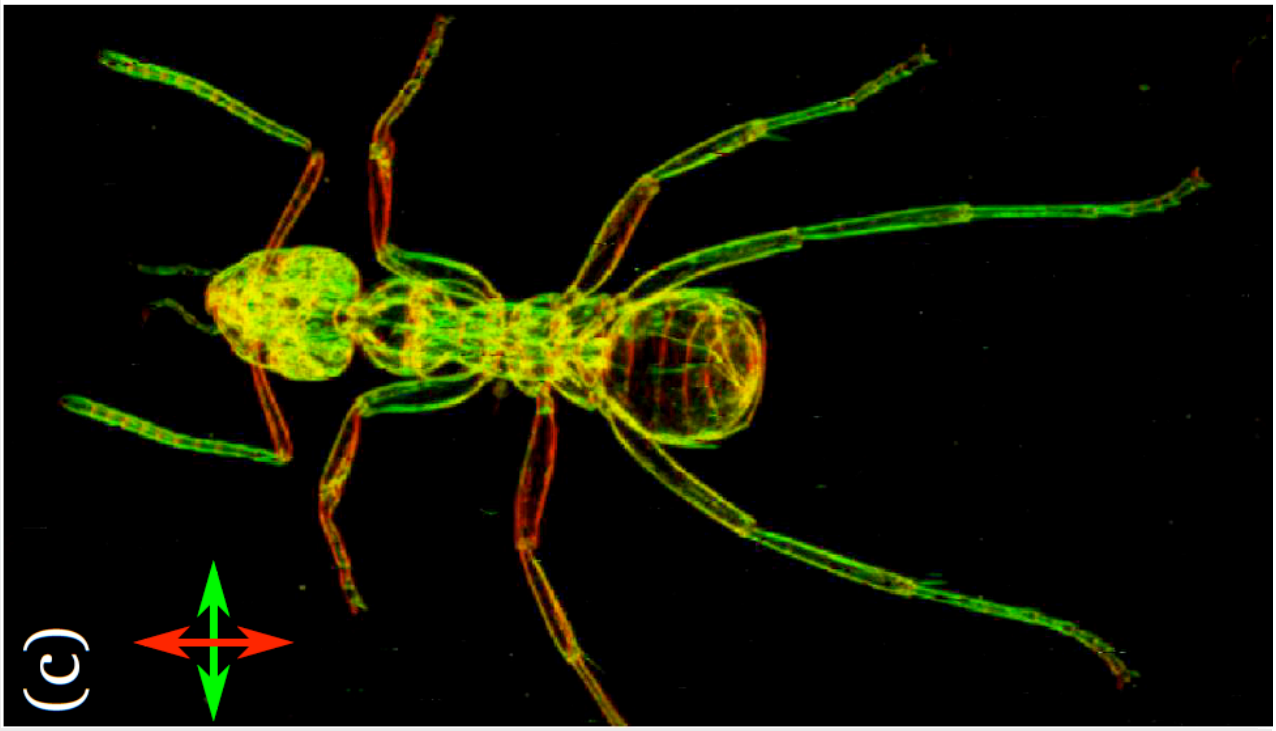

Figure 2: False-color dark-field image of an ant. Green channel: scattering in the vertical direction, red channel: scattering in the horizontal direction.

The defects in the 2D absorption grating highlighted in Fig. 1 cause image artifacts. These artifacts can be seen in the background of the differential phase image of an ant as shown in Figure 3 where the gray window was adjusted to highlight the defects in the background.

Karlsruhe Nano Micro Facility (KNMF)
Karlsruhe Institute of Technology (KIT)
Hermann-von-Helmholtz-Platz 1
76344 Eggenstein-Leopoldshafen
Germany

User Office
Phone: +49 (721) 608-3123
Fax: +49 (721) 608-6273
Email: knmf-useroffice@kit.edu
Web: www.knmf.kit.edu

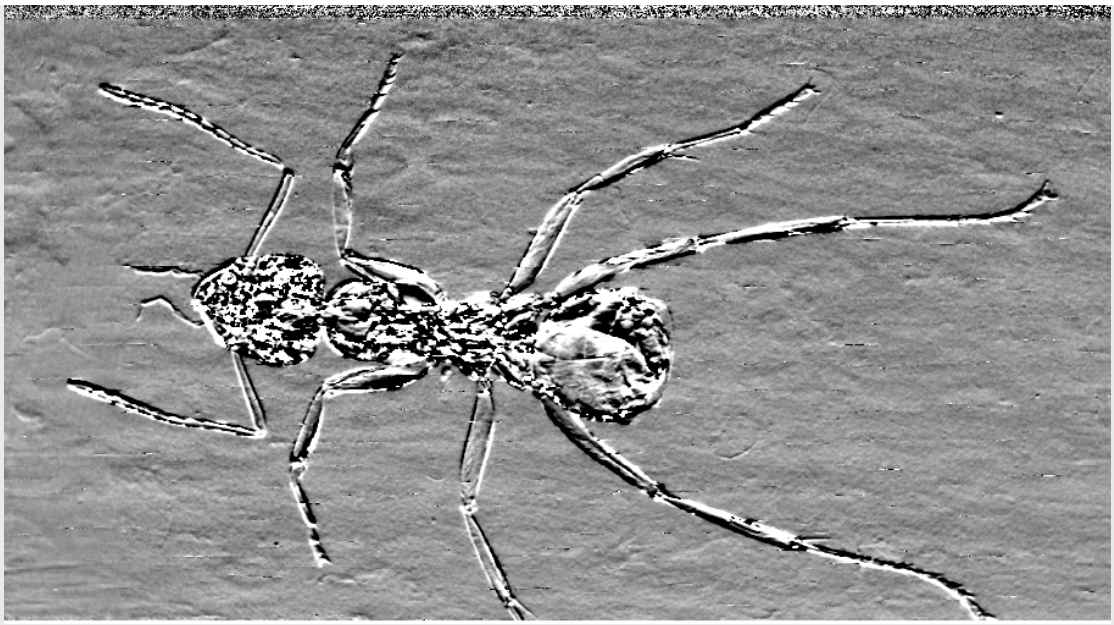

Figure 3: the structures in the background of this differential phase image are artifacts from the defects shown in Fig. 1.

These defects should be investigated and, if possible, corrected.

3. Publications (please stick to the user guidelines for publications and acknowledgements on www.knmf.kit.edu)**:**

Below are the publications on 2D grating interferometry that used gratings obtained from KNMF.

1) Zanette, I., Weitkamp, T., Donath, T., Rutishauser, S. & David, C. (2010), *"Two-Dimensional X-Ray Grating Interferometer"*, Physical Review Letters. Vol. 105, pp. 248102.

2) Rutishauser, S., Zanette, I., Weitkamp, T., Donath, T. & David, C. (2011), *"At-wavelength characterization of refractive x-ray lenses using a two-dimensional grating interferometer"*, Applied Physics Letters. Vol. 99(22), pp. 221104.

3) S. Rutishauser, M. Bednarzik, I. Zanette, T. Weitkamp, M. Börner, J. Mohr, C. David, *"Fabrication of two-dimensional hard X-ray diffraction gratings",* submitted (2012).

4) Zanette I., Rutishauser S., David C. & Weitkamp T. (2011), "*X-ray interferometer with two-dimensional gratings*", AIP conf. Proc., Vol. 1365, pp. 325-328.

5) Weitkamp T., Zanette I., Schulz G., Bech M., Rutishauser S., Lang S., Donath T., Tapfer A., Deyhle H., Bernard P., Valade J.-P., Reznikova E., Kenntner J., Mohr J., Müller B., Pfeiffer F., David C. & Baruchel J. (2011), "*X-ray grating interferometry at ESRF: applications and recent technical developments*", AIP Conf.

Proc., Vol. 1365, pp. 28-31

6) I. Zanette, S. Rutishauser, C. David, F. Pfeiffer, J. Mohr, and T. Weitkamp, "*Multidirectional X-ray dark-field imaging with two-dimensional gratings*", X-ray and Neutron Phase Imaging with Gratings, Tokyo, Japan AIP Conference Proceedings, submitted (2012).

7) C. David, S. Rutishauser, M. Sprung, I. Zanette, and T. Weitkamp, "*X-ray grating interferometry - Applications in Metrology and Wave Front Sensing*", X-ray and Neutron Phase Imaging with Gratings, Tokyo, Japan AIP Conference Proceedings, submitted (2012).

Moreover, an article on the ESRF highlights 2011 (pp. 116-117) has been published with results obtained with the absorption gratings obtained with this proposal.

4. Comments (max. 1.800 characters)**:**

We have characterized, and used for imaging, the 2D absorption gratings obtained with this proposal. The gratings match the specifications, provided good visibilities and high quality images. However, defects on one side of the wafer seem to affect the final images. These defects should be investigated and, if possible, corrected. Moreover, 2D gratings with less orthogonality error are desirable for further implementations of the 2D grating interferometer to reduce the impact of residual moiré fringes on the quality of the images.

Proposal 2010-003-000230

Electron Tomography of nanoparticles in III-V semiconductors

Wolfgang Jäger

Christian-Albrechts-Universität zu Kiel (CAU)
Kiel
Germany

Note: *Please fill in this report form and save/print it as a PDF file, then upload it to the KNMF proposal submission system. A cover page containing proposal title, proposer name(s), and technologies selected will be added by the system. A link for the download of the complete report as a PDF file will be displayed in the system.*

Final Report

Electron Tomography of Nanoparticles in Zn-Doped GaAs Semiconductors

Dr. Christian Kübel
Institute of Nanotechnology, Karlsruhe Institute of Technology, 76344 Eggenstein-Leopoldshafen, Germany
Karlsruhe Nano Micro Facility (KNMF), Karlsruhe Institute of Technology, 76344 Eggenstein-Leopoldshafen, Germany

Dipl.-Ing. C. Dieker, Prof. Dr. Wolfgang Jäger
Microanalysis of Materials, Institute of Materials Science, Christian-Albrechts-University of Kiel, 24143 Kiel, Germany

Support in FIB-based TEM sample preparation by D. Esser and Dr. H.J. Penkalla, Institute of Energy Research, IEF-2, Forschungszentrum Jülich GmbH, 52425 Jülich, Germany, is gratefully acknowledged.

Keywords: STEM, electron tomography, nanoparticles, semiconductors, doping effects

1. Project goals (max. 1.800 characters):

The microscopic investigations of nanoparticles in III-V semiconductors aim at an improved understanding of the structure and the morphology of nanoparticles in semiconductors. In a first set of experiments, the proposed project aimed at investigating relevant aspects by performing tomography STEM investigations for a selected and pre-characterized set of GaAs specimens containing metallic gallium nanoparticles, crystalline nanoparticles with a Zn_3As_2 phase, and nanovoids. Previous investigations for Ga-based III-V semiconductor materials have shown that such nanoparticles form during high-concentration dopant diffusion by an interstitial-substitutional exchange mechanism using Zn in-diffusion from strong diffusion sources. These investigations are of interest in a quantitative understanding of the structure and of the morphology of such nanoparticles in semiconductors, especially also in view of their equilibrium shapes in the single-crystalline compound semiconductor material, the internal solid-liquid interface, and the wetting properties.

2. Project results (max. 7.000 characters + figures):

Electron tomography is now established as a powerful tool to image complex structures with nanometer resolution in 3D. In materials science, the use of BF-TEM tomography is limited as BF images do not fulfill the projection requirement for crystalline materials and thus cannot be used for tomography of most crystalline samples. To fulfill the projection criterion, alternative imaging techniques have been explored for use in tomography. The most universal approach for tomography in materials science is high-angle annular dark field (HAADF) imaging in a scanning transmission electron microscope (STEM), which has been fully automated over the last years [1]. In addition to the advances in tomography acquisition, new reconstruction algorithms are also significantly improving tomography results. For example, the simultaneous iterative reconstruction technique (SIRT) results in a significantly reduced noise compared to the classical weighted back-projection (WBP).

The methodologically oriented study aimed at high-resolution analyses of nanometer-scale particles and inclusions in III-V compound semiconductor materials by applying HAADF-STEM tomography. Different types of nanoparticles, such as small Ga precipitates, voids, and Zn-rich crystalline Zn_3As_2 precipitates, form during high-concentration zinc diffusion in GaAs [2] or GaP [3] semiconductors. The predominant type of nanometer-scale inclusions in the diffusion front region of GaAs are Ga precipitates with voids (typical diameter range 10-50 nm) which form in the GaAs matrix material from liquid droplets upon cooling from the chosen diffusion temperature [2]. Appropriate specimens for the electron tomography investigations have been prepared from the diffused semiconductor material by focused-ion-beam (FIB) preparation techniques. Our electron tomography investigations reveal that a complete 3D characterization of such complex nanoinclusions can be performed successfully by applying HAADF-STEM tomography. Fig. 1 shows the 3D morphology of two inclusions in GaAs. The local intensity differences in one of the inclusions are due to density and thus compositional differences within a single inclusion. By combining this HAADF-STEM tomography analysis with local energy-dispersive X-ray spectroscopic analyses, it was found that the precipitate contains largely Ga, with a small fraction of Zn. Fig. 2 is an example for the determination of the angle (in a 2D slice of the reconstructed volume) between precipitate and pore of the nanoinclusion. A quantitative investigation of the wetting angle is of interest especially in view of understanding equilibrium shapes of nanoinclusions in single-crystalline compound semiconductor materials, the internal solid-liquid interface, and the wetting properties of the precipitate material.

For such systems, the benefits of HAADF-STEM tomography consist in the potential to directly detect nanometer scale composition fluctuations inside inclusions and to measure interface and wetting angles in 3D.

[1] C. Kübel, A. Voigt, R. Schoenmakers, M. Otten, D. Su, T.-C. Lee, A. Carlsson, J. Bradley, *Microsc. Microanal.* 11(5) (2005) 378.
[2] A. Rucki and W. Jäger, Defect and Diffusion Forum 194-199 (1997) 723.
[3] Ch. Jäger and W. Jäger: J. Physics: Condensed Matter 14 (2002) 12865.

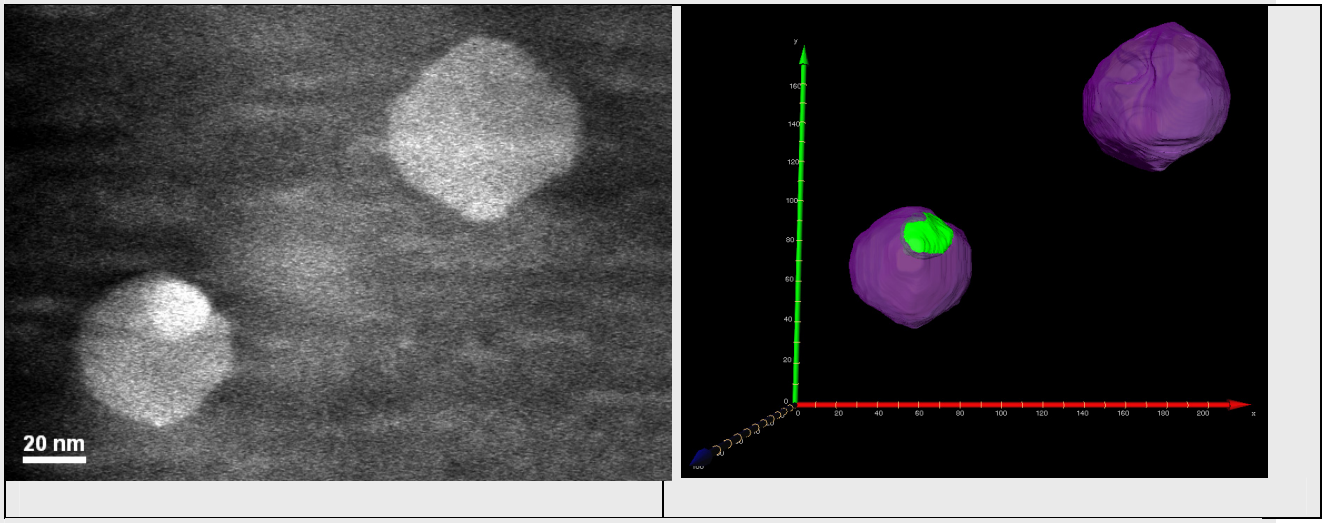

FIG. 1. Nanoinclusion in GaAs: Digital slice through the reconstructed volume and surface rendering revealing density (composition) differences within a nanoinclusion.

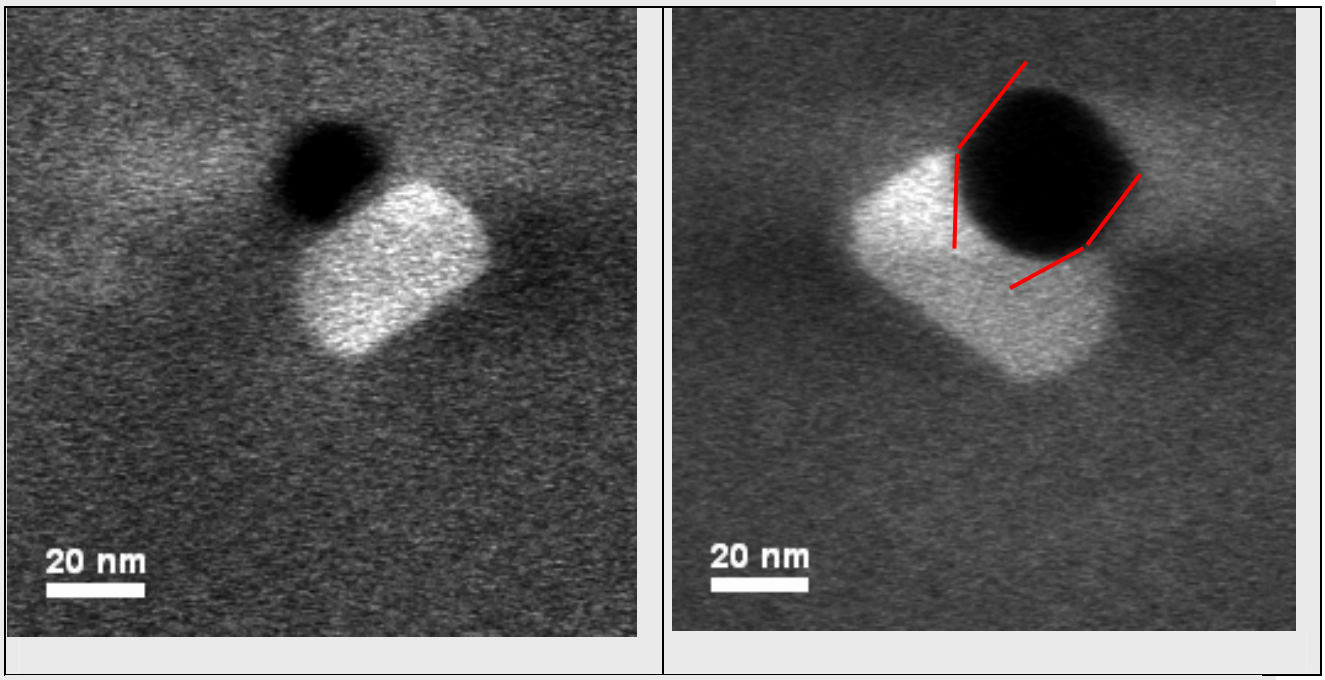

FIG. 2. Digital slice through the reconstructed volume: Inclusions adjacent to a pore and indication of the wetting angle.

Karlsruhe Nano Micro Facility (KNMF)
Karlsruhe Institute of Technology (KIT)
Hermann-von-Helmholtz-Platz 1
76344 Eggenstein-Leopoldshafen
Germany

User Office
Phone: +49 (721) 608-3123
Fax: +49 (721) 608-6273
Email: knmf-useroffice@kit.edu
Web: www.knmf.kit.edu

3. Publications (please stick to the user guidelines for publications and acknowledgements on www.knmf.kit.edu)**:**

C. Kübel, Ch. Dieker, D. Esser, H.J. Penkalla, W. Jäger: *Electron Tomography of Nanoparticles in Zn-doped GaAs Semiconductors,* Proc. IMC17 17th International Microscopy Congress, Rio de Janeiro, I7526 (2010).

C. Kübel, Ch. Dieker, D. Esser, H.J. Penkalla, W. Jäger: *Electron Tomography of Nanoparticles in Zn-Doped GaAs Semiconductors,* Proc. Microscopy Conference MC 2011, Kiel, Germany, 28.08.-02.09.2011, ISBN 978-3-00-033910-3 (Copyright) 2011 DGE - German Society for Electron Microscopy, Germany (2011).

4. Comments (max. 1.800 characters)**:**

Further experiments aim at obtaining complementary information about the elemental distributions in complex nanoinclusions by energy-dispersive X-ray spectroscopy at high spatial resolution. Such investigations will require an optimization of the FIB-preparation of the TEM specimens.

Proposal 2010-003-000238

Study of Deformation Behaviour in Molecular Crystals

Chilla Malla Reddy

Indian Institute of Science Education and Research (IISER), Kolkata
Mohanpur, Nadia, West Bengal
India

Note: *Please fill in this report form and save/print it as a PDF file, then upload it to the KNMF proposal submission system. A cover page containing proposal title, proposer name(s), and technologies selected will be added by the system. A link for the download of the complete report as a PDF file will be displayed in the system.*

Final Report

1. Project goals (max. 1.800 characters)**:**

Experimental evaluation of the previously proposed model for the mechanical bending of organic single crystals. The HRTEM technique will be utilized to characterize the mechanically bent single crystals (hexabromobenzene) to understand the defects in the crystal packing. The observed defects shall guide the evaluation of bending deformation mechanism in organic crystals.

2. Project results (max. 7.000 characters + figures)**:**

Materials and Preparation (at IISER Kolkata): The hexabromobenzene (C_6Br_6) was purchased from Aldrich and used as received. The single crystals of C_6Br_6 were prepared by thoroughly dissolving the compound in hot tetrahydrofuran (THF) solvent, followed by slow evaporation at ambient conditions. Microcrystals were obtained in 4 to 5 days, which were used for HRTEM experiments.

HRTEM Experiments (KNM Facility): The HRTEM experiments were performed at the facility. The undeformed single crystals of C_6Br_6 were first checked for the beam sensitivity. Although the melting point of the sample is above 250 °C, the compound did not show adequate beam stability at room temperature. However, some useful images could be obtained from the reference (undeformed) crystals, prepared using microtome. The analysis of the results suggests the presence of some defects, even in the undeformed reference crystal (i.e. even without mechanical bending). The defects are probably generated in the crystal easily due to the high plasticity of the material. The analysis of the images and diffraction pattern confirmed the defect formation in certain orientations. However, further characterization was not possible due to the low beam stability of the sample as this not allow multiple scans in the selected areas. However, the successful images suggest that the material develops edge dislocations. But at the moment it is not possible to comment whether these defects takes place in addition to the molecular movements proposed in the earlier model or not.

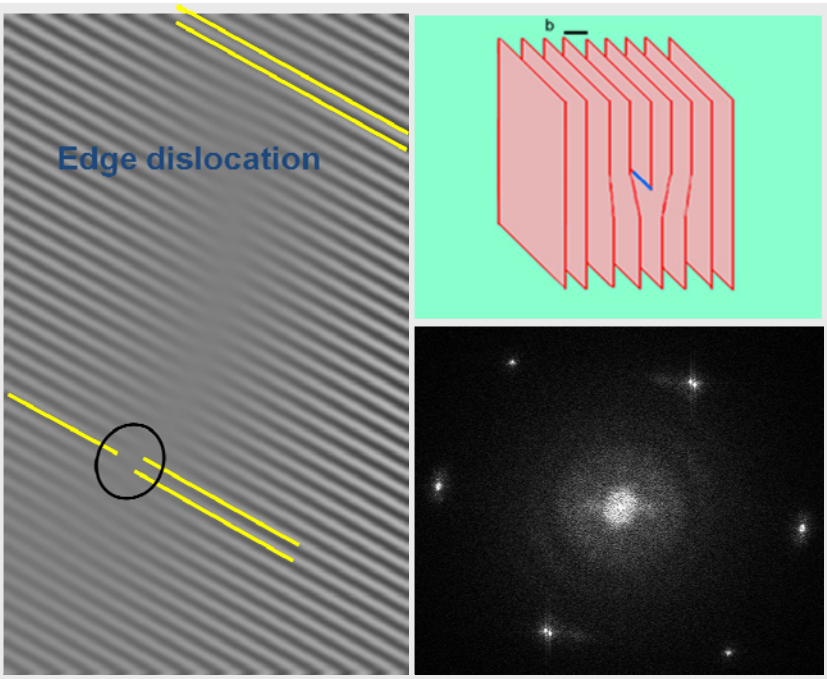

Figure 1. HR-TEM image from undeformed crystal. (left) The region in the middle shows the edge defect while the packing is normal on the top portion (yellow lines). (top-right) The model to show edge defects and Burgers vector (b). (bottom-right) Diffraction pattern from the defect region shows the splitting of spots due to the resulted misalignment of molecules across tow regions on either side.

3. Publications (please stick to the user guidelines for publications and acknowledgements on www.knmf.kit.edu)**:**

The project remains inconclusive, hence it is not yet clear if a publication will arise out of this work.

4. Comments: In the absence of low temperature attachment facility at the HR-TEM facility, the work could not be completed. However, this opportunity by KNMF was very helpful which guided us for concluding the work using other techniques (such as Raman spectroscopy) at our institute. We will be glad to acknowledge the facility in our publication.

Proposal 2010-004-000270

Screening of the Surface Structure and Modification of Carbon Nanotubes and Cellulose

Christopher Barner-Kowollik

Karlsruhe Institute of Technology (KIT)
Karlsruhe
Germany

Note: *Please fill in this report form and save/print it as a PDF file, then upload it to the KNMF proposal submission system. A cover page containing proposal title, proposer name(s), and technologies selected will be added by the system. A link for the download of the complete report as a PDF file will be displayed in the system.*

Final Report

1. Project goals (max. 1.800 characters)**:**

The scientific aspect that drove the current KMNF proposal are the ability to analyze the physical and chemical properties of polymer-functionalized surfaces. A variety of surfaces was employed ranging from nano-objects to macroscopic sheets, including carbon nanotubes (CNTs), cellulose and functionalized silicon surfaces, which were subjected patterning and functionalization with clickable polymer substrates. The functionalization of these surfaces occurred within the context of a number of cutting-edge projects within the team of Prof. Barner-Kowollik. To obtain an in-depth understanding of the molecular structure, properties and grafting density, **X-Ray Photoelectron Spectroscopy (XPS)** was utilized as a powerful tool for the (spatial) analysis of these materials to obtain precise information on the molecular composition of the modified structures and the precise location of the (active) compounds on the substrates.

2. Project results (max. 7.000 characters + figures)**:**

Modification of variable surfaces with polymers drastically enhances their potential applications, for example with cellulose, where functionalization can lead to its improved utility as a membrane material or impart anti-bacterial properties. Cellulose is a prime example because it has many useful properties, yet for a number of potential applications it lacks some fundamental properties which can usually be found in synthetic polymers. We were able to modify cellulose substrates via a modular ligation technique and to characterize the resulting surfaces in detail with XPS. Specifically and in the context of the current KMNF project, the synthesis of cellulose-*g*-poly(isobornyl acrylate) *via* the RAFT hetero Diels-Alder concept was demonstrated. *Via* a mild and modular cycloaddition approach, poly(isobornyl acrylate) was attached at ambient temperature to pre-functionalized cellulose sheets decorated with highly reactive cyclopentadiene units. The initially present hydroxyl groups of the cellulose substrate were converted into a tosylate leaving group and subsequently substituted by a cyclopentadienyl functionality (Cp) *via* an ambient temperature procedure employing nickelocene as the key ingredient. The reactive Cp functionality acts as a diene, reacting with RAFT generated poly(isobornyl acrylate) acting as electron-deficient dieneophile to afford an efficient [2+4] cycloaddition. X-Ray photoelectron spectroscopy, scanning electron microscopy,

high resolution Fourier transform infrared microscopy and elemental analysis prove the successful grafting procedure at ambient temperature conditions within a grafting time of 15 h. XPS gave precise information on the molecular composition and we were able to calculate loading capacities of the functionalized materials.

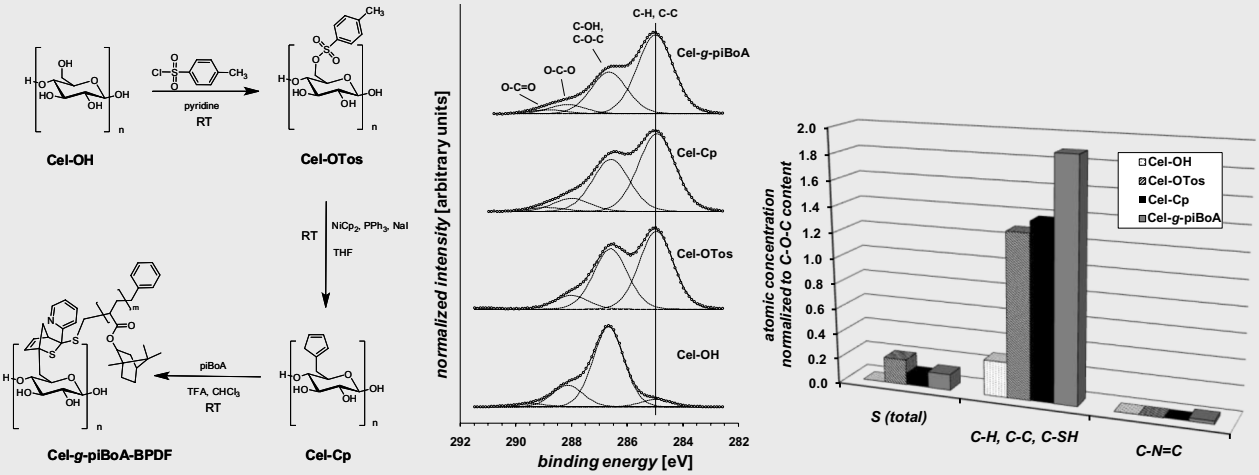

Figure 1. *Left: Strategy for surface-modification of cellulose via RAFT hetero Diels-Alder cycloaddition. C 1s XPS spectra of Cel-OH, Cel-OTos, Cel-Cp, Cel-g-piBoA. Middle: The spectra were normalized to the peak with the highest intensity. Right: Bar chart comparison of the individual atomic concentrations of Cel-OH, Cel-OTos, Cel-Cp and Cel-g-piBoA for sulfur (S (total)), the peak for C-H/C-C/C-SH and C-N=C calculated from the XPS spectra. The spectra were normalized to C-O-C content (publication 1).*

CNTs are further substrates with many uses, most importantly as reinforcement materials in e.g. polymer, metals and ceramic matrices, yet these composites often suffer from problems during melt-processing. To overcome the problem of π-stacking driven bundling of CNTs especially in polymer matrices, CNTs were modified on their surface via a novel and none destructive Diels-Alder based approach. The [4+2] cycloaddition of cyclopentadienyl end-capped poly(methyl methacrylate) to single-walled carbon nanotubes was performed under mild conditions, without catalyst and at ambient temperature as well as at 80°C. Among other characterization techniques, XPS confirms the success of the reaction and allowed to estimate the grafting density of the polymer chains on the SWCNTs (see publication 2).

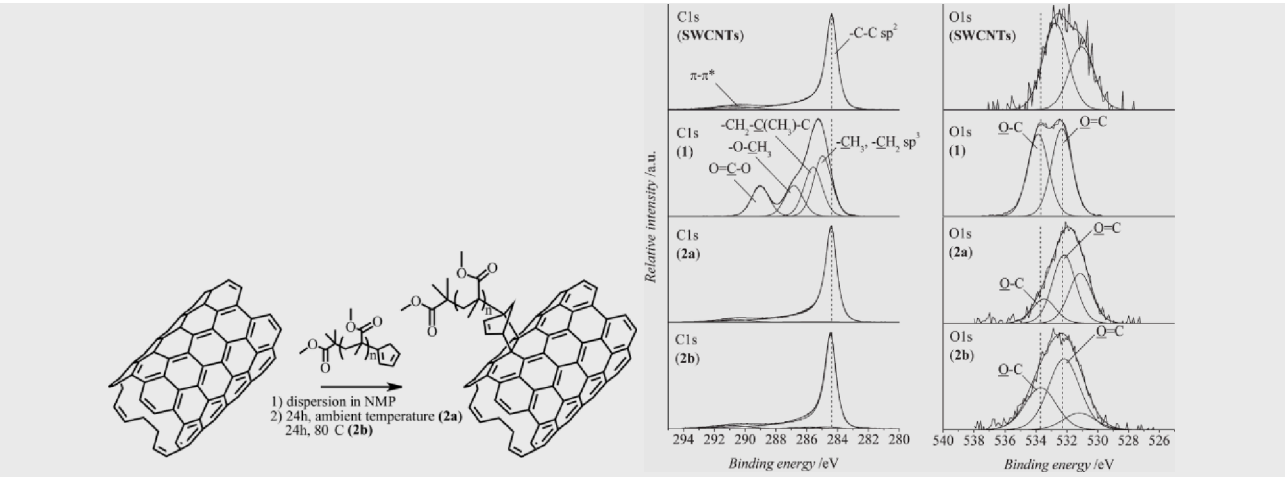

Figure 2. *Mild and orthogonal modification of CNTs and characterization with XPS of the single steps of the materials (publication 2)*

The grafting reaction was additionally quantitatively evidenced by macroscopic measurements (TGA, EA) with spectroscopic tools (XPS) and observed at the nanoscopic scale (HRTEM).

Surface designs with expressed hetero Diels-Alder (HDA) linkages also allows a retro Diels-Alder (rDA) reaction to be employed, whereby it is possible to use heat to pattern a surface, leaving an active DA surface where the polymer has been removed. Within the current KMNF project, a powerful and efficient reaction pathway for the synthesis of a polysiloxane assembly decorated with a highly reactive cyclopentadiene terminus on a solid substrate was carried out. The high reactivity of the formed self-assembly is demonstrated by the rapid conjugation of polymers bearing dienophile end groups to the coated substrates at ambient temperatures without the need for catalysis in drastically shorter reaction times than in other reported systems. The XPS technique allowed the tracking of the dynamic covalent reactions that are possible on the surfaces constructed via Diels-Alder and rDA reactions (see publication 3). As a representative example, the C 1s spectra for substrate Si-PEG are shown in Figure 3. When comparing substrate Si-PEG after removal of the PEG (Si-PEG-rDA) to the originally transformed substrate Si-Cp, very little difference is seen.

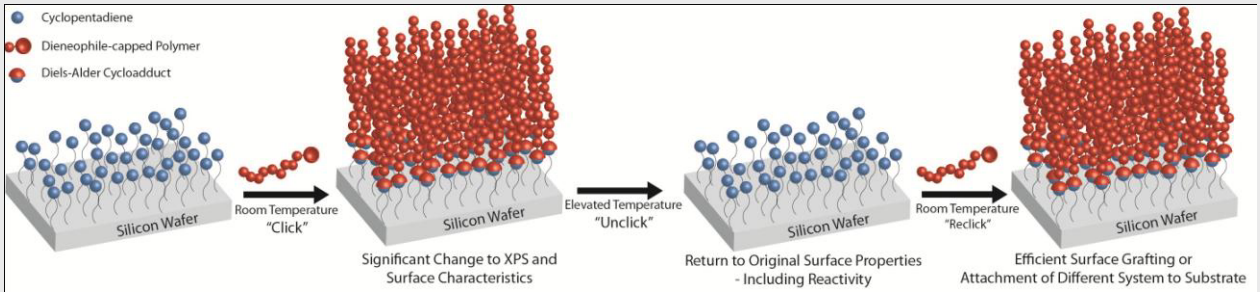

Karlsruhe Nano Micro Facility (KNMF)
Karlsruhe Institute of Technology (KIT)
Hermann-von-Helmholtz-Platz 1
76344 Eggenstein-Leopoldshafen
Germany

User Office
Phone: +49 (721) 608-3123
Fax: +49 (721) 608-6273
Email: knmf-useroffice@kit.edu
Web: www.knmf.kit.edu

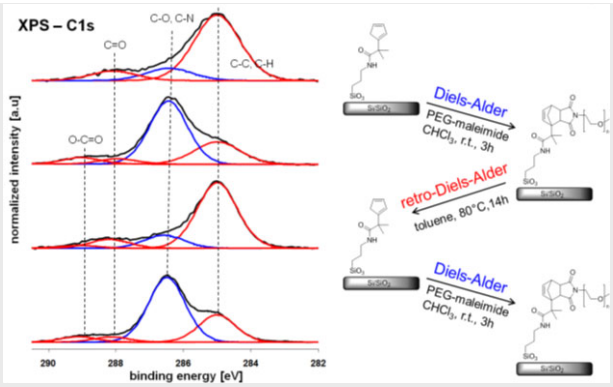

Figure 3: *Dynamic covalent reactions on silicon surfaces: High-resolution XPS of the C 1s region of substrates* ***Si-CP*** *(a),* ***Si-PEG*** *(b),* ***Si-PEG-rDA*** *(c), and* ***Si-PEG-DA*** *(d). The cycling between poly(ethylene glycol) being attached or removed from the surface is clearly observed through the dramatic intensity change in major peaks in the XPS data and wettability of the surfaces as well as the associated AFM data (publication 3).*

3. Publications (please stick to the user guidelines for publications and acknowledgements on www.knmf.kit.edu):

1. *Mild and Modular Surface Modification of Cellulose via Hetero Diels-Alder (HDA) Cycloaddition* Goldmann, A.S.; Tischer, T.; Barner, L.; Bruns, M.; Barner-Kowollik, C. ***Biomacromolecules*** **2011**, 12, 1137–1145.
2. *One-step Functionalization of Single-Walled Carbon Nanotubes (SWCNTs) with Cyclopentadienyl Capped Macromolecules via Diels-Alder Chemistry,* Zydziak, N.; Hübner, C.; Bruns, M.; Barner-**Kowollik, C.** ***Macromolecules*** **2011,** 44, 3374–3380.
3. *Dynamic Covalent Chemistry on Surfaces Employing Highly Reactive Cyclopentadienyl Moieties,* Blinco, J.; Trouillet, V.; Bruns, H.-M.; Gerstel, P.; Gliemann, H.; Barner-Kowollik, C. ***Adv. Mat.*** **2011**, 23, 4435-4439.

4. Comments (max. 1.800 characters):

We enjoy an outstanding and very fruitful collaboration with Dr. Bruns and his team in all matters related to XPS analysis.

Proposal 2010-004-000342

TEM Characterization of Semiconductor Nanocrystals

Anand Pathak

University of Hyderabad
Hyderabad
India

I- AlGaN/GaN work

We have attempted to address some of the basic mechanisms pertaining to defect propagation in AlGaN/GaN multi-quantum wells (MQWs) grown on sapphire by metal organic chemical vapor deposition(MOCVD), with the effect of swift heavy ion irradiation as a function of projectile and its energy which are essential for device performance. In the present study, electronic energy loss (S_e) is the decisive parameter which determines the important phenomena like crystallization or amorphization due to excitation or ionization of target electrons in the epilayers, while nuclear energy loss (S_n) is dominant in dislodging the atoms from their lattice sites at the end-of-the-ion range which is deep inside the sapphire substrate. Subsequently, ion beam effects on composition, periodicity and strain of MQWs have been studied. These have been investigated with analytical and high-angle annular dark field scanning transmission electron microscopy (HAADF-STEM) and the results have been further confirmed by high-resolution X-ray diffraction. The interface quality has been analyzed with aberration-corrected high-resolution TEM. Specimens for cross-sectional transmission electron microscopy (TEM) analysis were prepared by mechanical polishing, followed by argon ion milling using a Gatan PIPS system using a FEI Strata 400 S Dual Beam FIB with in-situ lift-out. HAADF-STEM, high-resolution TEM (HRTEM) and qualitative energy-dispersive X-ray (EDX) nano analysis were performed using a FEI Titan 80–300 equipped with an objective lens aberration corrector at Karlsruhe Nano Micro Facility (KNMF), Germany. HRXRD measurements were done with Cu Kα radiation (λ = 0.15406 nm) using a Bruker D8 DISCOVER at University of Hyderabad, India. Effects of electronic energy loss on Raman modes have also been studied.

Conclusions

1. Interface quality and reduced defect density along the *c*-axis have been observed in the MQW region due to AlN and GaN buffer layers. A number of misfit dislocations from the AlN/GaN interface are seen to bend close to the interface and thread through the AlGaN layers. Our present results are consistent with those of Bai et al. and Egawa et al.
2. HAADF-STEM image from Ni ions irradiated MQWs does not reveal a significant difference in structure as compared to pristine sample. However, after 120MeV Au irradiation, a drastic decrease in MQW quality and a significant increase in defect density are observed.

3. HRXRD results revealed that moderate S_e irradiation has improved the quality of the interfaces as compared to pristine MQW interfaces. Degradation of interfaces is observed as S_e increases.
4. Raman Spectroscopy: At higher S_e, there are two significant observations: (a) a red shift and asymmetry in the $E_{2(}H)$ mode, which are attributed to ion-beam-induced intermixing and (b) a decrease in free carrier concentration where larger lattice damages are introduced.

Publication:

1. **Ion beam treated strained AlGaN/GaN multi quantum wells: HAADF- STEM, HRTEM, Raman and HRXRD characterizations,** G. Devaraju, A. P. Pathak, N. Srinivasa Rao, V. Saikiran, D. Wang, T. Scherer, A. K. Mishra & C. Kübel, **Radiation Effects & Defects in Solids,** http://dx.doi.org/10.1080/10420150.2011.642872

II- Si/Ge work

The structural, optical and electronic properties of low dimensional, indirect band gap materials have been investigated extensively over the past few years. When the size of these nanocrystals is smaller than the exciton Bohr radius, carriers can be three-dimensionally confined and the properties of such semiconductor nanostructures embedded in dielectrics show very interesting and useful properties. Semiconductor nanostructures such as silicon (Si) and germanium (Ge) have been studied widely because of their potential applications in optoelectronics and nanophotonics. Although Ge and Si nanocrystals were prepared by various methods, researchers are looking for variety of new synthesis methods for various industrial applications. This motivated us to prepare nanocrystals using various novel synthesis methods. We have given four samples which were prepared by different methods for TEM analysis expecting nanocrystals.

Two samples were characterized using TEM out of four samples:

1. Sample ID: **3016-Ge-SiO_2:** Here 400 keV Ge ions were implanted into SiO_2 matrix and subsequently irradiated with 150 MeV Ag ions with fluence 3E13. TEM images show that Ge is distributed inside the SiO_2 interface with the highest concentration close to the middle of the SiO_2 layer. In addition, a noticeable amount of Ge is also found at the SiO_2/Si interface. No well-defined or crystalline Ge particles could be detected. The roughness of the SiO_2/Si interface varies locally.

2. Sample ID: **D152E13**: This sample is prepared by RF sputtering and subsequently irradiated with 100 MeV Ag ions with fluence 2E13. Expecting Si nanocrystals in this film. But TEM images show that Ag is distributed fairly uniformly across the SiO_2 layer. No concentration gradient is observed. No crystalline Si particles could be detected.

The following samples are yet to be characterized:

1) Sample ID: **3509M800**. This sample is a Ge+SiO_2 composite film prepared by using RF sputtering and subjected to microwave annealing at 800^0C. We are expecting Ge nanocrystals embedded in SiO_2 matrix in these samples.

2) Sample ID: **3514M900**. This is a GeO_x film. The reactive sputtering was performed in an Argon and oxygen atmosphere. Eventually, this sample is subjected to microwave annealing at 900^0C. We are expecting GeO_2 nanocrystals in this film.

Proposal 2010-004-000365

Metallic Micro Nailheads MAde by LiG process - MiNiMAL

Felix Greiner

Technische Universität Darmstadt
Darmstadt
Germany

Final Report

1. Project goals:

Micro- and nanowires with high aspect ratios, arranged as slim and tall standing metal pillars offer promising features for micro systems. The goals are:

- 1st fabrication of high aspect ratio out of plane metal wires next to low aspect ratio metal blocks,
- 2nd multilayer material link of these structures,
- 3rd realization and characterization of an acceleration sensor applying these structures.

The KNMF services refer to the fabrication of aligned templates made by X-ray lithography (1st point), referred by *X-ray template*. The remaining process steps are to be processed at Technische Universität Darmstadt (TUD), see Fig. 1.

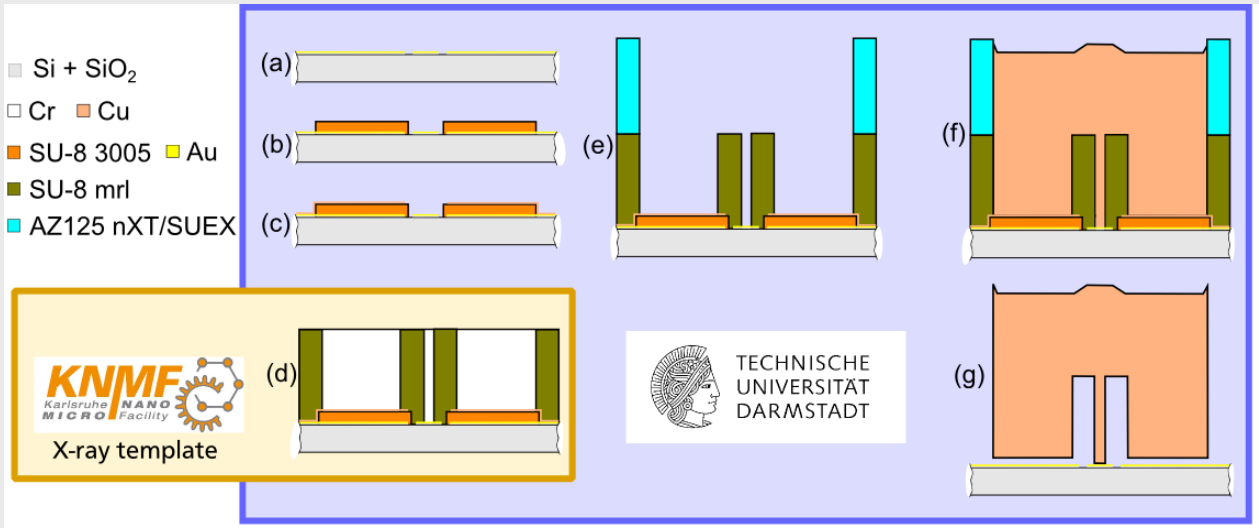

Fig. 1: Process flow: (a) - (c) UV lithography at TUD; (d) Aligned X-ray lithography at KNMF for X-ray template; (e) UV lithography at TUD; (f) Electroforming at TUD; (g) Photoresist removal and etching at TUD.

The high aspect ratio templates (*X-ray template*) provide vertical cylindrical holes with aspect ratios from 16 to 33 next to template openings with low aspect ratios (Fig. 1 d). X-ray lithography is the only technique suitable for the fabrication of these templates.

For the second goal, structures beneath and above the *X-ray template* are necessary. Beneath, there are structured circuit paths (Fig. 1 a), sacrificial layers (Fig. 1 b), and seed layers (Fig. 1 c). Above, there is a low aspect ratio electroforming template (Fig. 1 e). They contribute to the functional integration of all structures into an electroformed accelerometer MEMS (Fig. 1 f).

For the third goal, the wafers are to be cut, the electroforming templates and the sacrificial layers are to be removed (Fig. 1 g), the dies are to be connected to evaluation electronics and a sensor characterization is to be executed.

2. Project results:

For the 1st goal, an intermediate mask and a working mask have been fabricated (Fig. 2 c). For the functional link of the structures defined by the *X-ray template*, an aligned X-ray exposure is essential. Therefore, alignment structures (crosses) have been foreseen in the first layer (circuit paths, Fig. 1 a) and in the second layer (seed layer, Fig. 1 c; Fig. 2 a and b). Furthermore, the crosses to be aligned have been structured into the X-ray working mask for optical alignment.
The layers beneath and above the *X-ray template* considerably influence the whole process flow and the MEMS functionality. There is an important risk that all project effort does not bring forth the tertiary goal of a working MEMS. For the reduction of this risk, in parallel to this project there has been intensive effort at TUD for the realization of a similar MEMS applying only UV lithography. This approach significantly decelerated the work on the topic KNMF project. Recently, the UV lithography based process flow has been shown [1], enabling the KNMF project to be executed.
Four wafers with structures beneath the *X-ray template* according to Fig. 1 a-c and Fig. 2 a, b have been fabricated (Tab. 1 and Fig. 2).
The wafers FG310 (Fig. 2 a, b, d) and FG311 (Fig. 2 e, f) have been manufactured completely; the results are presented in [2].

Tab. 1: Wafers and their status sorted by their processing order (process step names referring to Fig. 1).

Wafer-ID	Status
FG312	•a-c: layers in **bad** condition •d: SU-8 mrl structured with 15 µm alignment error •e: skipped •f: very inhomogeneous electrodeposition due to issues in current control and electrolyte additive control •Chip separation: bad adhesion to dicing tape
FG312	•a-c: layers in **bad** condition •d: SU-8 mrl structured with well aligned X-ray exposure
FG310 Fig. 2 a, b, d	•a-c: layers in **good** condition •d: SU-8 mrl structured with **well aligned** X-ray exposure •e: SUEX 200 µm structured with good adhesion •f: Microcrystalline electrodeposition, but adhesion issue of SU-8 mrl •Chip separation: good adhesion to dicing tape
FG311 Fig. 2 e, f	•a-c: layers in **good** condition •d: SU-8 mrl structured with **well aligned** X-ray exposure •e: AZ 125 nXT structured with good adhesion •f: No adhesion issue of SU-8 mrl, but granular crystalline electrodeposition •Chip separation: good adhesion to dicing tape •g: complete removal of polymer material, but issue to etch the seed layer

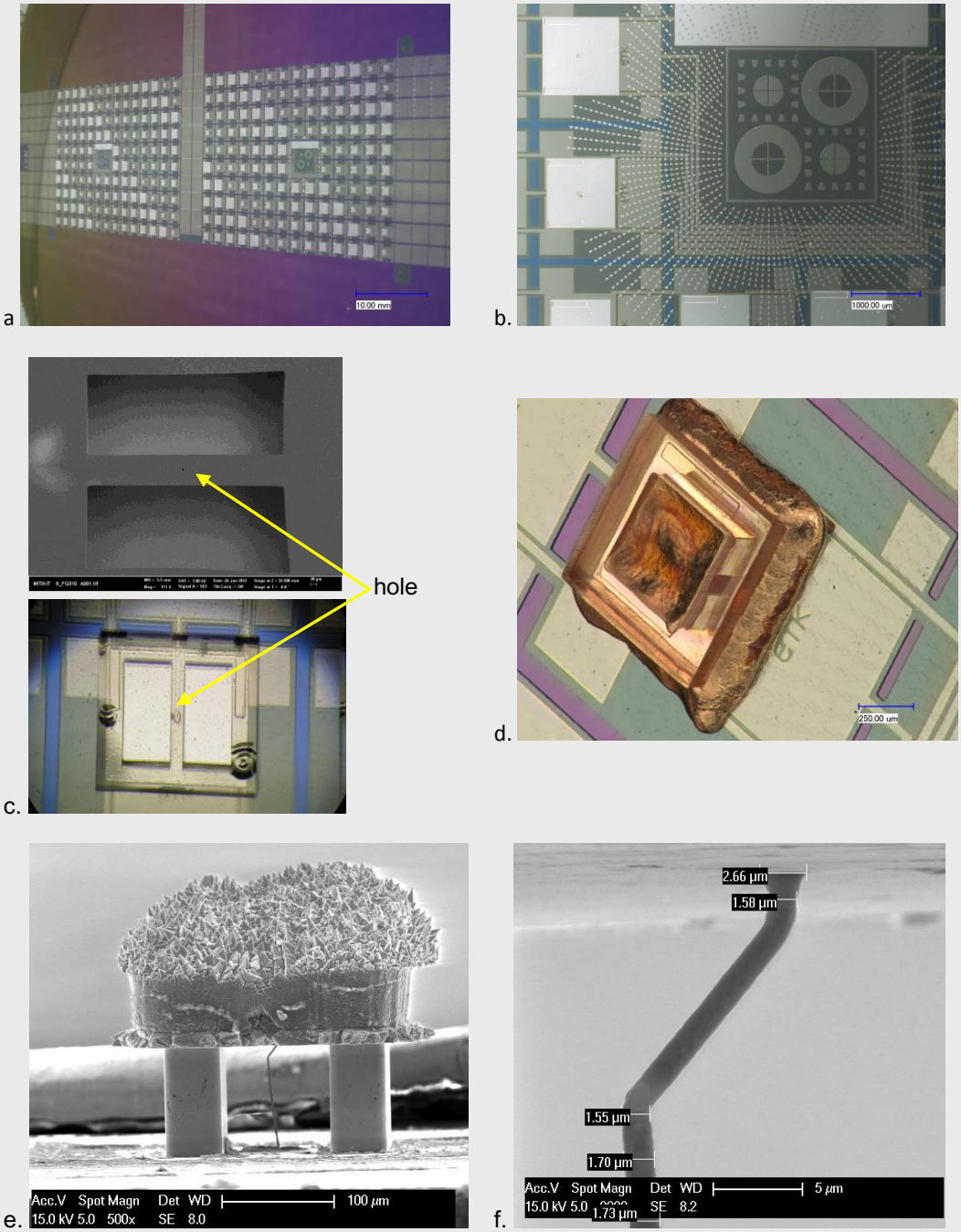

Fig. 2: Microstructures realized in the KNMF 2010-004-000365 project: (a) FG310 before application of SU-8 mrl, (b) Detail of (a) showing structures for X-ray exposure alignment, (c) example of an *X-ray template* after X-ray exposure and development, (d) FG310 with structured SU-8 mrl (X-ray) and SUEX (UV) after copper electroforming, (e) Copper structure of FG311 after final polymer removal in R3T at TUD, (f) Detail of (e) showing the buckled wire (designed diameter: 3 µm).

Karlsruhe Nano Micro Facility (KNMF)
Karlsruhe Institute of Technology (KIT)
Hermann-von-Helmholtz-Platz 1
76344 Eggenstein-Leopoldshafen
Germany

User Office
Phone: +49 (721) 608-23123
Fax: +49 (721) 6082-26273
Email: knmf-useroffice@kit.edu
Web: www.knmf.kit.edu

Wafers FG312 and FG313 show a rough surface due to processing issues of the sacrificial layer (Fig. 1 b). They have been used for testing the aligned X-ray exposure and the wafer dicing. Two main issues still remain before the MEMS can prove to work as an inertial sensor:

1. The structures (columns) on the X-ray exposure mask are approximately 1 µm smaller than designed. Therefore, the vertical wire is less robust and buckles (Fig. 2 e, f). Hence, the mass load has to be reduced and the process steps in Fig. 1 g have to be designed for a better wire protection. The *mass load reduction* can be achieved by a reduced electroforming height in Fig. 1 f. The process steps can more efficiently *conserve the wire*, if the seed layer is designed differently. The connection from the bottom circuit path on top of the seed layer currently runs at the outer edges of the mass block (Fig. 3 a). There, it has to be wet etched for an efficient removal of the sacrificial layer. This step can be omitted, if the connection from the circuit path to the seed layer runs at the inner edges of the mass block (Fig. 3 a).
2. The electrodeposition shows to be inhomogeneous due to the design of the circuit path layer. The circuit path layer shows substantial resistances and it delivers the electrodeposition current. A layer redesign including local thickening can solve this problem (Fig. 3 b).

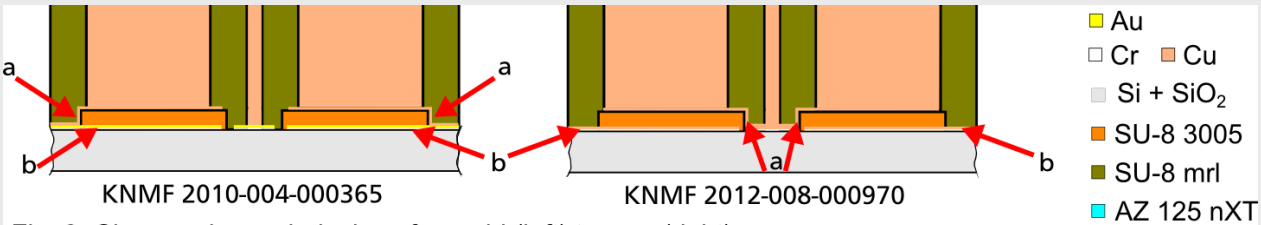

Fig. 3: Changes in mask designs from old (left) to new (right):
(a) Seed layer connecting the top of the sacrificial layer from outer edges to inner edges.
(b) Circuit path material from Au (150 nm) to Cu (300 nm + thickened regions of 3 µm),

Both improvements shown in Fig. 3 have been successfully implemented for the UV lithography approach at TUD and are scheduled in the KNMF proposal 2012-008-000970.

3. Publications:

[1] F. Greiner and H. Schlaak, "High aspect ratio metal micro and nano pillars for minimal footprint MEMS suspension," *Microsystem Technologies*, 2012, DOI 10.1007/s00542-012-1659-x.

[2] F. Greiner, S. Quednau, F. Dassinger, R. Sarwar, H. F. Schlaak, M. Guttmann, and P. Meyer, "Fabrication techniques of multiscale 3D-MEMS with vertical metal micro- and nanowire integration," *J. Micromech. Microeng.*, submitted, 2012.

4. Comments:

The aligned X-ray exposures done by F J Pantenburg and P Meyer are greatly acknowledged. A KNMF project could profit by a scholarship for the person in charge, similarly to projects running at GSI Helmholtz Center of Heavy Ion Research.

Proposal 2010-004-000368

Injection-molded photonic crystal slabs for surface contrast microscopy

Yousef Nazirizadeh

Christian-Albrechts-Universität zu Kiel (CAU)
Kiel
Germany

Final Report

1. Project goals (max. 1.800 characters)**:**

Photonic crystal slabs (PCS), which are composed of a periodic nanostructure in a high index layer (see image below), become in recent years more and more a powerful tool in label-free bio-photonics. In molecular interaction experiments they serve as the sensor surface. On the other side in microscopy the PCS can be used as the specimen holder and allows advances in microscopy, e.g. contrast enhancement or topography measurements of objects on the surface. As working in a sterile environment is crucial for many experiments the PCS has to be designed as a disposable. In this project we investigated injection molding as the fabrication method for the nanostructure, which promise a simple and cost-efficient method for mass fabrication of these structures.

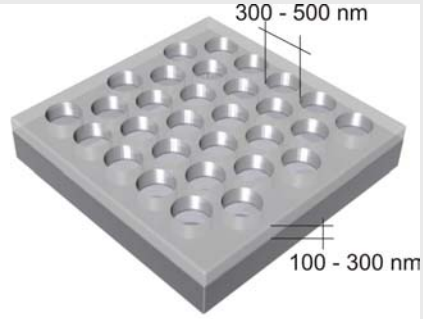

Photonic crystal slab

2. Project results (max. 7.000 characters + figures)**:**

We could successfully fabricate PCSs using injection molding. In Fig. 1 the fabrication procedure is shown. After the transformation of the nanostructure into a nickel mold, hot PMMA was injected in the injection molding tool, composed of the nickel mold and sidewalls. After cooling down the tool was opened and the nanostructured substrate was obtained (Fig. 1(a)). In a sputtering process a Ta2O5 layer was deposited on the substrate. The result is show in Fig 1 (b and c) as a SEM and digital image of the nickel mold and its PMMA replica.

Karlsruhe Nano Micro Facility (KNMF)
Karlsruhe Institute of Technology (KIT)
Hermann-von-Helmholtz-Platz 1
76344 Eggenstein-Leopoldshafen
Germany

User Office
Phone: +49 (721) 608-3123
Fax: +49 (721) 608-6273
Email: knmf-useroffice@kit.edu
Web: www.knmf.kit.edu

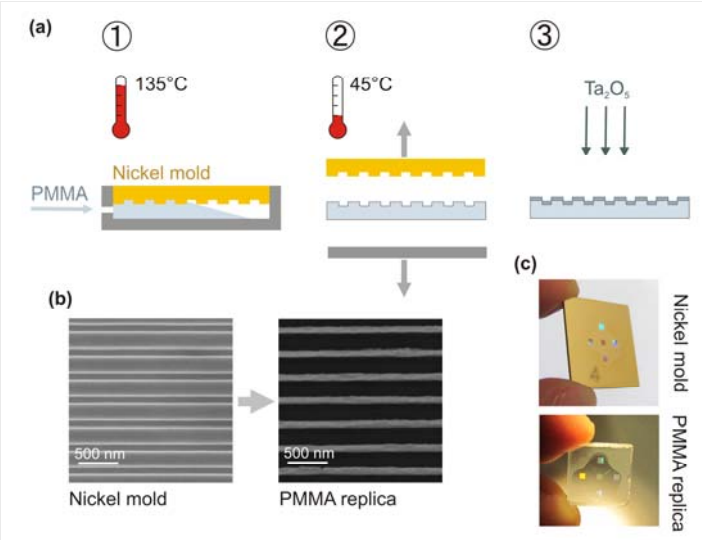

Fig. 1 (a) Sketch of PCS fabrication using injection molding and sputtering. (b and c) SEM and digital images of the nickel mold and the replica of it.

The sensitivity of PCSs is one of the most important parameters, which is the resonance shift divided by the refractive index change of the surface. As the resonance shift is usually the signal, the higher the sensitivity the better the performance for the bio-photonic application. Here we investigated the influence of geometric parameters of the PCS on the sensitivity. In Fig. 2 experimental data and simulations are shown. We observe that the sensitivity is the highest for a slab thickness of 99nm and a duty cycle of 0.7.

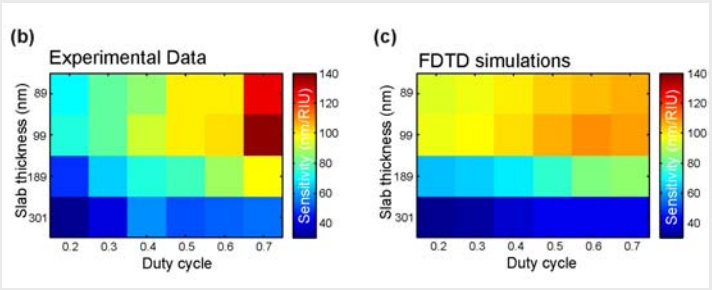

Fig. 2 (b) Experimental bulk sensitivity as a function of high index slab thickness and periodicity duty cycle. (c) Experimental bulk sensitivity as a function of high index slab thickness and periodicity duty cycle.

3. Publications (please stick to the user guidelines for publications and acknowledgements on www.knmf.kit.edu):

[1] Yousef Nazirizadeh, Florian von Oertzen, Klaus Plewa, Nicole Barié, Peter-Jürgen Jakobs, Markus Guttmann, Harald Leiste, and Martina Gerken, "Sensitivity optimization of low-cost photonic crystal slabs for biosensing applications" in preparation.

[2] Nicole Barié, Markus Guttmann, Peter-Jürgen Jakobs, Harald Leiste, Yousef Nazirizadeh, Klaus Plewa, and Martina Gerken, “Novel Process Chain for Mass Fabrication of Nanostructured Low-cost Photonic Crystal Slabs”, in preparation.

4. Comments (max. 1.800 characters)**:**

We enjoyed the cooperation with the KNMF and the KIT. The KNMF provides a win-win situation for both parties, which results in this case in potentially two papers.

Karlsruhe Nano Micro Facility (KNMF)
Karlsruhe Institute of Technology (KIT)
Hermann-von-Helmholtz-Platz 1
76344 Eggenstein-Leopoldshafen
Germany

User Office
Phone: +49 (721) 608-3123
Fax: +49 (721) 608-6273
Email: knmf-useroffice@kit.edu
Web: www.knmf.kit.edu

Proposal 2010-004-000369

Fabrication of optimized diffraction gratings for differential phase contrast imaging on a compact setup

Thomas Thüring

Paul Scherrer Institut
Villigen PSI
Switzerland

Final Report

1. Project goals (max. 1.800 characters):

The goal of this proposal is to optimize the parameters of bendable phase gratings to maximize the visibility on a compact Talbot interferometer.
Under perfect coherence conditions, visibility maxima are located at odd Talbot orders (m=1,3,5,...). If the coherence becomes critical, these maxima are damped and shifted upstream. We optimized the inter-grating distance for a maximum visibility by using software simulation tools. It turned out that the visibility maximum is not necessarily at exact odd Talbot orders.

With the optimized gratings, we believe that a remarkable improvement for DPC imaging with a compact setup and only 2 gratings can be achieved. For example at 40keV photon energy, the theoretical results predict a visibility increase of approximately 50% compared to gratings fabricated at exact odd Talbot orders. Earlier experiments verified, that in general, a visibility below 10% is insufficient for reasonable imaging

2. Project results (max. 7.000 characters + figures):

The fabricated gratings with the optimized parameters lead to the expected visibility increase and could dramatically improve the performance of the imaging system. With a total source to detector distance of approx. 340mm, we were able to design the most compact grating interferometer setup ever.
Although the visibility could be increased, we are still below the desired 10%. Therefore, further optimizations of the system design parameter and the grating quality are still necessary.
In a next step, the sensitivity of the system might be further increased by changing from a Talbot interferometer to a Talbot-Lau type (includes a source grating). This solution will be evaluated next.

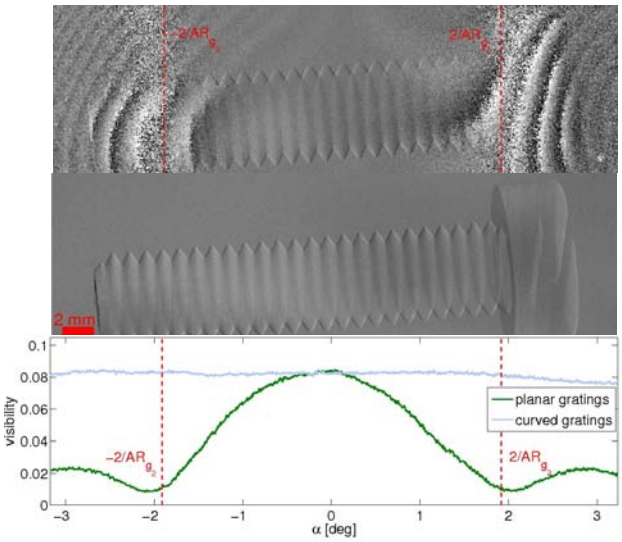

Karlsruhe Nano Micro Facility (KNMF)
Karlsruhe Institute of Technology (KIT)
Hermann-von-Helmholtz-Platz 1
76344 Eggenstein-Leopoldshafen
Germany

User Office
Phone: +49 (721) 608-3123
Fax: +49 (721) 608-6273
Email: knmf-useroffice@kit.edu
Web: www.knmf.kit.edu

3. Publications (please stick to the user guidelines for publications and acknowledgements on www.knmf.kit.edu)**:**

T. Thüring, P. Modregger, T. Grund, J. Kenntner, C. David, and M. Stampanoni, Applied Physics Letters 99, 041111 (2011)

4. Comments (max. 1.800 characters)**:**

Karlsruhe Nano Micro Facility (KNMF)
Karlsruhe Institute of Technology (KIT)
Hermann-von-Helmholtz-Platz 1
76344 Eggenstein-Leopoldshafen
Germany

User Office
Phone: +49 (721) 608-3123
Fax: +49 (721) 608-6273
Email: knmf-useroffice@kit.edu
Web: www.knmf.kit.edu

Proposal 2010-004-000370

Interface effects on magnetic moments in multilayers

Inga Ennen

Technische Universität Wien
Vienna
Austria

Summary Report

1. Project Objectives (250 words)

The main objective of the experiment was the investigation of magnetic moments at the interface between magnetic and nonmagnetic materials with a high lateral resolution. Therefore, the electron energy loss magnetic chiral dichroism (EMCD) effect has been used which exploits faint differences in the double-differential scattering cross section of the electrons in the diffraction plane of a transmission electron microscope (TEM).
We planned to investigate two different thin film samples: a half-metallic Heusler compound which is of great technological interest for spintronic applications and, furthermore, a ferromagnet (FM)/ nonmagnet (NM) multilayer (e.g. Fe/Au) with different layer thicknesses for a more systematic study of the influence of layer thickness on the magnetic moments at the interface.

2. Project Achievements (1000 words + figures)

For the experiments we chose a Ni_2MnSn Heusler compound which is currently worldwide under strong investigations due to its shape memory properties. The 100 nm thick layer of the Heusler alloy has been grown by sputter deposition onto a MgO substrate and covered by a thin MgO layer. A cross section sample has been prepared by a classical grinding and ion milling process. A Co/Cu multilayer has been used as an example for the FM/NM system. This multilayer is easier to grow epitaxially than the Fe/Au multilayer mentioned in the proposal. Unfortunately, the sample turned out to be not suitable for the planned experiment, because a slight oxidation occurred during transport and the followed plasma cleaning process which has caused the formation of a polycrystalline film on the surface of the specimen. Therefore, we have concentrated on the detailed analysis of the technologically more interesting Heusler sample.
At first, the crystallinity of the sample especially in the interface region between the Ni_2MnSn layer and the MgO substrate has been investigated by high resolution (HR-) TEM and selected area electron diffraction. In the HRTEM image (Fig. 1) the lattice planes and steps in the MgO substrate oriented in the [001] direction can be seen nicely.

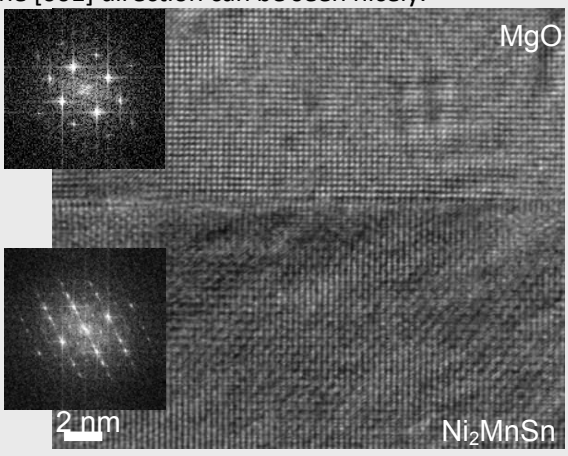

Fig. 1: Aberration corrected HRTEM image of the interface between the MgO substrate and the Ni_2MnSn layer. Insets: Corresponding Fourier transformed images.

To perform an EMCD experiment in the scanning mode of the TEM (STEM) the sample has been tilted

into the three beam case (3BC) by minimizing the excitation error. The convergence angle has been changed to α= 3.25 mrad to ensure that the diffraction discs in STEM geometry do not overlap. Afterwards the axis of the 3BC has been aligned perpendicular to the energy dispersive axis of the energy loss spectrometer (see Fig. 2). This has been done by a reorientation of the specimen in the sample holder and by a slight manual change of the currents of the projector lenses. The diffraction discs have been shifted out of the 2 mm spectrometer entrance aperture (SEA) in order to select one half of the symmetry plane defined by the axis of the 3BC. Hereby, the differences of the chirality in the electron energy loss spectra (EELS) become visible.

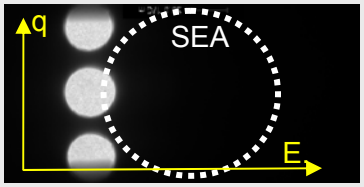

Fig. 2: Diffraction image of the sample tilted in three beam condition. The axis of the diffraction spots (q) has been aligned perpendicular to the energy dispersive axis (E) of the spectrometer. The position of the spectrometer entrance aperture is indicated by the white dashed circle.

After this time consuming adjustment of the best configuration of sample and microscope settings, series of EDX and simultaneous EELS line scans in the above described EMCD geometry have been carried out for seven different sample thicknesses. An integration time of 4 s for each spectrum has been used to minimize beam damage of the specimen.
In Fig. 3 an example of an EEL spectrum extracted from a line scan consisting of 30 measurements at a sample thickness of approximately 25 nm is shown (left images). By extracting intensity profiles at the marked positions A and B of the spectrum the dichroic signals can be determined to be about 16 % at the Ni L_3-edge and 9 % at the Mn L_3-edge.

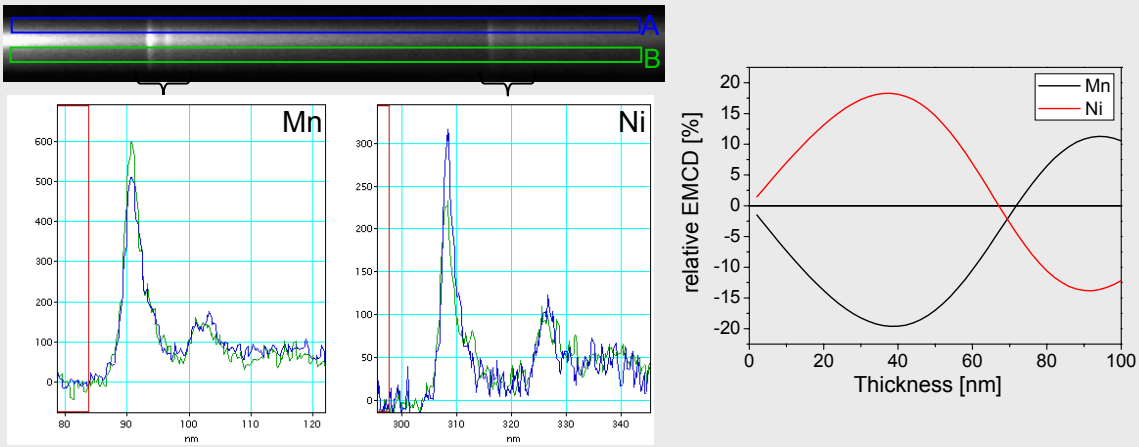

Fig. 3: Left: Example of an EEL spectrum measured during a line scan (upper image). Intensity profiles have been taken from the rectangles A and B which indicate the regions of different dichroic signs ("EMCD positions"). An integration size of 30 pixel have been chosen for the integration to improve the signal to noise ratio in the lower images. They show the extracted EEL spectra at the Mn and the Ni L-edge for both EMCD positions A and B. Right: Calculated thickness dependence of the dichroic signal.

Interestingly, the dichroic signal of Mn and Ni shows a different sign (at the Ni L_3-edge: signal A shows the larger amplitude; at the Mn L_3-edge: signal B is higher). This reversal of the sign of the dichroic signal has been expected from simulations of electron Bloch waves in this material. It originates from

the specific position of the Ni and Mn atoms in the unit cell. The calculated dependence of the EMCD signal from the sample thickness for Mn and Ni is given on the right hand side of Fig. 3.
The results of a total line scan are summarized in Fig. 4, where the EDX analysis and the corresponding EMCD measurements for Mn and Ni are given. Although the EMCD measurements are quite noisy, it can be seen that an enhanced dichroic signal can be observed in the interface regions. This may be attributed to a higher Mn content in this area which has been found in the EDX investigations.
The question whether interface effects play a major role in the enhancement of the magnetic signal or whether this enhancement is exclusively due to the variation of the alloy composition and, therefore, the density of states is subject of ongoing simulations.

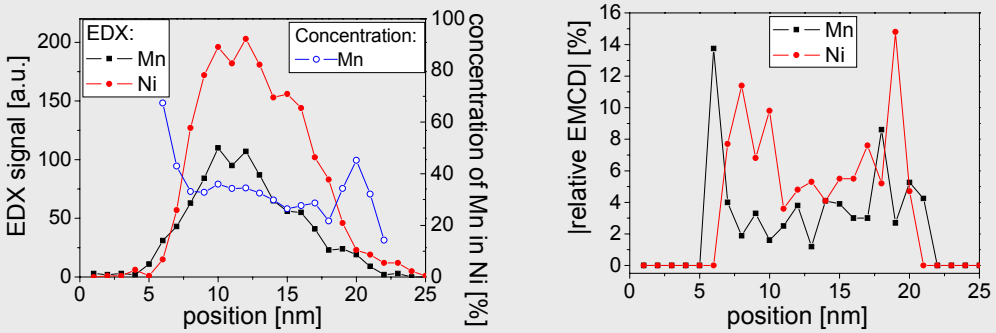

Fig. 4: Left: EDX concentration profile for Ni (red) and Mn (black). The blue curve belongs to the right scale and shows the corresponding Mn concentration in Ni. Right: Modulus of the corresponding EMCD signal.

Finally, we can conclude that we have performed successful EMCD experiments on a Ni_2MnSn specimen with a Titan microscope. For the first time a reversal of the EMCD amplitude within one elementary cell has been observed as it has been predicted for this material by theory. Furthermore, the strong dependence of the EMCD signals and, thus, the magnetic moments on the local composition of the alloy can be figured out by the correlation of the measured EMCD/ EDX signals and corresponding simulations.

3. Instruments Used (comma separated)

FEI Titan

4. Publications
Please note that the following acknowledgement has to be included in journals, proceedings, presentations and at any other public publications: "*We acknowledge the Karlsruhe Nano Micro Facility (KNMF, www.kit.edu/knmf) of the Forschungszentrum Karlsruhe for provi-sion of access to instruments at their laboratories and we would like to thank x for assistance in using laboratory y.*"

to be published	• EMCD study of Ni_2MnSn

published	•

5. Comments (250 words)

It was a great pleasure to work with the experimental team of the TITAN microscope. The great experimental experience and knowledge of the microscope of Christian was of enormous help.

Proposal 2010-004-000374

Multi-period nanostructured OLEDs for enhanced outcoupling efficiency

Michael Rädler

Christian-Albrechts-Universität zu Kiel (CAU)
Kiel
Germany

Final Report

1. Project goals (max. 1.800 characters):

The goal of the project was to investigate experimentally a new outcoupling structure for organic light-emitting diodes (OLEDs). Due to waveguiding of the high-index OLED stack, the OLED outcoupling efficiency is limited. Bragg gratings near the emitting layer can increase the light outcoupling by scattering of guided modes, but lead to unwanted angular features in the emission spectrum. In this project, compound binary Bragg gratings that combine multiple space frequencies were investigated for their use in organic light-emitting layers. The resulting angular spectral emission and color impression were in focus of this project.

2. Project results (max. 7.000 characters + figures):

The KNMF fabricated two nickel shims that comprised 49 different gratings, providing a large parameter space. Each grating was of 300µm * 300µm size. The compound gratings were designed as the superposition of multiple binary gratings with different periods as depicted in Fig. 1(a). The grating profiles were combined by a logical disjunction operation yielding again a binary grating. The master structures on nickel shims were fabricated by electron beam lithography with a grating depth of 100 nm. A scanning electron microscope (SEM) image of a nickel shim with periods of 350 nm and 450 nm is exemplary shown in Fig. 1(b).

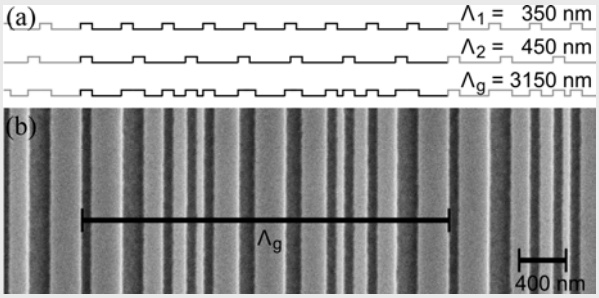

Fig. 1 (a) Two binary gratings with periods of 350 nm and 450 nm are combined by a logical disjunction operation yielding a compound binary grating with the least common multiple period of Λg=3150 nm. (b) SEM image of the compound grating nickel master stamp.

The nickel shims could be successfully used as master stamps in our nanoimprint lithography (NIL) process. NIL was used to transfer the grating structures into 100-nm emission layer of phenylene substituted poly(para-phenylenevinylene) (superyellow, Merck), an organic light-emitting polymer. The photoluminescent emission spectra were subsequently measured by means of a goniophotometer.

It could be shown that each period component produces two outcoupling features due to first-order Bragg scattering of the TE0 guided mode (Fig. 2).

Karlsruhe Nano Micro Facility (KNMF)
Karlsruhe Institute of Technology (KIT)
Hermann-von-Helmholtz-Platz 1
76344 Eggenstein-Leopoldshafen
Germany

User Office
Phone: +49 (721) 608-3123
Fax: +49 (721) 608-6273
Email: knmf-useroffice@kit.edu
Web: www.knmf.kit.edu

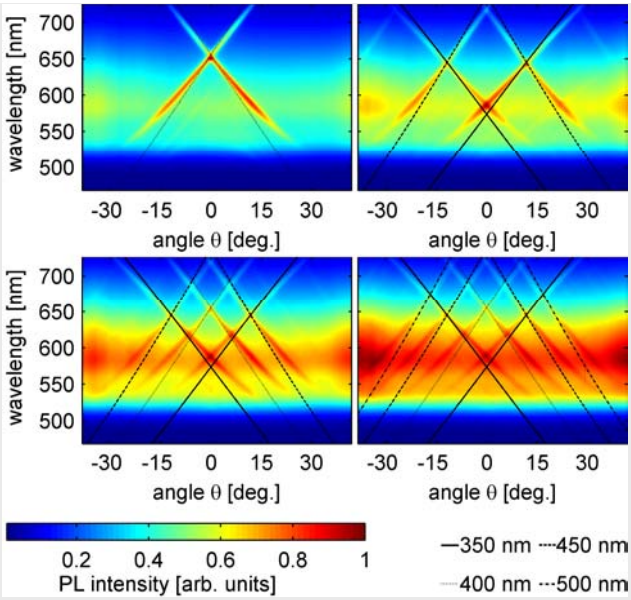

Fig. 2 Angle-resolved PL spectra of samples with (a) one period component of 400 nm, (b) two superimposed grating periods of 350 nm and 450 nm, (c) three superimposed grating periods of 350 nm, 400 nm and 450 nm, and (d) four superimposed period components of 350 nm, 400 nm, 450 nm, and 500 nm. The lines indicate the calculated Bragg scattering of the TE0 mode for an effective waveguide index of 1.69 at the period components (legend in the lower right). An increased number of period components increases the number of waveguide outcoupling features.

The extraction of several wavelength components at a single emission angle reduces angle-dependent color effects. The averaged angular color change is reduced by up to a factor of 11 compared to a single-period grating structuring.

3. Publications (please stick to the user guidelines for publications and acknowledgements on www.knmf.kit.edu):

[1] C. Kluge, M. Rädler, A. Pradana, M. Bremer, P.-J. Jakobs, N. Barié, M. Guttmann, and M. Gerken, „Extraction of guided modes from organic emission layers by compound binary gratings“, Opt. Lett., **37**, pp. 2646–2648, 2012.

4. Comments (max. 1.800 characters):

The KNMF is a valuable facility for high-quality nanostructures. We like to thank the KNMF team for the fruitful collaboration.

Proposal 2010-005-000387

Point defect concentrations in nanocrystalline metallic films

Harald Schmidt

Technische Universität Clausthal
Clausthal-Zellerfeld
Germany

Summary Report

1. Project Objectives (250 words)

Thin metallic films with a thickness in the nanometer range are important for various areas of science and technology: microelectronics, optoelectronics, data storage, micro-electromechanical systems (MEMS), catalysts, hard and abrasive coatings and environmental and chemical protection. Devices in these fields all depend critically on the microstructure and the stability of thin metal films deposited on appropriate substrates. Important characteristics are residual stress and strain, which often develop in film/substrate combinations. An unfavorable consequence of high stress is crack formation, local plastic deformation and layer delamination. Consequently, an understanding and controlling of stress in thin films is an important task in modern technology. Isothermal annealing at temperatures close to room temperature leads to stress/strain relaxation and a structural re-organization of the material. Such anneals are governed by a substantial change in point defect concentration (defect annihilation or creation).

The overall aim of the present research project is a quantitative experimental investigation on the modification of vacancy concentration during stress relaxation in nano-crystalline metallic films, using Platinum films as model system. These experiments are carried out using scattering methods at synchrotron facilities. For a reliable data interpretation, a characterization of the nanostructure and of the bonding properties during isothermal annealing is indispensable. This was the aim of the present KNMF proposal.

2. Project Achievements (1000 words + figures)

Samples: Pt films with a thickness of about 40 nm are deposited by magnetron sputtering on pre-oxidized (400 nm) silicon wafers. Annealing of the samples is carried out in a vacuum of about 3 x 10^{-6} mbar at a temperature of 130, 180, 300 and 400 °C for several hours.

TEM characterization: Measurements were one using a FEI Titan 80-300 microscope with Cs correction at 300 kV. The samples were investigated in cross-sectional geometry prepared by FIB and in plain view geometry, using BF-TEM, DF-TEM, HR-TEM and STM-HAADF in combination with SAED.

Fig. 1 shows selected images of the Pt layers. The as-deposited sample (Fig. 1 a-d) is nano-crystalline. A nanostructure is visible that is composed of columnar grains, which are oriented perpendicular to the sample surface. The grains have a diameter of 10 – 20 nm in the film plane and a thickness of approximately 40 nm corresponding to the film thickness. The columnar grain structure is not developed over the whole film in any cases. Tilting of grains is also observed. During annealing up to 180 °C the grain structure is unchanged in good approximation, meaning that no significant grain growth processes take place. At 400 °C significant anomalous grain growth parallel to the film surface is observed. Further, a reorientation of the grains is found leading to the formation of a well-developed (111) texture as proven by SAED. Up to 180 °C, where a stable nano-structure is present, time resolved modifications of strain and vacancy concentration were investigated by X-ray scattering methods. A stable nano-structure is the premise for a reliable data acquisition and a straightforward data interpretation.

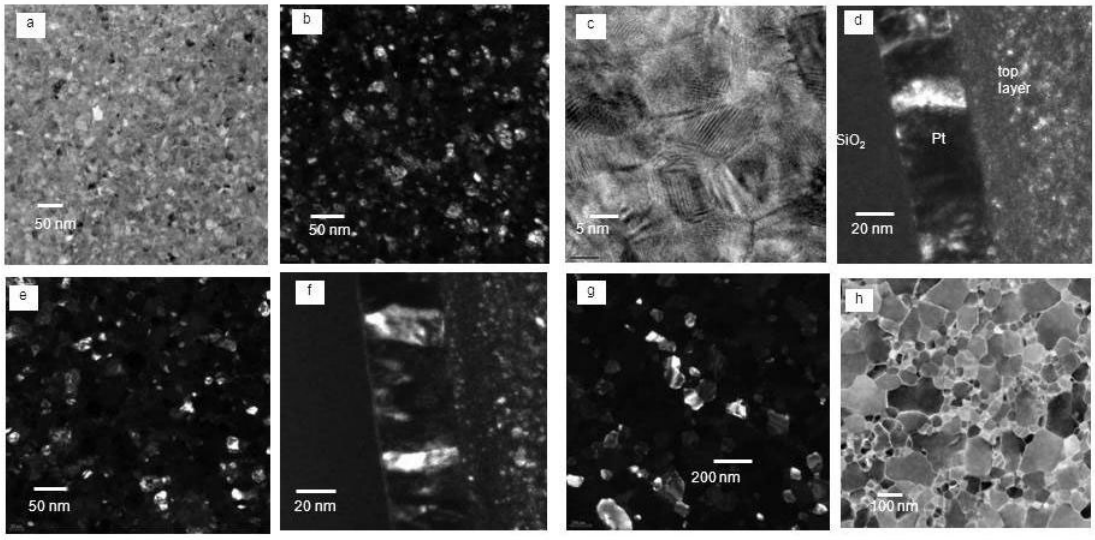

Abb. 1 TEM images of Pt films. (a) as-deposited (plain view, STEM), (b) as-deposited (plain view, DF-TEM), (c) as-deposited (plain view, HR-TEM), (d) as-deposited (cross-sectional view, DF-TEM), (e) 180 °C (plain view, DF-TEM), (f) 180 °C (cross-sectional view, DF-TEM), (g) 400 °C (plain view, DF-TEM), (h) 400 °C (plain view, STM-HAADF).

XPS characterization: A K-Alpha XPS Spectrometer was used using a monochromatic AlK_α X-ray source with a spot size of 400 µm and an energy resolution < 0.5 eV at 500 eV Ar+ ion energy.

For the as-deposited Pt film the only elements detected at the surface were carbon, platinum and oxygen. High resolution XPS spectra were recorded and the fitting procedure was done using the peak form of a Pt reference. XPS peaks at a binding energy of 71.1 and 74.4 eV were found, corresponding to Pt $4f_{7/2}$ and Pt $4f_{5/2}$ emissions of Pt^0, identical to those of the reference. Comparison to literature [1,2] gives that peaks that correspond to PtO, $Pt(OH)_2$ or PtO_2 species should be shifted to higher energies by 1.5 to 3 eV. Such lines are not observed, excluding the presence of platinum oxide at the surface.

For O1s, a single peak is visible which can be fitted by two lines located at 531.2 and 532.7 eV and for C1s, three lines at 284.7 (main line), 286.5 and 288.3 eV (satellites) are present. By comparison to Ref. 2 the following conclusion can be drawn. The peaks at 532.7 and 286.5 eV correspond to chemisorbed CO. The peak located at 531.2 eV might be from chemisorbed CO_2, COOH or O_2. In the C1s spectra no indication of CO_2 at 291.0 eV is found, however, COOH species correspond to the peak at 288.3 eV. The peak at 284.7 eV might be due to elemental carbon. Adsorbed water is not detected.

Annealing at 130 °C leaves the peak position nearly unchanged, while the amount of CO is slightly enhanced. At 300 °C all peaks are shifted to higher values by about 0.2 – 0.5 eV, indicating a stronger surface interaction. Further the amount of CO species rises. Element depth profiles recorded for Pt, O and C exhibit no significant difference for the different temperatures. The O signal of the adsorbed species vanishes within the first 0.3 nm to a background level of less than 1 at. % oxygen, indicating that only a mono-layer of adsorbed species is present. The main result of XPS is that an oxid formation at the film surface can be excluded during annealing up to 300 °C.

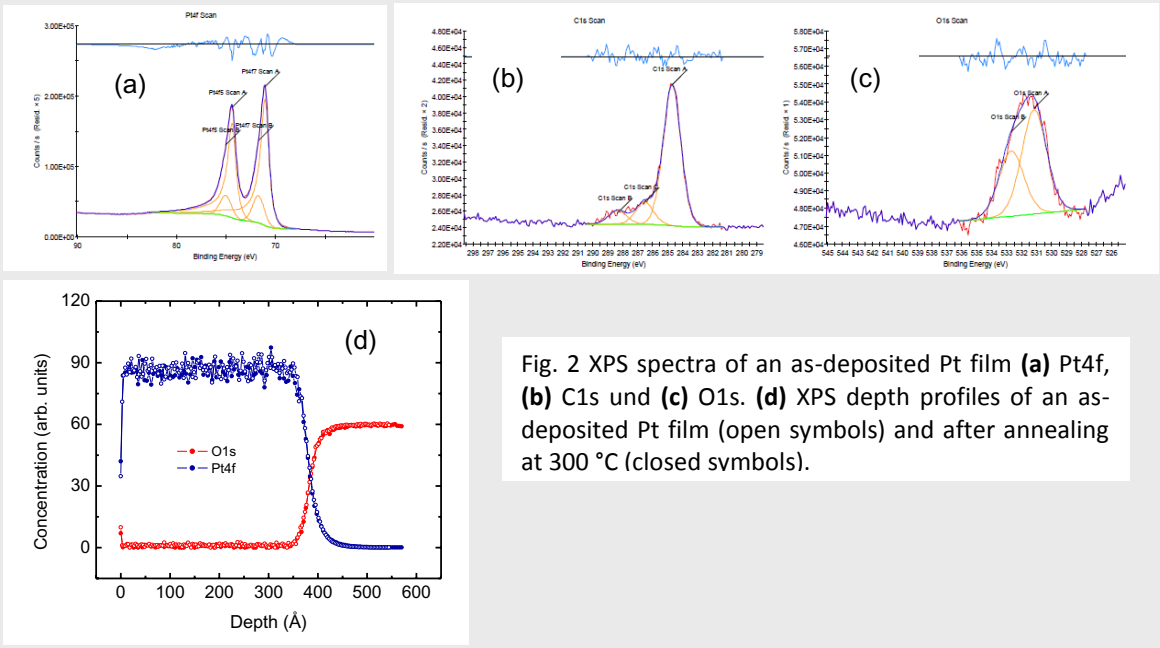

Fig. 2 XPS spectra of an as-deposited Pt film **(a)** Pt4f, **(b)** C1s und **(c)** O1s. **(d)** XPS depth profiles of an as-deposited Pt film (open symbols) and after annealing at 300 °C (closed symbols).

[1] http://srdata.nist.gov/xps/main_search_menu.aspx
[2] M. Huang, A. Adnot, S. Suppiah, S. Kaliaguine, J. Molec. Catalys. A 104 (1995) L131.

3. Instruments Used (comma separated)

Transmission Electron Microscopy, Focused Ion Beam, X-Ray Photoelectron Spectroscopy

4. Publications

to be published	•
published	• W. Gruber, S. Chakravarty, C. Baehtz, W. Leitenberger, M. Bruns, A. Kobler, C. Kübel, *Strain relaxation and vacancy creation in thin platinum films,* Physical Review Letters **107** (2011), 265501.

5. Comments (250 words)

Proposal 2010-005-000399

Solvothermal conversion of T1 cadmium thiophenolates into a crystalline superlattice of the largest characterized CdS nanoclusters

John Corrigan

The University of Western Ontario
London
Canada

1. Project goals

Low-dimensional semiconductor structures (*e.g.*, nanoparticles and their assemblies) have been attracting increasing attention due to their unique size-dependent electronic properties, making them excellent candidates for usage in optical and electronic devices. The optimal development of the technologies is often hampered by the variation of size and shape (polydispersity) of the semiconductor nanoparticles that are incorporated in them. One route to circumvent polydispersity may lie in the synthesis of nanoclusters – particles with exactly the same size, shape, and surface chemistry. A principle limitation in size using established preparative methods still exists, and the largest isolated tetrahedral CdS nanoclusters ($[Cd_{54}S_{32}(SPh)_{48}L_4]^{4-}$) are 1.9 nm in size.

We are developing a novel approach to the synthesis and crystallization of large monodisperse CdS nanoclusters. We expect to demonstrate that formation of CdS nanoclusters larger than 2 nm can be achieved by simple, thermally induced conversion of the single-source T1 cadmium thiophenolate precursor in the presence of alkylammonium salts. Our preliminary results show, that the developing approach is efficient for fine tuning of the size of CdS nanoclusters. Comprehensive characterization of the 3D arrangement of these monodisperse systems requires state-of-the-art electron microscopy facilities.

Using KNMF facilities (HRTEM and STEM) it was planned to determine the size of monodisperse CdS nanoclusters and parameters of their 3D arrangements (including superlattice parameters, and preferential orientation of nanoclusters in superlattice).

2. Project results

A typical preparation procedure involves synthesis of CdS nanoclusters under solvothermal conditions in the presence of alkylammonium salt, then separation by centrifugation, thorough washing and vacuum-drying. The resulting bright yellow-orange solid was characterized by different methods, including Raman and UV-Vis absorption spectroscopy, and powder XRD. Specimens for the electron microscopy (on carbon coated copper grids) were prepared using suspension of the product samples in volatile organic solvents.

The TEM and STEM images show an array of monodisperse CdS clusters of several nanometers in size (*fig. 1*), which is in agreement with observed excitonic features in UV-Vis absorption spectra recorded at room temperature for solutions of corresponding samples. On TEM images the CdS cluster cores appear as dark regions and the SPh^- shell as lighter spaces, while on STEM images CdS – bright dots and SPh^- shell – dark spaces. The size of crystalline core of these CdS clusters can be measured as 2.3 nm, which means they are the largest

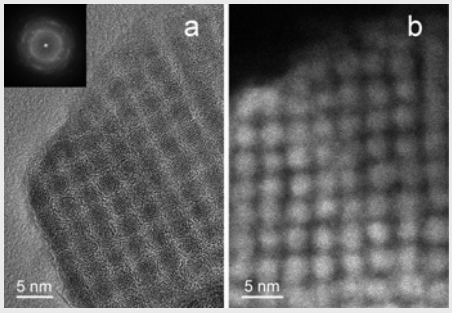

Figure 1. a) HRTEM and b) HAADF-STEM images of nanoclusters superlattice.
Inset: Fourier transform of the HRTEM image.

Karlsruhe Nano Micro Facility (KNMF)
Karlsruhe Institute of Technology (KIT)
Hermann-von-Helmholtz-Platz 1
76344 Eggenstein-Leopoldshafen
Germany

User Office
Phone: +49 (721) 608-3123
Fax: +49 (721) 608-6273
Email: knmf-useroffice@kit.edu
Web: www.knmf.kit.edu

CdS nanoclusters isolated to date. The shell of surface SPh^- ligands maintains a constant 1.1 nm spacing between the nanoclusters, in agreement with the SPh^--rich surfaces revealed by Raman spectroscopy. Ordered rows of CdS nanoclusters are seen to form regular rectangular packing consistent with cubic superlattice. Similar crystalline superlattice have been reported previously for $[Cd_{54}S_{32}(SPh)_{48}L_4]^{4-}$ nanoclusters (characterized by single crystal XRD). Because of significant difficulties with growing single crystals of the proper quality for the large nanoclusters, valuable structural information was expected to be obtained using TEM and STEM.

Internal lattice imaging shows a projection of Cd and S atoms along the <110> direction in Hawleyite (crystalline CdS with a cubic lattice) as can be deduced from the Fourier transform (FT) of the HRTEM image (*fig. 1a, inset*). Furthermore, the rectangular packing and the corresponding low-angle reflections in the fast FT suggest a cubic packing of the nanoclusters in superlattice. Detailed analysis was necessary to confirm this observation.

Electron tomographic analysis was performed using HAADF-STEM tilt-series consisting of 75 images acquired over a tilt-range of ±75°. The tilt-series were aligned with IMOD Version 4.1 using gold labels deposited on the carbon grid.

An HAADF-STEM electron tomographic reconstruction of the nanocluster packing in 3D reveals a simple cubic packing of nanoclusters with lattice parameters of (3.40±0.05) nm and (90±3)°. The first value is in good agreement with interplanar spacing d = 3.5 nm calculated from the low angle PXRD data, since for simple cubic packing the unit cell length would also correspond to the interplanar spacing. The volume rendering (*fig. 2*) shows a visualization of the reconstructed 3D volume along the <100> direction together with three digital slices through the reconstructed volume corresponding to the [100], [110], and [010] planes.

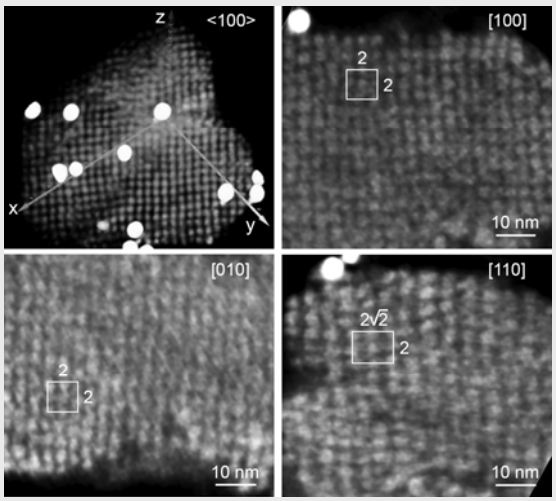

Figure 2. Volume rendering showing the 3D packing of the CdS nanoclusters along <100> orientation (larger and brighter particles are 5 nm gold labels used for tomographic alignment) together with 2x2 unit cells indicated in the slices along the [100], [110], and [010] planes of the superlattice.

These results illustrate the successful synthesis of monodisperse CdS nanoclusters 2.3 nm in size from a convenient molecular precursor and their assembly into a crystalline superlattice. HRTEM and STEM tomography provide concrete data for the nature of the nanoclusters and their crystallographic repeat.

3. Publications

Levchenko T., Kübel C., Huang Y., Corrigan J.F. *Chem. Eur. J.* **2011**, 17, 14394-14398.

Karlsruhe Nano Micro Facility (KNMF)
Karlsruhe Institute of Technology (KIT)
Hermann-von-Helmholtz-Platz 1
76344 Eggenstein-Leopoldshafen
Germany

User Office
Phone: +49 (721) 608-3123
Fax: +49 (721) 608-6273
Email: knmf-useroffice@kit.edu
Web: www.knmf.kit.edu

Proposal 2010-005-000416

Phase seperation in amorphous and partially crystallized SiCx

Harald Schmidt

Technische Universität Clausthal
Clausthal-Zellerfeld
Germany

Summary Report

1. Project Objectives (250 words)

Non-stoichiometric $Si_{1-x}C_x$ films deposited on silicon substrates are important for various branches of technology like electronics, optoelectronics and photovoltaic. Characteristic applications are window layers in solar cells, insulating layers in thin film transistors, thin film light emitting diodes, color displays, UV detectors, and micro electro-mechanical systems (MEMS). A straightforward research field is the design of silicon quantum dots embedded in an amorphous matrix of silicon carbide for applications e. g. as tandem solar cells. For these applications a fundamental understanding of the formation, growth and modification of nano-crystallites in silicon–rich $Si_{1-x}C_x$ is of large importance.

Using magnetron sputtering, films of high quality with reproducible properties can be deposited on various substrates. After deposition the films are expected to be amorphous. Annealing at elevated temperatures leads to precipitation and crystallization. Nucleation and growth processes affect the microstructure of the polycrystalline films. In order to get direct insight into the nanostructural modifications during crystallization, high resolution TEM measurements are necessary. This was the aim of the current experiments.

2. Project Achievements (1000 words + figures)

Samples: Non-stoichiometric films with a chemical composition of Si_2C and a thickness of about 1.5 μm are deposited by magnetron co-sputtering of silicon/carbon composite targets on silicon wafers. Crystallization is induced by annealing the samples at 800 and 1200 °C. Four types of samples were characterized by TEM: (1) an as-deposited sample, (2) a sample annealed for 1 h at 800 °C (3) a sample annealed for 2 h at 1200 °C and (4) a sample annealed for 120 h, respectively.

TEM characterization: Measurements were done using a FEI Titan 80-300 microscope with Cs correction at 300 kV. The samples were investigated in cross-sectional geometry prepared by FIB using BF-TEM, DF-TEM, HR-TEM and STM-HAADF in combination with SAED, EDX and EELS.

For the as-deposited sample, BF-TEM, STM and SAED revealed the presence of a homogeneous amorphous film on a single crystalline Si substrate with smooth interfaces. Some isolated pores with a diameter of about 100 nm can be found sporadically at the Si_2C/Si interface. A phase separation in Si and SiC_x rich regions could not be proven.

The sample annealed at 800 °C (Fig. 1) gives a completely different picture. At the surface of the film faceted particles with dimensions of about 500 nm are visible. These particles are composed of crystalline silicon as shown by SAED and EDX. The particles grow on a completely sharp SiC surface. The Si surface and the Si/SiC_x interface are oxidized. Further, HAADF-STEM and EELS/EDX profiles show that at the edges of the particles, very likely, a carbon rich phase is segregated. The film itself seems to be phase separated. Very small, isolated SiC crystallites of about 2-3 nm can be found in the amorphous matrix. In conclusion, the data at 800 °C can be interpreted in way that the Si_2C film decomposes at the surface by forming Si surface-crystallites and carbon, which is released from the sample. Such surface-crystals were not observed in literature up to now in the present context.

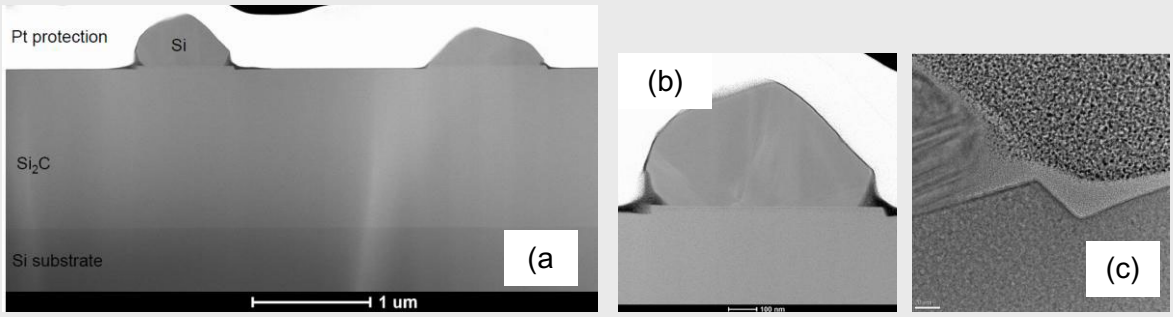

Fig. 1 TEM images of a Si_2C film on a Si substrate in cross sectional geometry annealed at 800 °C. (a) HAADF-STM (b) HAADF-STM around the Si particle, and (c) BF-TEM at the Si particle edge.

At 1200 °C (2 h) the situation changes again completely. The main part of the film is porous with oxidized layers at the surface. A sequence of a SiO_2 layer (300 nm) and two different SiC_xO_y layers (50 nm each) are identified. The film is composed of Si crystallites, 3C-SiC crystallites and pores all in the range of some tens of nm. HAADF-STEM shows that the phase separation/pore structure occurs at a smaller length scale at the top of the film compared to the bottom (interface). At the Si substrate interface an about 1 μm thick pore is found. This pore is located on a single crystalline silicon precipitate that is epitaxial grown on the substrate. In addition, further small Si crystallites are found at the substrate interface by HRTEM. This finding is confirmed for other FIB lamella. This result illustrates that silicon is transferred from the Si_2C film matrix to the substrate interface during annealing.

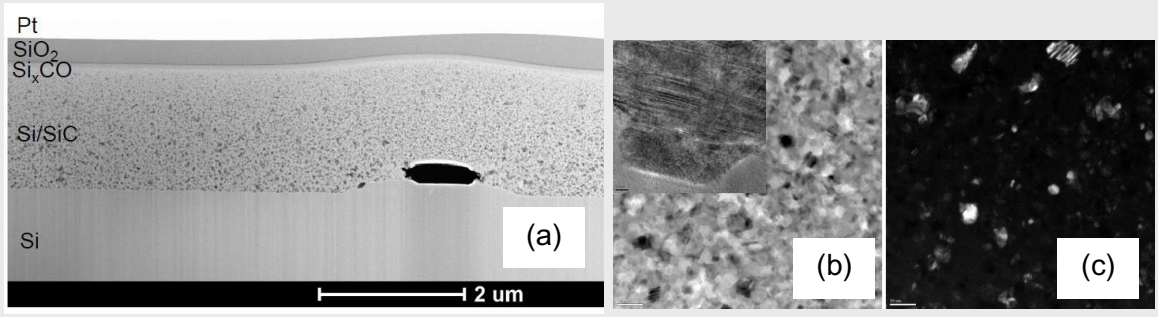

Fig. 2 TEM images of a Si_2C film on a Si substrate in cross sectional geometry annealed at 1200 for 2 h °C. **(a)** HAADF-STM **(b)** BF-/HR-TEM of the film, and **(c)** DF-TEM of the film.

If the annealing time at 1200 °C is prolonged to 120 h the complete film is crystallized to polycrystalline 3C-SiC (5-50 nm) with a rough surface structure and a high porosity within the film. Si crystals are no longer present. On top, SiC crystals are found embedded in a SiO_2 layer. A very interesting, at the moment hardly understandable result is, that the substrate is no longer single crystalline, but consists of highly porous polycrystalline SiC. To explain this result, further measurements are necessary.

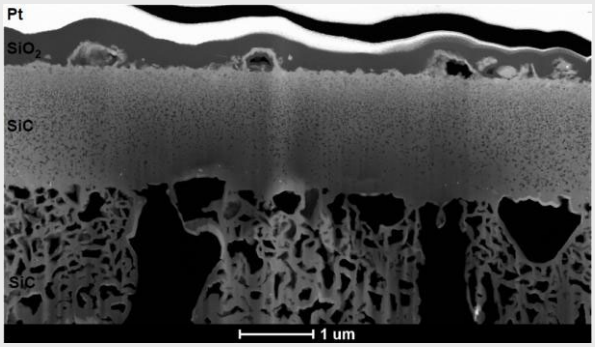

Fig. 3 HAADF-STM image of a Si_2C films in cross sectional geometry annealed at 1200 °C for 120 h.

3. Instruments Used (comma separated)

Transmission Electron Microscopy, Focused Ion Beam

4. Publications
Please note that the following acknowledgement has to be included in journals, proceedings, presentations and at any other public publications: "*We acknowledge the Karlsruhe Nano Micro Facility (KNMF, www.kit.edu/knmf) of the Forschungszentrum Karlsruhe for provi-sion of access to instruments at their laboratories and we would like to thank x for assistance in using laboratory y.*"

to be published	• W. Gruber, U. Geckle, M. Bruns, C. Kübel, *Microstructural Development During Crystallization of Amorphous Si_2C deposited on Si substrates*.
published	•

5. Comments (250 words)

Proposal 2011-005-000477

Laser Assisted Micro-texturing of Surface Nitrided Ti-6Al-4V

Jyotsna Dutta Majumdar

Indian Institute of Technology (IIT)
Kharagpur
India

Final Report

1. Project goals / Introduction

Titanium and its alloy are popular bio-implant material due to its high strength to weight ratio, good chemical inertness, reasonably lower young modulus (as compared to AISI 316 stainless steel) [1]. However a relatively poor wear resistance and bio-inertness at the problems causing release of titanium after long term application due to its interaction of bone and poor adherence of tissue on the surface of titanium [2]. Wear is indeed a surface dependent property which may be enhanced by improving the hardness of the surface [3]. In the past, laser surface nitriding was successfully employed on Ti-6Al-4V substrate to improve its hardness value significantly for bio-implant application [4]. However, important surface characteristics, which can contribute to improved cell/tissue adherence are (1) the existence of polar chemical groups or coupling agents on the surfaces that are available for bonding; and (2) increased surface roughness, which gives rise to improved mechanical interlocking [5]. Hence modification of surface topography can be used as a tool for improving the tissue of surface metallic implants [5]. In the past, several attempts have been made to improve cell adherence on metallic and ceramic substrate by modification of surface topographical features to make it rough along prefer direction may be termed as surface texturing [6-8]. Laser surface texturing is a process of roughening the surface along preferred direction using laser beam as source of heat to applied material to the surface [9]. In past, laser surface texturing has been successfully used for the modification of the surface of bio-implant metallic material [10]. However the nature of roughness and its periodicity required for maximum bio-compatibility, soft tissue adherence has not be investigated in detail. In the present study attempts have been made to understand the effect of laser surface texturing on the microstructure, composition and phase change associated with laser processing and the subsequent change in bio-compatibility of Ti-6Al-4V samples.

2. a) Project results / Experimental

In the present investigation, Ti-6Al-4V (Ti64) of dimensions 10 mm x 10 mm x 5 mm in as-received condition was used as substrates. The substrate surface was carefully polished by mechanical polishing to a roughness of 3 m in order to clean the surface. Laser surface texturing was carried out in two patterns (line and hole pattern). Hole texturing was carried out by using a UV laser (with a wavelength of 193 nm) at an applied energy density of 3.2 J/cm^2, frequency of 200 Hz with 100 no. of pulse in air. On the other hand, line texturing was carried out using a UV laser (with a wavelength of 193 nm) at an applied energy density of 2.4 J/cm^2, frequency of 200 Hz with 50 no. of pulse in air. Following laser surface texturing, the microstructure of the as received and textured surface (both Ti-6Al-4V and laser surface nitride Ti-6Al-4V) was characterized by optical and scanning electron microscopy. The surface roughness of the textured samples was measured by the laser scanning profilometer using a 10 mW He-Ne laser. A detailed analysis of the phases present on the surface was carried out using X-ray diffractometer. Residual stress was measured by a stress goniometer attached to an X-ray diffractometer applying Cohen's theory [11]. The microhardness was measured by a Vickers microhardness tester using a 100 g applied load. The electrochemical property of the laser textured surface in terms of corrosion resistance resistance was compared to that of the as-received Ti-6Al-4V and as-

received Ti-6Al-4V nitrided by potentiodynamic anodic polarization study in Hank's solution with the following electrolytic composition (g/L): 0.185$CaCl_2$, 0.4KCl,0.06KH_2PO_4, 0.1$MgCl_2$, 6H2O, 0.1$MgSO_4$7H_2O,8NaCl, 0.35$NaHCO_3$, 0.48Na2HPO4, and 1.00 D-glucose. In the corrosion study, a standard calomel electrode was used as the reference electrode and platinum was used as the counter electrode. Polarization was carried out from_2000 to+7000 mV(SCE) at a scan rate of 2 mV/s. The pitting corrosion behavior was determined by measuring the primary potential for pit formation, Epp1 (the potential at which there is a sudden rise in current density with a small increase in potential) [12]. The wettability of the simulated body fluid (SBF) on the surface of the as-received and laser surface textured was evaluated using the sessile-drop technique [13]. During the measurement, a drop (of diameter 0.5 to 1 mm) of SBF was released from the tip of a syringe onto a sample surface, and the contact angle the drop made with the surface was measured by taking a digital image of the drop. The accuracy of the contact angle measurements was within ±1 deg.

Titanium and its alloy are popular bio-implant material due to its high strength to weight ratio, good chemical inertness, reasonably lower young modulus (as compared to AISI 316 stainless steel) [1]. However a relatively poor wear resistance and bio-inertness at the problems causing release of titanium after long term application due to its interaction of bone and poor adherence of tissue on the surface of titanium [2]. Wear is indeed a surface dependent property which may be enhanced by improving the hardness of the surface [3]. In the past, laser surface nitriding was successfully employed on Ti-6Al-4V substrate to improve its hardness value significantly for bio-implant application [4]. However, important surface characteristics, which can contribute to improved cell/tissue adherence are (1) the existence of polar chemical groups or coupling agents on the surfaces that are available for bonding; and (2) increased surface roughness, which gives rise to improved mechanical interlocking [5]. Hence modification of surface topography can be used as a tool for improving the tissue of surface metallic implants [5]. In the past, several attempts have been made to improve cell adherence on metallic and ceramic substrate by modification of surface topographical features to make it rough along prefer direction may be termed as surface texturing [6-8]. Laser surface texturing is a process of roughening the surface along preferred direction using laser beam as source of heat to applied material to the surface [9]. In past, laser surface texturing has been successfully used for the modification of the surface of bio-implant metallic material [10]. However the nature of roughness and its periodicity required for maximum bio-compatibility, soft tissue adherence has not be investigated in detail. In the present study attempts have been made to understand the effect of laser surface texturing on the microstructure, composition and phase change associated with laser processing and the subsequent change in bio-compatibility of Ti-6Al-4V samples.

2. b) Project results / Results and Discussions

Figures 1(a-b) show the scanning electron micrographs of the (a) top surface of laser surface textured Ti-6Al-4V lased with a UV laser (with a wavelength of 193 nm) at an applied energy density of 3.2 J/cm^2, frequency of 200 Hz with 100 no. of pulse in air, showing periodic spherical hole geometry with a hole diameter 50-60 µm and a depth of 10 µm and (b) the same at a higher magnification. From Figure 1(a) it is clear that the degree of texturing is uniform all throughout. Furthermore, the interface between hole and base metal is continuous and defect free with large accumulation of material at the edge due to accumulation of molten material and subsequent solidification. The textured surface at a high magnification shows the presence of ultra-fine grained □-Ti and the presence of β-Ti (with very fine dot like morphology) in the grain boundary

regions. Few coarse grained TiN particles were also dispersed in the microstructure possibly due to the formation of TiN phase while laser processing in air.
Figure 2 shows the scanning electron micrograph of the top surface of laser surface textured Ti-6Al-4V lased with a UV laser (with a wavelength of 193 nm) at an applied energy density of 2.4 J/cm^2, frequency of 200 Hz with 50 no. of pulse in air, showing periodical linear texture with a width of 20 µm and a depth of 10 µm. The microstructure of the linear textured surface at high magnification shows the similar features as the same with hole geometry.

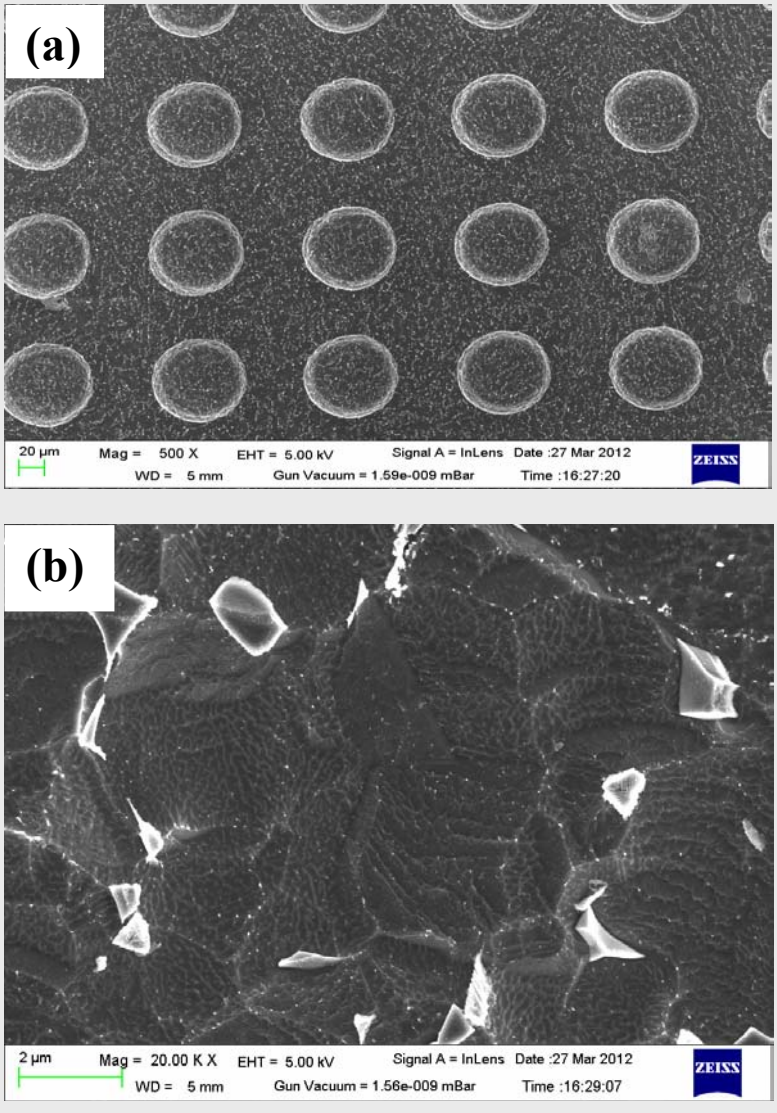

Figure 1: Scanning electron micrographs of the (a) top surface of laser surface textured Ti-6Al-4V lased with a UV laser with a wavelength of 193 nm at an applied energy density of 3.2 J/cm^2, frequency of 200 Hz with 100 no. of pulse in air and the same (b) at a high magnification.

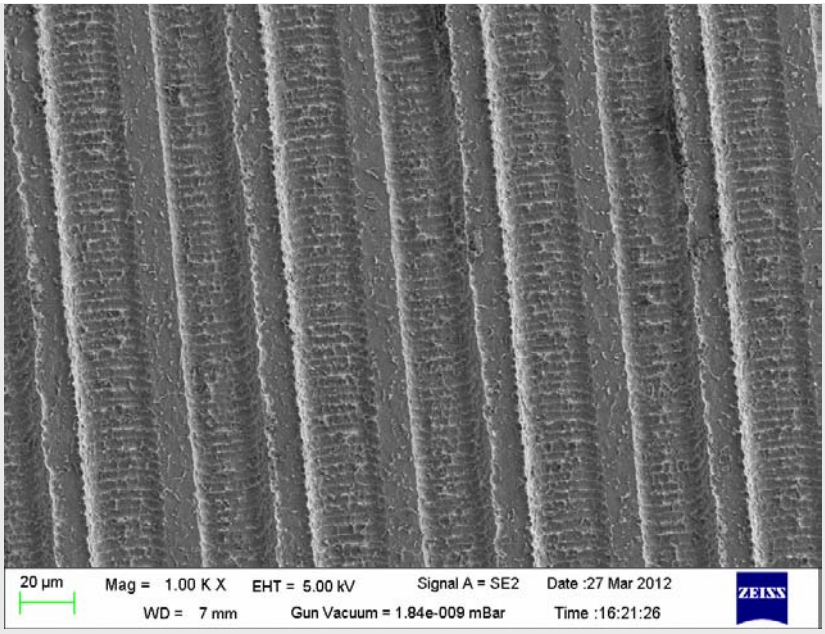

Figure 2 : Scanning electron micrograph of the top surface of laser surface textured Ti-6Al-4V with a linear texture lased with a UV laser (with a wavelength of 193 nm) at an applied energy density of 2.4 J/cm^2, frequency of 200 Hz with 50 no. of pulse in air.

A detail study of the phases present in the textured sample was analyzed by X-ray diffraction technique to understand the effect of laser surface texturing on the phase formation. Table 1 summarizes the result of X-ray diffraction profile. Form Table-1 it may be concluded that the phases present in both as received titanium and textured titanium are predominately α-Ti with a few α-Ti and there was a significant peak broadening, the average lattice strain was calculated using scherrer's formula and it is observed that lattice strain was maximum in linear textured surface. In hole textured surface the extent of lattice strain was however, insignificant. A detail study of residual stress developed on the textured sample was evaluated by a stress Ganiometer attached to X-ray diffractometer which is summarizes in Table1. From Table 1 it may be noted that the residual stress was compressive in as-received Ti-6Al-4V, which is attributed to the fact that the Ti-6Al-4V used in present study was cold rolled. In linear textured surface residual stress was tensile with a very low magnitude (60MPa).The tensile residual stress developed due to texturing is possibly due to surface melting operation during laser melting and rapid quenching cause introduction of quenched stress. In the hole textured surface the magnitude of residual stress was very low and compressive in nature (-42MPa), the low compressive residual stress is possibly due to significantly lower quenching stress developed due to localized melting.

Karlsruhe Nano Micro Facility (KNMF)
Karlsruhe Institute of Technology (KIT)
Hermann-von-Helmholtz-Platz 1
76344 Eggenstein-Leopoldshafen
Germany

User Office
Phone: +49 (721) 608-3123
Fax: +49 (721) 608-6273
Email: knmf-useroffice@kit.edu
Web: www.knmf.kit.edu

Table I: Summary of X-ray Diffraction Studies of Laser Surface Textured Ti-6Al-4V

Sample	Phases	Lattice Strain	Residual stress (MPa)
Ti6Al4V	α Ti and β Ti	0.27	-151.2
Linear textured Ti-6Al-4V	α Ti and β Ti	0.327	59.5
Hole textured Ti-6Al-4V	α Ti and β Ti	0.26742	-42.1

A detail study of the surface roughness value was undertaken by a contact pro-stylus with the help of surface profilometer, Table-II summarizes the average roughness of different samples. From Table-II it is noted that the average roughness in hole textured Ti-6Al-4V was 12µm and the same for linear textured was 6mm as compare to 3 µm as received Ti-6Al-4V.on the other hand the surface roughness value of linear textured Titanium nitride was 12 µm and same for hole textured was 15 µm as compared of that 3 µm for as received titanium nitride. Hence it may be concluded that due surface texturing, there is significant increments in roughness value for both as received and laser surface nitride titanium. The average microhardness of the textured surface was also measured to see the effect of laser texturing on hardness value (see Table-II). From Table -II it may be noted in linear textured Ti-6Al-4V, there is significant enhancement in hardness (720 VHN) as compared to as received (280 VHN).The significant improvement in hardness linear textured surface is possibly due to refinement of microstructure and presences of few titanium nitride particle. In hole textured region, inside the hole textured microhardness would not be evaluated because very narrow treated region. The average microhardness of linear and hole textured was however improved significantly as compared to as received titanium. A detail study of wettability was undertaken by liquid droplet measurement technique and its result is summarizes in Table-II. From Table-II it is noted that there is marginal enhance of wetability (in terms of decrease in contact angle in textured sample as compared to as received sample. The enhance of wetability is accordance with increments in surface roughness. A detailed study of the wear behavior of laser surface textured Ti-6Al-4V and surface nitrided Ti-6Al-4V has been reported elsewhere [14].

Table II: Summary of physical (surface roughness and wettability) and mechanical (microhardness) properties of textured surface.

Sample	Average Roughness(mm)	Average Microhardness (VHN)	Wetability
Ti6Al4V	3 µm	280	69.5
Laser surface textured Ti6Al4V with hole geometry	12 µm	Could not be measured and nano-indentation needs to be undertaken	64
Laser surface textured Ti6Al4V with linear geometry	6 µm	721.3	65

A detail study of corrosion behavior of as received Ti-6Al-4V and laser surface textured Ti-6Al=4V in as-received and laser surface nitrided conditions were was undertaken in hank's solution to understand the effect of surface texturing on the corrosion behavior of the surface. Table-III shows the corrosion parameter derived from corrosion study. From Table-III it is noted that there is a significant reduction corrosion rate in laser surface textured Ti-6Al-4V as compared to as received one and hole textured surface showed a maximum enhancement. Study of mechanism of corrosion is being undertaken. Similarly due laser surface linear textured surface showed a maximum reduction in corrosion rate. The mechanism of corrosion is under investigation [14].

Table III: Summary of electrochemical behavior of as-received and laser surface textured Ti-6Al-4V and surface nitrided Ti-6Al-4V.

Sample details	I CORR	I CORR(a/CM2)	E CORR	Corrosion rate(mm/year)	E_{pitt}
As received Ti-6Al-4V	3.242E-06	7.047E-06	-0.614	1.225E-1	0.010
Laser surface textured Ti6Al4V with hole geometry	1.648E-08	2.746E-08	-0.259	4.772E-4	-0.113
Laser surface textured Ti6Al4V with linear geometry	1.054E-6	1.621E-06	-0.493	2.817E-2	-0.349
Laser surface nitrided Ti-6Al-4V	4.675E-07	1.798E-06	-0.632	3.125E-2	0.007
Laser surface textured nitrided Ti6Al4V with linear geometry	2.769E-07	4.196E-07	-0.256	7.292E-3	-0.008
Laser surface textured nitrided Ti6Al4V with hole geometry	1.041E-06	1.679E-06	-0.674	2.919E-2	-0.014

Bio-compatibility behavior

The bio-compatibility behavior of as received and laser surface textured Ti-6Al-4V (in both as-received and laser surface nitrided state) was evaluated by XTT assay testing (using 3T3 fibroblast cellline), the details of the text is reported elsewhere [14]. Figure 6 summarizes the cell viability of different samples. All materials tested were highly biocompatible and performed in some cases even better than the control. However, a detailed study needs to be undertaken to quantify the cell proliferation and adherence behavior.

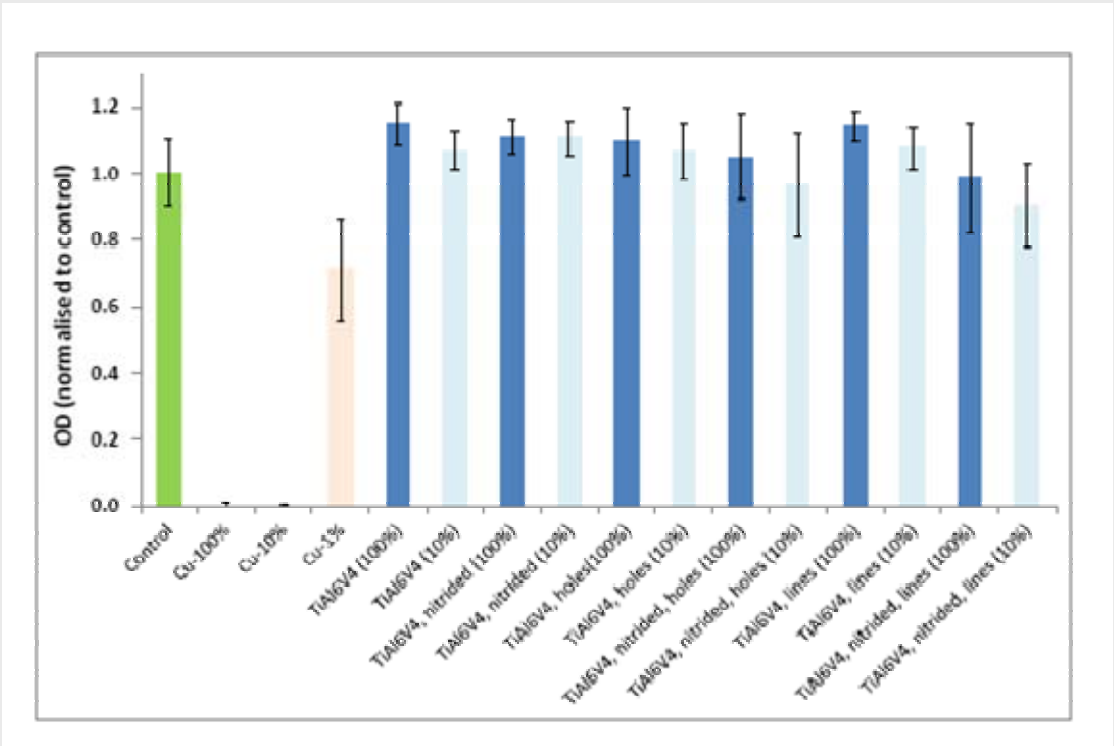

Figure 6: Summary of cell proliferation behavior in cell line by XTT assay test [14]

Summary and Conclusions

In the present study, initial attempt have been made to texture the surface of Ti-6Al-4V (in as-received condition) using a UV laser. Two different texture geometry was attempted: linear and hole geometry. In as-received Ti-6Al-4V, both the linear and hole geometry were successfully achieved with a significant improvement in hardness value due to grain-refinement and formation of nitride phase dispersed due to the interaction of nitrogen with molten Titanium. The corrosion resistance was improved with an improvement in bio-activity, though bio-compatibility was not influenced significantly. Due to microstructural refinement and homogenization there was enhancement of microhardness and corrosion resistance. Due to increased roughness of the surface, there was increased wettability. However, a detailed study needs to be undertaken to optimize the surface texturing pattern and optimize the laser parameters to achieve improved wettability. Bio-compatibility behaviors need to be studied in detail in terms of kinetics of cell proliferation and cell attachment strength.

3. Publications

1. Titanium and Titanium Alloys, M.J. Donachie, Jr., ed., ASM, Metals Park, OH, 1982, p. 3.
2. E.I. Meletis, C.V. Cooper, and K. Marchev: Surf. Coat. Technol., 1999, vol. 113, pp. 201–09.
3. K. G. Budinski, Surface Engineering for Wear Resistance, Englewood Cliffs, NJ, Prentice Hall, New Jersey, 1988.
4. A. Biswas, L. Li, U. K. Chatterjee, I. Manna and J. Dutta Majumdar, Metallurgical and Materials Transaction A, 40 A (2009) 3031.
5. R.R. Wang, G.E. Welsch, and O. Monteiro: J. Biomed. Mater. Res., 1999, vol. 46, pp. 262–70.
6. H. J. Busscher, I. Stokroos, J. G. Golverdingen, and J. M. Schakenraad, *Cells Mater.,* 1 (1991) 243–249.
7. D. Despina, D. Nikoleta, D. Katsala, G. Petros, G. Koutsoukos, M. F. Yiannis, Biomaterials, 22 (2001) 87-96.
8. M. Nardin, D. Bernache-Assolant, C. Rey, P. Delannoy, L. Sedel, P. J. Marie, J. Biomed. Mater Res 2000;50:353-364.
9. R. Ranjan, D. N. Lambeth, M. Tromel, P. and Y. Li, J. Appl. Phys., **69**~8!, pp. 5745–5747.
10. N. Mirhosseini, P.L. Crouse, M. J. J. Schmidth, L. Li, D. Garrod, Applied Surface Science 253 (2007) 7738–7743.
11. B.D. Cullity and S.R. Stock: Elements of X-Ray Diffraction, 3rd ed., Prentice Hall, N. Delhi, 2001, p. 435.
12. M.G. Fontana: Corr. Eng., McGraw-Hill, New York, NY, 1987, p. 71.
13. W. Adamson: Phys. Chem. Surf., John Wiley, New York, 1990, p. 298.
14. Studies on Laser Surface Texturing of Ti-6Al-4V (under preparation)

4. Comments

Karlsruhe Nano Micro Facility (KNMF)
Karlsruhe Institute of Technology (KIT)
Hermann-von-Helmholtz-Platz 1
76344 Eggenstein-Leopoldshafen
Germany

User Office
Phone: +49 (721) 608-3123
Fax: +49 (721) 608-6273
Email: knmf-useroffice@kit.edu
Web: www.knmf.kit.edu

Proposal 2011-005-000483

Structural study of Metal-Oxide-Semiconductor devices based on SiGe and CdSe nanocrystals grown for flash memory applications

Sergey Levichev

Universidade do Minho
Braga
Portugal

Summary Report

1. Project goals:

Structual study of Metal–oxide–semiconductor (MOS) structures with Si_xGe_{1-x} and CdSe NCs embedded in dielectric matrix (with total thickness from 20 to 40 nm) on p-Si(100) substrates fabricated by RF- magnetron sputtering technique at room temperature with subsequent rapid thermal annealing.

Correlation of structural results with electrical properties obtained by means of Capacitance-Voltage (C-V) and Current-Voltage (I-V) measurements and finding appropriate growing conditions for better carrier storage response.

2. Project results (1–2 pages):

The produced Metal Oxide Semiconductor (MOS) nanostructures, containing SiGe and CdSe nanocrystals (NCs) have been analyzed structurally by High Resolution Transmission Electron Microscopy (HRTEM) and X-ray Photoelectron Spectroscopy (XPS) during our first experiments at KNMF on May of 2011 (Proposal 2011-005 000483).

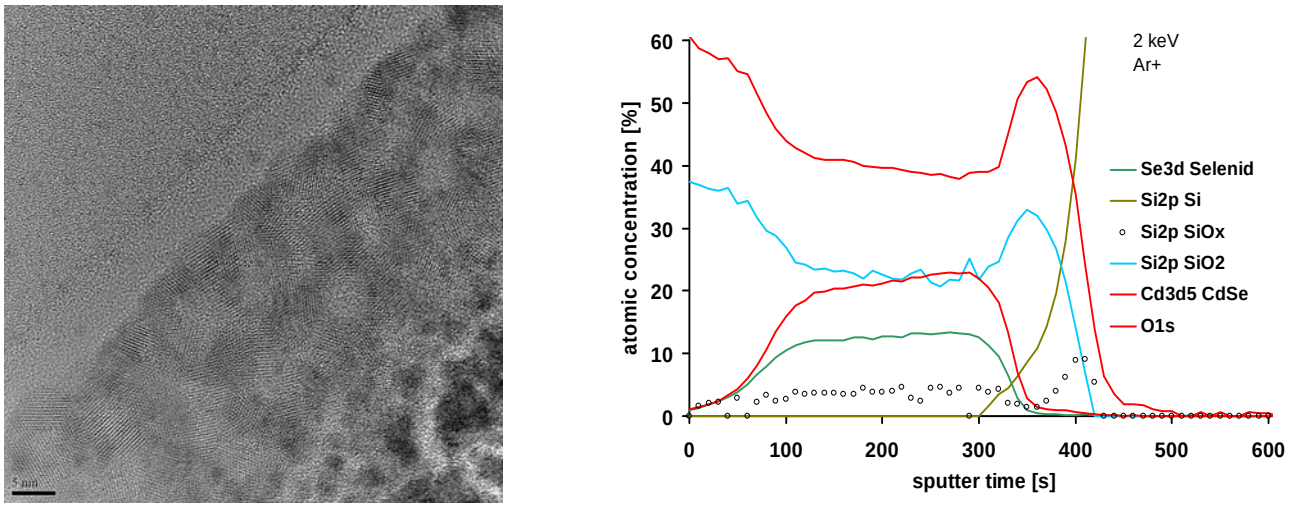

Fig. 1. HRTEM image (left) and XPS depth profiling (right) of MOS nanostructure with CdSe NCs in silica matrix.

Karlsruhe Nano Micro Facility (KNMF)
Karlsruhe Institut of Technology (KIT)
Hermann-von-Helmholtz-Platz 1
76344 Eggenstein-Leopoldshafen
Germany

User Office
Phone: +49 (0)7247 82-3123
Fax: +49 (0)7247 82-7273
Email: knmf-useroffice@kit.edu
Web: www.kit.edu/knmf

Fig. 1 show HRTEM image (left) and XPS depth sputter profile (right) of CdSe NCs in SiO_2 matrix. It is clearly seen from HRTEM results that dense CdSe NCs array is formed in silica matrix. CdSe NCs layer is mostly located in the middle of MOS structure, but some diffusion to the surface silica top oxide layer was revealed. The results show that the reduction of CdSe doping level of SiO_2 layer is necessary.

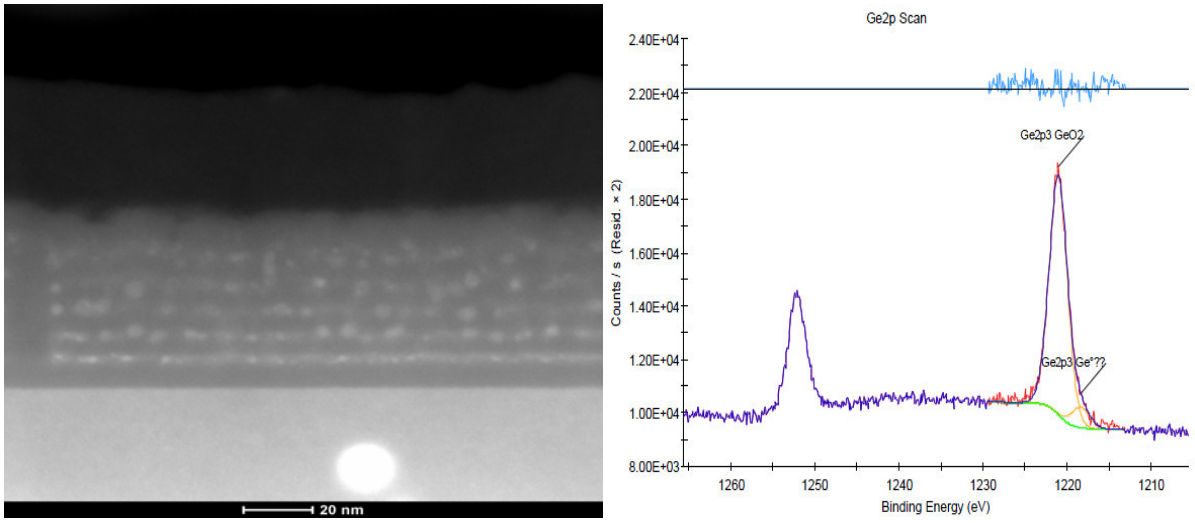

Fig. 2. STEM image (left) and Ge2p XPS scan (right) of multilayered Ge/SiO_2 nanostructure annealed at 900 ºC for 60s.

The STEM micrograph of produced and annealed at 900 ºC 5x[Ge/SiO_2] thin film is presented by Fig.2. Nanoparticles are clearly visible in the layers parallel to the substrate and the layers are well separated from each other, but HRTEM investigations did not revealed any crystalline Ge phase on this nanostructure as well as on other ones annealed at lower temperatures for smaller times. XPS investigations discovered that Ge atoms inside the nanoparticles are mostly amorphous. As these samples show good memory window (carrier's charging properties) the structural findings allowed us to conclude that it is related to the amorphous Ge nanoparticles and the paper is under preparation now.

Proposal 2011-005-000493

Preparation of reactice surface areas by DPN for site selective self assembly of virus-like particles

Christina Wege

Universität Stuttgart
Stuttgart
Germany

Note: *Please fill in this report form and save/print it as a PDF file, then upload it to the KNMF proposal submission system. A cover page containing proposal title, proposer name(s), and technologies selected will be added by the system. A link for the download of the complete report as a PDF file will be displayed in the system.*

Final Report

1. Project goals (max. 1.800 characters)**:**

The main focus of the project is on the development of an innovative approach to immobilize viral RNA site-selectively on the surface of substrates for a bottom-up self assembly of cylindrical virus-like particles (VLP) of the tobacco mosaic virus (TMV) type. The TMV particles consist of a well-defined number of coat protein (CP) units arranged around an RNA strand in an exactly predetermined geometry. The surface-bound TMV-like particles (TLPs) will be used as carrier systems for bio-active molecules as e.g. enzymes. They shall act as a spacer in order to avoid a direct contact between the active molecules and the substrate, which often is the reason for a reduction of enzymatic activity. An innovative coupling strategy based on the site-selective immobilization of aminated linker DNA (DNA-NH_2) on aldehyde-terminated substrate areas, followed by the coupling of genetically modified (non-infectious) virus-derived RNA and self-assembly of the CP tubes could recently be published for the first time.[1] However, as the density of the assembled viral particles was rather limited in that case, new combinations of coupling surface chemistry and structuring methods are sought-after. Therefore, an alternative chemical linking strategy was followed, based on isothiocyanate (ITC)-terminated substrates as coupling reactant for the DNA-NH_2. As this coupling is a one-step process, one goal of the project was to combine the ITC-chemistry-based coupling strategy with dip-pen nanolithography (DPN) as a method (i) with high lateral resolution and (ii) with the opportunity for the parallel preparation of a high amount of nanostructures with varying size and distances between each other[2-5] (Figure 1).

Karlsruhe Nano Micro Facility (KNMF)
Karlsruhe Institute of Technology (KIT)
Hermann-von-Helmholtz-Platz 1
76344 Eggenstein-Leopoldshafen
Germany

User Office
Phone: +49 (721) 608-3123
Fax: +49 (721) 608-6273
Email: knmf-useroffice@kit.edu
Web: www.knmf.kit.edu

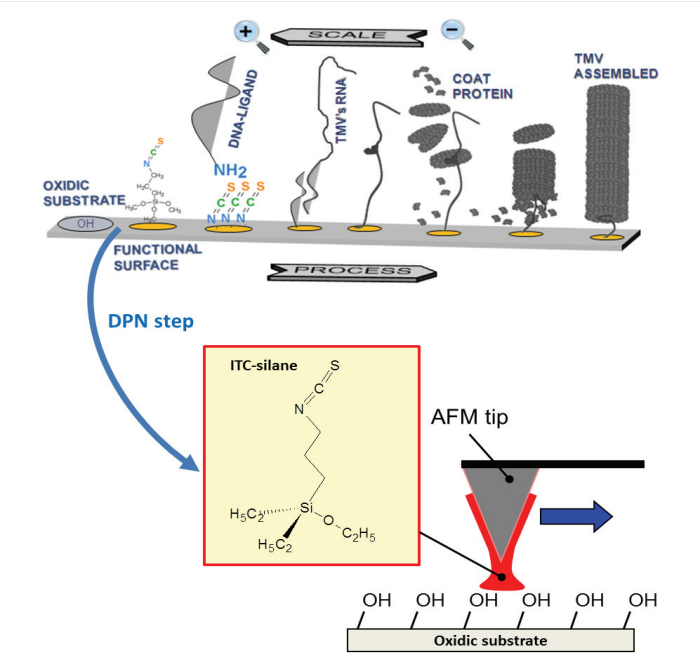

Figure 1: Scheme of the site-selective bottom-up assembly of TLPs. Isothiocyanate-terminated structures are created by the DPN technique. Then an amino-terminated DNA-ligand is coupled to the ITC-silane-functionalized surface pattern by forming a thiourea bonding; a complementary viral RNA strand is immobilized and, finally, the coat proteins are added for TLP assembly.

2. Project results (max. 7.000 characters + figures):

As described in the first chapter, the bottom-up assembly of TMV-like particles (TLPs) includes five experimental steps: (1) substrate cleaning, (2) coupling the ITC-terminated silane, (3) coupling the amino-terminated DNA-linker, (4) immobilizing the viral RNA and (5) adding the CPs for VLP assembly. Therefore, the very first goal of the project was to prove, whether the coupling of the ITC-silane to an oxidic surface can be carried out homogeneously over wide surface areas. For that purpose a non-structured glass substrate was cleaned and chemically functionalized by the coupling of 3-isothiocyanate-propyl-triethoxysilane (ITCPTES) to the OH-terminated substrate according to the procedure described in for Si wafers.[6] Then 1 mM solution of aminofluorescein (F-NH_2) was spotted on the ITC-terminated surface with a microspotter robot machine, followed by a fluorescence investigation of the spotted areas using a microarray scanner. In Figure 2a the corresponding chemical process is illustrated. The formation of the thiourea bond results in a decrease of the intramolecular resonance of the p-electron system with the fluorescence light, and with that in an increase of the fluorescence yield which can be detected. Therefore, (1) bright areas of fluorescence on a substrate are an indirect proof for the

successful coupling of the ITC-silane to the oxidic surface and (2) the distribution of the fluorescence intensity over the spotted areas will give information about the density of coupled ITC-groups. In Figure 2b the fluorescence image of a glass substrate functionalized with ITCPTES is shown after spotting the F-NH_2 solution. The dots have an average diameter of 100 µm and a zoom-in shows sharp edges of the spotted areas as well as a homogeneous distribution of the fluorescence intensity. These results are a proof (1) for the successful chemical coupling of the ITC-silane to the oxidic glass surface, (2) for the preservation of the reactivity of the ITC-groups after the ITC-silane immobilization and (3) for a homogeneous distribution of the ITC-groups on the glass substrate. The sharp edges of the spotted areas and the fact that no background fluorescence can be detected in-between the dots demonstrate the highly site-selective reaction of the F-NH_2 with the ITC-surface. For comparison, a glass slide not functionalized with ITC-silane was also spotted with the F-NH_2 solution under exactly the same experimental conditions as used for the ITC-terminated glass (shown in Figure 2b). The corresponding fluorescence microscopy image is presented in Figure 2c. Here significant background fluorescence and irregular-shaped spotting areas with inhomogeneously distributed fluorescence intensities are detected. This is the result of nonspecific physisorption of F-NH_2 on the glass substrate.

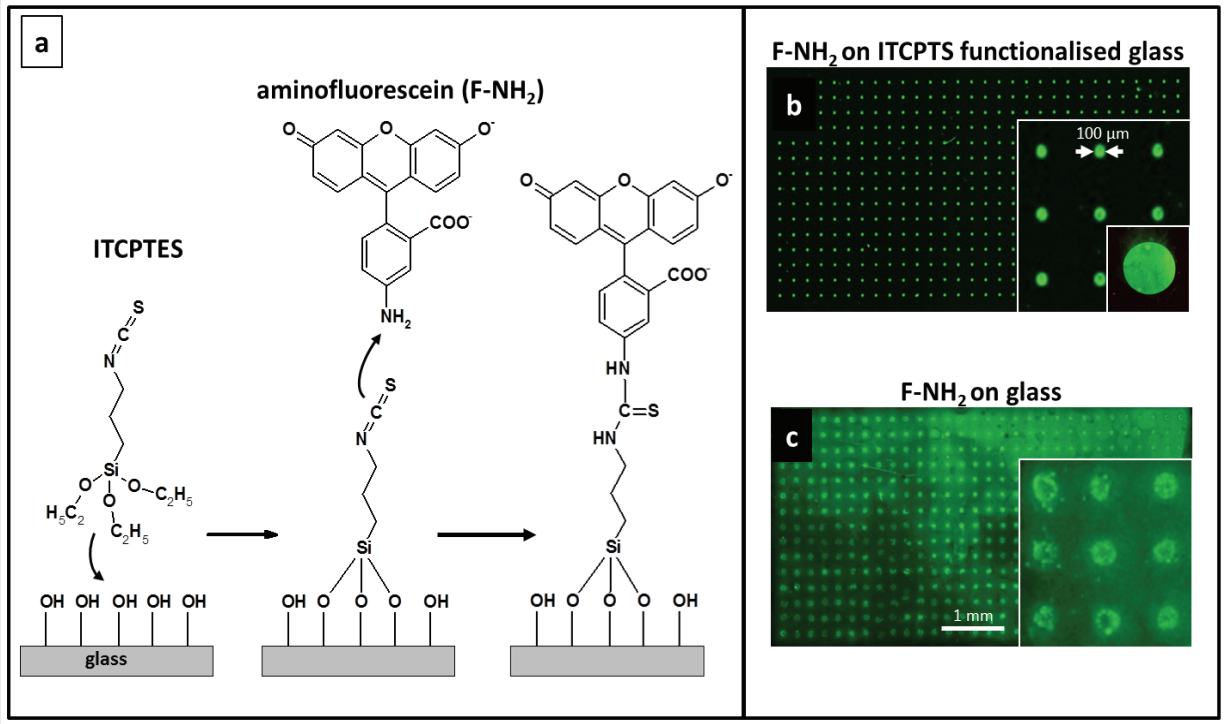

Figure 2: Scheme of the coupling of aminofluorescein (F-NH_2) to ITC-terminated substrates (a). (b) and (c) show the fluorescence microscopy images of F-NH_2 arrays spotted on ITC-terminated and non-functionalized glass, respectively.

With the experiment described above we proved that the coupling chemistry of the ITC-silane to the OH-terminated glass slide is successful.

Karlsruhe Nano Micro Facility (KNMF)
Karlsruhe Institute of Technology (KIT)
Hermann-von-Helmholtz-Platz 1
76344 Eggenstein-Leopoldshafen
Germany

User Office
Phone: +49 (721) 608-3123
Fax: +49 (721) 608-6273
Email: knmf-useroffice@kit.edu
Web: www.knmf.kit.edu

In a second experiment we used the DPN method to create arrays of ITC-terminated spots on a cleaned glass slide and labeled those spots with F-NH_2 in a second step before the fluorescence was investigated. DPN was performed with ITCPTES on glass square coverslips (18x18 mm², VWR, Germany) that were cleaned by serial ultrasonication in chloroform, iso-propanol, and MilliQ water for 10 minutes each. After that, the coverslips were blow-dried with nitrogen and DPN was performed using a NLP 2000 system (NanoInk Inc., USA). 1-dimensional cantilever arrays (F-Type, NanoInk Inc, USA) with 26 cantilevers in a pitch of 35 µm were dipped into pure ITCPTES, and the excess was blown away with a nitrogen gun. Patterns of 5 x 5 dots separated by 5 µm spacing were written with a dwell time of 0.5 s and at different relative humidity between 20±1% and 40±1% r.H., respectively, at a temperature of (25.0±0.5) °C. After silanization, the patterned glass slips were immersed in a solution of F-NH_2 and fluorescence images were recorded (Figure 3). The fluorescent dots show sharp edges, and no significant background fluorescence was detected in between the 5 x 5 spot arrays. With increasing r.H. the diameter of the spots increases, which can be explained by a flowing out of the spotted droplets. In addition an increase of the fluorescence intensity could be detected. The differences in the fluorescence intensity between the 5 x 5 arrays in one line is a result from different tip properties (e.g. different amounts of ink on the tips) and could not be influenced during the experiment.

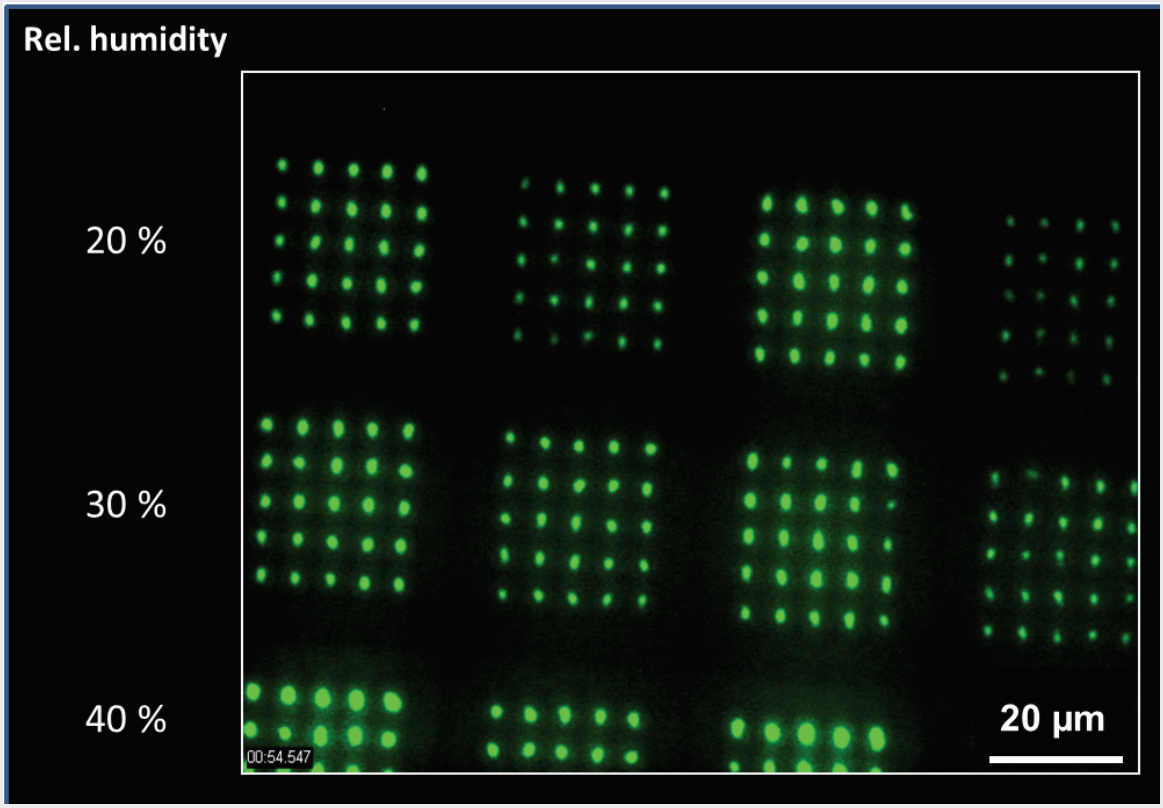

Figure 3: Fluorescence microscopy image of several 5 x 5 arrays of fluorescent spots, created with the DPN technique by first spotting ITCPTES solution, followed by coupling F-NH_2 site-selectively to the spots. The different array lines were created under different humidity conditions.

Karlsruhe Nano Micro Facility (KNMF)
Karlsruhe Institute of Technology (KIT)
Hermann-von-Helmholtz-Platz 1
76344 Eggenstein-Leopoldshafen
Germany

User Office
Phone: +49 (721) 608-3123
Fax: +49 (721) 608-6273
Email: knmf-useroffice@kit.edu
Web: www.knmf.kit.edu

After the successful application of DPN to create ITC-terminated surface patterns labeled with F-NH_2, the lithography experiments were repeated, however, in this case to initiate the bottom-up assembly of TMV-like particles on the spotted areas according to Figure 1. In contrast to the coupling of F-NH_2 in the results shown before, now the coupling of the amino-terminated DNA-linker was carried out after the lithography step, followed by immobilization of the viral RNA and CP assembly. For more experimental details see.[1] Figure 4 shows AFM topography images of a 5 x 5 spot array after the deposition of ITCPTES droplets by DPN (Figure 4a), after the coupling of the DNA linkers to the silanized areas (Figure 4c), and after the self-assembly process of the TMV-like particles (Figure 4e). Figures 4b, d and f are detail images of a single spot of the arrays shown in Figures 4a, c and e. The spots in Figures 4a and 4b have an average height of 25 nm. This is significantly higher than it would be expected for a monolayer of the ITC-silane on the surface. However, in contrast to the preparation of the ITC-terminated Si wafers as described before, the deposition of small ITC-silane droplets on the glass by the DPN method occurred in air with a relative humidity of 30%. Under these conditions and without any washing or rinsing step, all deposited molecules can polymerize and thus form an ITC-silane multilayer, which explains the observed height. The polymerization of silanes under high humidity is well-known in the literature.[7]

After coupling of the DNA linker (Figure 4c and 4d), RNA strands were hybridized and nanotube assembly induced by the addition of a suitable TMV CP preparation. As a result, TMV-like particles were formed specifically on the areas of the spots. A significant decrease in height of the spotted areas was observed. This is probably due to a partial removal of the polymerized non-covalently bound material by several washing steps following RNA immobilization and assembly of the nucleoprotein tubes, resulting in spotted areas with an average height of 10 nm thereafter (Figure 4f). As there was no unspecific adsorption of the assembly-directing RNA to the silanized surface in the absence of DNA linkers (Figure 4c), the appearance of TMV-like particles on the spotted areas proves that a site-selective permanent immobilization of DNA oligomers took place on the silanized spots. The surface concentration of TLPs decreased from the rim of the spot to its center (Figure 4f). This density gradient can be explained by a diffusion of the DNA-containing solution underneath the polymerized silane, which was just loosely bound to the substrate and washed away during subsequent preparation steps. The DNA thus was immobilized by those ITC-terminated silane molecules which were covalently bound to the glass substrate and were not removed during the washing procedures.

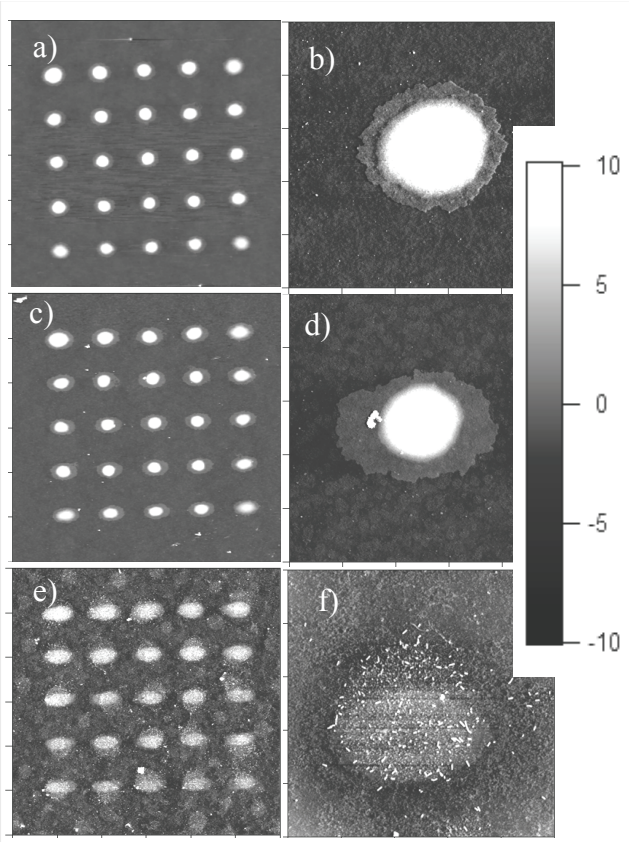

Figure 4. AFM topography images of a 5 x 5 array of ITC-terminated spots after deposition of ITCPTES by DPN (a), after coupling with linker DNA (c) and after TLP self-assembly (e). (b), (d) and (f) show the magnification of individual spots of (a), (c) and (e), respectively.

In conclusion, it was shown successfully that DPN is a structuring method which is perfectly compatible with the ITC-based chemistry used for the site-selective bottom-up assembly of viral nanoparticles on oxidic surfaces. This result is an important milestone on the way to the preparation of submicron-sized surface areas as coupling sites which will offer the opportunity to control the density of the TMV-like particles on a substrate according to the requirements of an application e.g. as carrier systems for enzymes.

The results of this project were published in Langmuir, DOI: 10.1021/la302774h (in print).

3. Publications (please stick to the user guidelines for publications and acknowledgements on www.knmf.kit.edu):

[1] Mueller, A.; Eber, F. J.; Azucena, C.; Petershans, A.; Bittner, A. M.; Gliemann, H.; Jeske, H.; Wege, C. *Acs Nano* **2011**, *5*, 4512.
[2] Piner, R. D.; Zhu, J.; Xu, F.; Hong, S.; Mirkin, C. A. *Science* **1999**, *283*, 661.
[3] Ginger, D. S.; Zhang, H.; Mirkin, C. A. *Angewandte Chemie International Edition* **2004**, *43*, 30.

[4] Salaita, K.; Wang, Y.; Mirkin, C. A. *Nat Nano* **2007**, *2*, 145.
[5] Wu, C.-C.; Reinhoudt, D. N.; Otto, C.; Subramaniam, V.; Velders, A. H. *Small* **2011**, *7*, 989.
[6] Azucena, C. *et al.*, *Langmuir* **2012**, DOI: 10.1021/la302774h
[7] Yang, L.; Feng, J.; Zhang, W.; Qu, J.-e. *Applied Surface Science* **2010**, *256*, 6787.

4. Comments (max. 1.800 characters)**:**

The authors Christina Wege and Fabian Eber thank the Baden-Württemberg Stiftung (KFN IV) as well as the DFG (SPP 1569) for funding this research, and Andre Petershans, Anna Müller, Alexander Bittner, Holger Jeske, Thomas Schimmel and Stefan Walheim for their support and valuable discussions. We are most grateful to Hartmut Gliemann and Carlos Azucena, and to the KNMF user office and facility team, for the fruitful and inspiring collaboration on the project.

Proposal 2011-006-000517

STEM tomography of whole cells

Niels de Jonge

Vanderbilt University School of Medicine
Nashville
USA

Final Report

1. Project goals (max. 1.800 characters)**:**

The current method to obtain three-dimensional (3D) information of the ultrastructure of cells is tilt-seriestransmission electron microscopy (TEM) on cells prepared into thin section. However, only thin sections can be examined and the cells are thus not intact. Scanning TEM (STEM) obtains nanometer resolution on heavy nanoparticles even through micrometers of a light material3-5. The idea is to specifically label proteins in cells, to prepare critically point dried whole cell samples6, and to image these with STEM. 3D information will be obtained via tilt-series STEM and tomography reconstruction. This approach should provide a 3D map of the protein locations in a whole cell with nanometer precision. The first aim is to test the feasibility of this methodology. If it works, we would like to use STEM tomography to study endocytosis of the epidermal growth factor (EGF) receptor in whole cells, exploring the 3D distribution of the receptor in vesicles at different stages of the process of endocytosis.

2. Project results (max. 7.000 characters + figures)**:**

Whole-mount fixed cellular samples were prepared. The level of membrane staining was kept much lower than is common practice in TEM analysis, such that contrast could be obtained on the labels throughout the entire cellular thickness. STEM tilt-series were recorded with a tilt-range of 80° only thus avoiding excessive beam broadening. The locations of the nanoparticles were nevertheless determined with high precision using computation. Similar as in fluorescence microscopy, the dataset did not reveal information about all organelles but addressed the locations of the labels. This method was applied to study the fate of sequentially up-taken low-density lipoprotein conjugated to gold nanoparticles (LDL-gold) in macrophages. Analysis of a 3D reconstruction revealed that newly up-taken LDL-gold was delivered to lysosomes containing previously up-taken LDL-gold thereby forming onion-like clusters.

3. Publications (please stick to the user guidelines for publications and acknowledgements on www.knmf.kit.edu)**:**

Whole-cell Analysis of Low-Density Lipoprotein Uptake by Macrophages using STEM Tomography
J.P. Baudoin, W. G. Jerome, C. Kübel, N. de Jonge, submitted to Biophysical Journal

Karlsruhe Nano Micro Facility (KNMF)
Karlsruhe Institute of Technology (KIT)
Hermann-von-Helmholtz-Platz 1
76344 Eggenstein-Leopoldshafen
Germany

User Office
Phone: +49 (721) 608-3123
Fax: +49 (721) 608-6273
Email: knmf-useroffice@kit.edu
Web: www.knmf.kit.edu

4. Comments (max. 1.800 characters)**:**

I was very happy with the KNMF.
Dr. Kuebel provided fantastic help.
The microscope worked great.
We have submitted a publication with the data.

Note: when asking for the report I recommend emphasizing that only a very short report is required. The indicated maximal length in characters suggests that a rather large report is required.

Karlsruhe Nano Micro Facility (KNMF)
Karlsruhe Institute of Technology (KIT)
Hermann-von-Helmholtz-Platz 1
76344 Eggenstein-Leopoldshafen
Germany

User Office
Phone: +49 (721) 608-3123
Fax: +49 (721) 608-6273
Email: knmf-useroffice@kit.edu
Web: www.knmf.kit.edu

Proposal 2011-006-000532

Investigation on the elemental distribution in amorphous IndiumZinc Oxide Phases

Jörg Schneider

Technische Universität Darmstadt
Darmstadt
Germany

Final Report

1. Project goals (max. 1.800 characters):

Amorphous semiconductors are a new class of materials with growing importance for the use in field-effect transistors (FETs). Whereas gas phase deposition is commonly used, solution deposition might be an attractive alternative. Thereby a mixture of soluble precursors is deposited and converted to the ceramic by annealing above the decomposition temperature of the precursors. The electronic properties, however, depend very much on the course of the processing, whereby the influence of distinct parameters can be difficult to explain. Minor differences in heating temperature and rate can strongly influence performance values such as charge carrier mobility, on/off ratio and threshold voltage. The cause of these effects can be manifold. Apart from film morphology and uniformity, microstructure and homogeneity on a nanometer scale as well as surface adsorbates and point defects might play a role.
The present work was carried out to enhance the knowledge of the performance of solution deposited indium zinc oxide (IZO) by studying structure-property relationships. Auger spectroscopy is a tool which can monitor differences in film composition over a larger area in comparably little time and at nanoscale resolution. The aim was to answer the question, whether differences in performance are due to variation in the composition of the film. This is potentially possible, since a mixture of precursors has to be employed to obtain the multinary oxide composition IZO.

2. Project results (max. 7.000 characters + figures):

IZO thin films (ratio indium to zinc = 60:40 in all cases) with a thickness of about 15 nm very were deposited from precursor solutions on prefabricated substrates for field effect transistors (Figure 1a). Different samples were obtained by variation of the annealing procedure and the electrical performance was measured. In addition a sample of indium oxide was produced for comparison purposes. The samples could be inserted in the Auger spectrometer without any problems or the requirement of further modification or conditioning. Thus, functional devices could be characterized directly. No electrostatic charging was observed. For each sample line scans, depth profiles, as well as elemental mapping overview spectra were recorded.

Linescans were carried out over various ranges. Larger distances (~ 10 µm) corresponding to the electrode distance were regarded as well as shorter distances (~ 0.25 µm; Figure 1b) which use the ultimate resolution of the instrument. Taking the indium oxide reference sample into account, the variation of the signal intensity in the line scans did not reveal any inhomogeneities. This is also true when IZO on the gold electrodes is compared with the part of the film on the silicon dioxide dielectric. Furthermore no obvious differences between samples with varying processing procedure were evident.

In the next step Auger depth profiles were measured. Although the lowest possible sputtering rate was chosen, the rather small thickness of the IZO films (~ 15 nm) limited the number of possible data points. A quantitative analysis of the oxygen signal allowed differentiating between contribution from the IZO semiconductor and the silicon dioxide dielectric (Figure 2). The depth profile confirmed the view that the IZO

films have a very uniform and homogeneous composition. There are indications that the situation directly at the semiconductor dielectric interface might be slightly different than in the bulk film. This could, however, not be resolved in the current measurements.

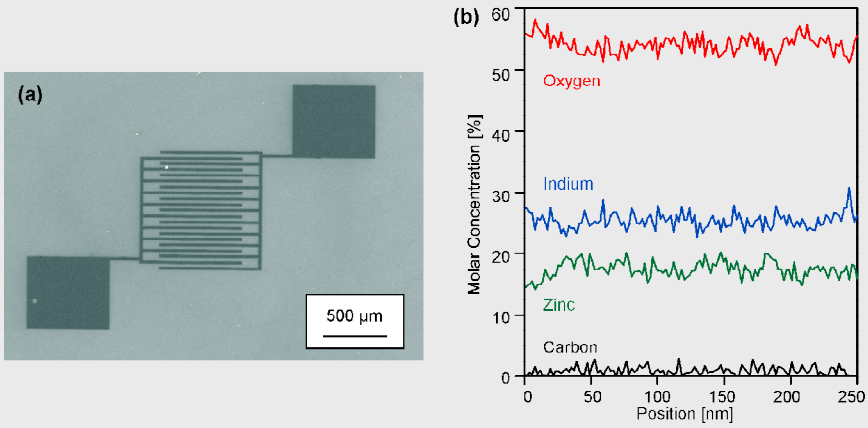

Figure 1: (a) SEM micrograph of a top view of the interdigital electrode structure used for FETs. Complete devices consist of a highly doped silicon substrate with silicon dioxide and gold electrodes whereby IZO is deposited on top (bottom gate/bottom contact set-up). (b) An Auger linescan (128 data points) of IZO film on FET substrate.

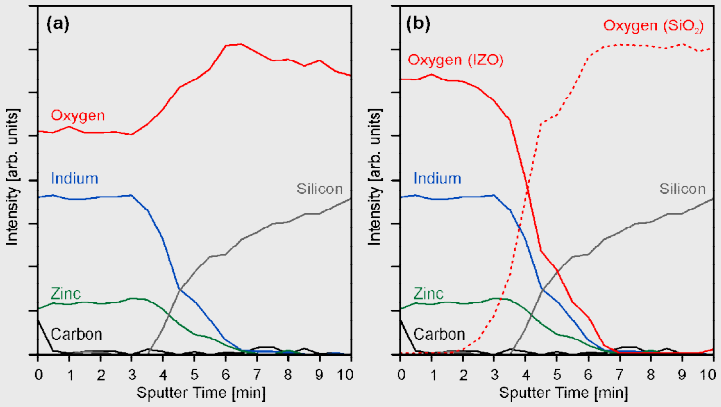

Figure 2: Auger depth profile (20 data points) of an IZO film on FET substrate. (a) total oxygen contribution, (b) oxygen signals for IZO and SiO_2 indicated separately.

In summary the Auger measurements discussed in this report revealed that different processing procedures did not affect the local composition or structure (within the range of the resolution of the instrument). This is a very important finding as it provides a basis for taking other factors into accounts for discussing device performance.

3. Publications (please stick to the user guidelines for publications and acknowledgements on www.knmf.kit.edu)**:**

J.J. Schneider, et al.; "Solution processed indium zinc oxide as semiconductor material in high performance field effect transistors"; currently in preparation.

4. Comments (max. 1.800 characters)**:**

Measurements were scheduled for 4 days from 5 to 8 December 2011. However, due to technical problems with the instrument (breakdown of the instrument's ultra-high vacuum system) the measurements were finished after 2 days on 7 of December. Although it might have been helpful to investigate more samples in depth, the series can be considered complete and sufficient information was gathered to obtain a complete picture. This is in agreement with our original time demand for 2 days of measuring time.

Karlsruhe Nano Micro Facility (KNMF)
Karlsruhe Institute of Technology (KIT)
Hermann-von-Helmholtz-Platz 1
76344 Eggenstein-Leopoldshafen
Germany

User Office
Phone: +49 (721) 608-3123
Fax: +49 (721) 608-6273
Email: knmf-useroffice@kit.edu
Web: www.knmf.kit.edu

Proposal 2011-006-000538

Nanoscale growth twins for the development of grain boundary engineered structures

Andrea Hodge

University of Southern California
Los Angeles, CA
USA

KNMF Annual Report 2011
2011-006-000538: Nanoscale growth twins for the development of grain boundary engineered structures

PI- Andrea M Hodge

During our use of the KNMF facilities, we were able to use the FIB for imaging top and cross section of several sputtered coating. The goal was to determine how the microstructure changed from the substrate side to the top and to see if there was a highly nanotwinned structure. In Figures 1 and 2 we show two views of two different nanotwinned samples. By using the FIB we were able to determine the effect of cooling the substrate. Additionally, non-twinned and less twin samples were also investigated in order to access the effect of sputtering conditions on the overall twin density as shown in Figure 3.

From this work we have written a manuscript titled: "Thermal stability of highly nanotwinned copper: the role of grain boundaries and texture" which has been submitted to Journal of Materials Research in May 2012.

The KNMF acknowledgment as stated on the website was included in the manuscript.

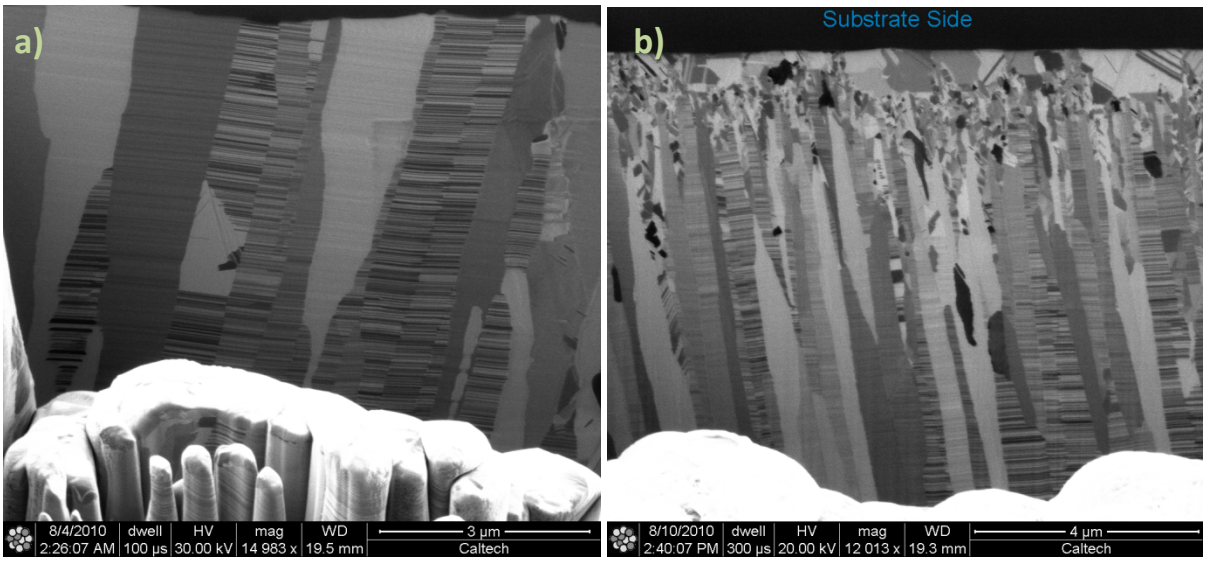

Figure 1 INT-THICK-, 0.8 nm/sec, , 9 hrs sputtering uninterrupted, 27 µm thick, uncooled substrate; a) top surface and b)substrate surface

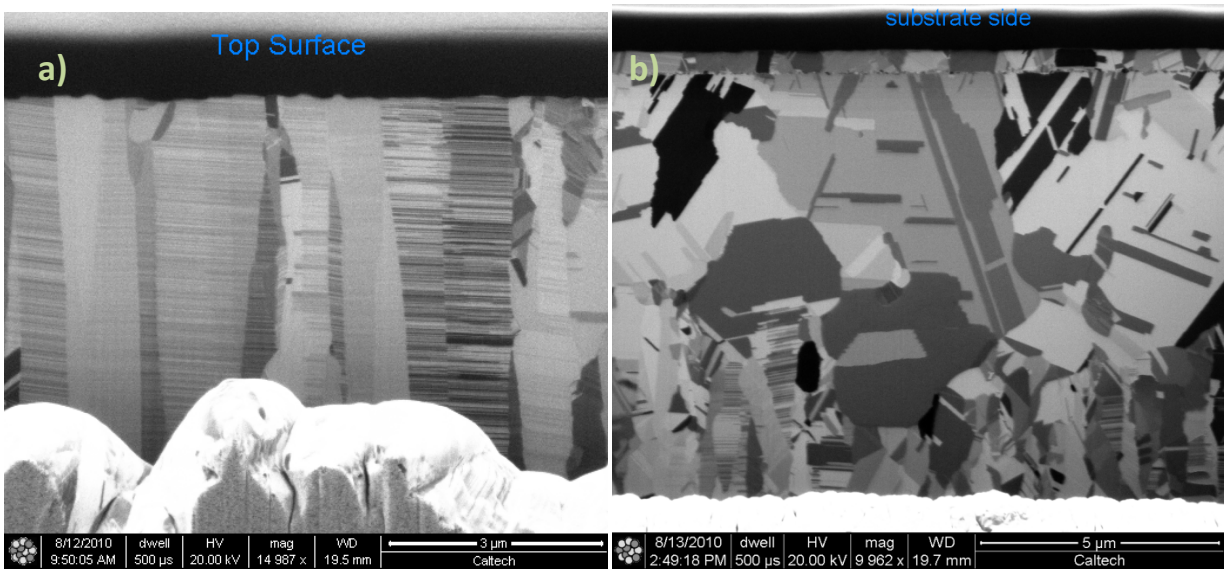

Figure 2 INT-THICK-2 :, 9 hrs sputtering uninterrupted, 27 µm thick, cooled substrate; a) top surface, b) substrate surface

INT-2011-02 -- FIB cross-section (cut from top surface)

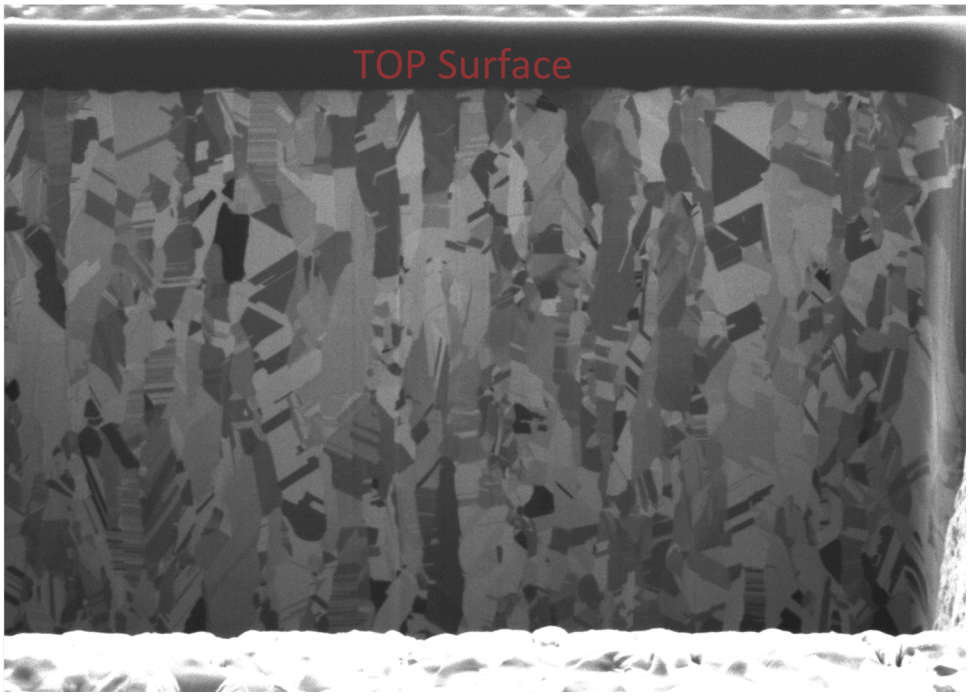

Figure 3. Columnar Copper samples with some nanotwins

Proposal 2011-006-000545

Laser-assisted localized contact angle modifications for thermoplastics in Lab-on-a-Chip applications

Frank Schwemmer

Albert-Ludwigs-Universität Freiburg
Freiburg
Germany

Note: *Please fill in this report form and save/print it as a PDF file, then upload it to the KNMF proposal submission system. A cover page containing proposal title, proposer name(s), and technologies selected will be added by the system. A link for the download of the complete report as a PDF file will be displayed in the system.*

Final Report

1. Project goals (max. 1.800 characters)**:**

Liquid flow in micro-domains is heavily dependent on the contact angle between the respective liquid and the substrate. Thus efficient manipulation of liquids in Lab-on-a-Chip technologies requires precise control over surface properties.
The main goal of the project was to explore the effects of laser induced µm-sized modifications on channel surfaces on the wetting properties. The long term vision of the project was to pave the way for replacing the currently used, expensive chemical surface modifications and introduce a simpler, cheaper and more reproducible alternative that relies on geometries that can be manufactured with replication technologies such as injection molding..
Finally, the aim was to test suitable reproduction techniques for these µm-sized features, in order to show the scalability of the technologies.
All of the technologies where tested for applicability in centrifugal microfluidics.

2. Project results (max. 7.000 characters + figures)**:**

Both faster and slower wetting of structures can be desirable in certain scenarios. These options were explored by designing and laser structuring of suitable layouts. All masters were micro-milled in polystyrol at IMTEK Freiburg and laser-modified at the Karlsruhe Institute of Technology.

Hydrophobic modification
In order to evaluate the applicability of µm-sized modifications for hydrophobic surfaces, a centrifugal aliquoting structure was designed (fig. 1). These structures require burst valves, which stop liquids up to a certain pressure. This can be achieved by a local hydrophobic modification, e.g. Teflon-carbon black in order to locally increase the contact angle. Liquid then stops at such a hydrophobic constriction, but can be released by larger pressures, which in turn can be obtained by higher spinning frequencies of the centrifugal microfluidic disk.
In this study 5 µm micro-grooves perpendicular to the flow direction or a multiscale roughness were introduced into the valve's surface. It was expected that such structures decrease wetting of the channel due to successive pinning of the liquid meniscus. Results can be seen in fig. 2.

Karlsruhe Nano Micro Facility (KNMF)
Karlsruhe Institute of Technology (KIT)
Hermann-von-Helmholtz-Platz 1
76344 Eggenstein-Leopoldshafen
Germany

User Office
Phone: +49 (721) 608-3123
Fax: +49 (721) 608-6273
Email: knmf-useroffice@kit.edu
Web: www.knmf.kit.edu

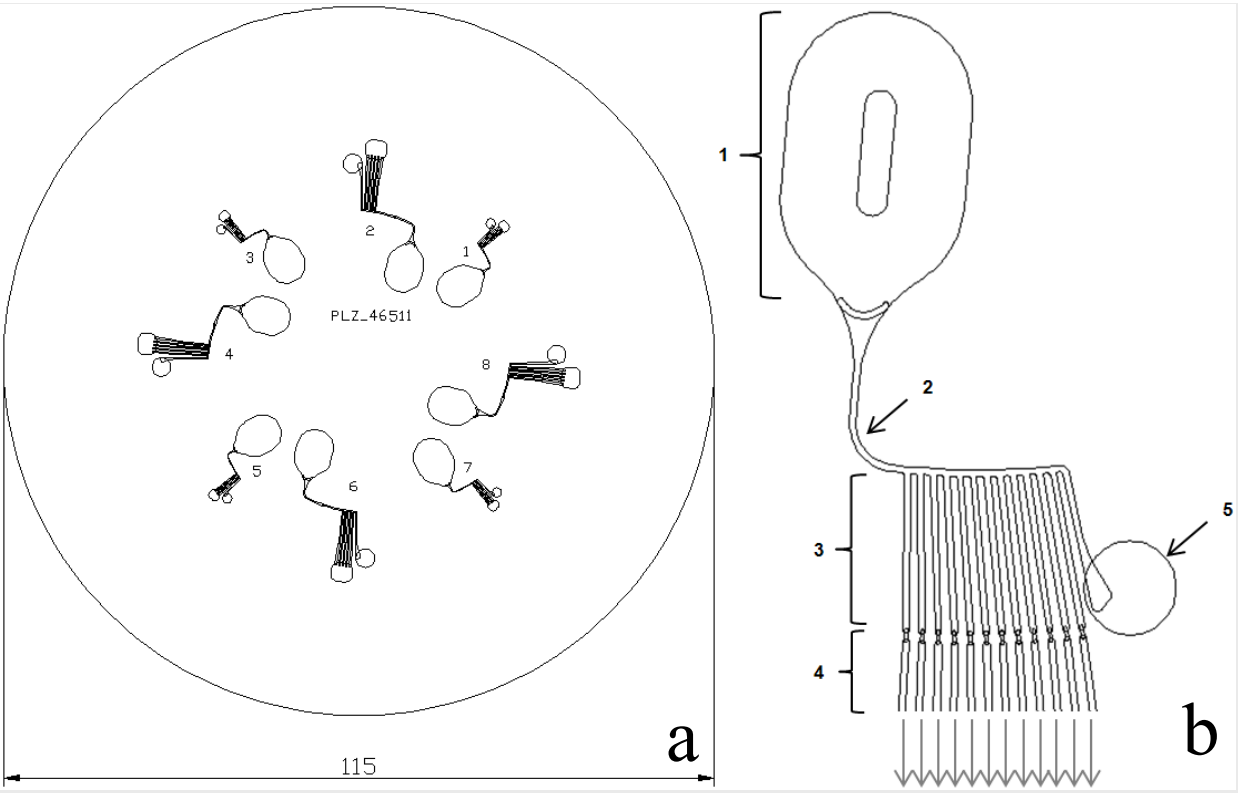

Figure 1: (a) *Design of the aliquoting disk (diameter 115 mm).* ***(b)*** *Functional parts of the aliquoting structure The sample is pipetted into the inlet (1). At medium frequencies (< 20 Hz) the liquid is transported via the supporting channel (2) to the metering fingers (3). The liquid stops at the hydrophobically modified valve (4) . Excess liquid is transported into the waste (5).*

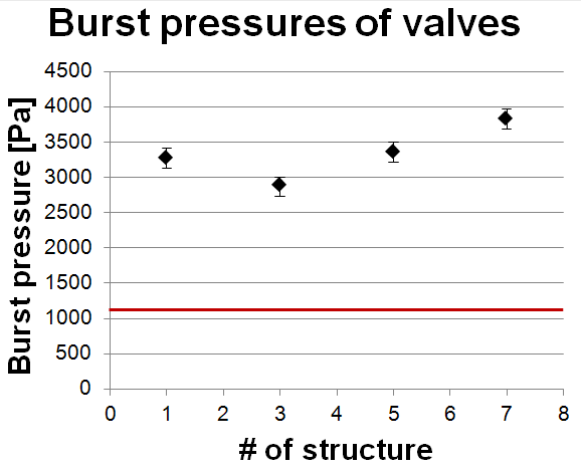

Figure 2: *Burst pressures for modified structures from figure* ***(1 a)****. The burst pressure for an unmodified valve was too little to be quantified and is less than the red line. Only small (odd numbered) structures could be evaluated, since burst pressures were too low in the large (even numbered) structures. Structures 1 and 3 were modified with perpendicular channels (5 µm width). Structures 5 and 7 were modified with a multi-scale roughness. Error bars indicate one standard deviation.*

Due to larger initial pressures the effect on contact angle of the microgrooves was too small to allow aliquoting and thus could not be quantified within the larger structures (even numbers fig. 1b). However, an **effective change in wetting**, compared to unmodified channels, **was observed for the smaller structures** (odd numbers fig. 1b).
This means that further study is required in order to optimize the microstructures and the fluidic layout to get a more robust valving, comparable to results with chemical surface modifications (~ 6250 Pa for Teflon - carbon black patch).

Hydrophilic modification
In order to investigate the effect of higher wetting of micro channels due to surface modifications, a capillary siphon was designed. The siphon was tested both unmodified and with 5 µm wide microgrooves parallel to the channel. Results can be seen in fig. 3.
It can be seen that in both tests, as expected, the parallel microgrooves increased the wetting of the siphon channel. The effect was especially significant for the micro channel with 0.8 mm width and 1.5 mm depth, compared to the channel with 0.7 mm width and 1.8 mm depth. This can be explained by the higher ratio of modified surface to total surface for this channel.
This can be investigated in future studies by further increasing the named ratio between modified surface and total channel surface and by further decreasing the pitch size of the microstructures, we expect to be able to further increase the wetting of the siphon channel.

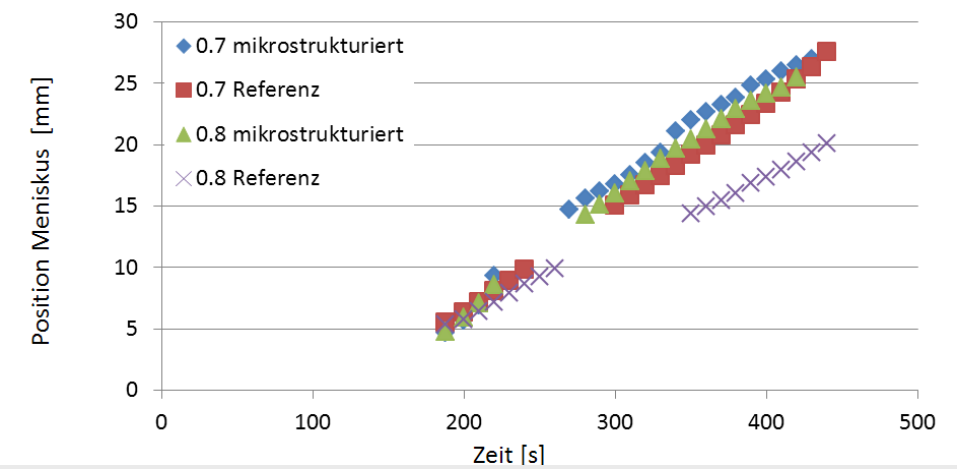

Figure 3: *Position of meniscus in siphon channel. The aim was to maximize the speed of the meniscus by surface modification. Microstructured channels were modified with 5 µm width microgrooves. Reference channels did not contain microgrooves.*

Reproduction of micrometer sized surface modifications
For replication of the microstructures a PDMS cast (Wacker RT 607) of the microstructures was generated. This cast could now be used as a masterstructure for rapid thermoforming. From fig. 4 it can be seen that the introduced microstructures could be reproduced in 188 µm COP foil with high accuracy. However, within the scope of this project the fluidic influences of these reproduced structures compared to reference structurs could not be evaluated anymore.

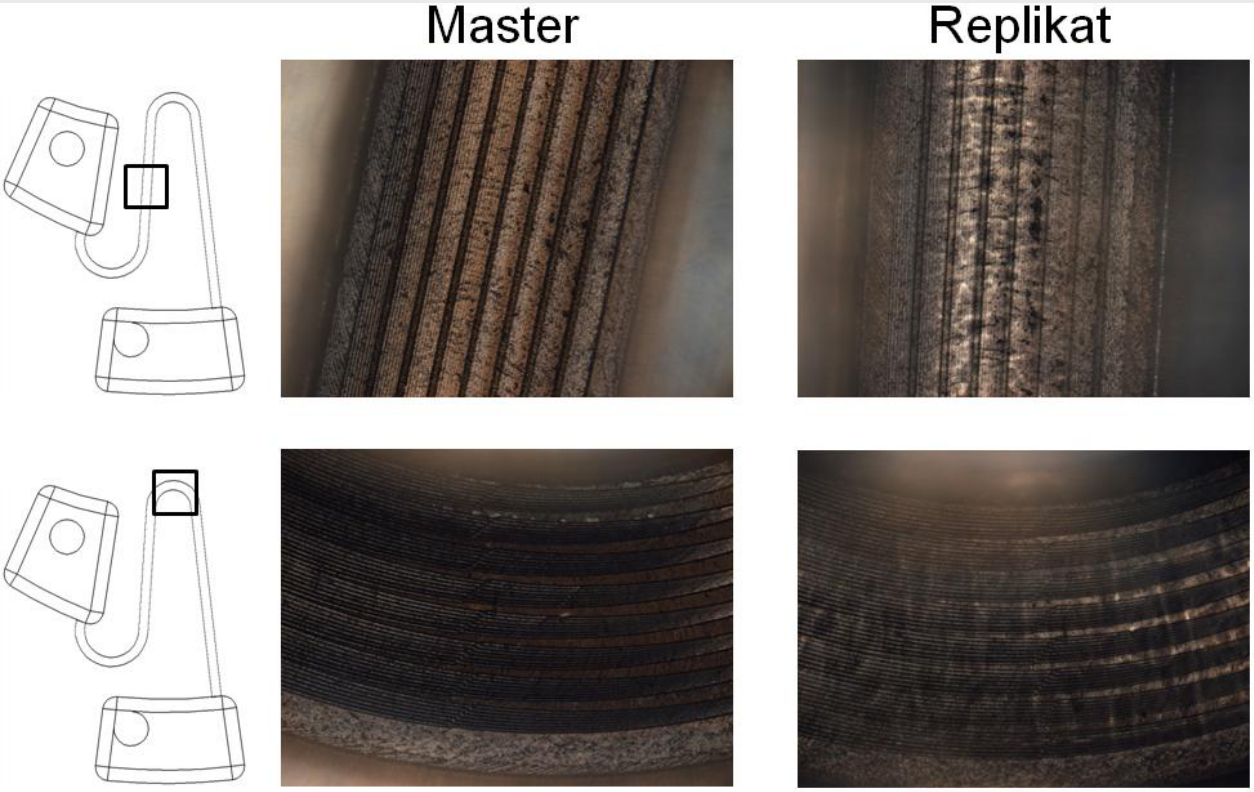

Figure 4: *Two different positions of the siphon channel in master and replicate.*

3. Publications (please stick to the user guidelines for publications and acknowledgements on www.knmf.kit.edu)**:**

No publications are prepared with the current data set. However, an expanded data set could lead to a manuscript that would most likely be considered valuable for the microfluidics community.

4. Comments (max. 1.800 characters)**:**

We thank Dr. Wilhelm Pfleging and Heino Besser for the laser modification of the substrates and helpful discussions within the project.

Proposal 2011-006-000556

Fundamentals of design and investigations of the characteristics of optoelectronic devices on the basis of controlled self-organization processes, self-assembly and super-structuring in the epitaxial alloys of III-V semiconductors

Pavel Seredin

Voronezh State University
Voronezh
Russia

Final Report

1. Project goals (max. 1.800 characters)**:**

Semiconductor alloys based on III-V compounds provide a considerable advantage over routine silicon electronics due to a number of properties: possibility to control the value of the band gap by varying their composition, direct band gaps of the alloys, high carrier mobility and so on. However, the use of III-V semiconductors is rather often limited by the difficulty in the choice of a suitable heteropair determined by the type of the structure that is required for a work. In order to elaborate and design the structures with 2D electron gas on the basis of heterojunction one should account for the main requirement of the equality of lattice parameters for both of semiconductors in heteropair. This condition imposes a number of limitations on the integration of III-V compounds to the component electronic base as well as its synthesis with silicon technology in electronics since the latter one has an indisputable advantage – the less cost. Moreover, the possibility and demand of integration in a wide range of compositions for III-V compounds with different substrates including silicon ones are provided by the requirements that are outside the present capabilities of III-V compounds. The aim of the Project is the investigations of the main possibilities for the integration of the epitaxial films of semiconductor alloys with silicon technology and investigations of the characteristics of these objects by structural and spectroscopic methods.

2. Project results (max. 7.000 characters + figures)**:**

During execution of the project we investigated the samples of epitaxial heterostructures (heterostructures based on $Al_xGa_{1-x}As$ whith high concentration of Si (more less 10^{20} cm^{-3}) and low concentration of phosphorus obtained jointly by Ioffe Physico-Technical institute of the Russian Academy of Sciences, Saint-Petersburg by MOCVD technique. We determined of fabrication conditions for obtaining non-strained epitaxial films of semiconductor $Al_xGa_{1-x}As$ alloys of different composition doped with silicon which are best fitted with monocrystalline substrate by crystal lattice parameter in order to achieve integration of the epitaxial films of semiconductor alloys with silicon technology as well as the studied of characteristics of these objects by structural and spectroscopic methods.

From the analysis of the experimental data obtained by XRD studies, Raman spectroscopy, elemental microanalysis, and Hall measurements in combination with the results of simulation of the technological conditions, it is possible to draw a number of inferences about the effect of doping with Si on the homoepitaxial GaAs:Si/GaAs(100) structures and $Al_xGa_{1-x}As$:Si/GaAs(100) heterostructures containing different proportions of Al in the alloy and different amounts of Si

dopants.
By analyzing the results, we can clarify some empirical correlations between the parameters of epitaxial heterostructures and the manufacturing conditions of growth. The results show that,
the lower the temperature of the substrate holder and the more intense the disilane (Si_2H_6) flux, the higher the content of Si atoms in the $Al_xGa_{1-x}As$:Si alloy.
A similar correlation can be observed for the Hall concentration of charge carriers: the concentration varies in the same manner as the temperature of the substrate holder and the disilane flux.
To find the optimal relation between the technological parameters of growth, i.e., the disilane flux and the internal reactor temperature that provide complete lattice matching of the epitaxial layer with dissolved silicon to the single_crystal substrate we determined the relation between the lattice mismatch Δa and the parameters of growth. To do this, we specifyed the flux–temperature–mismatch (V–T–Δa) coordinate system and, on the basis of the experimental data, construct the diagrams of the dependences Δa(V, T) for the homoepitaxial structures and
heterostructures with $x \approx 0.25$ and $x \approx 0.40$. Thereafter, using the methods of regression
analysis of the software package Sigma Plot 11, we approximated the relation between the quantities
Nevertheless, it should be noted that the high level of doping with Si is bound to yield a high concentration of charge carriers (up to ~10^{20} cm^{-3}). However,Hall measurements yield substantially lower concentrations. Taking into account noticeable deviations of
the lattice parameter from the generalized Vegard's law, we can infer that such substantial deviations of the experimental concentrations from the expected values
are indicative of the formation of deep levels. Such levels are created by complex defects and complexes produced as a result of formation of ternary and quaternary alloys with Si. Undoubtedly, in $Al_xGa_{1-x}As$:Si alloy silicon atoms can replace not only gallium but also aluminum atoms in the metal sublattice. With the same concentration of aluminum and gallium atoms in the alloy under substitution of aluminum atoms with donor impurity atom $Al_xGa_{1-x}As$:Si the lattice parameter changes to smaller values to a greater extent than in the case of gallium substitution, due to the essential difference of atomic radii of the latter ones. In addition, at high concentrations of silicon, the impurity can behave itself like an amphoteric one, substituting arsenic atoms. The data analysis of elements concentrations in MOCVD epitaxial films shows different possibilities in the behavior of silicon during the replacement of elements in $Al_xGa_{1-x}As$:Si alloy. The detailed Raman spectroscopy analysis has helped in solving this task. We shown that changes of the stoichiometry can occur in the case of the formation of DX-centers in $Al_xGa_{1-x}As$:Si alloys, accompanied by the break of donor-crystal bond and the displacement of the donor atom, the change of bond lengths in the crystal lattice, and the decrease of the lattice parameter.
Thereby, using the X_ray diffraction and Raman spectroscopy of KNMF KIT allowed to obtain the data for MOCVD $Al_xGa_{1-x}As$:Si alloy. A similar correlation can be observed for the GaAs(100) heterostructures and homoepitaxial GaAs:Si/GaAs(100) structures doped with Si to a content of up to ~1 at %. It is now clear that the controllable introduction of Si dopants provides a means for completely matching the lattice parameters of the $Al_xGa_{1-x}As$:Si alloys and the single crystal substrate and, thus, for solving one of the basic manufacturing problems, i.e., the problem

of growing heterostructures matched in lattice parameter.

3. Publications (please stick to the user guidelines for publications and acknowledgements on www.knmf.kit.edu)**:**

1. Structure and surface morphology of AlxGayIn1-x-yAszP1-z/GaAs(100) heterostructures / 20th Int. Symp. Nanostructures: Physics and Technology" Nizhny Novgorod, Russia, June 24-30, 2012 //accepted for publication

2. Investigation of structure and optical property of AlGaAsP:Si/GaAs(100) heterostructures // sent to the journal '"Semiconductors"

4. Comments (max. 1.800 characters)**:**

Proposal 2011-006-000569

Controllable preparation of Cu and Cu/Cu2O core/shell nanoparticles

Andrew Wheatley

Cambridge University
Cambridge
United Kingdom

Note: *Please fill in this report form and save/print it as a PDF file, then upload it to the KNMF proposal submission system. A cover page containing proposal title, proposer name(s), and technologies selected will be added by the system. A link for the download of the complete report as a PDF file will be displayed in the system.*

Final Report

1. Project goals (max. 1.800 characters)**:**

The work carried out at the KMNF was intended to characterise nanoparticles using STEM and other analytical techniques available in the microscope's scanning mode. Samples of iron-platinum were analyzed with the intention of confirming that particles were alloyed in nature. A second goal was to confirm the presence of gold coatings on FePt nanoparticles using EDX and EELS line scans and mapping. Copper nanoparticles were analysed to establish the nature of their oxidation state – whether the sample was a mixture of oxide/metal, or whether the oxide was forming a stable shell around the particles.

2. Project results (max. 7.000 characters + figures)**:**

A number of FePt samples were analysed. These used different amounts of gold precursor in an attempt to control the thickness of the formed shell. Analysis of the FePt samples showed that the gold had not, in fact, coated the seed nanoparticles in any of the samples, but had formed innumerable small clusters of around 1nm in size (Figure 1), as well as a large number of bigger gold particles. Work can now be done to adjust our coating procedure in the hope of better results in the future. The extent of the formation of tiny gold nanoparticles had not been identified on the bright field microscope in Cambridge, but because of the high resolution of the dark field imaging on the FEI Titan, and the high Z contrast of gold, the particles were much more obvious here. EDS & EELS mapping was performed, showing little evidence of the possibility of core/shell particles (Figure 2). The background of gold particles also meant that whichever region was selected for EDS, gold was detected.

Karlsruhe Nano Micro Facility (KNMF)
Karlsruhe Institute of Technology (KIT)
Hermann-von-Helmholtz-Platz 1
76344 Eggenstein-Leopoldshafen
Germany

User Office
Phone: +49 (721) 608-3123
Fax: +49 (721) 608-6273
Email: knmf-useroffice@kit.edu
Web: www.knmf.kit.edu

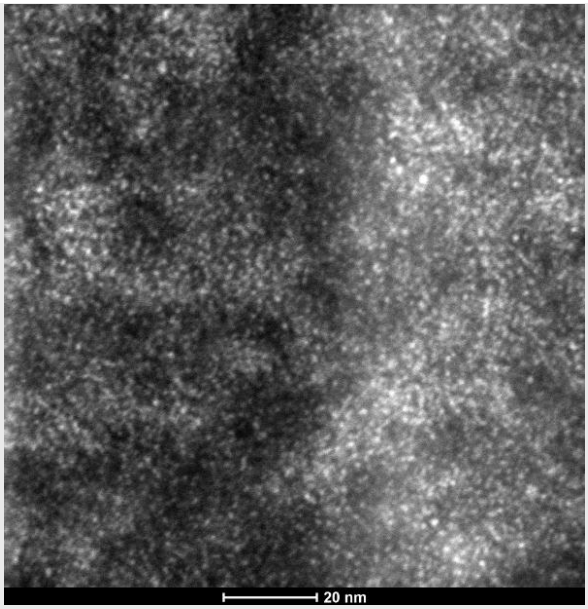

Figure 1 - A dark field image of BKFePt7@Au1 showing the background of small gold particles covering the carbon film.

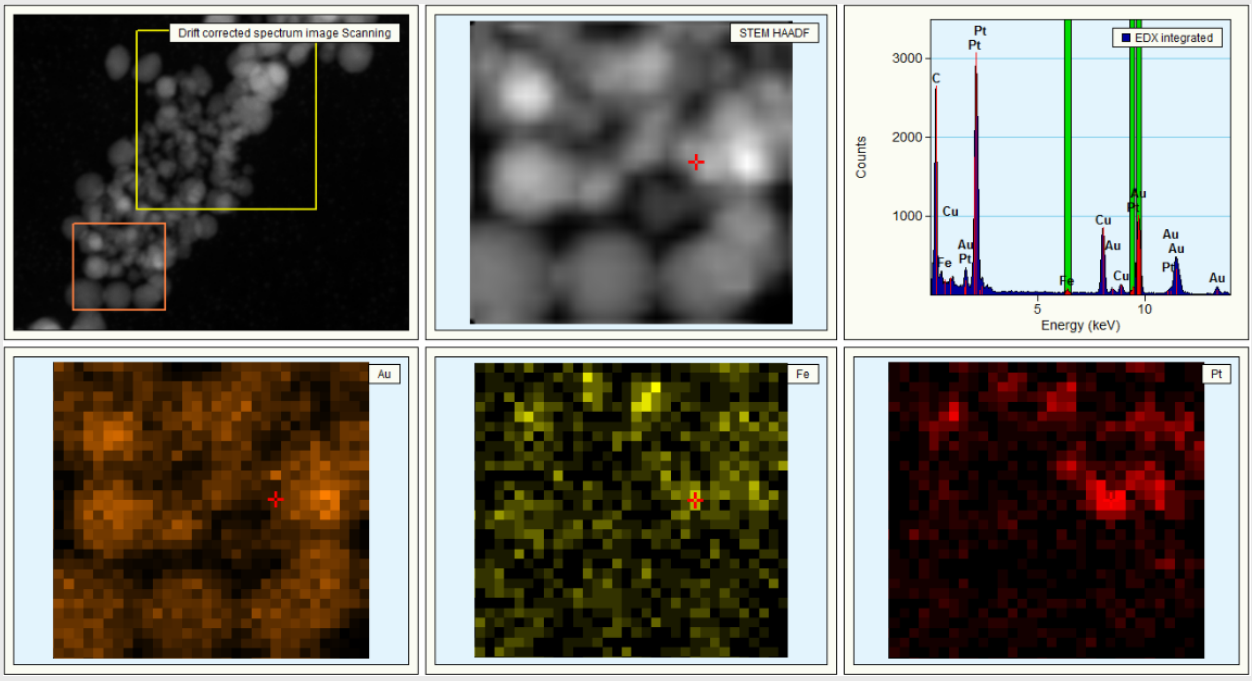

Figure 2 - EDS map of BKFePt5@Au1 particles, showing that the larger particles observed appear to be gold rather than gold coated FePt.

Karlsruhe Nano Micro Facility (KNMF)
Karlsruhe Institute of Technology (KIT)
Hermann-von-Helmholtz-Platz 1
76344 Eggenstein-Leopoldshafen
Germany

User Office
Phone: +49 (721) 608-3123
Fax: +49 (721) 608-6273
Email: knmf-useroffice@kit.edu
Web: www.knmf.kit.edu

Copper particles were analysed for evidence of an oxide shell – The first sample analysed, PACu215, had very small particles (1-3 nm, Figure 3), and fringe spacing analysis and EDX confirmed that the sample was copper rather than copper oxide. Were the sample to oxidise, it was agreed that the particles in this sample would be likely to oxidise completely, rather than form a stable core-shell structure.

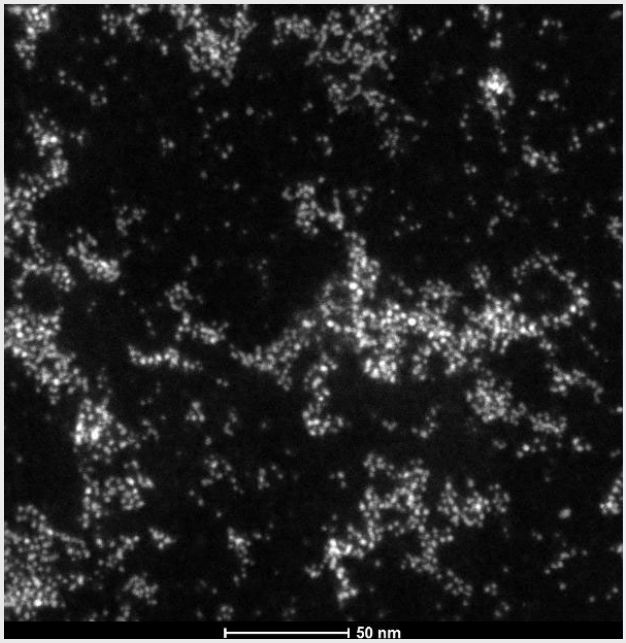

Figure 3 - Dark field image of PACu215 particles.

PACu205 contained a combination of small and much larger particles (Figure 4), but again, no evidence of oxidation or oxide shells were observed. Both the large particles and smaller particles were confirmed by EDS to be copper. The smaller particles aggregated on the carbon film, presenting as large, low contrast discs.

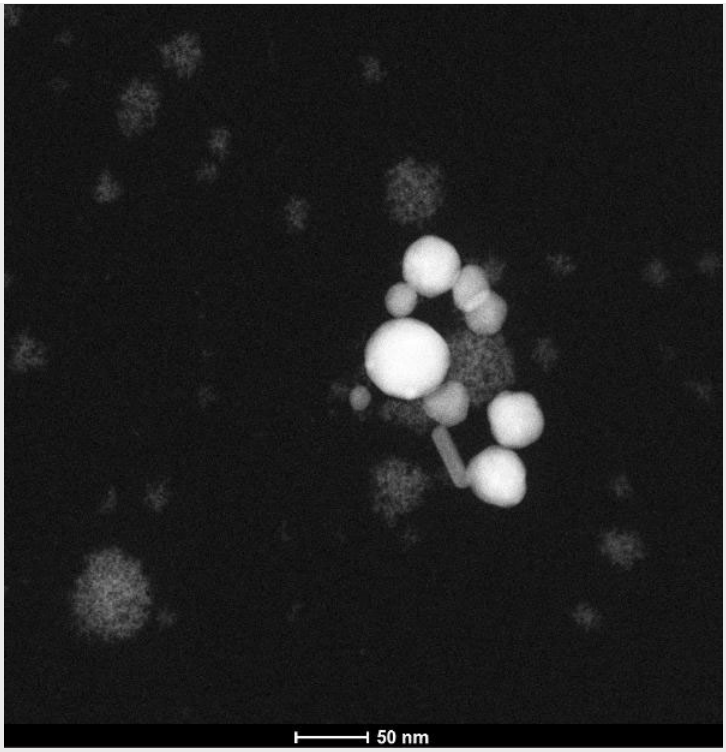

Figure 4 - Dark field image of PACu205.

PACu210 showed the possibility of an oxide shell from a line scan (Figure 5). However the evidence is not entirely convincing, and many more line scans would need to be run on different particles to confirm the nature of the sample. The grid was quite heavily loaded, and low contrast patches were observed on the grid, which are suspected to be silicon contamination from the joint sealant used during the synthesis. Care can now be taken to keep the use of this sealant to a minimum, particularly when organic solvents are being used.

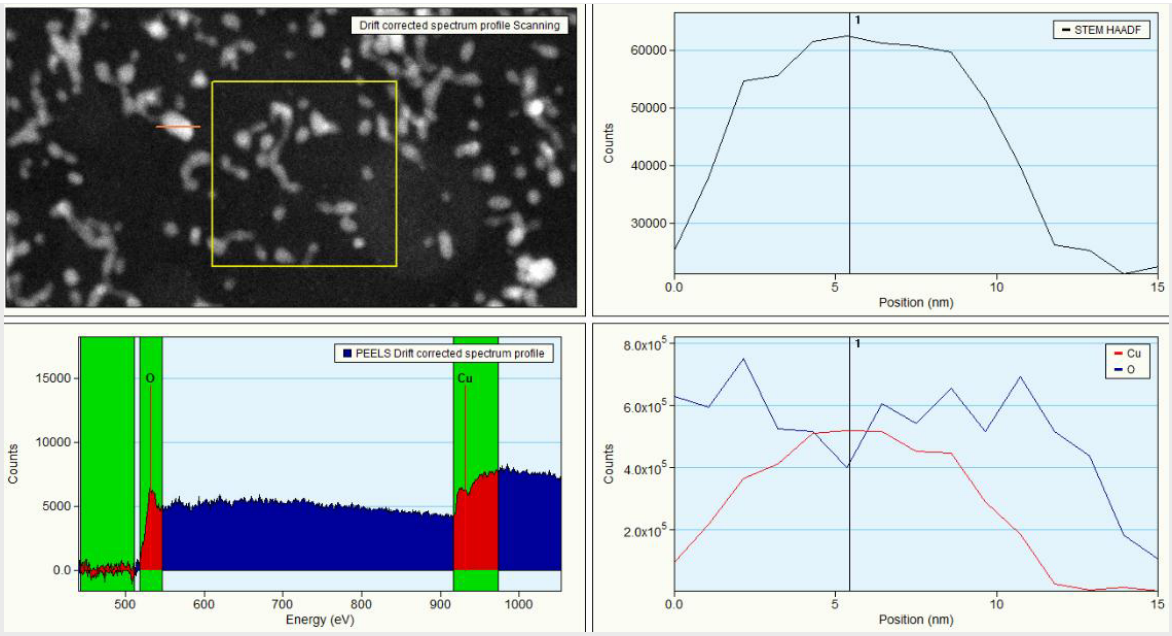

Figure 5 - Line scan EELS and EDS data from a particle in PACu210.

In summary, the copper samples analysed showed good oxidative stability, with little evidence of an oxide shell observed in the majority of samples. A line scan from a particle in PACu210 showed some evidence of an oxide shell, though the noise in the EDS was too high to be assured of such a structure. More analysis of this type will hopefully be carried out in the future since the achievement of stable Cu(0) nanoparticles would be a highly significant result.

FePt samples showed again little evidence of core-shell structures, with EDS mapping suggesting seggregation of the gold from the FePt. The FePt samples could be separated from the gold particles using a magnet, such that any gold present in EDS analysis will be purely from gold stuck to the surface of FePt.

3. Publications (please stick to the user guidelines for publications and acknowledgements on www.knmf.kit.edu):

A paper based on the copper samples analysed is being prepared for submission to RSC journal *Nanoscale*. Results will also be reported at a special session on nanoscale oxides at DSL2012 in Istanbul later this month.

4. Comments (max. 1.800 characters)**:**

The time spent working with Drs. Kübel and Wang in the KMNF were incredibly useful, both as a learning experience and a chance to acquire data from a range of techniques. Both microscopists were very knowledgeable, and I thank them for their time and patience in analyzing our samples and explaining the various processes to me. Since this trip, progress has been made in synthesizing a Co@Fe (core@shell) sample, and the learning experience from Karlsruhe has meant that we better understand the techniques which are available and useful for the identification of core-shell particles. We hope to use the present data to prepare new and more refined systems for study at the KMNF in the future.

Proposal 2011-006-000608

Crystalline superlattices of nanoscopic binary ME and ternary MM'E materials

John Corrigan

The University of Western Ontario
London
Canada

1. Project goals

The synthesis of low-dimensional semiconductors is a focus of intensive research worldwide because of the remarkable potential for their application in optics, electronics and biological labeling. Strict control of size dispersity (for example, by the synthesis of nanoclusters – particles with exactly the same size, shape, and surface chemistry) allows effective utilization of the size-dependent properties of such materials.

The characterization of nanoclusters often involves studying secondary structures or superstructures constructed from thousands of individual elements. Synergistic properties of such superstructures are expected to elucidate properties of individual nanoclusters and to facilitate their application. For instance, superlattices of nanoclusters often can be prepared and isolated as single crystals; thus, complete structural information can be obtained using single crystal XRD. The characterization of superlattices of large nanoclusters is problematic due to challenges with growing quality single crystals. For large systems valuable structural information can be obtained using HRTEM and STEM.

The present project is part of our systematic work on developing a novel approach to the synthesis of large monodisperse CdS and CdSe nanoclusters and their subsequent self-organization into secondary structures. We expect to demonstrate that adjustment of the preparation conditions (*i.e.*, presence and nature of additives) enables creation of monodisperse nanoclusters of tailored size and secondary structures of different morphologies.

Using KNMF facilities (HRTEM and STEM) it was planned to confirm existence of well-defined secondary structures and determine the parameters for the regular 3D arrangement of monodisperse nanoclusters.

2. Project results

A typical procedure for the preparation of CdS nanoclusters and nanoparticles with their subsequent self-organization into 3D secondary structures involves heating a solution of a readily prepared cadmium thiophenolate precursor in the presence/absence of an alkylammonium salt additive under solvothermal conditions.

Solvothermal treatment of the precursor results in the formation of a pale yellow solid material (**1**). Examination of the morphology of the as-synthesized solid using SEM reveals perfectly faceted cubic crystals of 2.5-7.5 µm in size (*fig. 1, left*). A limited amount of solid aggregates, which are apparently non-crystalline and much smaller in size than those cubes, is also present in **1**.

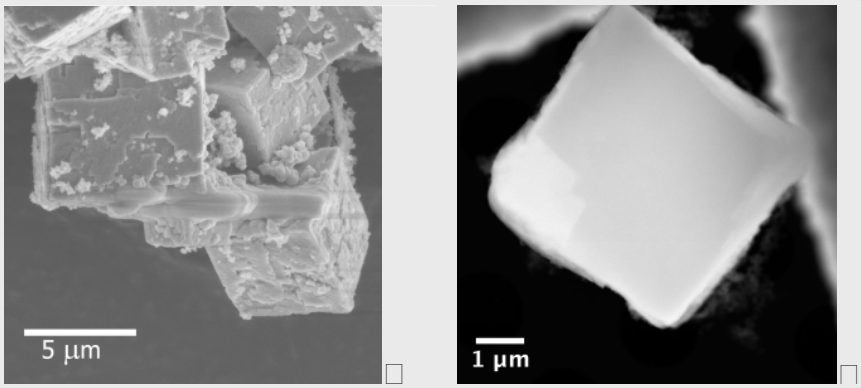

Figure 1. SEM (left) and STEM (right) images of cubic crystals of **1**.

Karlsruhe Nano Micro Facility (KNMF)
Karlsruhe Institute of Technology (KIT)
Hermann-von-Helmholtz-Platz 1
76344 Eggenstein-Leopoldshafen
Germany

User Office
Phone: +49 (721) 608-3123
Fax: +49 (721) 608-6273
Email: knmf-useroffice@kit.edu
Web: www.knmf.kit.edu

STEM and TEM images for the samples, prepared using suspensions of **1** in organic solvents ("wet preparation"), show the presence of limited domains of a well-ordered superlattice of monodisperse CdS nanoclusters. The apparent rectangular packing of nanoclusters is in agreement with a primitive cubic 3D arrangement with a lattice parameter 2.9 nm. This value is very close to interplanar spacing d = 3.0 nm, calculated from the powder XRD data for **1**. Some ordered domains are found to be detached, but they are mostly present on the surface of the cubes. Based on an intense and sharp low angle peak in the powder XRD pattern for **1**, it was postulated that much larger domains of ordered superlattices should exist inside the cubes.

To confirm this, an alternative method of sample preparation was used. It included selective material ablation from micrometer-sized cubes of **1** using focused ion beam (FIB) creating thin slices, transparent for the electron beam in TEM ("FIB preparation"). For as-prepared samples of **1** STEM and TEM images indeed show the presence of continuous domains of superlattice (*fig. 2*); the cubic lattice parameter was found to be very similar to those for the superlattice domains observed on the surface of cubes using wet preparation of samples.

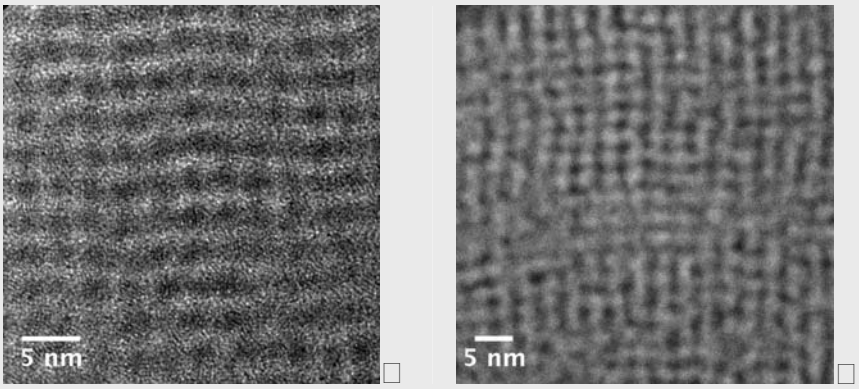

Figure 2. Bright field TEM (left) and STEM (right) images of inner structure of cubes **1** (FIB preparation).
TEM shows the CdS as dark regions and the SPh^- shell as lighter spaces; on STEM CdS appears as bright dots and SPh^- shell – as dark spaces.

It was demonstrated previously that solvothermal treatment of a cadmium thiophenolate precursor in the presence of CTAB (hexadecyltrimethylammonium bromide, an alkylammonium salt with long side chain) results in the formation of $Cd_{130}S_{103}(SPh)_{54}$ nanoclusters [1]. The situation is dramatically different while using short chain alkylammonium salts, *e.g.* tetramethylammonium chloride Me_4NCl. Solvothermal treatment of the precursor in the presence of Me_4NCl results in the formation of a red-orange solid (**2**). SEM analysis of **2** reveals the presence of spheres of 0.5-2.5 µm in size (a few up to 5 µm in size) (*fig. 3, left*).

STEM and TEM images for wet-prepared samples of **2** show the presence of quite large domains of superlattice on the surfaces of spheres. The lattice parameter for this arrangement is found to be 3.4 nm (primitive cubic superlattice), with corresponds to the superlattice formed by $Cd_{130}S_{103}(SPh)_{54}$ nanoclusters. Despite the remarkably large size of the nanoclusters, such domains are generally similar to those found on the surface of cubes of **1**. Meanwhile, STEM and TEM images for FIB-prepared samples of **2** provide decisive evidence that the morphology of the spheres is more complex than the one of the cubes. At least some spheres (*fig. 4, left*) have a clearly distinguishable core-shell structure, with relatively compact outer and

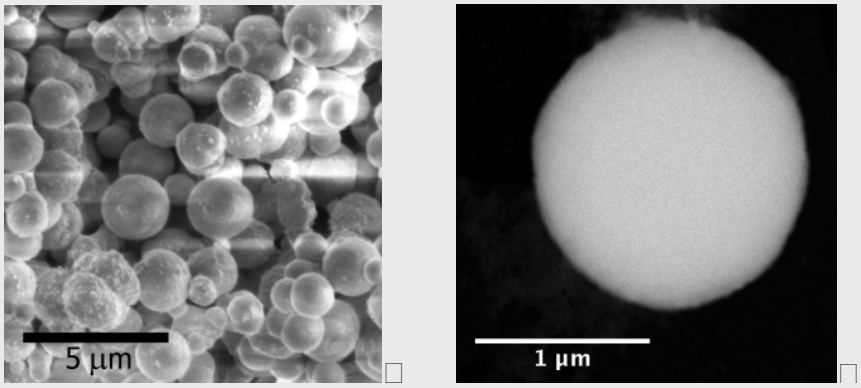

Figure 3. SEM (left) and STEM (right) images of spheres of **2**.

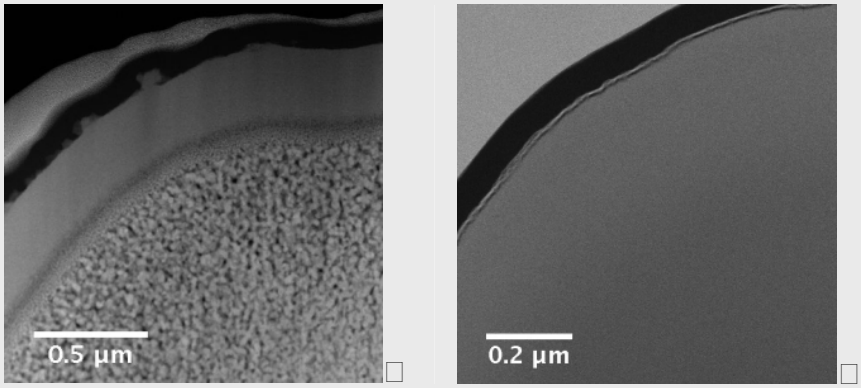

Figure 4. STEM images of thin slices of different spheres from **2**: gradient (left) and homogeneous (right) structures in different samples. In top left corner of both images black area – carbon coating, white area – Pd coating; both introduced as a part of sample preparation by FIB ablation.

inner shells and bulky core. The outer shell (~ 300 nm) there is composed of 2.3 nm sized monodisperse nanoclusters (corresponds to $Cd_{130}S_{103}(SPh)_{54}$). The inner shell (~ 100 nm) has a gradient of nanoparticles ranging in size from 2.5 to 20 nm going from surface to center. The large core of such spheres is composed of nanoparticles at least 20 nm in size (*fig. 4, left*). For some other spheres no obvious size gradient of composing nanoparticles was found (*fig. 4, right*). Such spheres are formed from nearly monodisperse ~ 2.3 nm nanoclusters; no sign of a superlattice or preferable orientation was found.

This confirms that the nature of additives in solvothermal synthesis with cadmium thiophenolate precursor has a great influence both on the size of the obtained nanoclusters and on the morphology of their secondary structure.

The results obtained for the CdS system were then extended to CdSe. It was found that synthesis in solvothermal conditions with the cadmium selenophenolate precursor results in the formation of transparent, cubic yellow crystals up to 0.5 mm in size (**3**). Despite the high beam sensitivity of this material, it was possible to obtain TEM images of **3** (sample prepared by dry spreading of a powdered solid), showing continuous domains of a primitive cubic superlattice of monodisperse nanoclusters with a lattice parameter 2.05 nm (*fig. 5*). This value is in good agreement with interplanar spacing d = 2.0 nm, calculated from the

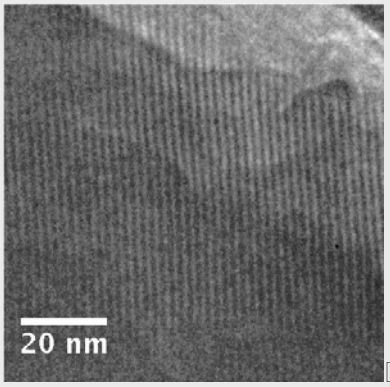

Figure 5. TEM image of cubic crystals of **3**.

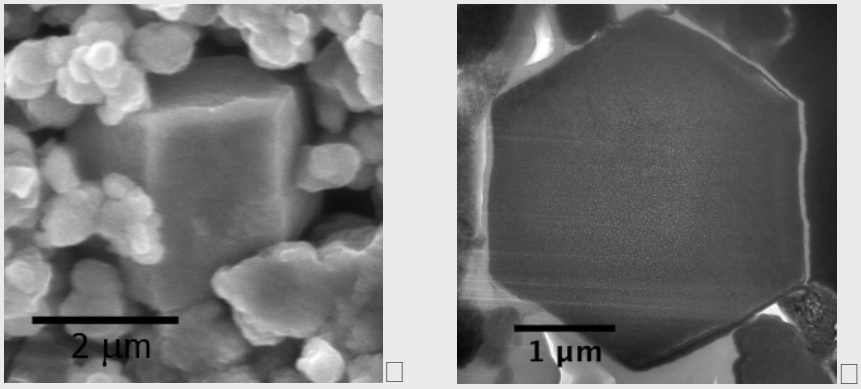

Figure 6. SEM image of hexagonal prism and amorphous material in **4** (left); TEM image of the thin slice of hexagonal prism from **4**, prepared by selective material ablation using FIB (right).

powder XRD data for **3**.

Solvothermal treatment of the same precursor in the presence of CTAB additive yielded a solid material (**4**), which contained limited amount of brick-red well-faceted hexagonal prisms up to 70 µm in size and a lot of apparently non-crystalline, smaller, yellow aggregates. A relatively small (3.6 µm between opposite corners of hexagonal base) hexagonal prism was localized in **4** under SEM (*fig. 6, left*) and used for sample preparation by FIB ablation (*fig. 6, right*). A thin slice was obtained perpendicular to the main axis of the hexagonal prism.

STEM and TEM examination of the as-prepared slice shows clear gradient in the size of the structural elements from lateral face to the center of the prism (*fig. 7, left*). The obtained images can be interpreted in two alternative ways: 1) the prism is composed of individual CdSe nanoparticles of different size, with a size gradient from small to large from surface to center; or 2) the prism represents continuous disordered 3D network of solid CdSe material with a more electron beam transparent to electron beam (most likely, organic) phase filling the voids (gyroid structure). Fourier transform of the TEM image of the central part of the prism shows reflections due to a coherent crystalline CdSe structure throughout the examined area (*fig. 7, right*), which presents an argument in favor of the second model. Additional examination will help to confirm the structure of the prism in **4**.

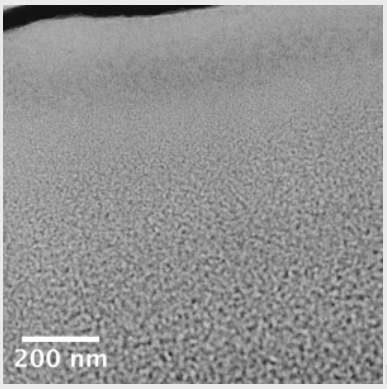

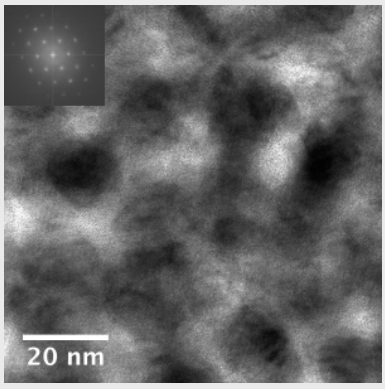

Figure 7. STEM image of thin slice through hexagonal prism from **4**: gradient from side to center shown from top to bottom (left); TEM image of central part of hexagonal prism (right). Insert: Fourier transform of TEM image showing reflections due to crystalline CdSe structure.

In summary, it was shown that with identical molar concentrations of a CdS or CdSe precursor, reaction temperature, and time of treatment, the particle sizes and morphology of secondary structure changes when alkylammonium salts were added to reactions. These results illustrate definite influences of the nature of additive used for solvothermal synthesis, although the exact role of the alkylammonium salt is at present unclear. TEM and STEM examination provide concrete data for the characteristics of the nanoclusters and the nature of their secondary structures. Further systematic work will be done on cementing the parameters that govern nanocluster growth and the self-assembly process.

3. Publications

[1]. Levchenko T., Kübel C., Huang Y., Corrigan J.F. *Chem. Eur. J.* **2011**, 17, 14394-14398.

4. Comments

The results obtained show the great importance of sample preparation method (wet or dry dispersing *vs.* FIB) in the case of TEM and STEM examination of secondary structures of nanodimensional CdS and CdSe.

As examination of the system will be continued, subsequent projects will certainly benefit from future collaboration with KNMF where both TEM and FIB techniques are available.

Proposal 2011-007-000774

Optimization of interferometric phase contrast imaging for dental imaging with higher energies up to 100 keV

Ciamak Abkai

Sirona Dental Systems GmbH
Bensheim
Germany

Note: *Please fill in this report form and save/print it as a PDF file, then upload it to the KNMF proposal submission system. A cover page containing proposal title, proposer name(s), and technologies selected will be added by the system. A link for the download of the complete report as a PDF file will be displayed in the system.*

Final Report

1. Project goals (max. 1.800 characters):

The main aim of this project was to compare simulation results and real experiment output for polychromatic Xray phase-contrast imaging (XPCI) for a given experimental setup and condition up to **100 keV** design energy.

Another target is to analyse the impact of XPCI for dental imaging, which could not be determined with provided gratings for a design energy of app. 23 keV.

By selecting a design energy of 100 keV and using xray sources powered with up to 125 kV we reach the maximum clinically possible energy for dental medical applications. Higher energies result in a more effective phase-contrast-ratio and reduce the patient effective dose.

2. Project results (max. 7.000 characters + figures):

A simulation and an experimental setup was realized during the project. Different visibilities V, for the different target energies 21.9 and 100 keV have been measured and simulated as shown in Table 1. As one can see the visibility for 100 keV is decreasing. The simulated results doesn't include the photon statistic and thus don't include SNR impact.

Design Energy [keV]	Visibility (Simulation)	Visibility (Experiment)
21.9	0.3688 ± 0.0017	0.1943 ± 0.0230
100.0	0.2447 ± 0.008	0.0546 ± 0.0010

Table1 : Simulated and experimentally obtained visibilities for the used setups

Karlsruhe Nano Micro Facility (KNMF)
Karlsruhe Institute of Technology (KIT)
Hermann-von-Helmholtz-Platz 1
76344 Eggenstein-Leopoldshafen
Germany

User Office
Phone: +49 (721) 608-3123
Fax: +49 (721) 608-6273
Email: knmf-useroffice@kit.edu
Web: www.knmf.kit.edu

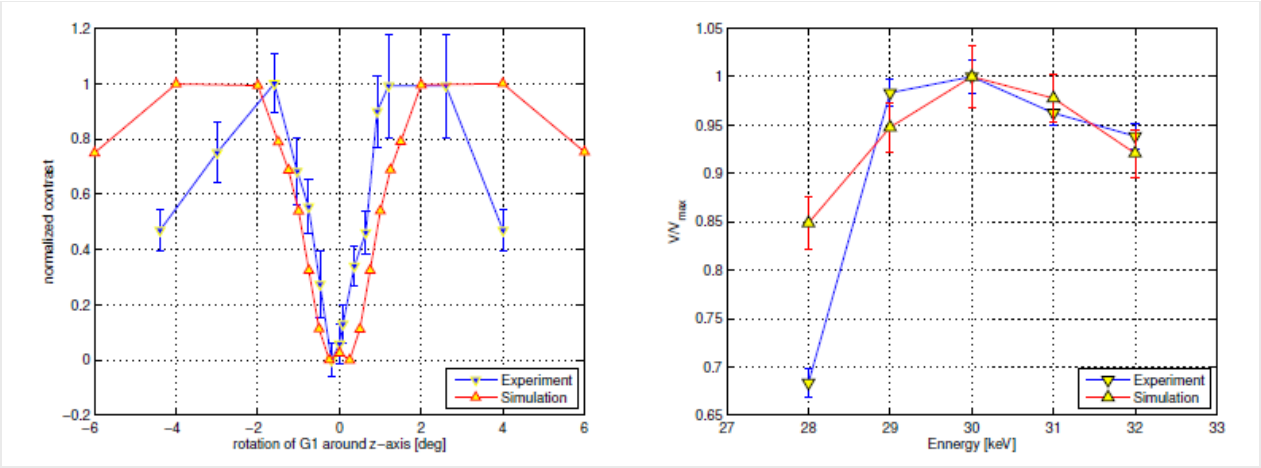

Figure 1: Sensitivity of the system : a) Influence of rotations of G1, b) Influence of tube voltage variations

Different Sensitivities have been examine in simulation and experiment, as shown in Figure 1.

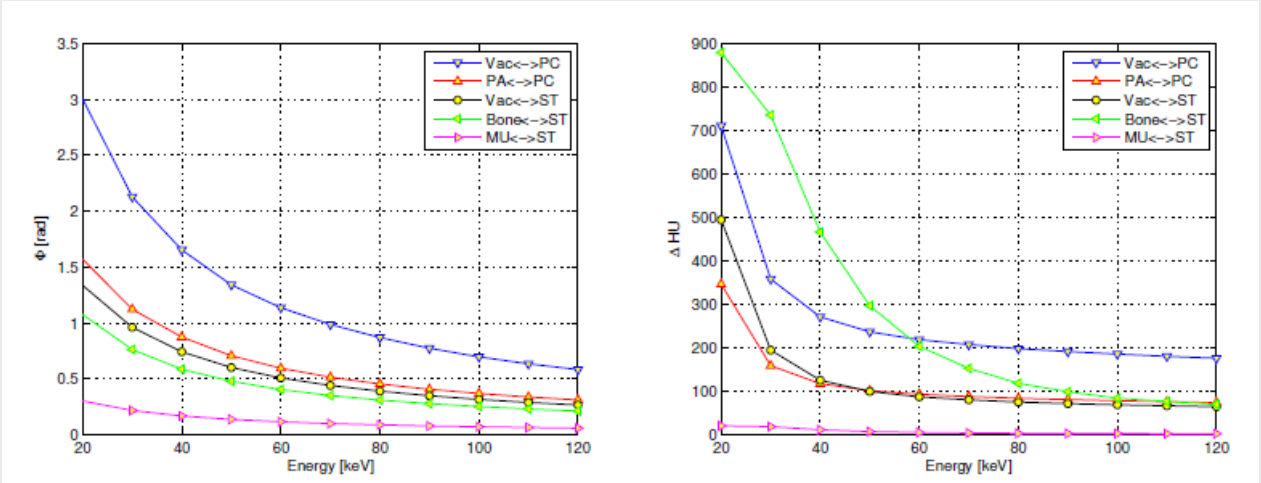

Figure 2: Expected phase shift and absorptions difference for different materials, depending on the mean xray energy.

The expected phase shift for higher energies is decreasing, as shown in Figure 2, for different materials. Experimental phase, absorption and darkfield results are shown in Figure 3. and 4. As one can see the results for 21.9 keV are very interesting, showing many details of the paraffin structure, however for 100 keV due to the bad Visibility, the results for phase-shift and dark-field images contain much less information in comparison to the absorption images.

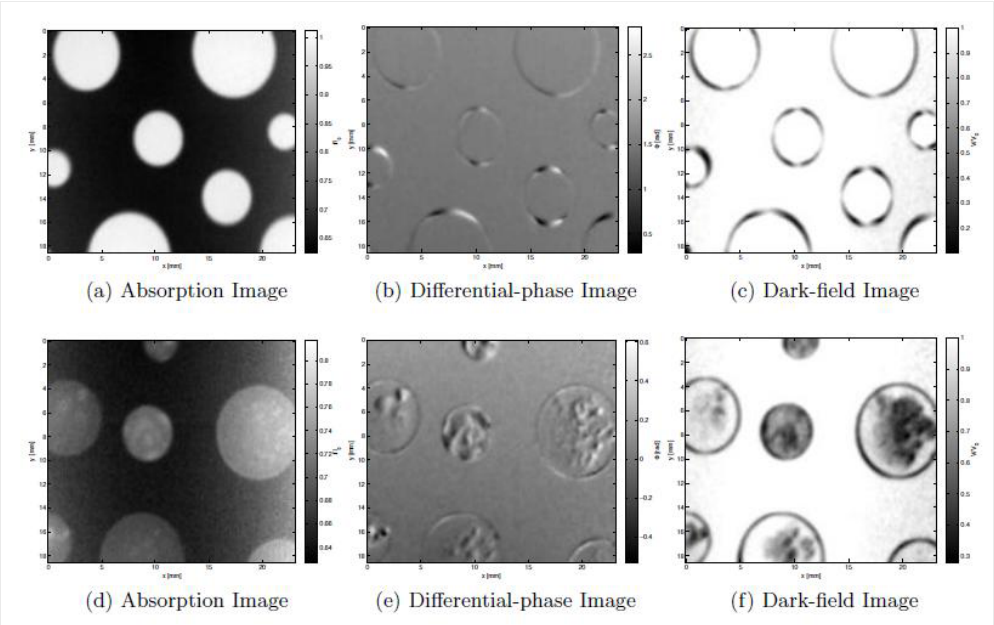

Figure 3: Results for 21.9 keV mean xray energy. Top: air gaps in polycarbonate phantom. Bottom: gaps filled with paraffin.

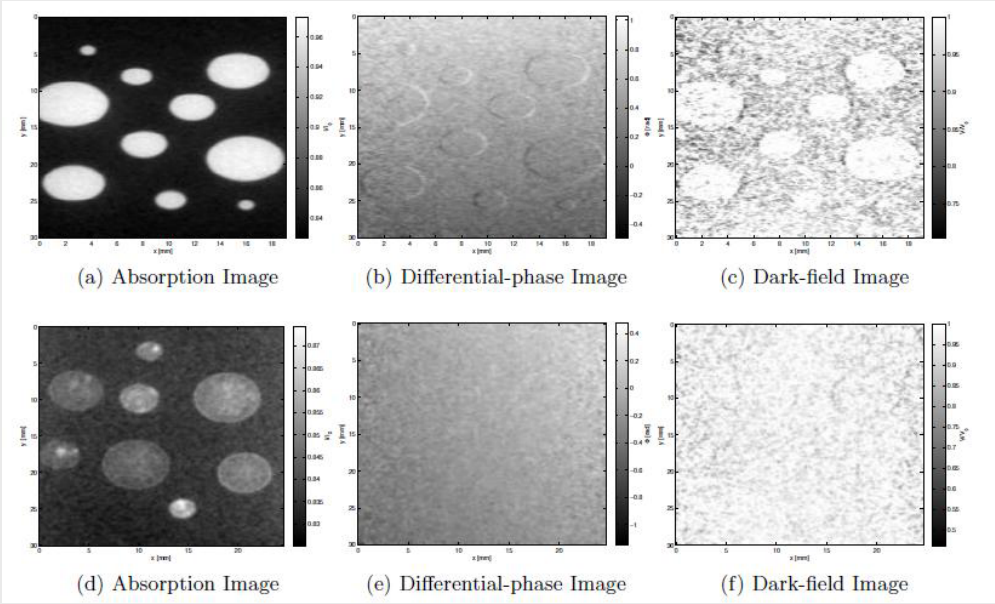

Figure 4: Results for 100 keV mean xray energy. Top: air gaps in polycarbonate phantom. Bottom: gaps filled with paraffin.

3. Publications (please stick to the user guidelines for publications and acknowledgements on www.knmf.kit.edu)**:**

Karlsruhe Nano Micro Facility (KNMF)
Karlsruhe Institute of Technology (KIT)
Hermann-von-Helmholtz-Platz 1
76344 Eggenstein-Leopoldshafen
Germany

User Office
Phone: +49 (721) 608-3123
Fax: +49 (721) 608-6273
Email: knmf-useroffice@kit.edu
Web: www.knmf.kit.edu

Publications are planed are in progress…

C. Guthier , C. Abkai, J. Ulrici, E. Hell, J. Schulz, J. Mohr, J.Hesser	First Interdisciplinary European Symposium on Biomedical Application of X-Ray Phase-Contrast Imaging Hotel Riessersee in Garmisch-Partenkirchen, Friday 13 Jan 2012.	2012

4. Comments (max. 1.800 characters)**:**

According to the experimental and simulated results, we can conclude that with the current limitations of the grating production process, it is not possible to use a system with 100 keV mean xray energy with reasonable contrast expectations for clinical and especially dental usage.

On the other hand the results for 21.9 keV are very promising for soft-tissue imaging, however due to the high z materials (bone, dentin, …) and the necessary high tube power not acceptable for dental applications.

Proposal 2012-007-000843

Design of 3D-micro batteries by combining laser-assisted printing and surface structuring

Alberto Pique

US Naval Research Laboratory
Washington, DC
USA

Final Report

1. Project goals (max. 1.800 characters):

The aim of this project was to establish a rather new type of electrode design appropriate for integration in compact micro battery devices. For this purpose, the electrodes made of lithium manganese oxide (LMO) or lithium cobalt oxide (LCO) were deposited by a laser forward transfer process developed at the US Naval Research Laboratory (NRL). The LDW technique has been used to deposit active materials such as LMO and LCO layers, while maintaining their electrochemical activity and structural integrity [1]. Unlike microbatteries based on sputter deposited thin film electrodes, the laser printed thick-film electrodes can provide much higher capacities per electrode unit area since their porous structure allows enhanced ionic and electronic transport through much thicker electrodes (~ 100 µm) without an increase in internal resistance [2].
At the Karlsruhe Institute of Technology (IAM-AWP) research activities are focused on laser structuring of thin film electrode materials for increasing the active surface area. This in turn leads to an improvement in electrochemical performance as presented in several publications [3,4]. This type of laser structuring process was applied to laser printed electrode materials for developing novel 3D structured lithium-ion micro batteries. The combination of rapid prototyping techniques such as LDW with a flexible design process like laser structuring allowed the rapid optimization of different micro battery designs and their high precision manufacture. A detailed investigation of the electrochemical properties as a function of the surface design enabled us to quantify and optimize improvements to our electrode design. Finally this was used to overcome the specific problems of Lithium-ion batteries with respect to mechanical and chemical degradation mechanisms especially when cycling the battery at high C-rates. This project brought together the strengths of the ongoing research at NRL on laser printing of energy storage materials [1,2] with the recent developments of the KIT group in laser texturing of electrode materials [3,4].

2. Project results (max. 7.000 characters + figures):

1.1 Laser-printed thick-film electrodes

Figure 1 shows SEM images from the laser printed cathode ($LiCoO_2$ + graphite + carbon black) and anode (MCMB 2528 + carbon black) layers. The agglomerated $LiCoO_2$ powder grains mixed with the much smaller graphite and carbon black are clearly seen in Fig. 1(a), while the MCMB 2528 spherical particles mixed with the smaller carbon black can be observed in Fig. 1(b). Both SEM images also show the highly porous structure of both layers. This high porous structure allows improved ionic and electronic transport without a significant increase in cell internal resistance.

Karlsruhe Nano Micro Facility (KNMF)
Karlsruhe Institute of Technology (KIT)
Hermann-von-Helmholtz-Platz 1
76344 Eggenstein-Leopoldshafen
Germany

User Office
Phone: +49 (721) 608-3123
Fax: +49 (721) 608-6273
Email: knmf-useroffice@kit.edu
Web: www.knmf.kit.edu

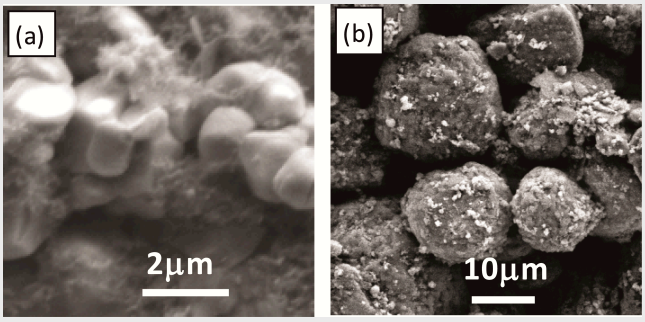

Fig. 1. SEM images of laser-printed (a) $LiCoO_2$ cathode and (b) carbon (MCMB2528) anode.

The thickness and mass of the laser-printed electrode are easily controlled by the number of LDW transfer passes. For example, the 25 μm-thick $LiCoO_2$ cathode film is obtained after 6 LDW passes (6x) and the 52 μm-thick cathode film is achieved after 12 LDW passes (12x). The film thickness is also controlled by the ink viscosity, i.e., the solids content, used for the laser printing. For high viscosity inks, fewer LDW passes are needed to achieve the same film thickness obtained with low viscosity inks. In the case of high viscosity inks, however, a higher laser power must be utilized to transfer the inks, which might affect the quality of the transfers.

Figure 2 shows discharge curves for the 5th cycle for packaged Li-ion microbatteries with $LiCoO_2$ cathodes of different thicknesses (25 – 105 μm). The batteries were charged and discharged at a constant current of 100 μA/cm^2. The achieved discharge capacity per active cathode area was proportional to the cathode thickness. The discharge capacity at the 5th cycle increases from 600 to 2360 μAh/cm^2 as the cathode thickness is increased from 25 to 105 μm. The coulombic efficiency of all the batteries becomes greater than 98% and stays almost constant for the rest of the following cycles.

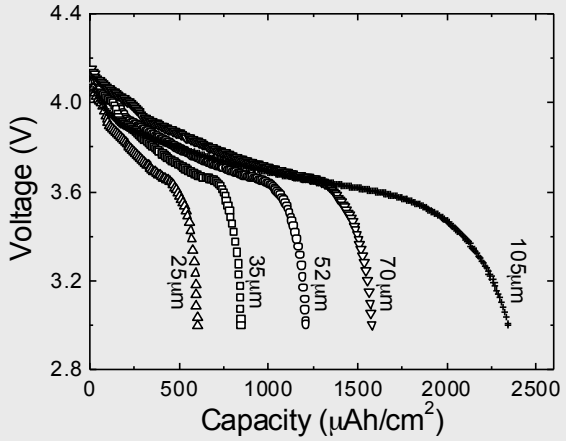

Fig. 2. Discharge capacity curves (5th cycle) for Li-ion microbatteries ($LiCoO_2$/GPE/MCMB) with laser-printed $LiCoO_2$ cathode films (25, 35, 52, 70 and 105 μm). The active electrode area is 0.49 cm^2. Batteries were charged at a constant current of 100 μA/cm^2. Based on the theoretical capacities of the $LiCoO_2$ cathode ($Li_{0.5}CoO_2$: ~140 mAh/g) and the MCMB anode (LiC_6: ~370 mAh/g), all microbatteries tested in this plot were cathode limited.

The battery performance of the laser-printed thick-film electrode microbatteries is compared against that of microbatteries fabricated with sputter-deposited thin-film electrodes. For example, Li-microbatteries with sputter-deposited 2.5 μm thick $LiCoO_2$ cathodes (active area = 1 cm^2) display capacities of ~160 μAh/cm^2 (or ~ 64 μAh/μm-cm^2) at a current density of 100 μA/cm^2 [5]. In this work, the Li-ion microbattery with a laser-printed 105 μm thick $LiCoO_2$ (active area = 0.49 cm^2) provided a capacity of ~2360 μAh/cm^2 (or ~ 22.5 μAh/μm-cm^2) at the same current density of 100 μA/cm^2. Even though the volumetric capacity is 3 times lower than that of the sputter-deposited thin-film cells, the laser-printed thick-film microbatteries can provide an order of magnitude higher discharge capacities per unit area. From this comparison, it is clear that laser-printed thick-film microbatteries are well suited for applications requiring not only high discharge capacity but also limited cell footprints due to size constraints.

Karlsruhe Nano Micro Facility (KNMF)
Karlsruhe Institute of Technology (KIT)
Hermann-von-Helmholtz-Platz 1
76344 Eggenstein-Leopoldshafen
Germany

User Office
Phone: +49 (721) 608-3123
Fax: +49 (721) 608-6273
Email: knmf-useroffice@kit.edu
Web: www.knmf.kit.edu

1.2 Laser structuring

Laser-printed $LiCoO_2$ thick films were further treated with laser structuring process using a KrF excimer laser in order to increase active surface area of the films for improving Li-ion diffusivity. In the first experiment the laser ablation conditions, such as laser pulse number and laser fluence, were investigated on the surface morphology of the $LiCoO_2$ thick films.

Variation of laser pulse number:

The influence of laser pulse number was investigated on the surface morphology of the $LiCoO_2$ films. For this purpose an area of 200 x 200 μm^2 was exposed to the laser beam with a fixed laser fluence of 1.5 J/cm^2. Figure 3 shows SEM images of laser structured $LiCoO_2$ thick films as a function of laser pulse number (N). After 100 laser pulses, surface melting is visible and formation of self-organizing surface structures is initiated with structure heights of several micrometers. For N = 200 pulses distinct micron-sized conical surface structures become visible. With further increasing the pulse number (N = 500 and 1000) the number of conical structures is reduced and the height of the cones is significantly increased. At a pulse number of N=1000 the aluminum substrate is exposed locally.

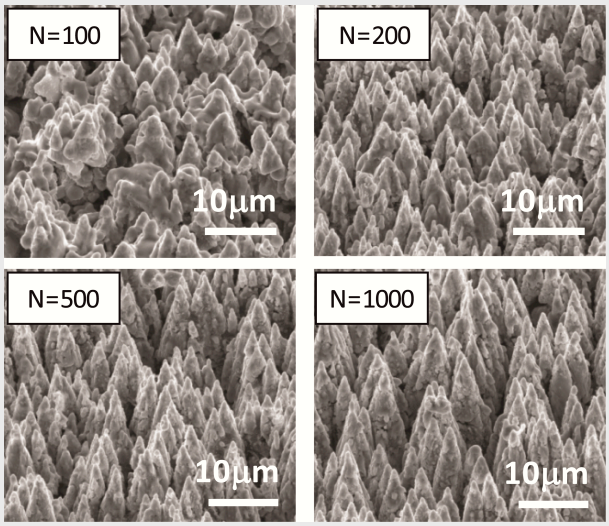

Fig. 3. SEM images of laser structured $LiCoO_2$ electrode with different laser pulse numbers (N). A KrF excimer laser (λ = 248 nm) was used to apply an energy density of 1.5 J/cm^2 with a pulse width of 5 ns and a laser repetition rate of 100 Hz.

Variation of laser fluence:

The laser fluence was observed to strongly affect the development of the self-organizing structures. Figure 4 shows SEM images of unstructured and laser structured $LiCoO_2$ electrodes. It can be seen that for a laser fluence of 1.0 J/cm^2 the height of the conical structures is in the range of about 5 µm. An increase of laser fluence leads to an increase in cone height. The height of the structures reaches values in the range of the film thickness (~35 µm) for a laser fluence of 1.5 J/cm^2. Furthermore, with increasing laser fluence the density of the conical structures is decreased. At a laser fluence of 2.0 J/cm^2 a significant amount of material is clearly ablated, leading to a sizeable loss in active material and substrate exposure. Therefore, a laser fluence of 1.5 J/cm^2 seems as suitable compromise between cone height, structure density and loss of active mass.

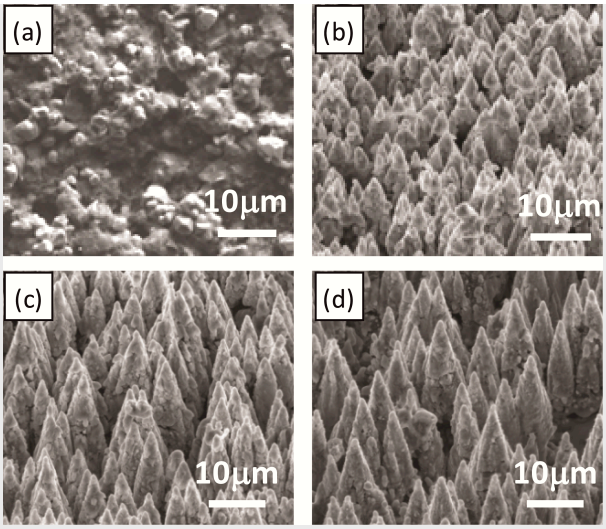

Fig. 4. SEM images of unstructured $LiCoO_2$ cathode film (a) and laser structured $LiCoO_2$ films with various laser fluencies of 1.0 J/cm^2 (b), 1.5 J/cm^2 (c), and 2 J/cm^2 (d). A laser pulse number was fixed at 1000 with a pulse width of 5 ns and a laser repetition rate of 100 Hz.

Electrochemical Analysis:

Electrochemical cycling was performed to investigate the influence of the laser-structured micro-structures on the electrochemical performance. Figure 5 shows the cycling performance of the unstructured and laser-structured $LiCoO_2$ cathode films at a constant current between 3.0 V and 4.2 V with a lithium metal anode and a liquid electrolyte of 1M $LiPF_6$ in ethylene carbonate/ dimethyl carbonate. A constant charge/discharge rate of C/5 was applied. The initial discharge capacities obtained are in the range of 100 -110 mAh/g. Although the unstructured electrode shows slightly higher starting capacities the laser structured cathodes exhibits improved capacity retention. After 25 cycles the capacities of both films reach to the identical value of ~90 mAh/g. At the end of the testing procedure (100 cycles) the laser structured electrodes showed a capacity of ~70 mAh/g, which was twice the remaining capacity of the unstructured cathode.

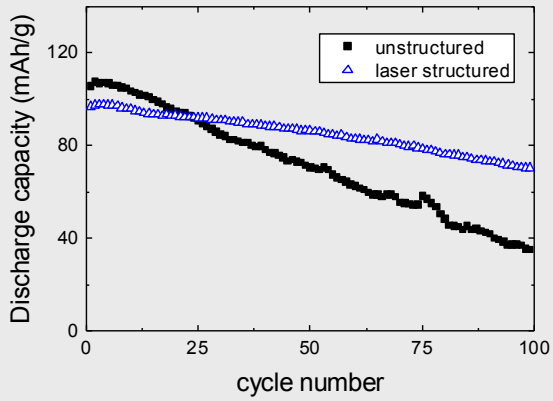

Fig. 5. Cycling performance of unstructured and laser structured $LiCoO_2$ cathode films. A laser fluence of 1.5 J/cm^2, laser repetition rate of 300 Hz and laser pulse number of 250 were used for laser structuring.

3. Publications (please stick to the user guidelines for publications and acknowledgements on www.knmf.kit.edu)**:**

[1] Kim, H., R.C.Y. Auyeung, and A. Piqué, *Laser-printed thick-film electrodes for solid-state rechargeable Li-ion microbatteries.* Journal of Power Sources, 2007. **165**(1): p. 413-419.
[2] Wartena, R., et al., *Li-ion microbatteries generated by a laser direct-write method.* Journal of

Power Sources, 2004. **126**(1-2): p. 193-202.
[3] Kohler, R., et al., *Laser micro-structuring of magnetron-sputtered SnO_x thin films as anode material for lithium ion batteries.* Microsystem Technology, 2011. **17**: p. 225-232.
[4] Proell, J., et al., *Laser microstructuring and annealing processes for lithium manganese oxide cathodes.* Applied Surface Science, 2011. **257**: p. 9968-9976.
[5] J. B. Bates, N.J. Dudney, B. Neudecker, A. Ueda, and C.D. Evans, Solid State Ion. **135** (2000) 33.

4. Comments (max. 1.800 characters)**:**

The combination of rapid prototyping techniques such as LDW with a flexible design process like laser structuring is very important for the optimization of current battery materials and the development of batteries with improved performance. The results of this project show great promise and demonstrate the potential of laser-based techniques for processing of battery materials and for the development of next generation energy storage systems. The resources provided by the KNMF proved of great value for the success of this project. It is my hope that we can continue our collaborative efforts with Dr. Wilhelm Pfleging's group in this area. Finally, a manuscript entitled "Laser-Printed and Processed $LiCoO_2$ Cathode Thick Films for Li-ion Microbatteries" describing the work performed under this project was submitted for publication in the Journal of Laser Micro/NanoEngineering on June 2012 and it is currently under review.